2013

Multiphase Hydrodynamics In Steady And Pulse Jet Mixing Systems

Ibraheem R. Muhammad
North Carolina Agricultural and Technical State University

Multiphase Hydrodynamics in Steady and Pulse Jet Mixing Systems

Ibraheem R. Muhammad

North Carolina A&T State University

A dissertation submitted to the graduate faculty

in partial fulfillment of the requirements for the degree of

DOCTOR OF PHILOSOPHY

Department: Mechanical Engineering

Major: Mechanical Engineering

Major Professor: Dr. John P. Kizito

Greensboro, North Carolina

2013

School of Graduate Studies
North Carolina Agricultural and Technical State University
This is to certify that the Doctoral Dissertation of

Ibraheem R. Muhammad

has met the dissertation requirements of
North Carolina Agricultural and Technical State University

Greensboro, North Carolina
2013

Approved by:

Dr. John Kizito
Major Professor

Dr. Gary Tatterson
Committee Member

Dr. Mannur Sundaresan
Committee Member

Dr. Arturo Fernandez
Committee Member

Dr. Nail Yamaleev
Committee Member

Dr. Samuel Owusu-Ofori
Department Chair

Dr. Sanjiv Sarin
Dean, The Graduate School

Biographical Sketch

Ibraheem Muhammad was born on August 14, 1986, in Dallas, Texas. He was raised in Richmond, Virginia. He graduated with honors, receiving a Bachelor of Science in Chemical Engineering from North Carolina A&T State University (NCATSU) in Greensboro, NC, in 2008. As an undergraduate he was an American Chemical Scholar. He received various awards and recognitions at NCATSU, including making the Dean's List (2005, 2006, 2007, and 2008); Venture Scholar; National Honor Society of Chemical Engineers (Omega Chi Epsilon). He participated in different societies and activities as an undergraduate including: the National Oceanic and Atmospheric Administration (NOAA) – Interdisciplinary Scientific Environment Technology (ISET) Scholar program; American Institute of Chemical Engineers (AIChE); National Society of Black Engineers (NSBE).

In 2008, Ibraheem Muhammad, directly entered the Mechanical Engineering Ph.D. program at NCATSU as a Title III fellow. As a student in the Ph.D. program he has not only participated in various research projects but also served as a supervised teacher in 2012. In November 2011, he participated as a panelist for the Quality Education for Minorities (QEM) Network, Professional Development Workshop for Underrepresented Minority Graduate Engineering and Materials Science Students. As a graduate student, Ibraheem has been a member of AIChE and American Society of Mechanical Engineers (ASME). He has also received recognition for his academic achievement, being invited into the Community of Graduate Scholars (COGs) at NCATSU and the Golden Key International Honor Society.

Dedication

I would like to dedicate this dissertation to Tamesha Hargraves, for all of her love and constant support throughout the long journey and to my mother and father, Terri and William, for all of the love, support, and guidance that helped shaped me to be the person I am today. Also, I would like to dedicate this dissertation to my sisters, Aliyah and Taahira and to the rest of my family and friends for their continuous motivation and inspiration.

Acknowledgments

I would like to first and foremost give thanks to God, for without Him, nothing is possible. I graciously thank my advisor, Dr. John P. Kizito, for all of his advice and mentorship through this journey in assisting me in completing the necessary research. Acknowledgment is given to Dr. G. Tatterson for his support in forming various experimental procedures. Also, thanks to Dr. A. Fernandez, Dr. M. Sundaresan, and Dr. N. Yamaleev is given for their advice and knowledge. Ackowledgment is given to the members of the Thermal-Fluids research group (Rodward Hewlin, Yacob Argaw, Richard Opoku, Elijah Kibler, Thomas Lawrence, Shiraz Moghul, Sanad Almahal, Md Monir Hossain, Katina Henson, Harry Bryant, and Monica Allen) for any assistance and/or advice that was received.

I would like to acknowledge the financial support of the Title III Program at North Carolina A&T State University, which is administered by the U.S. Department of Education, Institutional Development and Undergraduate Education Services. A special acknowledgment is given to Ms. Willetta Stamp, of Title III, for her constant support and guidance throughout the duration of the Ph.D. program. Thanks is given to Dr. Bala Ram as well.

Table of Contents

List of Figures

List of Tables

Abstract

The goal of the present study is to evaluate the mixing performance of jet mixers in both liquid and solid-liquid mixing processes. Jet mixers have been studied for decades for its uses in liquid blending and solid-liquid mixing applications. In solid suspension processes, jet mixers can be just as useful if not more useful than conventional impeller mixers. However, there is a lack of phenomenological models that exist. The erosion and subsequent suspension of solids beds, as well as the suspension of a low concentration of solid particles must be better understood. The specific objectives were to develop analytical, experimental and numerical models that simulate a liquid, submerged, steady or pulsing jet mixer. Furthermore, specific objectives were to determine the performance of jet mixers in solid suspension processes by measuring the cloud height, develop a model that describes the erosion of a solids bed, and determine the effect of cohesive particles on the dispersion of particles once eroded. The results showed that the mixing performance, in terms of mixing time, was not enhanced with the use of pulsing jet flows. The results showed that the cloud height below about 24000 is not dependent on the jet Reynolds number. The erosion profiles of solids were found for solids beds composed of particles with different Archimedes numbers and results showed that there appears to be two different regimes present. The regimes occur based on the erosion mechanisms that are taking place, mainly entrainment and surface erosion. Results of the axial concentration studies showed that the time dependence of the concentration ceases to exist after a certain period, which is a function of the weight percent of cohesive particles.

CHAPTER 1

Introduction

The overall goal of the present study is to study the hydrodynamics of steady and pulsing jet mixers. Single and multiple jet mixer systems are developed to study the mixing performance in liquid blending and solid suspension processes. Jet mixers can be used for various applications, including liquid blending, storm water treatment, pH neutralization, flash mixing, hazardous waste remediation, and other solid suspension processes. The advantages to using jet mixers compared to other more conventional mixers, such as impeller mixers, are that they are able to provide high turbulence and high shear rates while operating with no moving parts, therefore enabling a long life cycle. Jet mixers are thus ideal for hazardous processes in which maintenance can be dangerous because of the aforementioned advantages.

Currently, one main application of jet mixers is in radioactive nuclear waste management. The nuclear waste has been stored in remote locations going back to WWII and it is necessary to remove the waste from these storage tanks for re-processing and final disposal. There is about 70,000 m.t. of waste that is currently being stored at various sites (Arm, S. T., 2010) and about 10,000 m.t of HLW being produced annually. Of the total amount of HLW being produced annually, 85% of it will not be recycled and will require safe long term disposal (Sovacool, B. K. and D'Agostino, A., 2010). Over the last 20 years, grave attention has been put on improving disposal technologies in such a way that they meet the environmental protection and pollution prevention standards. The main option for a safe, long-term, the waste, especially the HLW, is nitrification, or blending the waste with solid glass material and treated with heat, then cooled and solidified in steel containers.

Since most of the nuclear waste, which exists in the form of sludge, slurry, and liquid, has settled at the bottom of the tank, it is necessary to suspend the solid material to create a fluidized mixture that can be pumped out of the vessel. The waste material is composed of solid particles of different shapes and diameters, therefore exhibiting different types of behavior. The smaller particles tend to increase the cohesiveness of the mixture. Such a phenomena causes the mixture to exhibit non-Newtonian behavior in which it acts like a Bingham plastic and possesses a yield stress which must be overcome for it to begin to move (Powell, M. R. et al., 1997). Studies have been completed in which larger, non-cohesive particles were studied, but the effect of smaller, cohesive particles within a solid-liquid mixture has not been studied extensively (Wells, B. E. et al., 2009).

Pulse jet mixers (PJMs) have been studied and used for suspension of sludge and slurries in nuclear waste remediation. However, submerged jet nozzle mixers with an arrangement similar to the current study have not been studied comprehensively for the re-suspension of solids. There are still many unknowns in the re-suspension of solids and the erosion of sludge mounds, including the behavior of solids once they are dispersed in the mixing tank (Tatterson, G. B., 1991; White, F. M., 1991; Yan-Fang, Y., 2011). More importantly, the erosion mechanics of solids containing varying amounts of cohesive materials is not well understood. Given the gaps in knowledge, the following specific objectives have been developed for the present study.

1.1 Specific Objectives

The specific objectives have been divided into how the solids bed is actually eroded and how the particles are dispersed once suspended.

1. To experimentally and numerically develop a hydrodynamic model that is capable of simulating the mixing behavior of a pulsing, submerged, liquid jet nozzle in a cylindrical mixing vessel.
    - The mixing patterns and characteristics jet mixers will be studied both experimentally and through the use of computational fluid dynamics software. The number of jets, orientation of the jets, and the jet height will be studied. The effect of different pulsing functions will be studied and compared to steady jet mixers.
    - An "in-house" particle image velocimetry system will be developed and used to measure the velocity flow field created by a vertical and angled impinging jet mixer.
2. To develop an analytical and experimental model that evaluates the performance of jet mixers in solid suspension processes by measuring the cloud height.
    - An analytical model is to be developed based on a balance of forces, including drag, weight, buoyancy, and added mass.
    - The cloud height will be measured using a visual technique in which the suspension of particles is recorded using a high speed camera.
3. To experimentally develop a model that describes the erosion of a solids bed using an impinging jet mixer.
    - The yield stress of varying amounts of mixtures of cohesive and non-cohesive particles will be determined. A Poiseuille flow tube rheometer will be constructed to determine the yield stress.

- The erosion profile will be determined as a function of time for two different solid beds composed of different particle sizes.
- The erosion mechanism of the solids bed will be observed for varying yield stress mixtures

4. To experimentally determine the effect of increasing amounts of cohesive particles on the dispersion of solid particles once eroded.
    - The concentration profile of the particles will be captured and analyzed using a non-intrusive imaging technique.

1.2 Overview of Dissertation

The current dissertation has been separated into five different chapters. The first chapter details the specific objectives and overall goal for the research aspect of the dissertation. Chapter 2 presents a literature review on jet mixers. The review includes general jet mixing information including the different types of jet mixers most closely related to that of the current work. Summaries on the operation of jet mixers in liquid-liquid and solid-liquid mixing systems are given. The review also gives summaries of the mechanisms on how jet mixers are able to erode, suspend, and mix in liquid-solid mixing systems.

Chapter 3 provides all of the methods and materials that were used to complete the research activities. A thorough description of the jet mixing system is given. The preliminary results used to help develop further methods and equipment is described. All analytical and numerical techniques that were used are also included in the chapter. Chapter 4 details all of the results and discussions of the present work. Chapter 5 presents the concluding remarks. Also, recommendations for future research work are reported.

CHAPTER 2

Literature Review

Liquid jets have been used for decades for various applications and its uses are still of growing interest. The current study uses a continuous and pulsing, submerged jet design which can be described as an unsteady, turbulent free jet. A thorough review on jet mixing system will be completed. The review will summarize literature on the mixing performance of submerged fluidic jets along with its use in solid suspension applications. Literature on the quantification of jet mixing, parametric jet mixing studies, and the mixing behavior will all be summarized in the following chapter.

2.1 Overview of Jet Mixing

Mixing is an important process in many industrial processes. Mixing in industrial processes is commonly achieved using impellers; however it can be done using other mechanical agitators, jet mixers, and acoustics. Certain applications limit the mixing technique that can be used. When dealing with the suspension of solid, radioactive waste in storage tanks, a mixer is needed which has no moving parts because of the safety risks that arise during maintenance of the equipment (Hylton, T. D. et al., 1995; Powell, M. R. et al., 1997; Meyer, P. A. and Etchells, A. W., 2007). In such an example, the preferred mixing technique is jet mixing. Jet mixers have been shown to be a viable mixing technique. Studies have reported that jet mixers are actually able to mix faster than regular impeller mixers (Fossett, H. and Prosser, L. E., 1949; Patwardhan, A. W. et al., 2003).

Jet mixing is a process employed in chemical, bio-chemical, pharmaceutical, and other industrial processes (Bathija, P. R., 1982). Jet mixing is ideal for the suspension of solid radioactive waste. When the liquid is discharged through a nozzle it exits at a high velocity. As

the jet travels it expands and entrains the bulk fluid; hence, creating mixing. Compared to mechanical agitators, jet mixers create high turbulence, high shear rates, and vortex motion to create rapid mixing (Manjula, P. et al., 2010). Jet mixers can operate with no moving parts inside the mixing vessel and therefore minimal maintenance is required. Jet mixers have life cycles much longer than conventional mixing operations, lasting around 25 years (Powell, M. R. et al., 1997; 1999; Patwardhan, A. W. and Gaikwad, S. G., 2003). During operation, the secondary waste is minimized, while installation is easy and the system can be moved to multiple tanks because of its design (Powell, M. R. et al., 1997; 1999; Patwardhan, A. W. and Gaikwad, S. G., 2003). The jet mixers can be used in combination with other jet mixers or other mixing equipment as well (Kurath, D. E. et al., 2006).

All fluid jet mixers discussed in this study have the same basic principle in common, which is a fluid is discharged from a nozzle. However, the actual design of the jet mixing systems may vary greatly. The next section describes various jet mixer designs that have been reported in literature.

2.2 Types of Jet Mixers

In the present study the term jet mixers refers to a class of mixers which withdraws liquid from a tank and discharges it back to the tank through a nozzle at high velocities. The difference between the different jet mixing designs are the driving force of the jet. As the jet is discharged through the nozzle it expands. As the jet expands, it entrains the surrounding liquid, creating circulatory patterns which act as a mixing mechanism (Jayanti, S., 2001; Patwardhan, A. W. and Gaikwad, S. G., 2003). The entrainment is due to the turbulent mixing layer that is created as a result of the velocity gradient between the jet and the slow or static bulk liquid (Perona, J. J. et al., 1998; Saravanan, K. et al., 2010). The vortices created at the outer edge of the jet are mainly

responsible for the mixing of the bulk fluid. There are several methods of introducing a jet into a bulk liquid.

One category of jet mixers is known as pulse jet mixers (PJMs). A schematic of a PJM system using two pulse tubes that was used by Meyer and Etchells (2007) is shown in Figure 2.1. The PJMs operate pneumatically, using compressed air as the driving force to force liquid through a nozzle. Using a submerged tube, the compressed air is vented and the tube refills with the contents of the tank, as the tube goes from high pressure to a vacuum. The pulse cycle is repeated whereas each periodic cycle constitutes a single "pulse" (Meyer, P. A. and Etchells, A. W., 2007).

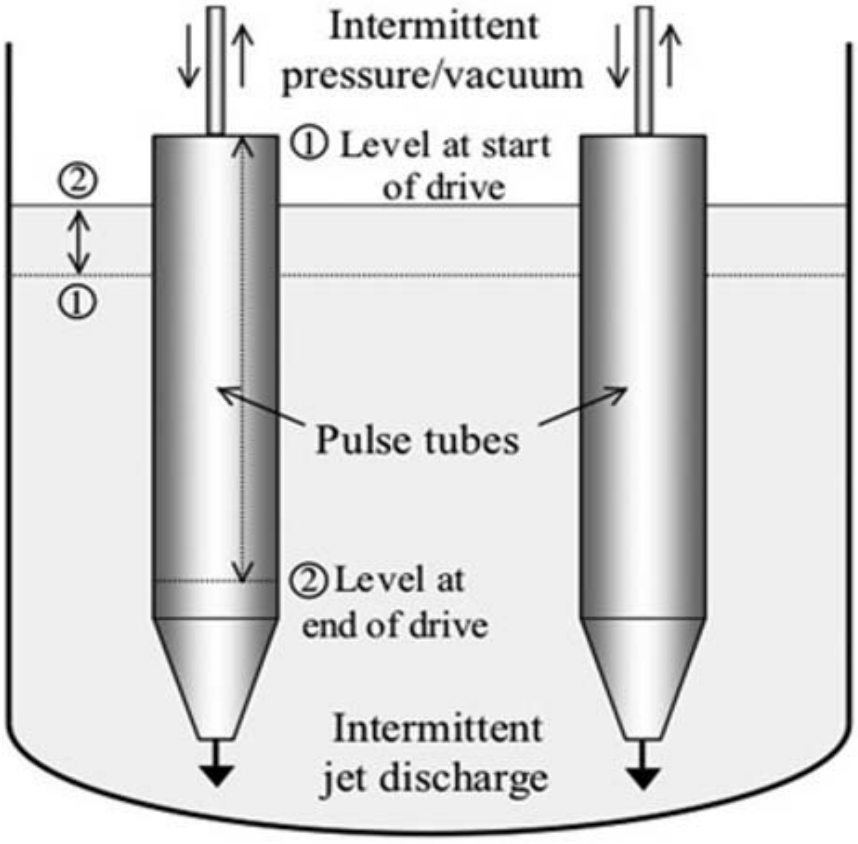

Figure 2.1. Illustration of a typical pneumatically operated pulse jet mixing (PJM) system presented by Meyer and Etchells (2007).

Extensive literature exists for the utilization of PJMs in the application of mobilization of solid material and more specifically, the suspension of radioactive waste (Hylton, T. D. et al., 1995; Chang, C. and Smith, P. A., 1996; Powell, M. R. et al., 1997; 1999; Meyer, P. A. et al., 2006; Meyer, P. A. and Etchells, A. W., 2007; Lee, S. et al., 2008; Caldwell, T. and Bhatt, P., 2009). The pulse jet mixers are extremely useful in nuclear waste remediation. However, issues have arisen with the nozzles becoming clogged as the equipment suctions and discharge various types of sludge and slurries through the same nozzle. The nozzle must be oriented at an angle like 45 or 60º to prevent the blocking of the nozzle.

Another class of jet mixers utilizes a pump to withdraw fluid from a tank and then discharges it back through a nozzle, to create a high velocity liquid jet. In some designs used in radioactive waste remediation applications, the entire mixture of sludge and water are withdrawn and discharged from the tank by a slurry pump, which is submerged in the sludge layer. The mixing systems are known as jet mixer pumps and submerged slurry pump is used within the mixture to create a jet (Hamm, B. A. et al., 1989; Powell, M. R. et al., 1997; Augeri, M. J. et al., 2004; Lee, S. et al., 2008; Lee, S. Y. et al., 2008; Ludwig, W. and Dziak, J., 2009). A vertical view of a slurry mixer pump is shown in Figure 2.2, where the suction and discharge locations can be visualized. It is shown the slurry material is suctioned in through the bottom of the apparatus and the material is discharged through numerous jet nozzles located at the outer edges of the pump riser. The slurry pump is submerged and it often rotates to create a sweeping motion along the tank surface, meaning it includes some kind of moving parts. Therefore, mechanical failure of some sort is ultimately inevitable. Using such an orientation can be hazardous as previously mentioned as any required maintenance would put workers in dangerous conditions. Also, the jet mixer pumps add heat to the waste in the storage tanks (1999).

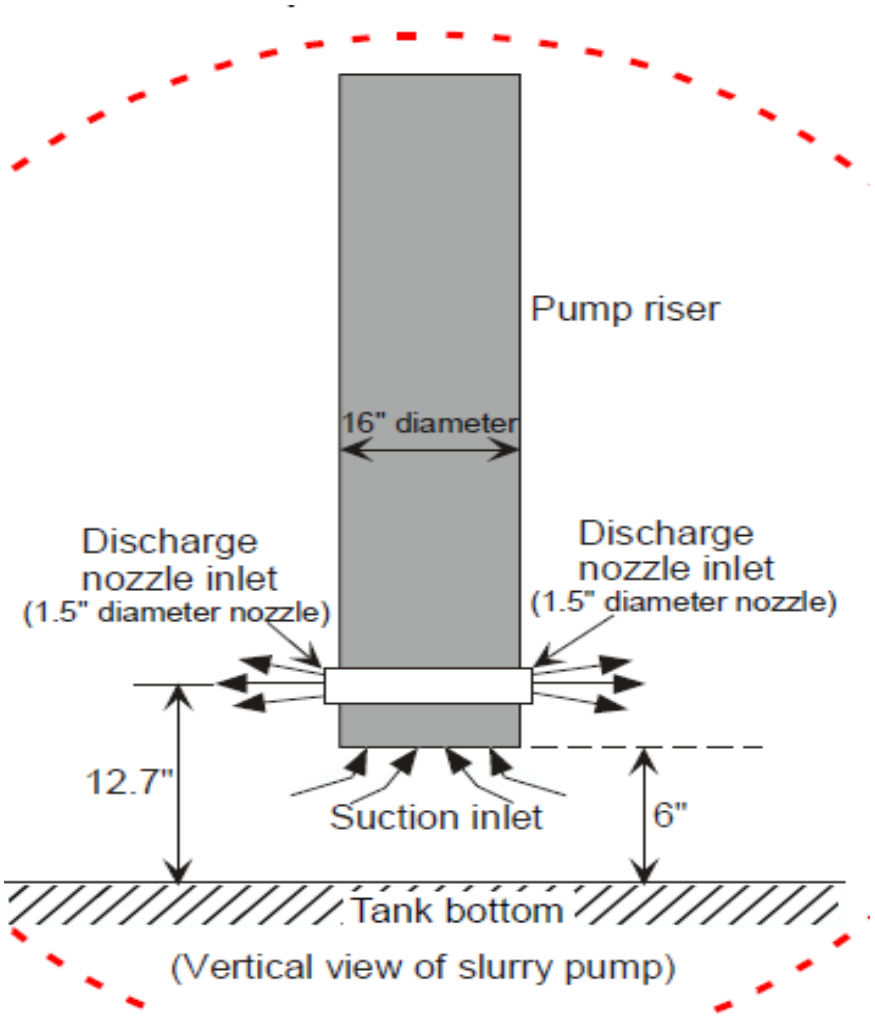

Figure 2.2. Schematic of a slurry mixer pump (SMP) presented by Lee and Dimenna (2008).

In other designs, an isolated pump is used to withdraw contents of the tank, either liquid or a mixture of liquid and solids, and discharged back through a nozzle, where the pump is located outside of the mixing tank (Patwardhan, A. W. and Gaikwad, S. G., 2003; Reshma, R., Daas, M., Srivastava, R., and Tansel, B., 2007). For distinction, these systems will be called submerged jet (nozzle) mixers. The jet nozzle mixing system used by Kale and Patwardhan (2005) is shown in Figure 2.3. The submerged jet nozzle mixers are different than the PJM's because they the driving force for the jet is a pump and they are different than the jet mixer pumps because they are stationary.

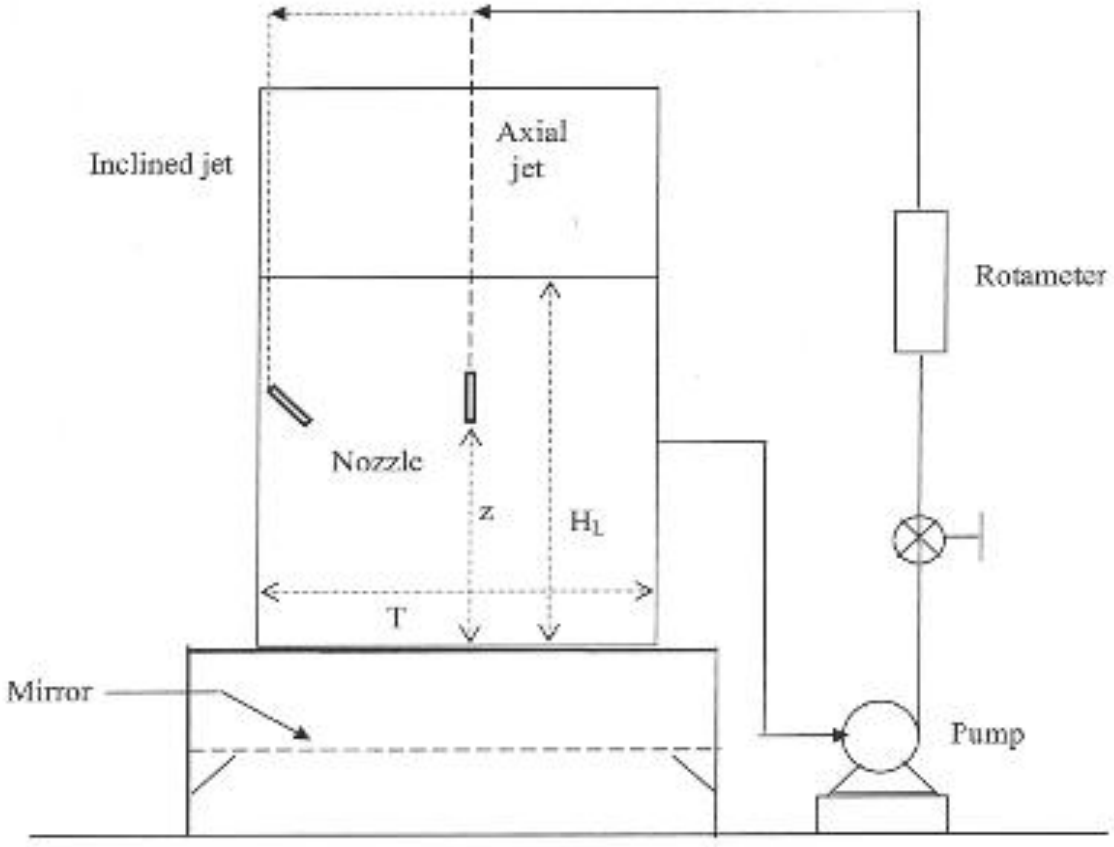

Figure 2.3. Schematic of submerged jet nozzle mixing system in which the nozzle is angled towards the base of the tank presented by Kale and Patwardhan (2005).

There are some issues that may arise when using PJMs and jet mixer pumps for solid suspension. The nozzle can become clogged as in the case with PJMs when suctioning and discharging out of the same nozzle. Also, when using PJMs, the driving force for the jet is compressed air. One disadvantage to using compressed air is to have air leaking in a chemically sensitive system (Mark Joy, 2010). When using slurry pumps, there is still a rotating pump submerged in the slurry, making maintenance more difficult and hazardous in the event of mechanical failure. Therefore, the present will focus only on jet flow created by submerged jet nozzles.

2.3 Jet Mixing Performance

The performance of jet mixers are usually determined by the extent of mixing that occurs and the length of time it takes to efficiently mix the vessel. The mixing time is often used to measure the mixing capability of jet mixers in liquid-liquid and solid-liquid systems and the effective cleaning radius (ECR) is used mostly in solid-liquid systems. The mixing time and ECR can be measured from experimental or numerical visualization studies and many correlations exist as a function of various system parameters.

2.3.1 Mixing time. The efficiency or the performance of jet mixers, or the extent of mixing, can be quantified by calculating the mixing time either from experimental or computational studies. The mixing time is defined as the amount of time it takes for 95% of the tank to become homogenized (Patwardhan, A. W., 2002; Zughbi, H. D. and Ahmad, I., 2005; Zughbi, H. D., 2006). Literature reports that a 99% homogeneity criteria for mixing time can also be used (Amiri, T. Y. and Moghaddas, J. S., 2010). Attention must be paid to the definition of the mixing time that each author uses because there can be a big discrepancy in results between reaching 95% homogeneity and 99% homogeneity (Jayanti, S., 2001). Concentration or temperature of a tracer are the parameters which are monitored to determine the extent of homogeneity, as the mixing time is determined as the time needed for the desired parameter to reach 95%, or 99%, of its final value (Zughbi, H. D. and Ahmad, I., 2005; Amiri, T. Y. and Moghaddas, J. S., 2010). Mathematically, the mixing time can be defined as

$$m = \left| \frac{C - C_f}{C_f - C_i} \right| \tag{2.1}$$

where C is the conductivity (or temperature) at a particular location in the system, C_i is the initial conductivity measurement, and C_f is the final value of the conductivity. Various tracers (i.e.

electrolyte, dye, hot water (Zughbi, H. D. and Ahmad, I., 2005)) are used for monitoring. Many researchers use mixing time as the sole variable to signify the extent of mixing and numerous correlations based on experimental studies have been developed, which will be discussed later in this chapter.

2.3.2 Effective cleaning radius. Another parameter used to quantify the performance of jet mixers is the effective cleaning radius (ECR). The ECR is defined as the sweeping, cleaning radius created on the bottom of the mixing tank as a pump rotates (Reshma, R., Daas, M., Srivastava, R., and Tansel, B., 2007; Lee, S. Y. et al., 2008). The ECR is a very useful indicator of jet mixer capabilities especially in applications where the bottom of a vessel needs to be cleared of solid mixtures. The effective cleaning radius can be expressed as a function of various parameters such as jet nozzle diameter, velocity, angle, and solution density.

B.V. Churnetski (1982) expressed an equation to predict the ECR as a function of various parameters as

$$ECR = C_1 D_o V_o \left(\frac{\rho}{2 g_c \tau_o}\right)^{0.5} exp\left(-C_2 \left[tan\left(\frac{1}{2\theta}\right)\right]\right) \quad (2.2)$$

where D_o is the jet nozzle diameter, V_o is the initial jet nozzle velocity, τ_o is the yield stress, g_c is the gravitational constant, and θ is the jet angle. The dimensionless constants, C_1 and C_2, have values of 4.0 and 6.2, respectively.

Hamm, et al. (1989) developed a phenomenological model for the cleaning radius and time in which they assumed a spherical expanding jet and sludge bank. The authors found that the following relationship exists between the cleaning radius and time when using a jet mixer pump:

$$X \propto t^b \quad (2.3)$$

Reshma et al. (2007) used a simulant slurry material exhibiting Bingham plastic behavior to visualize the ECR created in the mixing vessel. A schematic diagram was presented for the ECR using a 0˚ jet nozzle configuration as shown in Figure 2.4.

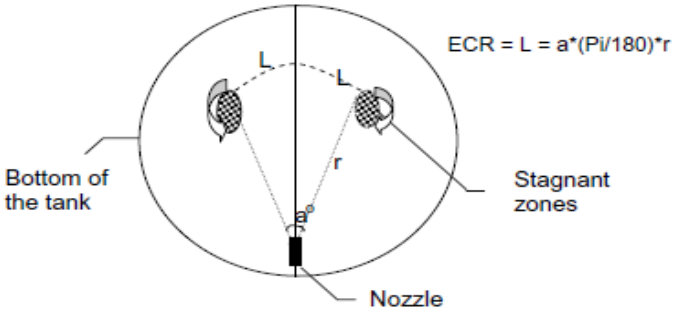

Figure 2.4. Schematic of ECR development as presented by Reshma et al (2007).

Reshma et al. also reported snapshots at different time frames were used to visualize the ECR as a function of time, which can be seen in Figure 2.5. The cleaning radius was found using a jet nozzle with an angle of 90º. The current study will look at the cleaning radius using computational methods, unlike previous authors, which mainly focused on experimental techniques.

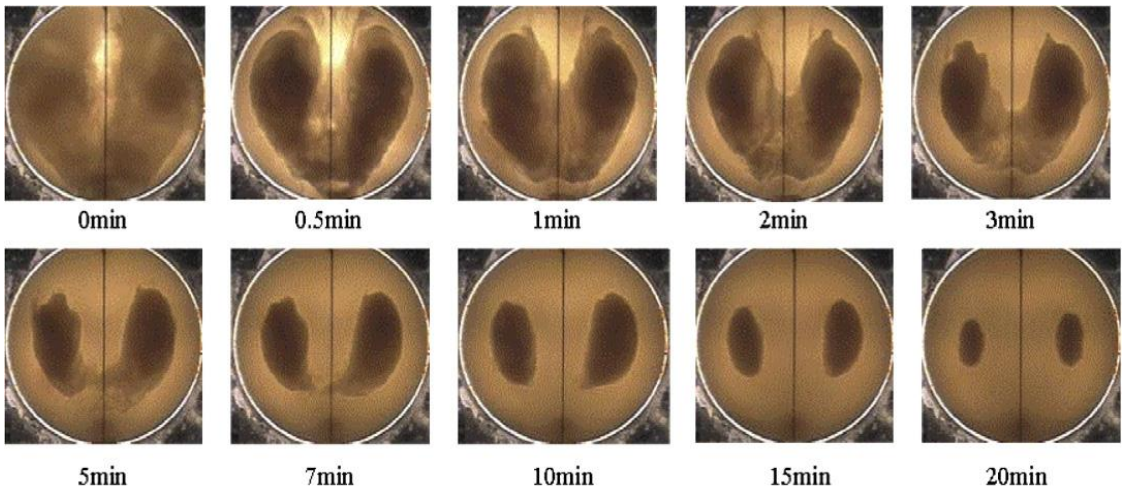

Figure 2.5. Visualization of the formation of the ECR as a function of time for a 90˚ nozzle angle as presented by Reshma et al (2007).

2.4 Jet Mixing Mechanisms

When a liquid jet is discharged from a nozzle, it expands and entrains fluids (Abramovich, G. N., 1963). The relative velocity between the jet and the bulk fluid creates a turbulent mixing layer which grows on the axis of the jet and entrains the bulk liquid. The entrainment is responsible for most of the mixing action in the tank (Rushton, J. H., 1980; Jayanti, S., 2001). Although the diameter of the jet actually grows due to entrainment of the bulk fluid, the centerline velocity of the jet decreases along its axis.

The pulsing, submerged jet used in this study acts as an unsteady jet and a turbulent jet; hence, it is important to review some of the literature on those jets which have been reported. The flow patterns created by the unsteady and turbulent jets have a vital role in the mixing behavior along with the axial velocity created by the jets.

2.4.1 Turbulent jets. Turbulent jet flows have been extensively studied in Newtonian fluids; however mixing of non-Newtonian fluids still lacks full understanding. Turbulent mixing is efficient as the irregular motions that are created over a wide range of length and time scales increases the interfacial area of contact. In fact, turbulence is the main reason that jets have the ability to mix equally or better than other techniques (Lee, S. et al., 2008). The nature of turbulent flow is characterized by large Reynolds numbers, diffusive velocity fluctuations, three dimensional vorticity fluctuations, and dissipation of kinetic energy (Tennekes, H. and Lumley, J. L., 1972). Turbulent flows are more capable of mixing than laminar flows because of the flow structures that are created.

As a fluid is discharged from a nozzle or an orifice, the jet flow becomes turbulent shortly after it is discharge. Abramovich (1963) reported that most of the mixing action occurs about 8 nozzle diameters from the jet discharge. As the jet travels, the velocity decreases along

the jet axis, but the jet spreads, entraining bulk fluid (Schlichting, H., 1979). As the cross sectional area of the jet increases, the momentum remains constant (Rushton, J. H., 1980). The angle at which the jet expands has been reported being between about 15˚ and 25˚ for flows outside the laminar region (Harnby, N. et al., 1992).

Figure 2.6 shows an example of a jet impinging on a solid surface and specifying the different regions which occur. Overall, there are three different regions: the free-jet, impingement, and wall jet regions. When the turbulent jet is discharge a free jet is created. The free-jet can be characterized in two distinct regions: the core, or flow development region, and the fully developed region. In the core region, the mixing layer penetrates inwards to the jet axis and a cone-like volume of jet liquid develops known as the potential core. The jet is said to be fully developed once the mixing layer has extended to the jet axis (Harnby, N. et al., 1992).

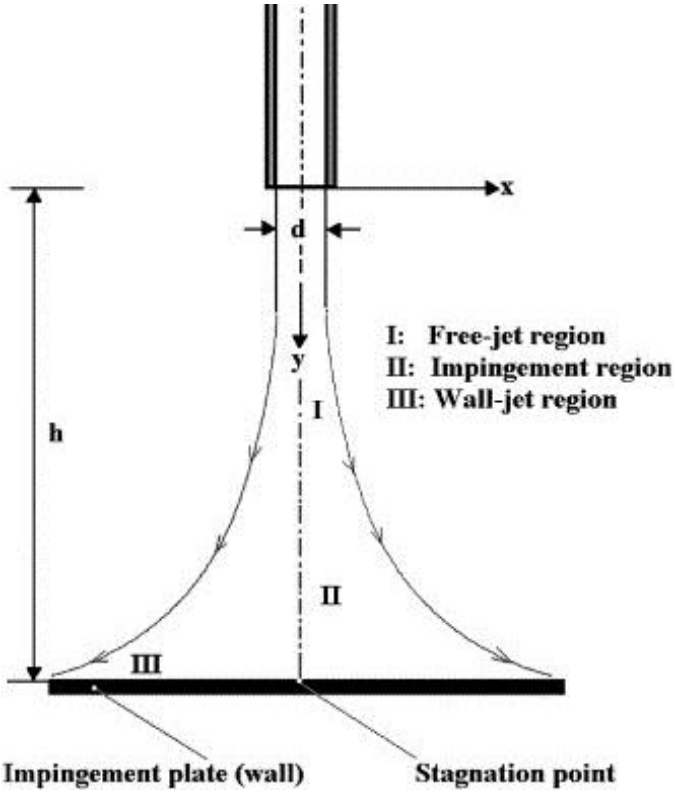

Figure 2.6. An impinging jet that shows the different regions of a discharging jet.

The jet velocity has a tremendous effect on the mixing in jet mixers. As the jet flow rate increases, the jet Reynolds number increases, which in turn increases the relative velocity between the jet and the bulk fluid (Amiri, T. Y. and Moghaddas, J. S., 2010). As the jet spreads radially outward, the jet velocity decreases because of turbulent mixing and entrainment of the bulk fluid.

Abramovich (1963) showed that a the non-dimensional velocity, V*, along the jet axis for a turbulent jet travelling through a relatively motionless bulk fluid is given by

$$V^* = C\left(\frac{d_j}{x}\right) \tag{2.4}$$

where C is a constant determined by the turbulent characteristics of the jet and x is the distance from the nozzle. Churnetski (1982) conducted large scale jet mixing experiments and found that the jet axial velocity can be predicted using

$$V_x = \frac{C_1}{x} V_o D_o exp\left(-C_2\left[\tan\left(\frac{1}{2\theta}\right)\right]^2\right) \tag{2.5}$$

where $\tan\left(\frac{1}{2\theta}\right)$ is a function of the kinematic viscosity, υ, which is given by equation (2.6) (Donald, M. B. and Singer, H., 1959; Rushton, J. H., 1980; Churnetski, B. V., 1982).

$$\tan\left(\frac{1}{2\theta}\right) = 0.238\nu^{0.133} \tag{2.6}$$

Rushton (1980) also developed an equation for the axial velocity for a circular jet, which is expressed as a function of the Reynolds number. The developed equation is expressed in equation (2.7).

$$V_x = 1.41Re^{0.135}\left(\frac{d_j}{x}\right) \tag{2.7}$$

Turbulent jets can be made unsteady by varying the discharge flow rate with respect to time. This creates another aspect of mixing which will be discussed in the following section.

2.4.2 Unsteady jets. Steady jets can be made unsteady by creating a pulsating jet flow as it is discharge from the nozzle. A pulsing jet can greatly affect mixing, as the flow field created by the jet is varied.

There is not extensive literature on pulsing jets in a submerged jet nozzle orientation similar to that used in the current study. Most of the literature on mixing using unsteady jets uses PJMs, where they are used for nuclear waste sludge suspension. When using unsteady jets, the initial period of discharge is the most important as this is the area which makes these jets different from steady jets.

Pulsing jets are advantageous as the initial penetration of the jet is enhanced, but this effect is not significant and it diminishes if momentum is not continuously supplied (Meyer, P. A. and Etchells, A. W., 2007). Pulsating jets creates unique mixing capabilities as the entrainment rate close to the jet is increased due to an increase in local vortices (Crow, S. C. and Champagne, F. H., 1971; Zhang, Q. and Johari, H., 1996). Zhang and Johari (1996) used flow visualization experiments to study the effects of acceleration on turbulent jets. A model was developed to predict the front position of the jet as a function of time.

Anders et al (2008) used large eddy simulations (LES) and Reynolds-averaged Navier-Stokes (RANS) simulations to study the interaction between an initial pulse followed by a subsequent pulse. Figure 2.7 shows an example of the LES of a pulse jet showing vorticity of 100,000 isosurface at 0.75, 1.0, and 1.25 ms. Results of the LES showed that there was a reduced strength of the vortex head from the first pulse. The results of the RANS showed that there was a decrease turbulent kinetic energy of the second pulse due to the first pulse.

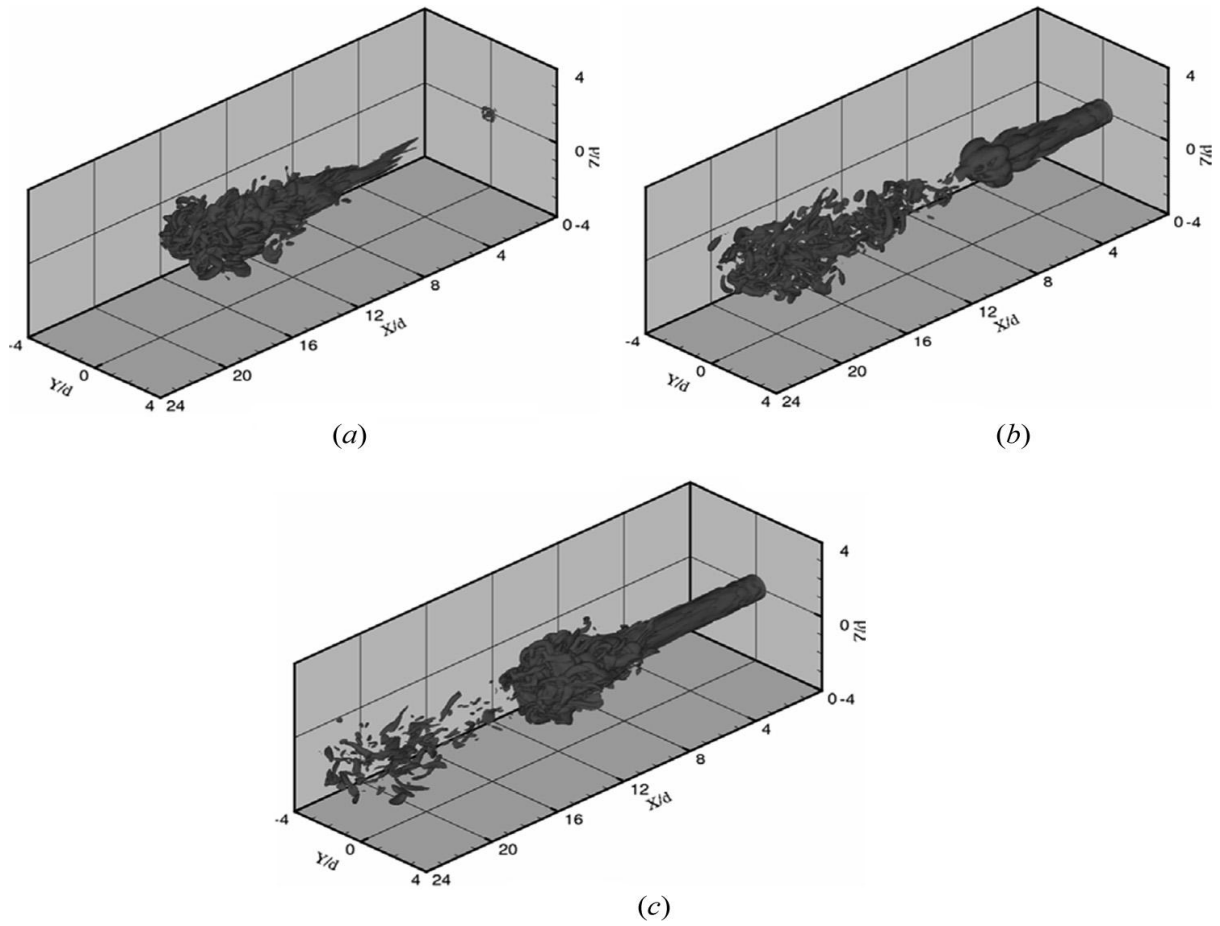

Figure 2.7. Vorticity results from LES of a pulse jet of 100,000 isosurface at (a) 0.75 ms, (b) 1.0 ms, and (c) 1.25 ms, courtesy of Anders et al. (2008).

The literature on pulsing jet helped design the pulsing jet mixer in the current study. Different pulse functions exist (i.e. ramp, square), but only square-wave pulses will be considered for this study. The pulses must be optimized such that the jet is discharging for a period of time and is stopped for another length of time to achieve the best mixing condition. Short pulses, where the jet is discharging for a short period of time and off for a short period of time, may not allow the jet to travel far, therefore making mixing inadequate in certain areas of the tank. On the other hand, an overly long pulse, where the jet discharges for a long time and is stopped for a short period of time, may simply behave more like steady jet.

2.5 Literature Review of Submerged Jet Mixers

Single and multiple submerged jet mixers are not widely researched, but the applications in widespread industrial processes make research essential. Various authors have researched the effect of a wide range of parameters on the performance of jet mixers. Various parameters affect the mixing patterns created in a mixing tank and ultimately the mixing time. The aim is to minimize the zones in the jet mixed tanks where mixing is minimal or non-existent, such that the tank is effectively mixed in the least amount of time possible. Longer mixing times leads to longer operation time and that ultimately leads to higher costs. Table 2.1 summarizes various correlations for mixing time that were developed by previous researchers for various jet mixing conditions and parameters. The existing literature on mixing time has been summarized in the current sections for submerged jet nozzle mixers for various jet configurations.

Table 2.1

Review of mixing correlations developed by previous researchers.

Author(s)	Jet Configuration	Mixing Time Correlation	
Fossett and Prosser (1949) and Fossett (1951)	Inclined side jet entry, D=1.5 m, H=0.9 m, d_j=0.002-5.7, Re_j=4500-80,000	$t_M = C_{inj}\frac{D^2}{V_j d_j}$	(2.8)
Fox and Gex (1956)	D = 0.305-1.524 m, V_j=0.3-15 m/s, d_j=0.00158-0.0381 m,	$t_M = C\frac{H^{0.5}D}{Re_j^{1/6}\left(V_j d_j\right)^{4/6} g^{1/6}}$	(2.9)
Van de Vusse (1959)	Inclined side entry jet	$t_M = 3.68\frac{D^2}{V_j d_j}$	(2.10)

Table 2.1

Cont.

Okita and Oyama (1963)	Inclined side entry jet	$t_M = 5.5\frac{D^{1.5}H^{0.5}}{V_j d_j}$	(2.11)
Hiby and Modigell (1978)	Axial jet	$t_M = 3.2\frac{D^2}{V_j d_j}$ $6000 < Re_j < 36000$	(2.12)
Lehrer (1981)	Model based on eddy viscosity	$t_M = \frac{0.658}{V_j}\left(\frac{\rho}{\rho_d}\right)^{\frac{5}{8}} d_j^{0.25}\left(\frac{V}{NA_j}\right)^{\frac{3}{4}} \cdot [-log(1-c^*)]$	(2.13)
Orfaniotis (1996)	D=500 mm, H=500 mm, d_j=9, 15 mm, H_j=H/2, H/3	$t_M = C\frac{D^{1.82}}{d_j^{0.82}V_j^{0.82}H^{0.09}}$	(2.14)
Grenville and Tilton (1996)	D=0.61-0.36 m, H/D=0.2-1.0, dj=5.8-50 mm	$t_M = 3\frac{L_j^2}{V_j d_j}$	(2.15)
Grenville and Tilton (1997)	D=0.61-0.36 m, H/D=0.2-1.0, d_j=5.8-50 mm	$t_M = S\frac{L^2}{V_j d_j}$ S = 9.34, Θ > 15° S = 13.8, Θ < 15°	(2.16)
Grenville and Tilton (2011)	D=0.61, 1.68, 3.98 m, H/D=0.2-4, d_j=5.8-47 mm, V_j=2.2-19.8 m/s	$t_M = 2.95\frac{L_j^2}{V_j D d_j}$	(2.17)
Perona (1998)	D=0.6 m, H=3 m, d_j=16, 22, 41 mm	$t_M = C\frac{V d_j}{Q L_j}$	(2.18)

One of the first jet mixing studies were conducted by Fossett and Prosser (1949; Fossett, H., 1951). The authors studied the use of jet mixers for blending aviation fuel in underground storage tanks. An electrolyte tracer was used to measure mixing time. The authors reported that the time for complete mixing is equal to about $8D^2/\sqrt{QU_j}$ seconds, as long as the injection time is less than half the total time. The jet mixers were predicted to take less time to mix a tank than standard mixing devices. Flow patterns for different jet arrangements were given, which are shown in Figure 2.8. The flow profiles were greatly affected by the number of jets and the orientation of the jets.

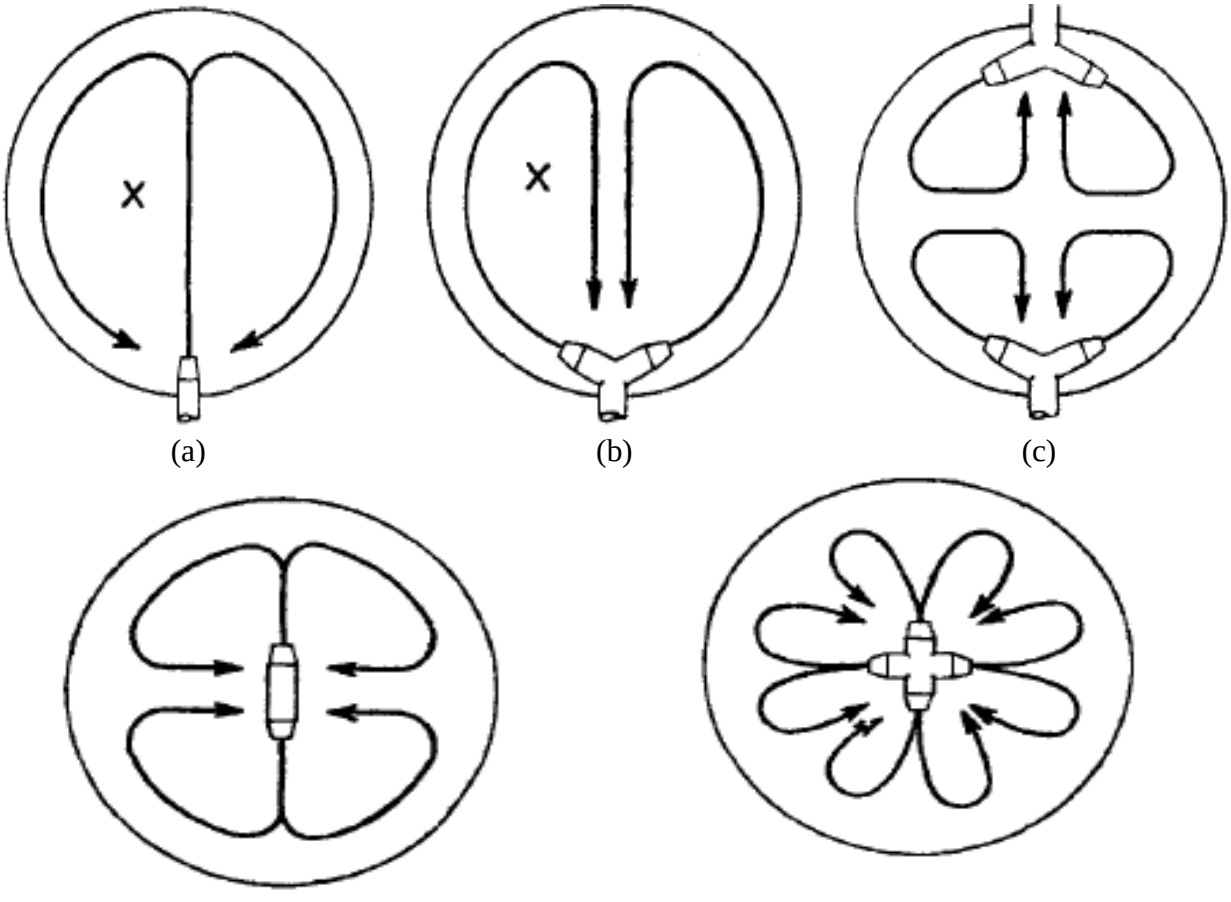

Figure 2.8. Flow patterns for various jet arrangements including (a) 1- jet, (b) 2-jets, (c) 4-jets, (d) 2-centered jets, and (e) 4-centered jets, presented by Fossett and Prosser (1951).

Fox and Gex (1956) used an acid neutralization reaction and a phenolphthalein indicator to calculate the mixing time of jets mixers and propellers in 1 – 5 ft. cylindrical vessels. The mixing time was calculated through visual observation of the indicator chemical. The tank diameter, aspect ratio, and jet velocity was varied and it was found that the mixing time using a turbulent jet is inversely proportional to the jet momentum flux by, $t_m = 1/M_j^{5/12}$. The results showed that less power is needed for a jet with a small diameter and high velocity rather than a jet with a large diameter and operating at low velocity. Van de Vusse (1959) and Okita and Oyama (1963) used an inclined side entry jet and disputed the results of Fox and Gex. The authors concluded that the mixing time is independent of the jet Reynolds number. Some of the discrepancy in the results was attributed to the manner in which Fox and Gex measured the mixing time.

P. W. Coldrey (1978) suggested a modified side entry jet mixing system. The author proposed that the longer jet length reduced the mixing time due to an increased mixing jet. Hiby and Modigell (1978) used a tracer to measure the 95% homogeneity mixing time in a flat bottom cylindrical tank, with an axial vertical jet. The researchers found that the mixing time is dependent on jet Reynolds number when the Reynolds number based on the tank diameter is less than 10^6. I. H. Lehrer (1981) proposed a mixing time model based on the assumption that the eddy viscosity is equivalent to the product of the jet Reynolds number and molecular viscosity.

Lane and Rice (1982; 1982) measured the 95% homogeneity mixing time using a violet dye tracer in a hemispherical base cylindrical tank with an axial jet mixer. System parameters such as jet velocity, tank dimensions, and fluid properties were used to develop a correlation for mixing time. The mixing time was found to be a function of the jet Reynolds number through

the use of a mixing time factor, F. The authors concluded that the mixing time dependency on the jet Reynolds number is substantial in the laminar regime and weak in the turbulent regime.

Maruyama et al. (1982) measured the 99% homogeneity mixing time in cylindrical tanks using an electrolyte tracer solution. An optimum condition of the jet nozzle height was found for a horizontal jet and mixing time was decreased using an inclined jet. Qualitative flow patterns were developed, as shown in Figure 2.9. Figure 2.9b shows that the mixing patterns created by the wall jets, are not conducive for effective mixing as the jet travels along the boundaries of the tank and not much mixing takes place in the middle of the tanks.. The wall effect causes most of the jet momentum to dissipate and further hinders it from being used for effective mixing throughout the entire tank.

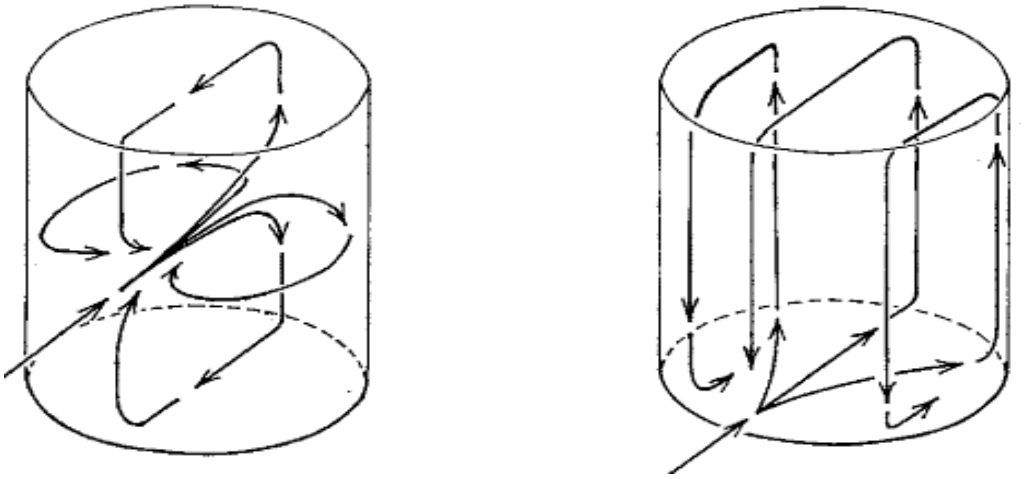

(a) (b)

Figure 2.9. Schematic of flow patterns induced by a (a) circular jet and (b) wall jet (Maruyama, T. et al., 1982).

Revill (1992) proposed a methodology for the design of jet mixed tanks. One of the main components of a good design is making sure the jet should be positioned so that the jet length is at its maximum. Maximum jet length is extremely important in jet mixed systems. Increasing

the jet length, in turn, increases the entrainment of the bulk fluid. The author proposed that jet mixers may be more economically feasible for processes, but they are less efficient than top entry agitators. The conclusion about the jet length being at a maximum is one of the most important aspects to designing a good jet mixing system for liquid blending processes.

Grenville and Tilton (1996) investigated mixing time by using an electrolyte pulse tracer with a jet mixer inclined at 45°. A correlation was developed based on the proposal that the local turbulent kinetic energy dissipation rate at the end of the jet path controls the mixing rate for the entire mixing tank. Grenville and Tilton (1997) later proposed a new correlation which utilizes mixing time being proportional to the circulation time. An assumption was made that the entrainment rate of the jet was proportional to the jet velocity and diameter. More recently, Grenville and Tilton (2011) reviewed the previous derived models and concluded that the model from Grenville and Tilton (1996) fits all data for $0.2 < H/D < 3$ and the blend time – circulation time ratio is dependent on the ratio of fluid depth to tank diameter.

Perona et al. (1998) studied the use of jet mixers in large storage tanks. Mixing time was measured using both single and double jet mixers. It was found that the mixing time was reduced greatly by using double jet mixers. Patwardhan and Gaikwad (2003) studied the effect of system parameters such as nozzle diameter, jet angle, and jet velocity on the mixing time. Contrary to other studies, a horizontal jet at the bottom of the tank provided lower mixing times than an inclined jet. At a given power consumption, the mixing time was reduced by increasing the jet nozzle diameter. Also, the correlation proposed by Grenville and Tilton (1997) was found to satisfactorily correlate the data.

In the past decade, more authors have used computational fluid dynamics (CFD) to study the performance of jet mixers. The use of CFD has allowed researchers to study the effect of a

wide range of system parameters on mixing time. One of the earliest CFD studies on jet mixing performance was completed by L. Brooker (1993). The model was able to predict the mixing time with a maximum error of 15%. P. D. Hoffman (1996) used 24,360 nodes to study half of a large storage tank, but the CFD model was not validated. S. Jayanti (2001) developed a CFD model to simulate jet mixing in a cylindrical mixing vessel. The effect of injection period and the geometry of the mixing vessel were studied. The flow pattern was found to be dependent on the shape of the mixing vessel. The flow pattern affects the mixing time and it is optimum when the dead zones, or the low velocity regions, are minimized.

A. W. Patwardhan (2002) provided a comprehensive CFD study on jet mixing performance by estimating mixing time. The k-ε turbulent model was with 216,000 nodal elements during meshing, which was the most for any jet mixing simulation up until that point. The model was compared to experimental results for a range of jet velocities, nozzle angles, and nozzle diameters. The CFD model was able to predict mixing time fairly well, but there was some discrepancies in the concentration profiles of the tracer, which was attributed to the eddy diffusivity levels. Patwardhan and Thatte (2004) used CFD and experimental studies to estimate the mixing time with varying jet velocities, liquid levels, and tank sizes. Similar to the results of other authors, the mixing time decreased with an increased in nozzle clearance from the bottom of the tank and increase in jet velocity.

Zughbi and Rakib (2002; 2004) evaluated mixing time in jet, pump-around configurations. The scalar quantity, temperature, was monitored to calculate a 95% homogeneity mixing time. Results showed that the jet angle of injection has a more significant impact on the mixing time than the jet path length. Also, the mixing time does not increase monotonically with the angle of injection or the height of the jets. But multiple jets do decrease the mixing time.

Figure 2.10 shows the results of Zughbi and Rakib compared to that of previous authors. The mixing time as a function of jet Reynolds number is exponential in nature for both the laminar and turbulent regime.

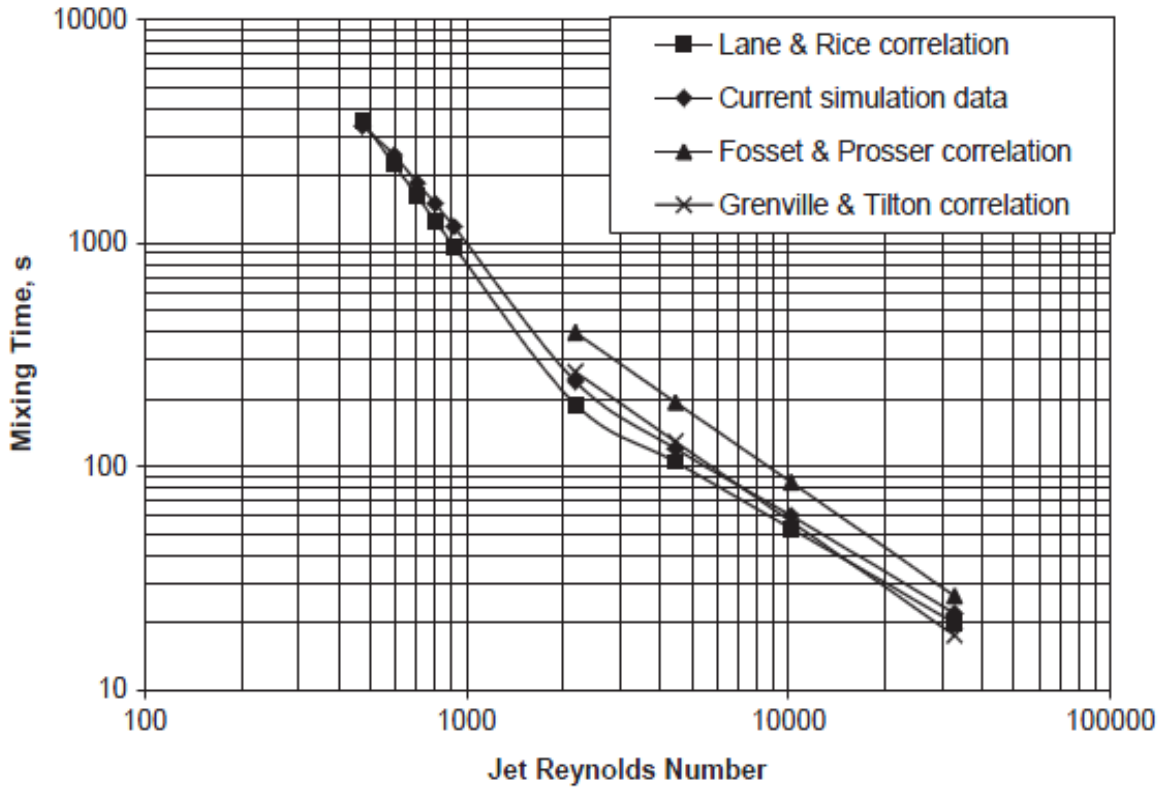

Figure 2.10. Results for mixing time versus jet Reynolds number as presented by Zughbi and Rakib (Zughbi, H. D. and Rakib, M. A., 2004).

The location of the jet is very important, as it affects the mixing patterns created in the tank. The mixing patterns is also affected by the geometry of the mixing tank (Zughbi, H. D., 2006). Zughbi and Ahmad (2005) discerned the effect of jet asymmetry on the mixing time by using both experimental testing and CFD modeling. Since the mixing time is strongly dependent on the flow patterns created in the tank, asymmetric jet configurations provided much lower mixing times than symmetrical jet configurations. Many other authors have studied the effect of system parameters on the mixing time in jet mixed tanks (Wasewar, K. L., 2006; Kalaichelvi, P.

et al., 2007; Sendilkumar, K. et al., 2007; Manjula, P. et al., 2010; Manjula, P. et al., 2010; Saravanan, K. et al., 2010; Yan-fang, Y. et al., 2010; Furman, L. and Stegowski, Z., 2011; Muhammad, I. R. and Kizito, J. P., 2011; Yan-Fang, Y., 2011) and research in the area of jet mixing using steady, submerged jet mixers are still being studied.

Some of the studies on submerged jet mixers have used not only steady jets, but unsteady jets as well. Simon and Fonade (1993) studied the mixing time using both steady and unsteady jets using an electrolyte solution. Jet configurations of one and two single jets and two alternate intermittent jets were studied. A mixing time factor, M, was assumed to evaluate the mixing time no matter the configuration. The unsteady jet mixers were found to be more energy efficient than the steady jets. Orfaniotis et al. (1996) studied both steady and unsteady jet mixing in a cylindrical reactor. The effect of jet height and liquid viscosity on mixing time was studied using eight conductivity probes. The results showed a decrease in mixing time with the use of alternating jets. Ranade (1996) studied flow patterns and mixing performance using a CFD model. The effect of steady and alternating jets were investigated. The alternating jets, in which multiple jets discharged a liquid jet in different periodic cycles, did not necessarily lead to lower mixing times. However, there was an increase in the initial dispersion of a tracer. The increase in the tracer dispersion can signify that the alternating jets might be effective in solid suspension processes. As the flow is accelerated to a certain value the fluid upstream of the jet increases in momentum because of the increasing jet velocity. But when the jet is being decelerated, the entrainment rates are much more noticeable (Johari, H. and Paduano, R., 1997).

From the literature on jet mixers, it is seen that most studies focus of jets that are introduced at the bottom of the tank and directed towards the liquid surface at an angle. When the jets are located at the bottom and directed upwards, the greatest jet path length is achieved

and ultimately, a greater entrainment rate of the jet. The jet length can be defined as the point at which its centerline velocity reaches about 1-5 % of its discharge velocity (Patwardhan, A. W. and Thatte, A. R., 2004). The jet length can also be defined as the point length from the jet nozzle to the point where it impacts the wall.

Several studies use impinging jet mixers in which the jet is directed towards the bottom of the vessel, such as the configuration used in the current study. Efficient mixing can be achieved with the jet directed toward the base of the vessel, due to the flow patterns created in the tank. When the flow pattern is able to circulate fluid from a high velocity, or "active region", of the tank to a low mixing zone, then effective mixing can be achieved.

2.6 Solid Suspension by Jet Mixers

For years now, jet mixing has been explored for solid suspension applications such as crystallization, dissolution, flocculation, and leaching. However, there is not much literature for solid suspensions using pulsing fluidic jets, especially in a design similar to the current study. Jet mixers can act just as efficiently in solid suspension applications compared to conventional impeller mixing. Bathija (1982) reported that jet mixers can perform 20-40% more efficiently that mechanical agitators for solid suspensions because of the entrainment of fluid from the bottom of the tank. The amount of increased efficiency depends on the desired amount of suspension. Thus, jet mixing is a suitable technique for various applications outside of the scope of this study as an alternate to conventional impeller mixed systems. The current section focuses on the use of jet mixers for suspending particles. The succeeding section will go on to review the use of jet mixers, specifically pulse jet mixers, for the erosion of sludge mounds.

Various forces act on the particle as a particle travels through a liquid. The drag, lift, buoyancy, and weight acting on a particle can be balanced to formulate equations which

calculate the settling (terminal) velocity of a free falling particle, assuming it to be spherical (Abulnaga, B. E., 2002; Wells, B. E. et al., 2009).

Various correlations for terminal velocity have been established in past literature and was summarized by Abulnaga (2002). The various terminal velocity correlations are valid for a particular range of particle diameter sizes. For instance, for very fine spherical particles, the flow is in the Stokes regime (Re << 1) and the terminal velocity is expressed as

$$V_t = \frac{(\rho_s - \rho) d_p^2 g}{18 \rho \mu} \tag{2.19}$$

where ρ_s is the particle density, ρ is the liquid density, and d_p is the particle diameter. Other equations exist for settling velocity depending on the particle Reynolds number or the regime that the particles exist in. Correction factors also exist which to account for particle interaction with the wall and particle-to-particle interaction. As a particle interacts with cylindrical walls or other particles, the settling rate is hindered. Therefore, the terminal velocity of a free falling particle can be thought of as the maximum settling rate of the particle, as no other interactions are present. In most applications, it is not only important to suspend solids from the bottom of a tank, but also to maintain suspension. Understanding the settling behavior of particles under various conditions is very important.

Particulates can be classified as being either cohesive or non-cohesive. Cohesive particles have an average diameter less than 0.0625 mm and non-cohesive particles have an average diameter greater than 0.0625 mm (Abulnaga, B. E., 2002). For very small particles, diameters less than 2 μm , other forces add to the cohesive nature such as van der Waals forces, Columbic attraction, electrical double layer forces, and hydration forces (Wells, B. E. et al., 2009).

In order for the suspension of non-cohesive particles to occur, the settling velocity must be overcome by an opposing force. The hydrodynamics forces being exerted on the materials must overcome the cohesive forces of the particles along with overcoming the settling nature to suspend and keep the particles in suspension (Lee, S. Y. et al., 2008; Wells, B. E. et al., 2009). Once the cohesion forces are weakened, the top layer of the sludge mound then erodes and is transported away by the jet entrainment. The erosion process continues until the entire material is disintegrated and suspended. Erosion mechanics will be discussed in more detail later.

2.6.1 Parameters affecting the suspension of particulates. There are various properties, such as fluid velocity, particle size, specific gravity of a particle, and tank liquid level that play a vital role in particle suspension applications (Lee, S. Y. et al., 2008). Others parameters such as jet injection location and angle are important for solids suspension using jet mixers. The main parameters used to measure the performance in solid suspension applications using a steady jet is the just suspension velocity, or the velocity at which the base of the tank is clear of all solids for a short period of time. The critical suspension velocity has been used in systems using an unsteady jet (Meyer, P. A. et al., 2009). Also, cloud height, or the distinct interface which is formed from suspended particles at which no particles are suspended above, is used to measure performance of jet mixers in solids suspension. Some studies on solid suspension investigating these parameters using both submerged jet mixers and pulse jet mixers have been summarized.

Racz et al. (1977) used a jet mixer for solids suspension and provided an empirical correlation to estimate the velocity of the jet nozzle required to suspend solids. P. R. Bathija (1982) studied jet mixing applications and reported a design process for jet mixers in solid suspension processes. Shamlou and Zolfagharian (1990) used an impinging jet mixer and

determined the just suspension velocity of the jets as a function of jet nozzle diameter, height, solid particle size, and particle density. The best results were found with the jet located at about half of the liquid height. Kale and Patwardhan (2005) studied the suspension of solid particles in water in a cylindrical vessel using axial jet mixers and inclined, submerged jet mixers. The effects of nozzle clearance, nozzle diameter, nozzle angle, nozzle location, particle size, and solid loading on the power needed for solid suspension were all studied. A semi-empirical model was created to predict the just suspension velocity for solid suspensions based on the various aforementioned parameters.

Reshma et al. (2007) used submerged jet nozzle mixers to study the suspension of non-Newtonian slurries in a cylindrical vessel. The jet system consisted of two horizontal discharge nozzles and all of the slurries tested exhibited behavior of a Bingham plastic. The authors reported that as the jet flow rate was increased, the ECR was also increased. Hamm et al. (1989) studied the suspension of sludge in large scale tanks using a jet mixer pump. A phenomenological model was developed, based on the process of the suspension of sludge, which can predict the cleaning radius as a function of time.

Various studies have been completed using pulsed jet mixers to suspend the particles simulating radioactive waste, exhibiting rheological behavior of a Bingham plastic. In pulsed tube designs, a cavern forms at the base of the tank and there is an observable line in the tank at which no solids lie above. This is known as the cloud height, or sometimes referred to as the cavern height (Meyer, P. A. et al., 2009). Researchers have found that the cavern is formed in both steady, axial, downward pointing jets and unsteady, axial jets. Models have been developed to predict the cavern height as a function of physical and flow properties in non-Newtonian fluids for steady jets, pulsed jets, and multiple pulsed jets (Bamberger, J. A. et al., 2005; Meyer,

P. A. and Etchells, A. W., 2007). The cloud height along with the critical suspension velocity is the key parameters used to characterize performance of PJMs for solid suspension. The cloud height will be measured in the present study. The studies that use submerged jet nozzle mixers similar to the apparatus used in the current study did not focus on the cloud height.

2.7 Non-Dimensional Parameters

There are several important non-dimensional parameters that are used in steady and pulsed jet mixing systems., which have been listed in Table 2.2. The non-dimensional parameters were derived for PJMs (Bamberger, J. A. et al., 2005; Meyer, P. A. et al., 2005; Meyer, P. A. et al., 2009), but have been extended to the specific arrangement in this study. The jet Reynolds number (Re_j) is the ratio of dynamic stress to viscous stress. The yield Reynolds number (Re_y) relates the dynamic stress to the relevant slurry shear stress, which is a big factor in the determination of the cloud/cavern height (Meyer, P. A. et al., 2005). The Strouhal number (St) is the ratio of the pulse time to the jet flow time scale. The Hedstrom number (He) is the ratio of the jet Reynolds number and the yield Reynolds number. The Deborah number (De) is the ratio of pulse time to material response time and it affects the ability of the unsteady flow at the cavern interface to suspend slurry particles (Bamberger, J. A. et al., 2005).

Table 2.2

Important non-dimensional parameters used in pulse jet mixing systems.

Non-dimensional Parameters		Variables	
Density ratio	$\varepsilon = \rho_s/\rho$	ρ_s	solids particle density
Solids volume fraction	$\Phi_s = V_s/V_{REF}$	ρ	liquid density
$V_{REF} = (\pi D^{3)}/4$		H	liquid height

Table 2.2

Cont.

Particle diameter ratio	ds/D	D	tank diameter
Nozzle diameter ratio	d/D	υ	kinematic viscosity
Aspect ratio	H/D	U	jet velocity
Pulse volume fraction	$\Phi_p = V_p/V_{REF}$	D	jet nozzle diameter
$V_{REF} = (\pi D3)/4$		U_t	unhindered terminal velocity
Jet Reynolds number	$Re_j = Ud_j/\upsilon$	d_s	diameter of solids particle
Froude number	$Fr = U^2/gd(\varepsilon-1)$	τ	fluid shear stress
Particle Reynolds number	$Re_P = U_t d_s/\upsilon$	τ_s	shear strength
Particle Froude number	$Fr_p = U_t^2/gd_s$	μ	fluid dynamic viscosity
Strouhal number	$St = t_D U/d_j$	t_D	pulse time
Yield Reynolds number	$Re_y = \rho U^2/\tau$	t_{mat}	material response time
Hedstrom number	$He = \rho\tau_s d^2/\mu^2 = Re_j^2/Re_y$		
Deborah number	$De = t_D/t_{mat}$		

Though it is known that jet mixers can be used for solid suspension and the erosion of sludge, slurry materials, much information is still missing on how that mixing is taking place and how the particles are dispersed in the mixing vessel (Thien, M. G. et al., 2010). In nuclear waste operations, it is not only important to suspend the solid material from the bottom but also to keep the solids in suspension. Because strict standards have to be followed, it is important that the dispersion of the solids once suspended is understood, as sampling issues may arise.

2.8 Erosion Mechanisms

There have been numerous studies completed on the mixing and suspension of sludge materials exhibiting non-Newtonian behavior, mostly using PJMs and SMPs. Though the erosion of the sludge has taken place, not much literature has been presented which explains the erosion and subsequent suspension behavior of the material. The method of erosion and suspension of non-cohesive materials should be studied, as well as paste-like slurries and sludge. Studies should then be extended to include mixtures containing both cohesive and non-cohesive particulates.

In mixing vessels, the behavior of non-cohesive slurries and cohesive slurries depends on the particle characteristics and the solids concentration. The different size particles and agglomerated particles settle in different manners (Gauglitz, P. A. e. a., 2010). There are different modes in which erosion of the sludge mounds take place. The different mechanisms of erosion of a homogeneous solids material (i.e. solids bed) can be grouped into the four categories (Abulnaga, B. E., 2002). The different mechanisms of erosion can be used to help explain results of the erosion studies. The erosion profile can vary depending on the mode of erosion that is present.

Entrainment occurs usually when the material strength is weak and the particle size is small, causing the material to act as a viscous fluid under an applied stress. A schematic of the entrainment mechanism is shown in Figure 2.11. Entrainment is one of the most prevalent erosion mechanisms found throughout nature. Entrainment is especially important in the current study as the phenomenon occurs at the outer edges of the jet as it discharges and expands. The entrainment of the bulk fluid and particulates is responsible for most of the mixing that occurs in jet mixed systems.

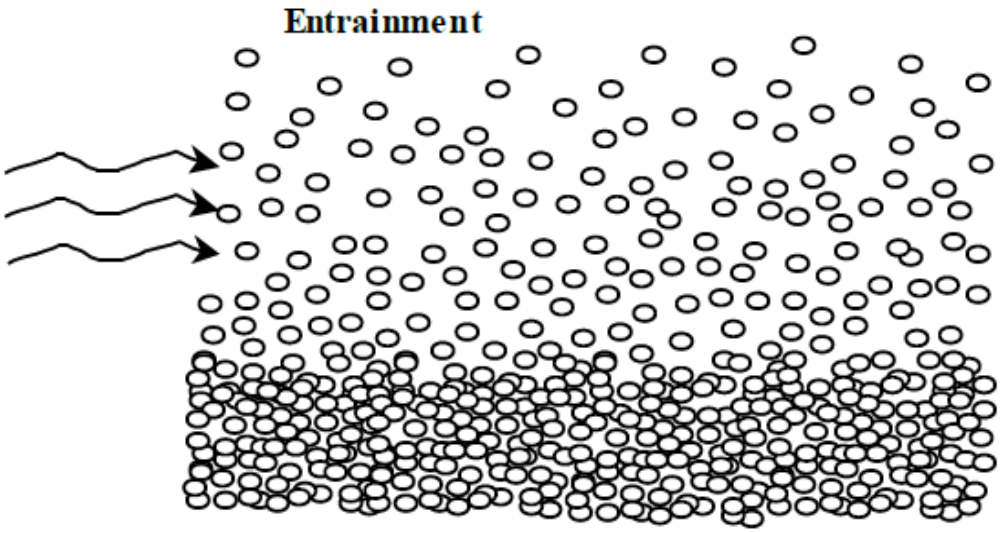

Figure 2.11. Entrainment of homogeneous solids bed (Abulnaga, B. E., 2002).

Floc erosion occurs when chunks of weakly bound particles through aggregation, known as flocs, are dislodged from the surface of the bed. A schematic of the erosion mode is shown in Figure 2.12.

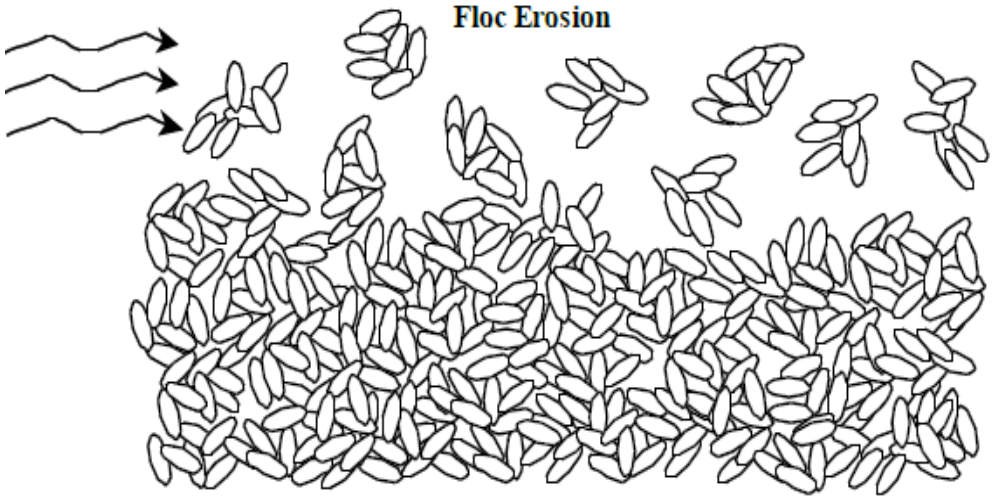

Figure 2.12. Floc erosion of a homogeneous solids bed (Abulnaga, B. E., 2002).

Surface erosion occurs when individual particles are removed from the bed surface, as the applied shear stress is equal to or greater than the bed's critical shear stress. Figure 2.13 displays a schematic of the surface erosion phenomena.

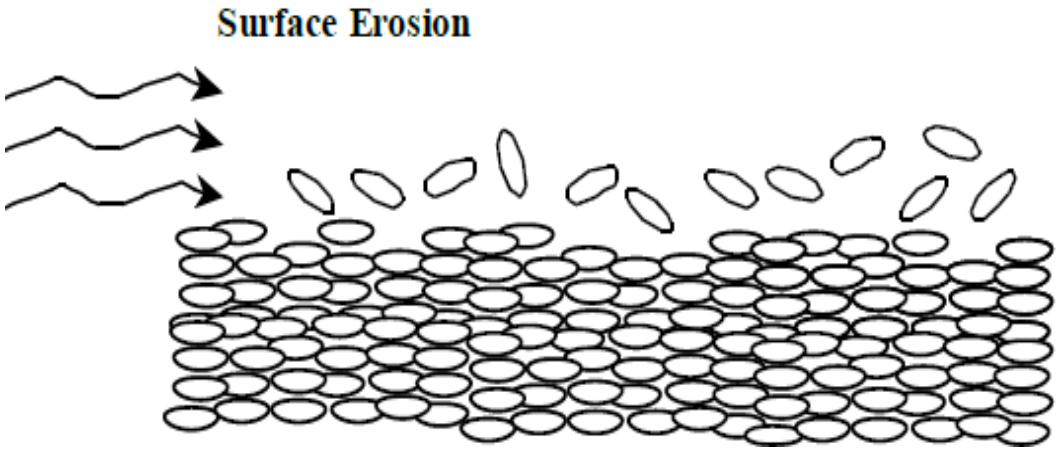

Figure 2.13. Surface erosion in a homogeneous solids bed (Abulnaga, B. E., 2002).

Mass erosion occurs when a plane below the bed surface fails due to the applied shear stress. If the excess shear stress is increased once surface erosion occurs, mass erosion begins to occur. This erosion mechanism is shown in Figure 2.14.

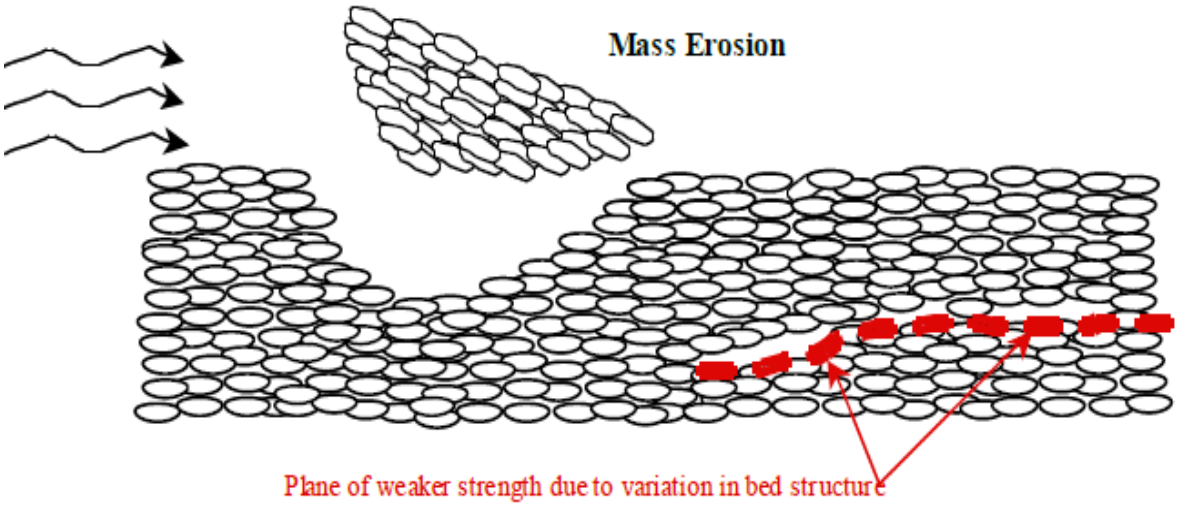

Figure 2.14. Mass erosion of a homogeneous solids bed (Abulnaga, B. E., 2002).

Different types of waste forms exists, where most of the solids are very small and the agglomeration of these small particles affects such properties as the slurry viscosity, yield strength, particle density, and sedimentation rates (Onishi, Y. et al., 1996). The smaller particles will agglomerate and form larger particles, if the flow of the slurry is slow enough (Onishi, Y. et

al., 1996). The rheological characteristics of the sludge or slurry should be known, which will be described in the next section.

2.9 Sludge Rheology

Powell et al. (1997) stated that the performance, or the effectiveness, of jet mixers for the erosion and suspension of sludge mounds depends on the axial decay of the turbulent jet, the impingement of the jet on the sludge mound, and the erosion mechanism of the sludge mound. Since most of the waste material is cohesive, the rheology, solid loading, hindered settling, interaction between solid concentration, and solid agglomeration, and mixing intensity all must be understood. The authors reported empirical equations for the deposition and erosion of fine cohesive sediment which were found by Partheniades (1962) and Krone (1962), respectively. The expressions for the deposition and erosion of fine cohesive sediments are shown below.

$$S_d = w_s c\left(1 - \frac{\tau_o}{\tau_{cd}}\right) \qquad for\ \tau_o < \tau_{cd} \tag{2.20}$$

$$S_e = E\left(\frac{\tau_o}{\tau_e} - 1\right) \qquad for\ \tau_o > \tau_{ce} \tag{2.21}$$

where c is the solid concentration, w_s is the apparent particle fall velocity, E is the erodibility coefficient, τ_o is the bed (mound) shear stress, τ_{cd} is the critical shear stresses for deposition, and τ_{ce} is the critical shear stresses for erosion. Also, S_d is the amount of solids deposited per unit bottom surface area per unit time and S_e is the amount of solids eroded per area per unit time.

The critical shear stress is an important parameter in the erosion of non-Newtonian mixtures or any cohesive materials. The critical shear stress, which depends on the composition of the material, particle size distribution, particle shape, and packing, is one of the main parameters that determines initial erosion of a sludge mound (Lee, S. Y. et al., 2008). For non-Newtonian material, once the critical shear stress threshold is reached, the material no longer

remains stationary. Various correlations exist to determine the critical shear stress in different conditions. One example on such a correlation is expressed as (Wells, B. E. et al., 2009)

$$\tau_c = 0.015(\rho_b - 1000)^{0.73} \tag{2.22}$$

where ρ_b is the density of a solids bed. The critical yield stress will be determined in the current study, but it will be obtained through experimentation. Correlations will be given for the yield stress as a function of wt. % of solids, unlike equation (2.24), which presents the critical yield stress as a function of the solids' bed density.

2.10 Erosion Rates

To understand how particles behave once suspended, it is necessary to comprehend not only how, but the time it takes to get in suspension. The erosion rates of cohesive materials have been presented in past literature. Wells et al. (2009) presented an equation originally used by A. Mehta (1991) for the erosion rate of cohesive materials. The equation, shown below, contains a linear relationship for the erosion rate and the excess shear rate.

$$E = M\left(\frac{\tau - \tau_c}{\tau_c}\right) \tag{2.23}$$

where M is the erosion rate parameter which is found experimentally, τ_c is the critical shear stress, and τ is the applied shear. There have been many discrepancies using the equation but other researchers have found that a linear relationship does exist for the rate of erosion and the excess shear as long as surface erosion is the mode of erosion.

Jet mixers have been used for a while now and will continue to be used in industry for various applications. Based on the lack of knowledge in literature on jet mixing systems, the specific objectives, presented in Chapter 1, were formed. Chapter 3 will present the detailed

methodology and all of the materials used to meet the specific objectives stated for the overall goal of the research.

CHAPTER 3

Methods and Materials

The following chapter will describe the methods of the experimental and numerical studies. The details of the components included in the submerged jet nozzle design and the equipment used to measure various parameters. The methods of the experimental and numerical studies will be described. Development of the analytical model describing particle suspension will also be discussed. Specific descriptions of all of the tasks involved will be given.

3.1 Problem Description

The present work studies the mixing hydrodynamics of submerged jet mixing systems. Liquid and solid-liquid mixing systems are studied using both steady and unsteady jet mixers. Figure 3.1 shows a schematic of the general problem description.

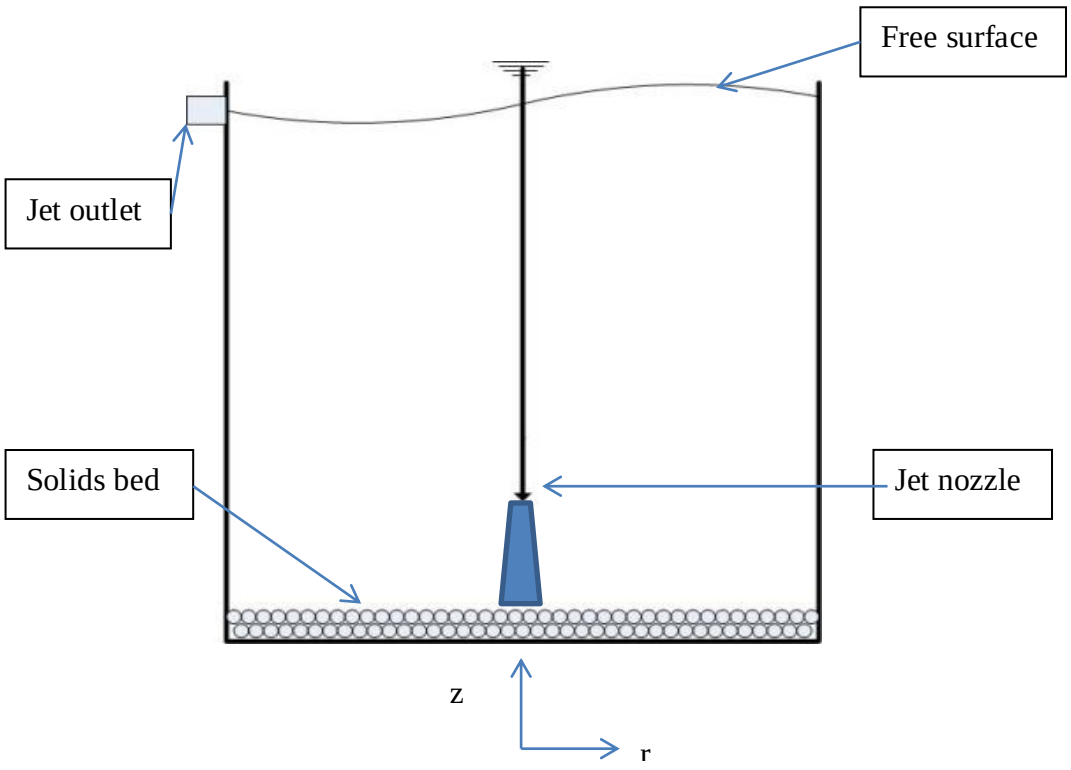

Figure 3.1. Schematic of the jet mixing system problem description.

The schematic shown in Figure 3.1 shows a liquid jet discharging from a submerged nozzle. As the jet impinges on the solids bed, the bed begins to erode away and the particles break up. The particles are then suspended into the bulk fluid creating a concentration gradient in the vertical direction of the tank. The system can be operated without the solids bed, where the jet would impinge on the bottom of the mixing tank, creating circulatory patterns in the tank and mixing the bulk fluid.

3.1.1 Boundary conditions. The boundary conditions that describe the fluid transport are given in equations (3.1) – (3.4). The no-slip, velocity inlet, and free shear surface conditions were all applied. The mathematical expressions for the boundary conditions are written as follows. The no-slip condition specifies that the fluid velocity at the walls is equal to the velocity of the walls, which is zero. The no-slip condition at the bottom and side walls is presented in equations (3.1) and (3.2), respectively.

$$V|_{z=0} = 0 \tag{3.1}$$

$$V|_{r=R} = 0 \tag{3.2}$$

The liquid surface is open to the atmosphere and is modeled as a free shear surface. The motion of the liquid surface is not significant. Equation (3.3) expresses the shear free surface condition.

$$\mu \frac{dV}{dz} = 0 \tag{3.3}$$

The velocity inlet condition is used to model the discharging jet from the nozzle. The velocity inlet is expressed as

$$V = V_o \tag{3.4}$$

where V_o is the discharge velocity.

3.2 Jet Mixer Design

The jet mixing system was designed to promote effective mixing in an efficient but safe manner. A schematic of the jet mixer design is shown in Figure 3.2. The driving force of the liquid jet is a centrifugal pump. Liquid is withdrawn from a holding tank, where it is then passed through a solenoid valve. The flow is either directed to the mixing tank where it is then supplied to the bulk liquid through a smaller diameter nozzle or the flow is bypassed to the holding tank. When the flow is bypassed, it passes through a needle valve, which acts to reduce the pressure before entering the holding tank.

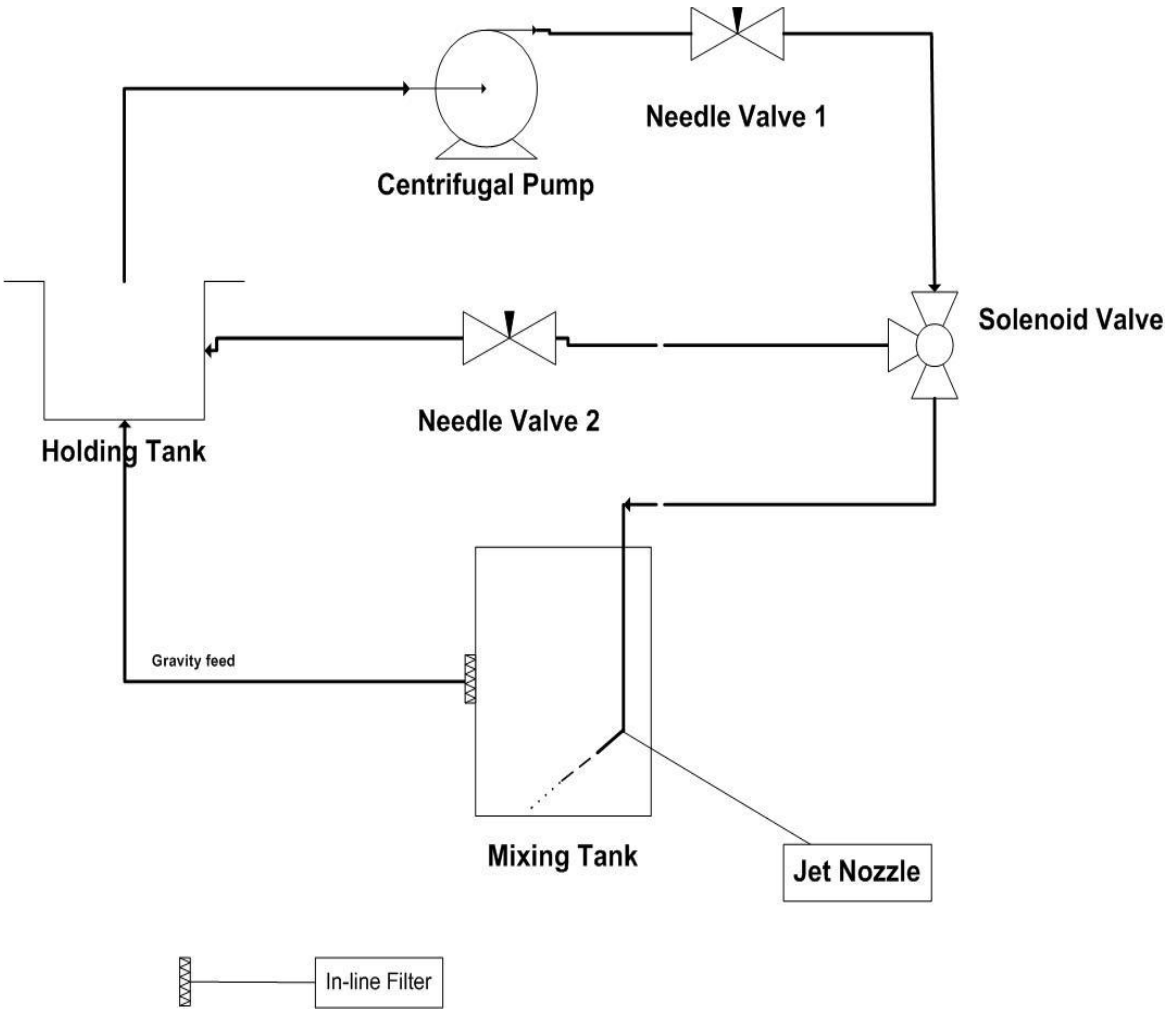

Figure 3.2. Schematic of jet mixing design for the current study.

The liquid height of the tank is maintained at a constant level by the use of an overflow port, which directs extra fluid from the mixing tank to the holding tank by means of gravity. A filter is inserted in the pipeline to ensure that particulates do not enter the holding tank and subsequently is not suctioned by the pump.

The experimental jet mixing assembly is shown in Figure 3.3. All of the piping in the system is made of copper tubing (McMaster-Carr) and has a 1.27 cm (½") outside diameter. The valves, fittings, and most other pieces of equipment are made of brass or stainless steel. The working fluid for all experiments was tap water. Each of the different components are described in the next sections. The entire jet mixing system was assembled on an aluminum cart as shown in Figure 3.3. The system is designed so that parts, including the pump, mixing tank, and valves can be interchanged and extra jets can be added.

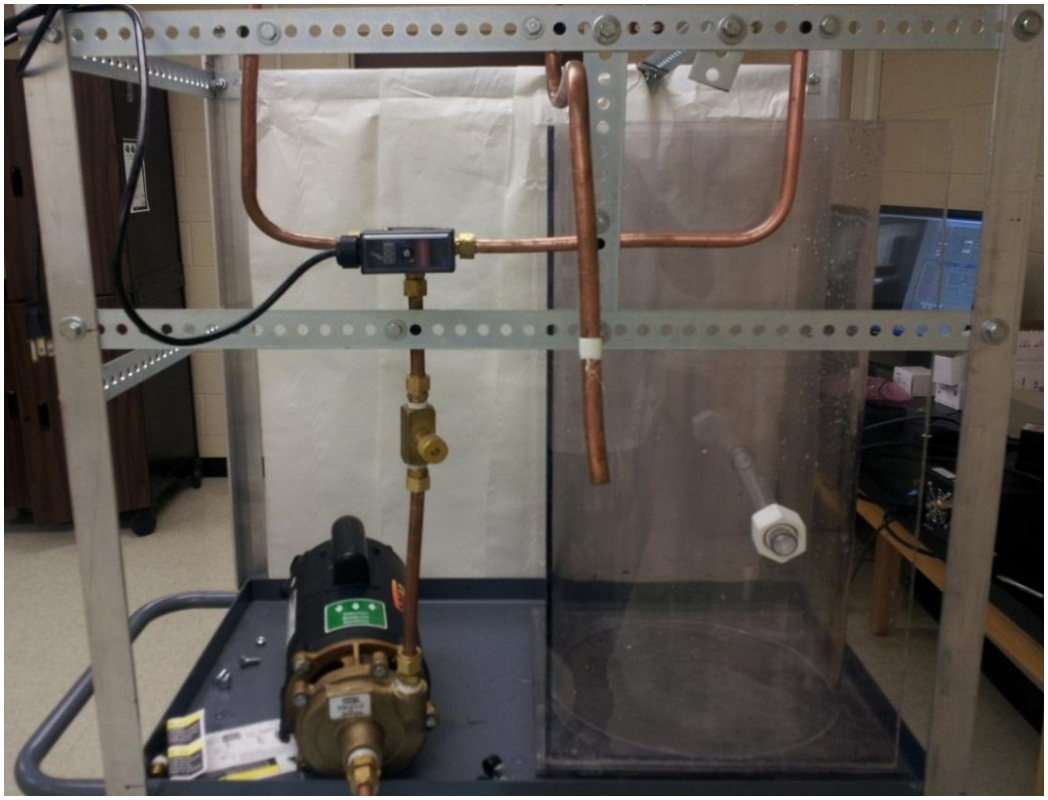

Figure 3.3. Actual jet mixing tank apparatus assembled on an aluminum cart.

3.2.1 Centrifugal pump. A 0.3 hp centrifugal pump with an open drip proof motor from McMaster-Carr is used as the jet driving force for all studies. Figure 3.4 shows the actual pump used in the system. The open drip proof motor allows for cooling air to enter the motor enclosure, but prohibiting liquids and solids. The pump consists of a stainless steel impeller enclosed in a bronze housing. The pump, which has a maximum allowable head of 17.4 m, is 19.685 cm in height, 30 cm in depth, and 13.5 cm in width.

The centrifugal pump is well documented in literature for having acceptable performance while pumping fluids through pipes. Centrifugal pumps are easy to operate, compact, and economically fit for laboratory scales studies, which led to its selection for use. One disadvantage, however, is that the centrifugal pumps are not self-priming, thus the entire line must be totally submerged in the fluid in order for the pump to operate properly and efficiently.

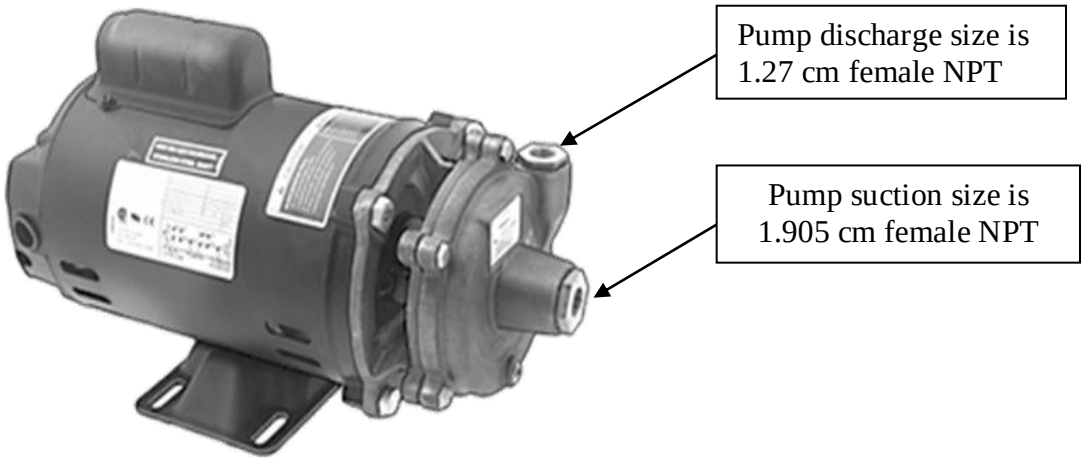

Figure 3.4. The 0.3 hp centrifugal pump used to power the jet in the jet mixing system.

The manufacturer specified the maximum pump flow rate is 0.00221 m^3/s (35 gpm). The pump performance curve, given by the manufacturers, is shown in Figure 3.5. The flow rate entering the mixing tank is not expected to be the same as that which immediately leaves the pump because of fittings and bends in the piping. Therefore, the max flow rate for the system

was initially estimated to be about 0.0014 m^3/s, which corresponds to about a head of 10 m. The actual jet velocity is calculated through experiments in which the volumetric flow rate is measured.

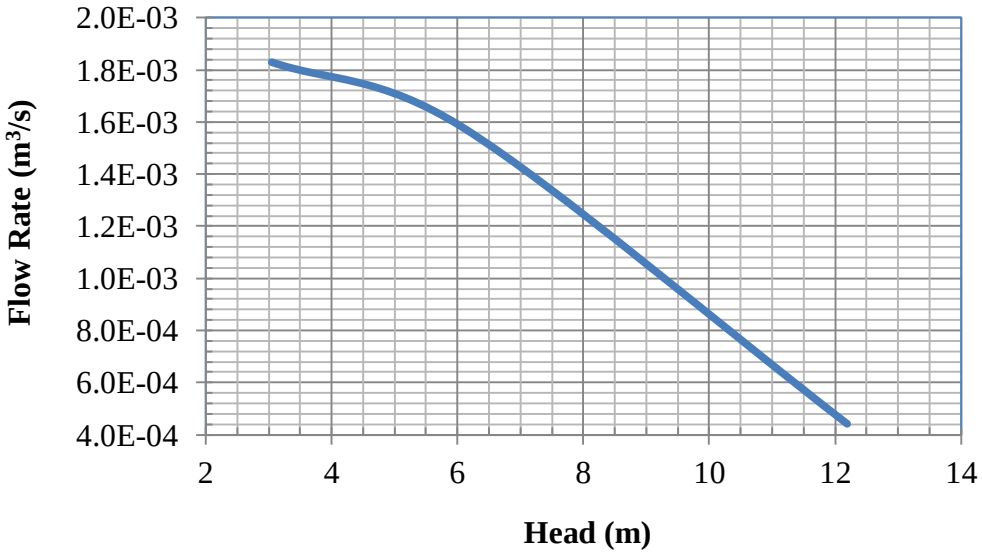

Figure 3.5. Centrifugal pump performance curve as supplied by the manufacturer.

3.2.2 Solenoid valve and needle valves. The jet flow was pulsed by using a direct-acting, brass solenoid valve shown in Figure 3.6a. The 3-way valve has an epoxy-encapsulated coil and manual override for emergency stops. The valve has an opening and closing time of 8 - 15 ms and operates in a normally-open position. The response time is so small in these systems that it is assumed it will have a negligible effect on the flow and on the square-wave pulses.

The solenoid valve was pulsed by the solenoid valve timer shown in Figure 3.6b, which is connected to the actual valve via pin connections in accordance with DIN 43 650. The programmable timer cycles on and off according to the time-on and time-off options. The time-on/off options are set in one of the 8 different timer ranges. The ranges include: 0.5 to 10 sec, 1.5 to 30 sec, 5.0 to 100 sec, 0.5 to 10 min, 1.5 to 30 min, 5.0 to 100 min, 12 to 240 min, and 0.5 to 10 h.

(a) (b)

Figure 3.6. The solenoid valve system including (a) the 3-way solenoid valve and (b) the solenoid valve timer used to control the opening/closing of the valve ports.

The time setting can be manipulated so that the time-on/off is set at a specific value in between the desired range. The valve is ideal for studying the effect of pulse frequencies, as a very wide range of frequencies can be used with the equipment.

Figure 3.7 shows the brass needle valves used in the jet mixing flow loop. A brass needle valve (McMaster-Carr) is used in the bypass line to make sure the pressure of the fluid entering the holding tank is not too high. Another needle valve is used in the discharge line of the pump to vary the flow rate exiting the pump.

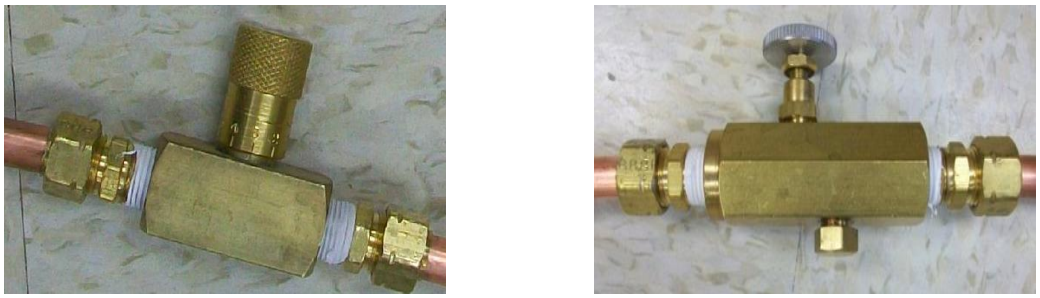

Figure 3.7. Brass needle valves used to control the flow rate leaving the pump and control the pressure of fluid entering the holding tank.

3.2.3 Mixing vessel. The cylindrical mixing tank used for experiments is shown in Figure 3.8. The mixing vessel was constructed of a cylindrical extruded piece of clear, polycarbonate tubing (Plastruct Canada) of 0.305 m outside diameter and 0.61 m in height. A 0.33 m x 0.33 m square polycarbonate slab of 1.27 cm thickness was adhered to the bottom of the cylindrical piece, which serves as a base.

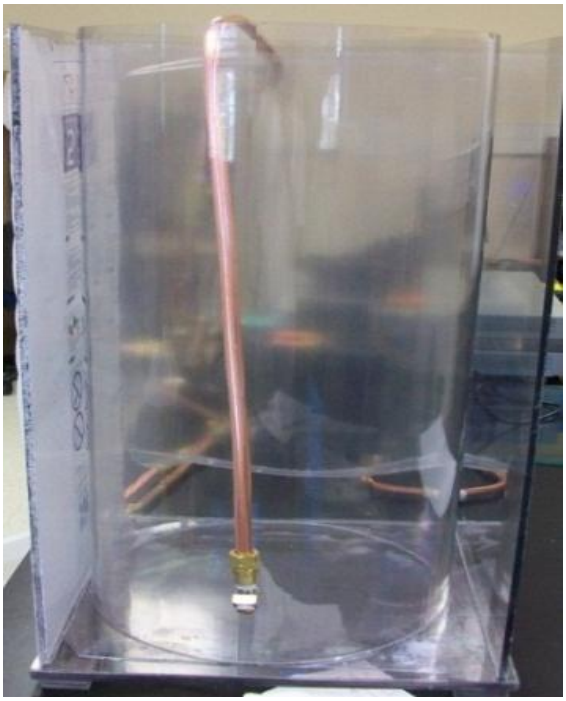

Figure 3.8. Mixing tank apparatus during the construction phase, which shows the rectangular prism around the cylindrical tank.

Polycarbonate is a very transparent material and the mixing vessel is cylindrical in shape, making it is necessary to account for the refraction of light (Merzkirch, W., 1987). A rectangular prism was constructed to surround the cylindrical tank to help correct viewing through the cylindrical tank. Four polycarbonate sheets were cut to size and connected to the base of the tank. The small gap in between the cylindrical tank and the sheet can be seen in Figure 3.8. The gap is filled with the same working fluid that occupies the cylindrical tank.

A hole, 1.905 cm (3/4 “) in diameter, was drilled in the cylindrical vessel and in the rectangular sheet on the same side for the overflow port at the location shown in Figure 3.2. The purpose of the overflow port is to maintain the liquid level in the tank. As the height in the tank increases, fluid exits the tank through a pipe attached to the overflow port which feeds fluid back to the 0.19 m^3 plastic (US Plastic Corp.) holding tank. A 1.905 cm OD polycarbonate tube was adhered to the tank in the hole used for the overflow port.

3.2.4 Jet nozzle. A snapshot of the constructed jet nozzle is displayed in Figure 3.9. The jet was created by connecting one end of a 45 degree, nickel-plated, brass elbow (McMaster Carr) to vertically positioned tubing and the other to a male, recessed plug orifice (McMaster Carr). Different size diameter orifice plugs are used for the studies. The elbow is able to withstand pressures up to 6.89 MPa (1000 psi) and the plug has a maximum pressure of 13.79 MPa and temperature range of 1.67° to 93.3° C. The angle of the jet is easily changed by using a different angle elbow and the jet diameter can by changed by using inserting various orifice size plugs or even connecting a short piece of piping with a smaller diameter.

Figure 3.9. Actual jet nozzle using 45 degree elbow and recessed orifice plug.

3.3 Analytical Calculations

Calculations of theoretical values were run before experiments to just justify the use of specific equipment and to give an idea of expected experimental results. For the current study, the pump is selected because it is able to suspend the solids based on the theoretical preliminary calculations. Preliminary calculations of jet entrainment, particle terminal velocities, and the required velocity for the suspension of particles are run using MATLAB.

One of the most important parameters in jet mixing systems is the jet velocity. The jet velocity can be determined by measuring the volume of fluid entering the tank within a specific time period. Rajaratnam (1976) found that a three-dimensional Newtonian, turbulent jet velocity can be expressed as

$$u(z) = C_j \frac{V D_j}{z} \tag{3.5}$$

where C_j is the jet decay constant, V is the jet velocity (m/s), D_j is the jet nozzle diameter (m), and z is the distance to any location along the path of the jet (m). The distance, z, is measured from the jet discharge location and extends along the path of the jet regardless of boundaries and change of direction. Using equation (3.1), the jet velocity can be estimated as a function of distance.

The theoretical entrainment for the jet based on a 14 degree initial entrainment angle is shown in Figure 3.10. The jet was placed at the maximum liquid level in the tank (0.305 m) and allowed to spread the full height for calculations. However, for experiments the jet is not positioned at the top of the tank because part of the study is focused on suspending solids. When the jet is positioned at the top of the tank, solid suspension would not be as efficient compared to when the jet is closer to the solids bed.

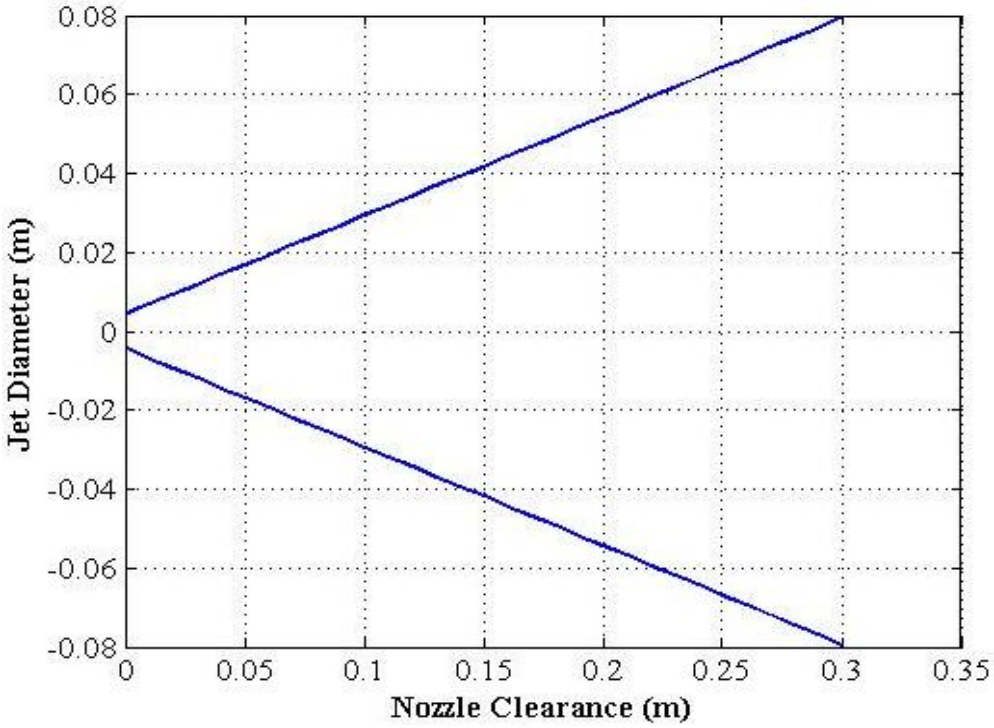

Figure 3.10. Jet entrainment based on a 14 degree initial entrainment angle.

The just suspension velocity, or the jet velocity needed to suspend solids to ensure the system is capable of suspending solids is calculated. Kale and Patwardhan (2005) presented an equation originally developed by Racz et al (1977) to determine the nozzle velocity required to suspend solids for a flat bottom tank, as shown in equation (3.6).

$$U_n = 2\frac{\nu^{0.16}\left[\Delta\rho/\rho\right]^{0.28} g^{0.42}T^{1.15}d_p^{0.1}}{d^{0.94}z^{0.05}} \tag{3.6}$$

where υ is the kinematic viscosity (m^2/s), g is the gravitational acceleration (m/s^2), T is the tank diameter (m), d_p is the particle diameter (m), d is the nozzle diameter (m), and z is the nozzle clearance (m). Equations for settling velocities were given for particles in the Stokes regime and the turbulent regime. Equations (3.7) and (3.8) show the settling velocity in the Stokes regime and turbulent regime, respectively.

$$U_{t_{Stokes}} = \frac{d_p^2 \Delta \rho g}{18\mu} \tag{3.7}$$

$$U_{t_{turbulent}} = 1.75\sqrt{\frac{d_p \Delta \rho g}{\rho}} \tag{3.8}$$

The results for the settling velocities in both the Stokes and turbulent ranges for particle sizes up to 800 μm are shown in Figure 3.11. To suspend solids, it is necessary to provide an opposing velocity to the settling velocity. The graph below is only for single particles and does not consider cohesive properties or particle-particle interactions. Also, it does not take into account that the solids are initially at rest; therefore the results of the calculations have to be used carefully.

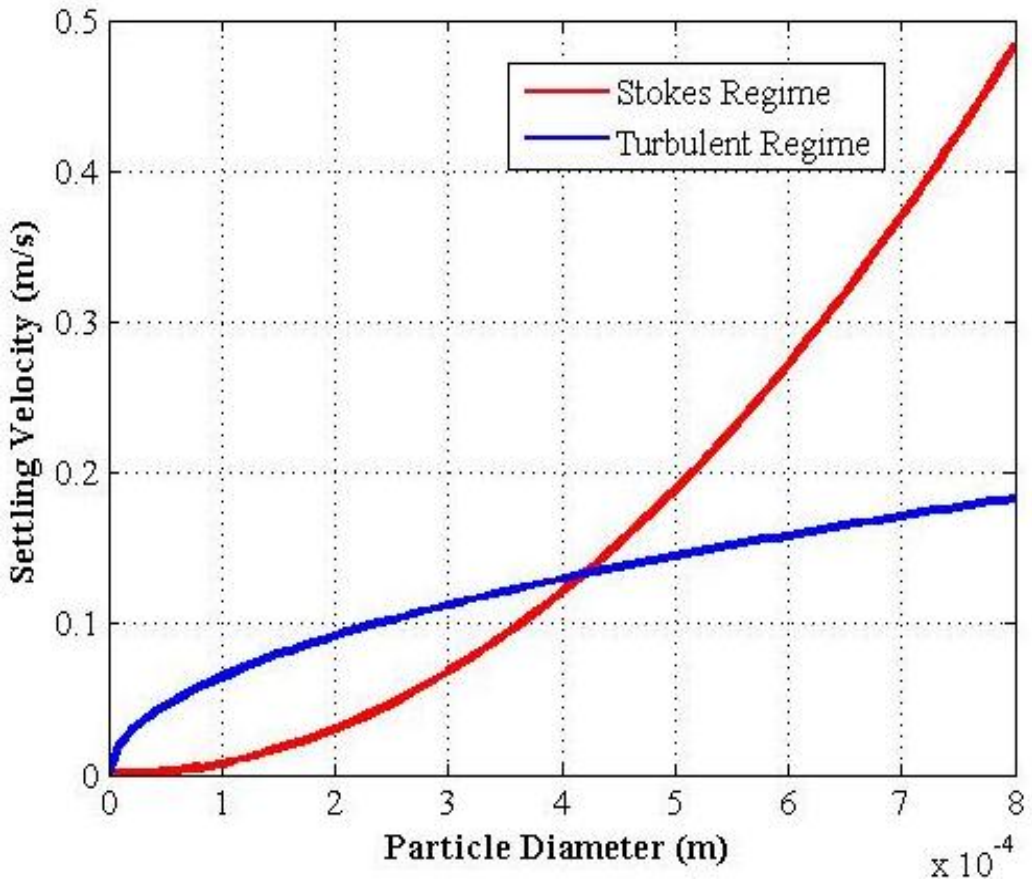

Figure 3.11. Settling velocity for particle flows in Stokes and turbulent regime.

Equation (3.6) was used as a starting basis to determine the needed velocity to suspend solids. The results are shown in Figure 3.12 for a 4.318 mm nozzle. The results suggest that a maximum velocity of 15 m/s is needed to suspend particles up to 800 μm in diameter. Equation (3.6) is useful for determining the velocity needed to clear the entire base of a tank, or a certain percentage of the tank base.

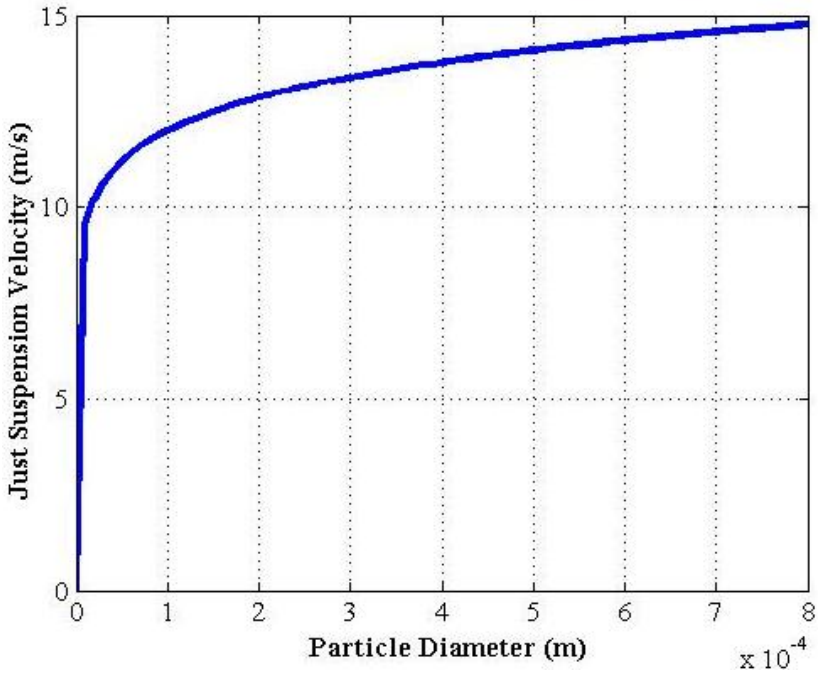

Figure 3.12. Velocity required for suspension of various particle sizes using a 4.318 mm nozzle diameter.

3.3.1 Solid suspension model. Solid suspension in jet mixers occurs slightly differently than in mechanical mixers. As the jet is discharged, a free jet forms, which expands until it impinges on the solids bed, or tank bottom. A wall jet is formed and results in solid particles rolling over outwardly from the impingement location. When the velocity becomes high enough, a region on the bottom of the tank is created which is free of solids, known as the effective cleaning radius (Hamm, B. A. et al., 1989). The particles create a mound of particles along the

outer edge of the tank. Solids begin to start suspending in the bulk fluid at a higher velocity, instead of just rolling,

Once a particle gets suspended, the flow field of the liquid jet and its interaction with the particle determines how the particle behaves. The flow fields of liquid jets are known so prediction of particle behavior once suspended can be predicted. When the upward velocity of the fluid throughout the tank is not sufficient, the terminal velocity of the particle will cause the particle to fall. The particle will either fall back to the bottom of the tank or to a point in which the drag overcomes the weight of the particle.

A physical model is developed to estimate the height rise of particles. The model is based on the suspension mechanism described above in which the motion and suspension of particles is due to the wall jet that is created once the jet impinges on the particle bed. The model assumes that the particles are spherical and particle-particle interaction was not considered. For initial development of the model, a single particle is used. Another assumption is that the particle reaches equilibrium when the settling velocity of the particle is balanced by the upward velocity of the jet.

Equation (3.5) is used to estimate the jet velocity at location, z, along the jet path. The jet velocity at point z, u(z), does not depend on whether the jet is impinging on walls or boundaries or just a wall jet. The constant, C_j, is a parameter which accounts for geometry and is usually between 5 and 6 for turbulent, circular jets. The equation for jet velocity presented by Rajaratnam (1976) represents the velocity of jet that is responsible for suspending the particles. The initial particle velocity is assumed to be equal to the jet velocity at the bottom corner of the tank base or solids bed. The jet is positioned at height, H_j, and on the center axis of the tank. Therefore, the initial location, z_o, is set to $H_j + D/2$.

A force balance is completed on a single particle to form an expression to measure the motion of a single, spherical particle. The steady forces acting on a single particle include drag, weight, and buoyancy. Also, a term for added mass is added to account for the inertia added due to a particle accelerating through the bulk fluid and displacing the bulk fluid as it travels. The drag force is expressed as

$$F_D = \frac{1}{2} C_D \rho A_p |U_f - U_p| (U_f - U_p) \tag{3.9}$$

where the drag coefficient, C_D, depends on Rep. For intermediate flow outside of the Stokesian regime, C_D can be expressed as

$$C_D = f \frac{24}{Re_p} \tag{3.10}$$

where f is a drag correction coefficient. The Re_p in the model is based on the slip velocity as

$$Re_p = \frac{d_p (U_f - U_p)}{\upsilon} \tag{3.11}$$

The correction coefficient used for the model is based on the widely used Schiller-Naumann drag coefficient (Schiller, L. and Naumann, A., 1933) which is written as

$$f = 1 + 0.15 Re_p^{0.687}. \tag{3.12}$$

The buoyancy and gravity force is expressed, respectively, as

$$F_B = \tfrac{1}{6} \pi d_p^3 \rho g, \tag{3.13}$$

$$F_g = \frac{1}{6} \pi d_p^3 \rho_p g. \tag{3.14}$$

The added mass term is written as

$$F_{AM} = \frac{1}{12} \pi d_p^3 \rho \frac{d(U_f - U_p)}{dt}. \tag{3.15}$$

The added mass is an important term as it gives an inertial mass which is different than the gravity mass. The values are much different when the density of a particle is close to that of the fluid (Mordant, N. and Pinton, J. F., 2000). For the current study, the density of the particles and fluid are of the same magnitude.

Combining all of the forces, the balance on a single particle can be written into a single equation as shown in equation (3.16).

$$m_p \frac{dU_p}{dt} = \frac{1}{2} C_D \rho A_p \left|U_f - U_p\right| \left(U_f - U_p\right) + \frac{1}{6} \pi d_p^3 g \left(\rho - \rho_p\right) + \frac{1}{12} \pi d_p^3 \rho \frac{d\left(U_f - U_p\right)}{dt} \quad (3.16)$$

The resulting equation for particle motion is based on the instantaneous velocity of the bulk fluid. Once the velocity of the particle is solved for, the height of the particle can be obtained from

$$U_p = \frac{dx}{dt} \quad (3.17)$$

where x is the position (m) of the particle.

All numerical methods are completed using MATLAB. Equation (3.16) and (3.17) is discretized using an Euler iterative process. To account for the non-linearity of the first term on the right hand side of equation (3.16), one of the slip velocities is solved at the present time step (i.e. t + dt), while the other slip velocity is set to the previous time step (i.e. t). The iteration process continued until the convergence criterion was met. The distinct interface between fluids and particles is formed due to the balancing of the downward velocity of the particles and the upward velocity of the fluid at the wall, which is a result of the jet (Bittorf, K. J. and Kresta, S. M., 2003). So for the current study, iterations are run until the upward velocity equaled the terminal velocity of the particles.

3.4 Experimental Methodology

Liquid blending experiments were run to measure the mixing time, dye flow visualizations, and particle image velocimetry (PIV) flow visualizations to successfully complete specific objective 1. Solid suspension experiments were run in which the cloud height of suspended particles and axial concentration profiles of suspended particles were measured to complete specific objective 2. The third specific objective was met by measuring the erosion profiles of a solids bed of non-cohesive particle. All experiments were run using the cylindrical mixing tank previously described. All of the details of the different experiments are described in the next subsections.

3.4.1 Mixing time and flow visualization. Experiments were run to study the liquid blending performance of the jet mixing system. The mixing time and flow patterns for continuous and pulsing, single and multiple jet mixer configurations were studied. A blue dye tracer was used to measure mixing time and visualize flow created by the jets. The height of the jet nozzle(s) is 0.07625 m from the bottom of the tank. When the single jet configuration was used, the jet was centered in the tank. The jets were positioned 0.02 m from the center of the tank during the dual jet configuration studies. Both jets were directed outward from the center and perpendicular to the outlet. The jet Reynolds number was varied from about 6000 – 22000.

A solenoid valve was used to create the pulsing jet. The valve was able to cycle the fluid momentum through the jet nozzle in an on/off manner. One complete cycle, known as the pulse cycle time (t_C), is 5.5s long. The pulse consisted of a discharge time (t_D) of 5 s and an off time of 0.5 s. The specific time was chosen through initial CFD results.

The concentration of the blue dye was measured using a spectrophotometer (Milton Roy SPECTRONIC 20D). An initial sample was used as a base measurement which will be

subtracted from subsequent samples which include dye. The absorbance was set to zero on the spectrophotometer for calibration. The absorbance and concentration of each subsequent sample, containing dye, was then taken by placing the sample in a test tube and measuring at the maximum wavelength of the dye.

The wavelength of the blue dye was not known before hand and was measured by plotting the absorbance as a function of wavelength. A blue dye sample was measured at incremental wavelengths of 10 nm. Figure 3.13 displays the absorbance as a function of wavelengths for a sample. The maximum wavelength (λ_{max}) was found to be 610 nm.

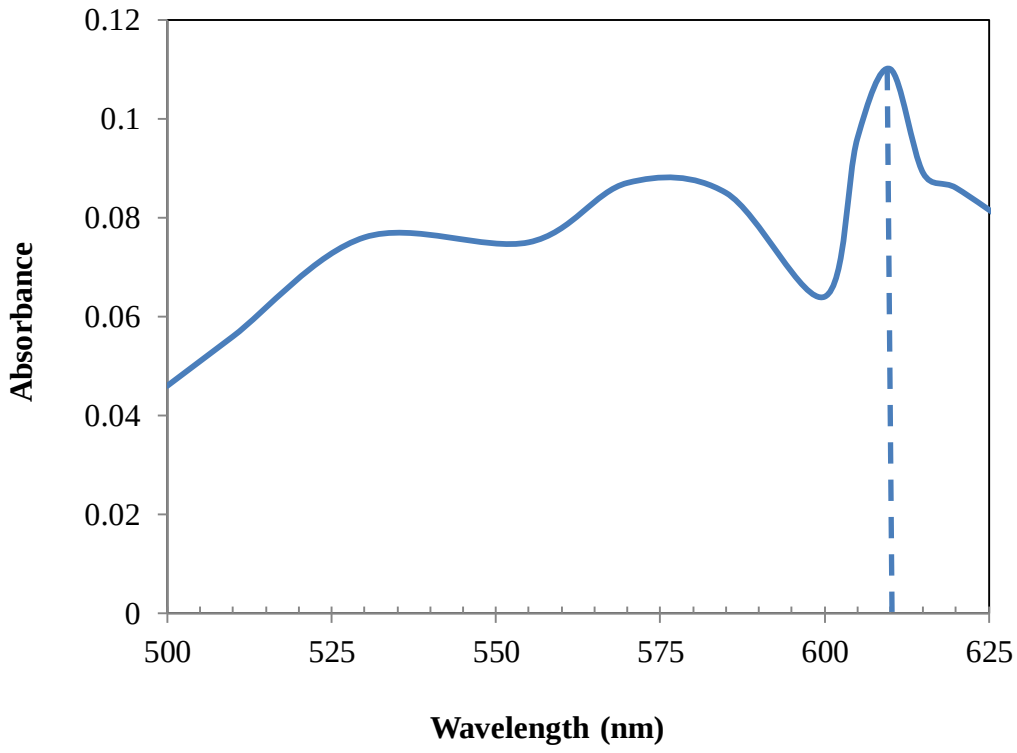

Figure 3.13. Maximum wavelength (λ_{max}) determined by absorbance vs. wavelength.

The experimental procedure is as follows. The centrifugal pump was turned on and the fluid was transferred from the holding tank to the mixing tank. Once the fluid height reached the level of the outlet port and begin to pour out, the three way valve that directed flow to the

holding tank was switched to divert flow directly back to the mixing tank. An initial sample was taken from the outlet of the tank and is used as the base sample. The initial concentration is measured to be zero, since no dye was yet present in the tank. The dye is then injected slowly into the tank so that momentum of the injection is not significant to affect its dispersion. Samples were taken at the tank outlet every 5 seconds for 5 minutes. Five minutes was an accurate length to allow for the dye in the tank to reach equilibrium. The equilibrium concentration is the final concentration used in calculations. Equation (1.1) is used to calculate the mixing time as a function of dye concentration. The measurement of mixing time was based on a 95% homogeneity criterion, or the time it takes for the concentration in the tank to reach 95 % of the fully mixed concentration. So, in equation (1.1), the mixing parameter, m, has to be less than 0.05.

The flow pattern created by the jet was monitored simultaneous to mixing time experiments. Dye has been used by previous researchers to determine flow patterns. Video images were captured using a Basler acA2040-180 km CMOS camera attached to a PIXC1-E8 frame grabber housed in a computer (Epix, Inc). The imaging equipment is described in more detail later in the PIV methodology section. The imaging equipment was set up perpendicular to the direction of the flow. Recording of images started slightly before dye was injected so that the initial dispersion of the dye could be captured. The video was then saved to the computer as a series of snapshots, so that video and useful snapshots could be viewed for observation.

3.4.2 Cloud height. Experiments were run to study the suspension of non-cohesive particles using steady jet mixers. Single jets were used for studies where the jet was centered in the center of the tank. The jet nozzle was not angled and was directed downward at 0°. The

velocity of the jet was varied from about 1.9 – 6.5 m/s. The jet Reynolds number was varied from about 8300 – 28000.

Various silicon dioxide particles (U.S. Silica) were used for experiments. The size distribution of the particles varied for each sample. Because there was a range for the particle sizes, the d50 particle size, or the diameter at which 50% of the solids are finer, was used. The d50 particle size for the three particulates used are 120, 265, and 700 µm. Figure 3.14 shows the size distribution for the three sets of solid particles that were used.

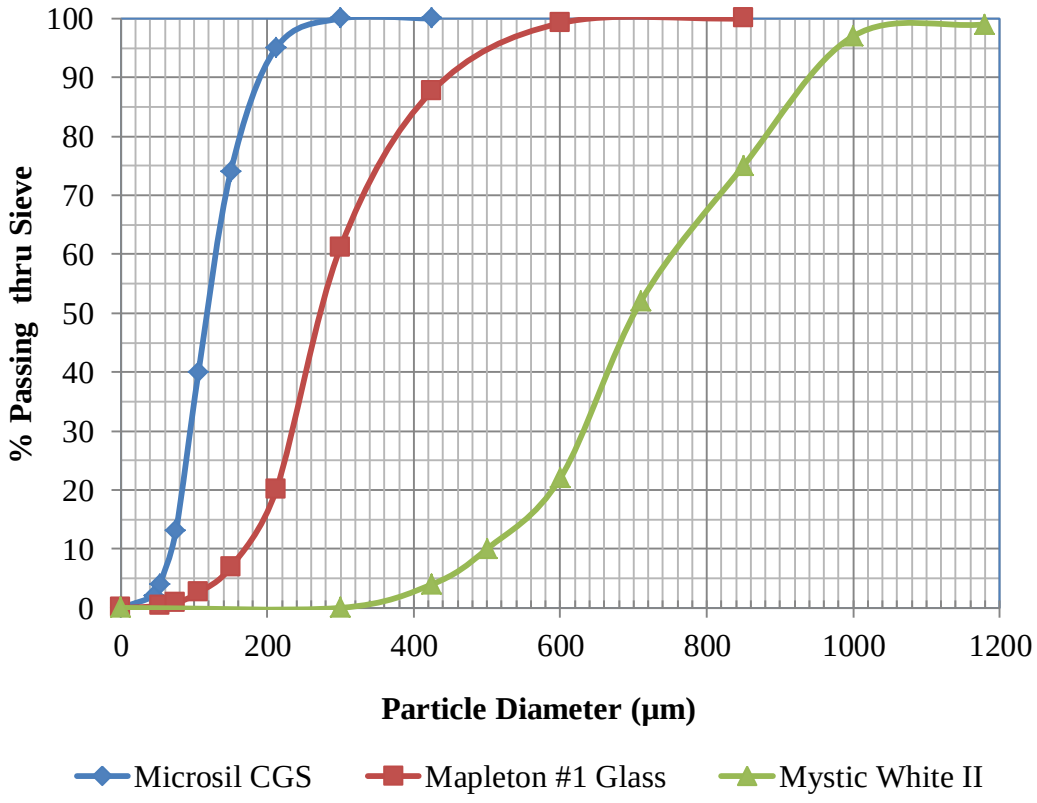

Figure 3.14. Size distribution for sand particles used in cloud height experiments.

Figure 3.15 shows microscopic images of the particles with d50 particles sizes of 120, 265, and 700 that are used in experiments. The images show that the particles used in

experiments are not spherical. The d50_120 and d50_265 particles are classified as sub-angular and the d50_700 particles are angular.

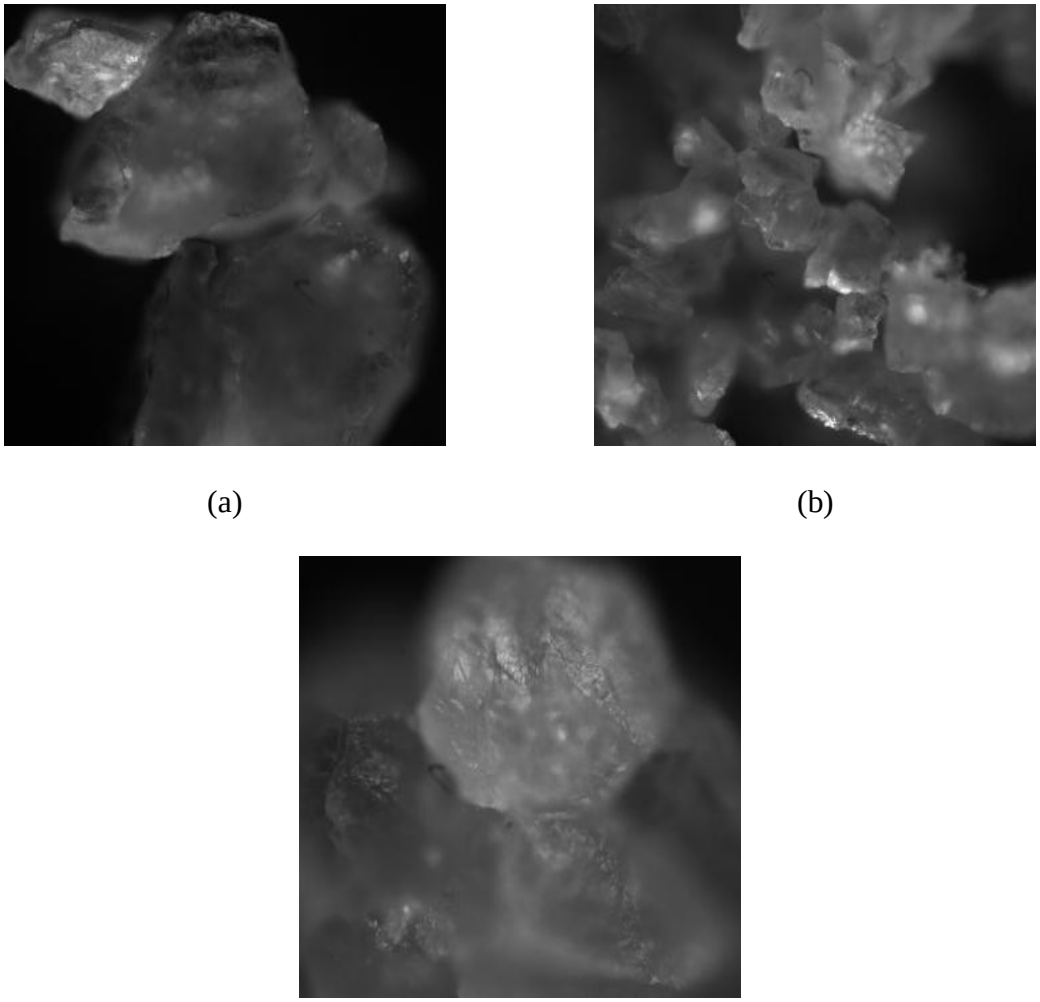

(a) (b)

(c)

Figure 3.15. Microscopic images for (a) Microsil CGS (d50_120), (b) Mapleton #1 Glass (d50_265), and (c) Mystic White II (d50_700) particles.

Table 3.1 summarizes the properties of the particles. A solids volume fraction, Φ_s, of 0.045 and weight percent of solids, w_s, of 10.6% was used for all tests. The particles have been classified by their median particle diameter, the settling velocity, the Archimedes (Ar) number, and the particle Reynolds number (Re_p).

Table 3.1

Properties of solid particles.

	Microsil CGS	Mapleton #1 Glass	Mystic White II
Sample No.	d50_120	d50_265	d50_700
Mineral	Quartz	Quartz	Quartz
d50 (µm)	120	265	700
Specific Gravity	2.65	2.65	2.65
Grain Shape	Sub-angular	Sub-angular	Angular
pH	6.5	7	6.5
V_t (m/s)	0.077	0.117	0.186
Ar	28	336	5551
Re_p^*	9	32	130

Cloud height experiments were initialized by filling the mixing tank with water until the water began flowing out of the outlet port. The pump was then turned off. About 1000 mL of solid particles was then poured into the tank. A round, flat tool was used to smooth the particles and evenly disperse the particles at the bottom of the tank as well as possible.

The imaging system used to visualize particle height included a CMOS sensor and solid state green laser (MGH-H-532, Opto Engine, UT, USA). The green laser was used to illuminate regions of the tank. The laser was positioned above the tank so that a thin laser sheet was created about 1 mm in front of the jet nozzle. Specific details about the laser will be given in the ensuing section about PIV flow visualization. The sensor was turned on just before turning on the pump.

The pump was then turned on and the jet was allowed to suspend the solids. The cloud height was considered the maximum formed interface after a period of time. The interface was not always constant and so a high and low cloud height value was recorded for each run. Tests were run for the various jet velocity settings for one set of particles. The height of the jet was then varied from 0.038 m to 0.07265 m. This same procedure was run for the other sets of sand particles.

3.4.3 Erosion profile. The erosion profiles of a solids bed of non-cohesive sand particles were measured as a function of time and jet velocity. The jet velocity was varied from about 1.4 – 4.4 m/s, which corresponds to a jet Reynolds from 6000 – 18660. Due to limited access in particulates, a solids bed was packed to a height from 6 – 9 cm high. Two different size particles were used: 265 and 700 μm. The erosion profile was observed using a high speed camera (FASTCAM SA4 Photron). The camera was used to capture images at a rate up to 1000 frames per second. Images of the erosion depth and area of the solids bed was captured as a function of time and jet velocity.

The images were cleaned up and converted to more useable forms with the help of imaging analysis software. An example of the imaging conversion process is shown in Figure 3.16. Initially, a video is created and images are selected at desired time intervals. The original raw image data is first converted to an 8-bit binary image. A distinct boundary of the solids bed is clearly mapped and observed. Creating the distinct boundary allows for the appropriate regions of the image to be filled in for better contrast and ultimately easier measuring. The imaging software is then used to calculate several points along the boundary and is plotted. The software is also able to calculate the eroded area. The measurement process is described in more detail below, along with the corresponding images.

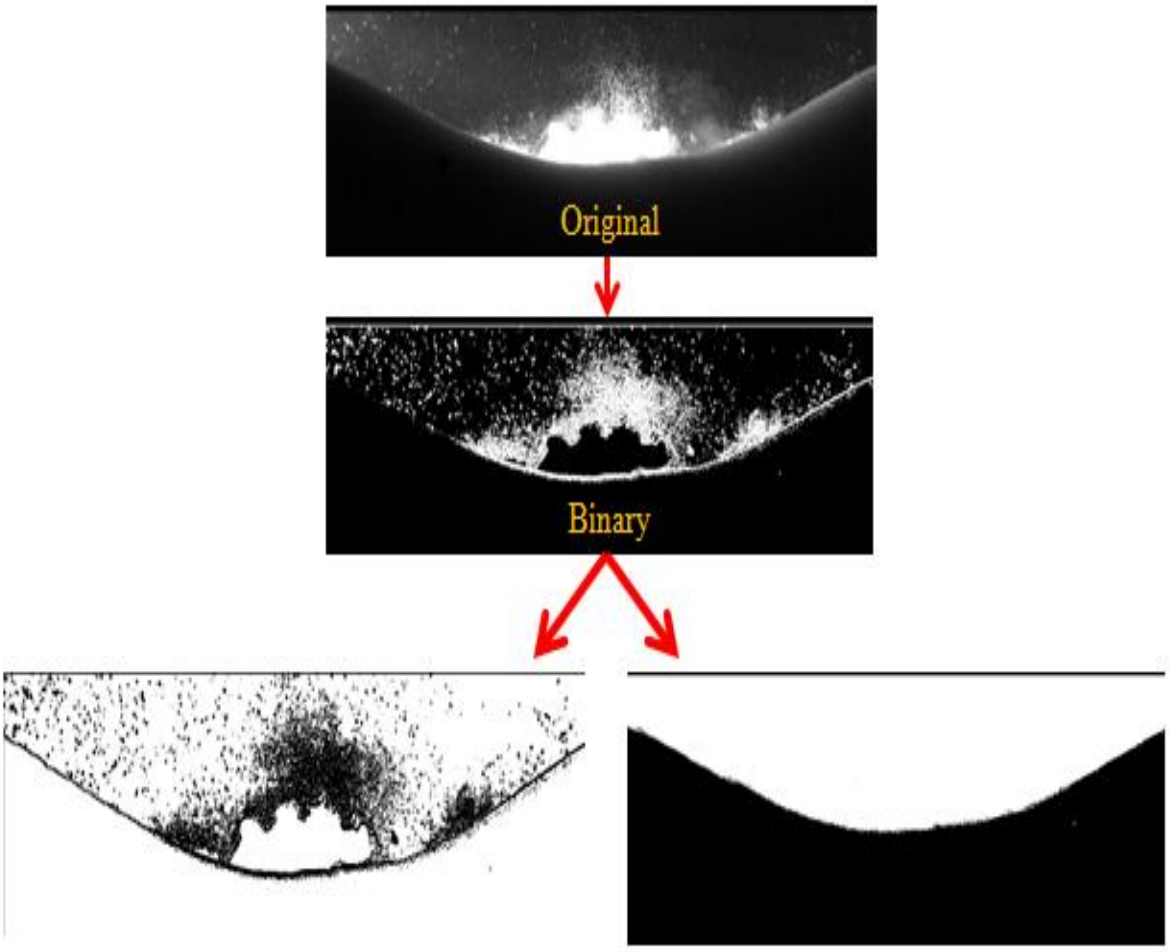

Figure 3.16. Example of imaging conversion process from the original image to the appropriate formats for analysis of the erosion depth and the eroded area.

To accurately measure the erosion depth, several steps were used. Before the jet was turned on, the level of the solids bed was measured in the snapshot at different horizontal positions, as shown in Figure 3.17.

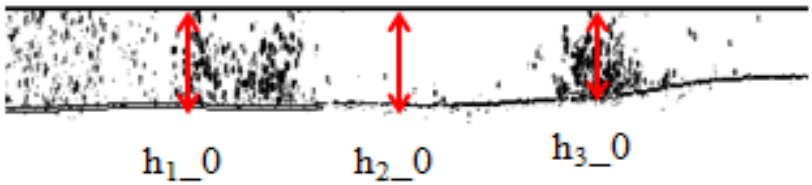

Figure 3.17. Surface of solids bed at initiation of jet discharge.

The jet was then turned on and allowed to run until the erosion depth no longer changed, or the depth reached the bottom of the tank. The height was then measured in various locations along the boundaries at various times, t, which is shown in Figure 3.18. The difference between the values at time, t, and the initial values, gives the eroded depth as a function of horizontal position.

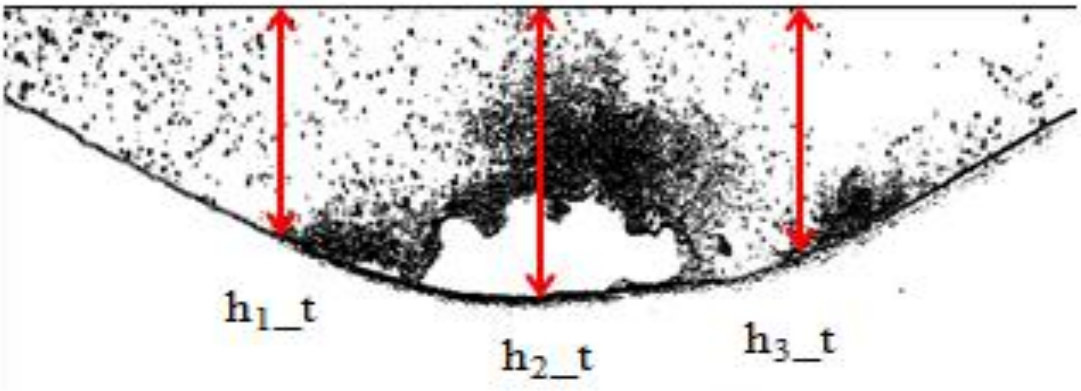

Figure 3.18. Erosion profile of solids bed after a certain elapse of time.

A similar analysis was used to calculate the eroded area in a 2-d plane. The same procedure used to measure the erosion depth was used to determine the eroded area. The images were converted as previously described, which results in an image as the one shown in Figure 3.19.

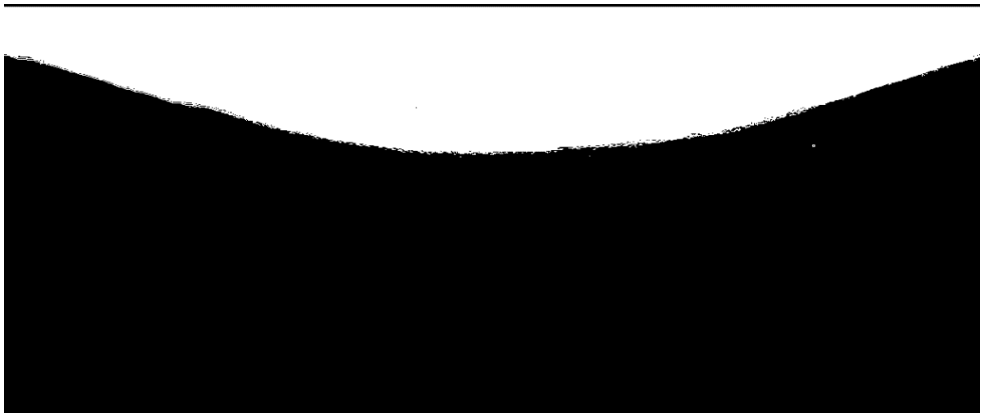

Figure 3.19. Transformed image used to measure the eroded area of a solids bed.

The area of the white space represents the area between the boundary of the solids bed and the top of the frame in the image. The white space area was determined initially before the jet was tuned on. The area was then measured for subsequent snapshots. The initial area was subtracted from the area calculated at time, t, and this was measured as the eroded area caused by the impinging jet.

3.4.4 Axial concentration profile. Experiments were run to determine the axial concentration profiles of suspended cohesive solids particles. The initial wt. % of kaolin clay particles were varied between 2 – 8 %. All other jet parameters were held constant for the different experimental runs. The liquid level was constant at about 0.305 m (12”). The jet velocity was set to about 4.4 m/s.

Measurements were completed using a non-intrusive technique. Such a technique is useful because as the particles mixed they made the water very cloudy due to their size being very small. A good way to calculate the concentration profile without actually sampling and disturbing the fluid is by the intensity of light that passes through as a function of height. Initially, a select amount of particles were put into the mixing tank with the liquid level at the desired height. The particles are then allowed to settle. Figure 3.20 shows an example of a mixing tank once the particles have been allowed to settle. The image of the mixing tank with the settled particles was used as a baseline from which subsequent images would be subtracted. Once the particles have settled, the jet mixing system is setup. The jet is initiated and images are recorded using the imaging system previously described. Figure 3.21 shows an example of the mixed kaolin clay, exhibiting a concentration gradient throughout the tank. The baseline images are subtracted from these images.

Figure 3.20. Settled kaolin particles in a mixing tank.

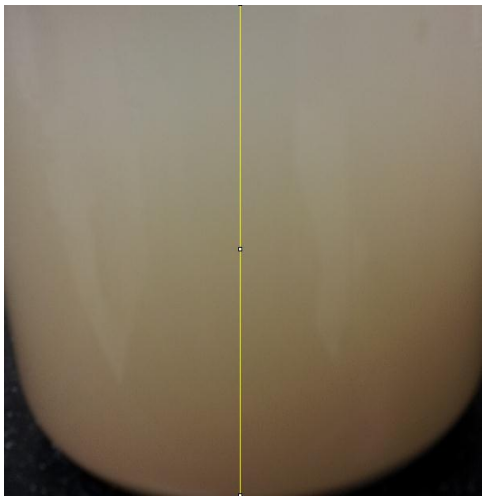

Figure 3.21. Concentration gradient of kaolin clay solid particles once mixed in a tank.

The obtained images are converted into 8-bit grayscale images in which range of grayscale intensities range from 0 (black) to 255 (white). Figure 3.22 shows an example of the 8-bit grayscale image of the mixed kaolin solution. The images were then analyzed to determine the grayscale intensity along any line. The intensities can be correlated to represent the grayscale intensity if the initial concentration of the solids is known at the bottom of the tank.

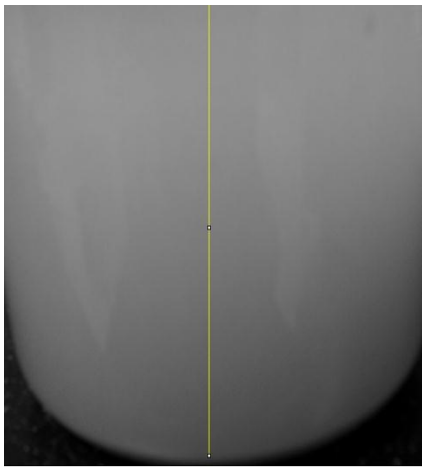

Figure 3.22. Example of the converted 8-bit image of the mixed solution in the mixing tank.

3.4.5 Yield stress measurement. Experimental tests were run using different mixtures of EPK kaolin clay (Edgar Minerals) and MICROSIL CGS silica-quartz (US Silica) in water. The kaolin clay is used as the fine, cohesive particles. The kaolin clay has an average particle size of 1.36 µm and a specific surface area of 28.52 m^2/g. The sand particles are used as the coarser, non-cohesive particles. The particle size of the sand is given as a histogram, shown in Figure 3.23.

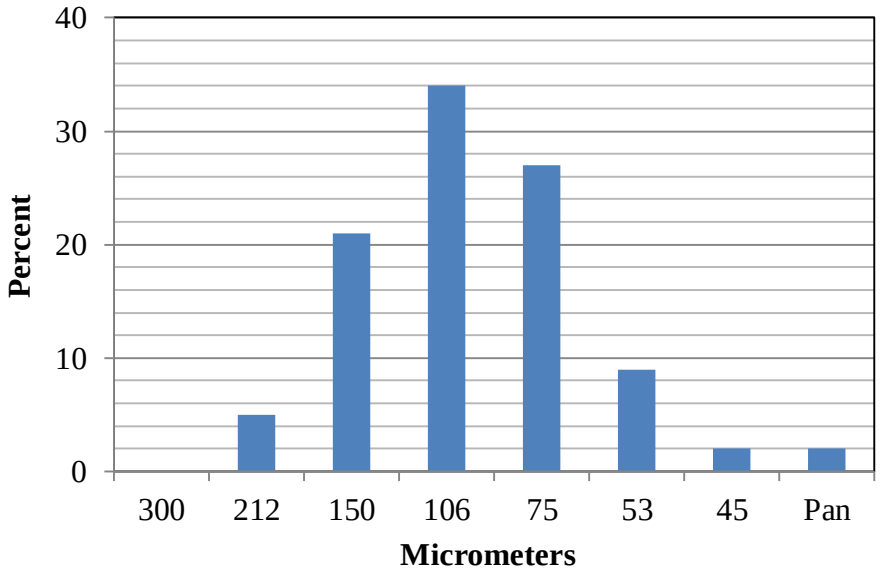

Figure 3.23. Histogram of particle size of sand used for studies.

Tests were run where the weight % of the total solids, φ_T, was varied from 50 to 60 %. Since the total solids are varied with different amounts of kaolin and sand, it is mathematically defined as

$$\varphi_T = \varphi_K + \varphi_S \tag{3.18}$$

where φ_K is the weight percent of kaolin and φ_S is the weight percent of sand. Within those total solids content, the clay-sand weight % was varied from 50 to 100% for each component. Though tested, some of the results are not presented due to limitations in the equipment, which is discussed later.

A Poiseuille-flow tube rheometer was constructed to measure the yield stress of the mixtures. Figure 3.24 shows a schematic of the apparatus used for the tests. The system was pressurized using compressed air. The pressure through the tube was measured using a liquid water manometer.

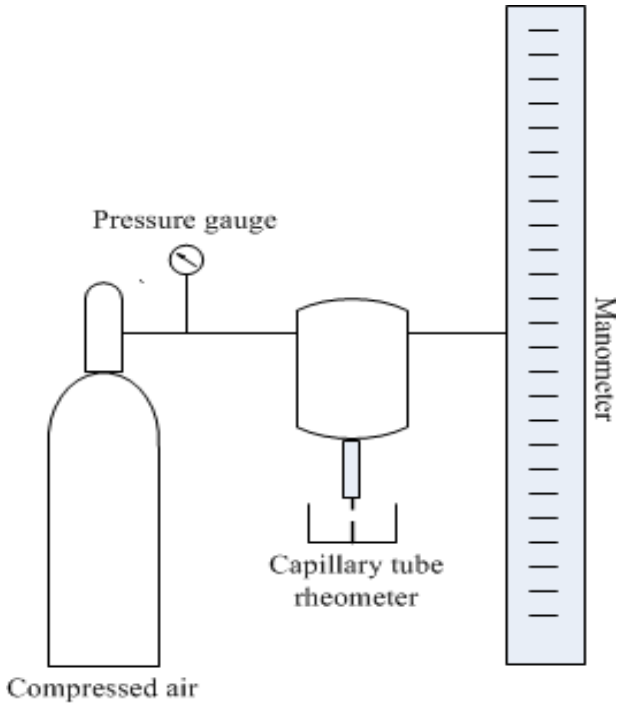

Figure 3.24. Schematic of capillary tube rheometer setup.

Figure 3.25 shows the actual equipment used in experiments. Figure 3.25a displays the rheometer apparatus, which includes a PVC reservoir (H = 11.7 mm and D = 10.2 mm) that was pressurized by compressed air. Figure 3.25b shows the U-tube water manometer that was used for measurement of pressure across the tube. The tube was made of brass and was connected to the bottom of the reservoir. Figure 3.25c shows examples of the tubes of different lengths and diameters which all could be equipped to the reservoir. The aspect ratio (L/R) of the tubes ranged from 9.625 - 90. The pressure drop across the capillary tube was measured using a 3.05 m (10") water, U-tube manometer. The maximum pressure that can be measured using the manometer is 29.84 kPa. The maximum shear stress that can be measured is about 783 Pa. The water manometer is advantageous due to its ease of construction, lost cost, and sensitivity. Unlike, other pressure measuring devices, such as transducers, no calibration is needed for the manometer.

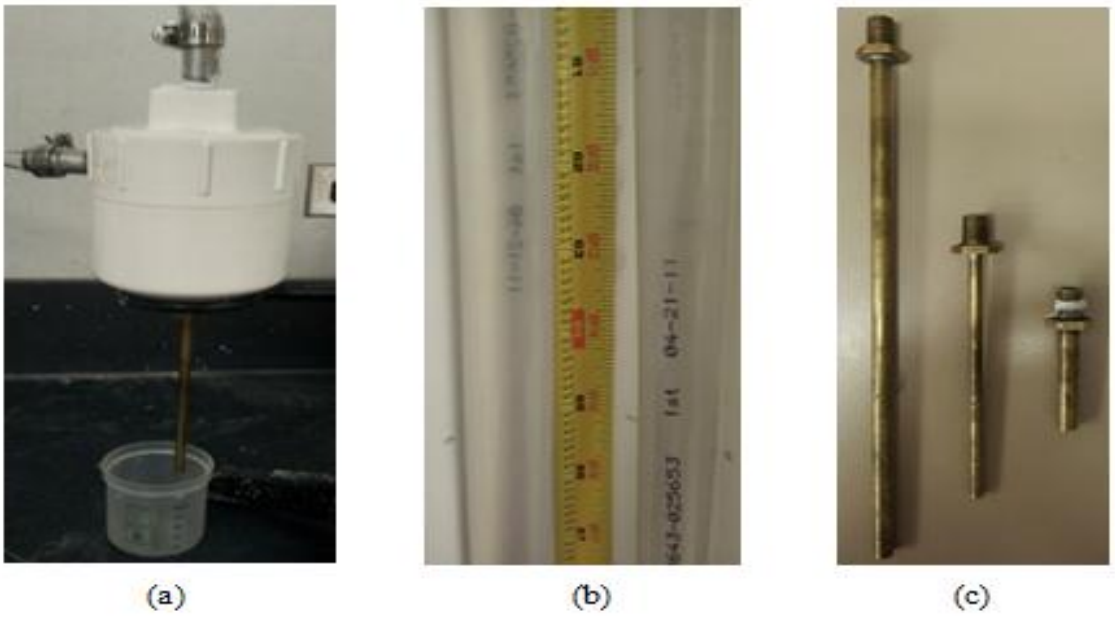

Figure 3.25. Individual pieces to the rheometer apparatus, including (a) the PVC reservoir, (b) the water manometer, and (c) the brass tubes.

A simple, fast, and easily constructed visual technique was used to measure the yield stress. Kaolin clay, sand, and water mixtures were created by carefully measuring the appropriate amount of each component and manually mixing. Mixing took place for about 15 minutes to ensure consistency throughout the mixture and then it was allowed to age for a period of 2.5 to 3 hours.

The mixture was transferred to the reservoir where it was filled to the half-way mark. The mixture was slightly mixed for 2 minutes while in the reservoir in attempt to eliminate any air pockets. The compressed air was increased until the mixture starts to flow out of the capillary tube. The pressure was then stopped and the material extruding from the tube was cleared. Cleaning the tube ensures that more accurate measurement of initial flow is taken as the fluid is filled to the very tip of the tube. The compressed air was then increased very slowly and the moment at which incipient motion occurs was recorded. The height difference in the manometer was measured and the yield stress was calculated. Each trial run was repeated 3 - 4 times.

The results obtained from the rheometer were compared to yield stress results using a Brookfield LV viscometer. Also, studies were run by following the same procedure as above but calculating the volumetric flow rate of material exiting the capillary as a function of pressure drop.

The equations for flow in a capillary is derived w fully developed, steady, isothermal, laminar flow with no flow in the r and Θ direction. Assumptions were made that there is no slip at the walls and the fluid is incompressible with viscosity independent of pressure. The maximum shear stress occurs at the wall and can be calculated as

$$\tau_w = \frac{\Delta P \cdot R}{2L} \tag{3.19}$$

$$\Delta P = \rho g h \tag{3.20}$$

where ΔP is the pressure drop across capillary tube, R is the radius of the capillary tube, L is the length of the capillary tube, ρ is the density of water, g is the gravity acceleration constant, and h is the height difference in the manometer. The apparent wall shear rate is presented in equation (3.21).

$$\dot{\gamma}_{aw} = \frac{4Q}{\pi R^3} \tag{3.21}$$

Several models exists to model non-Newtonian fluids, including the Bingham, Casson, and Power –law (Macosko, C. W., 1994). Some fluids can be modeled using more than one model, which would provide different yield stress values. Thus, the yield stress can be looked at as not being an absolute quantity (Nguyen, Q. D. and Boger, D. V., 1992).

The power law model is used to model the mixtures in the current study. The shear stress can be expressed for power law fluids flowing through a pipe, as

$$\tau = K\dot{\gamma}^n \tag{3.22}$$

where K is the consistency coefficient and n is power law index. The power law index, n, is less than 1 for shear thinning fluids, greater than for shear thickening fluids, and equal to 1 for Newtonian fluids. The shear rate at the wall can be found from equation (3.23).

$$\dot{\gamma}_w = \frac{4Q}{\pi R^3}\left[\frac{3}{4} + \frac{1}{n}\right] = \dot{\gamma}_{aw}\left[\frac{3}{4} + \frac{1}{n}\right] \tag{3.23}$$

The viscosity can then be calculated from equation (3.24).

$$\eta = {}^{\tau_w}/_{\dot{\gamma}_w} \tag{3.24}$$

Manometer calibration. Though calibration is not needed using manometers, some testing was done to ensure the system was able to measure pressure accurately. The pressure

calculated by the height difference in the manometer was tested against the readings of a pressure gauge and the results are shown in Figure 3.26. The pressure was measured at various intervals. The results show that there is very little deviation measured using the pressure gauge and the manometer. The low percent of error was expected as water manometers are known to be accurate, as previously mentioned.

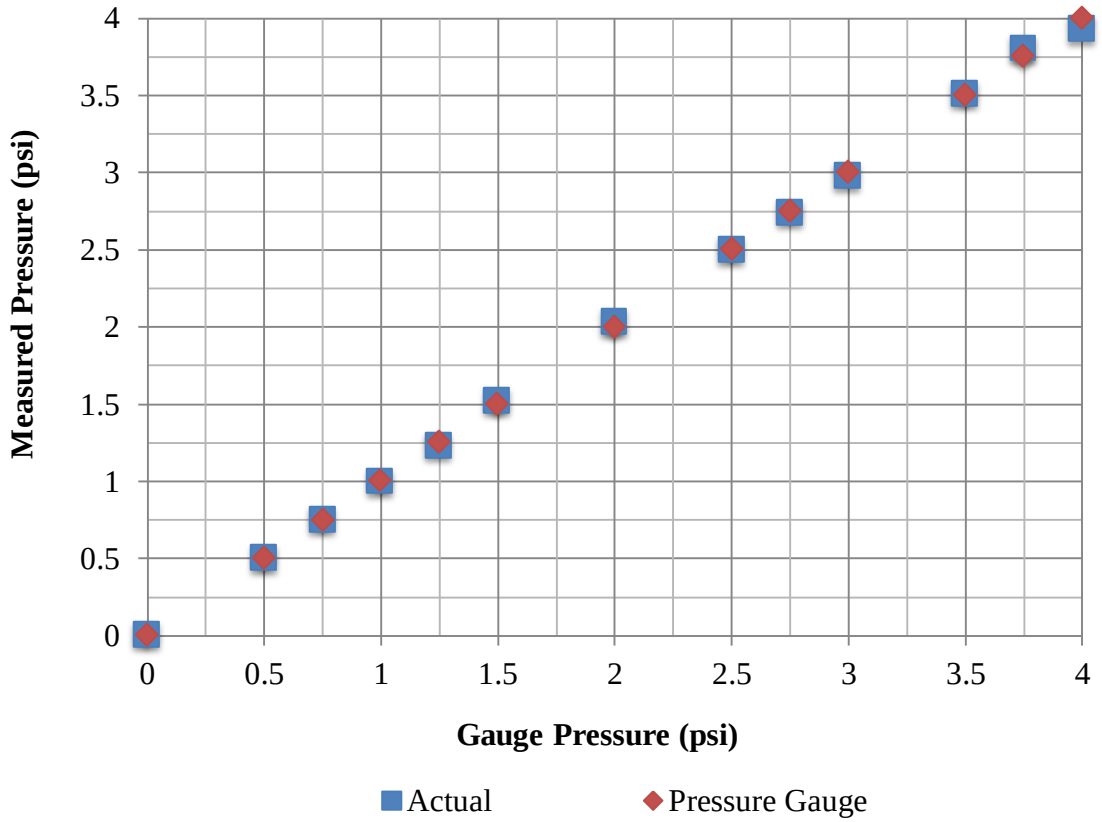

Figure 3.26. Manometer pressure readings at given gauge pressures.

Figure 3.27 displays the percent of deviation between the manometer and pressure gauge readings. The highest deviation was only 1.9%, which was found at 4 psi. The percentage of uncertainty can be attributed to human error, which results from inaccurate measuring of the meniscus in the tubes. However, the deviation is small enough to be deemed acceptable within experimental error limits.

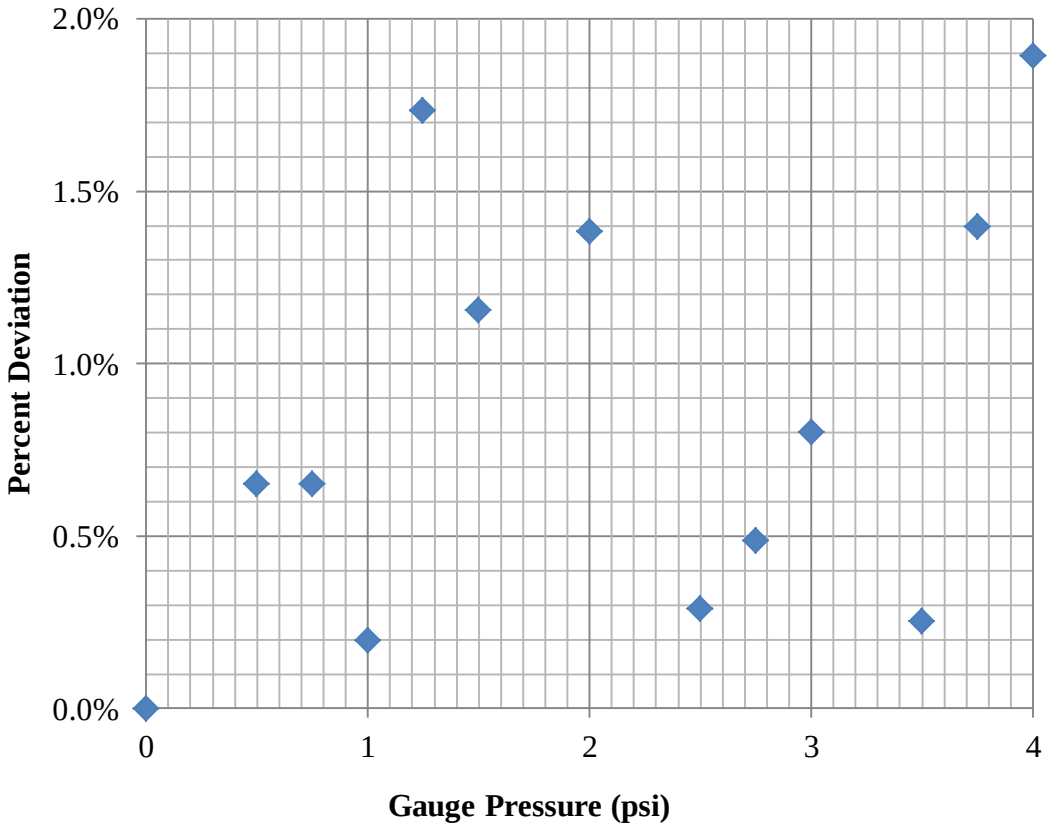

Figure 3.27. Uncertainty of readings from manometer compared to pressure gauge.

3.4.6 Particle image velocimetry (PIV). Particle image velocimetry is a very useful technique that is used to obtain 2-d or 3-d instantaneous velocity field distributions within a flow field. The velocity field can then be used to calculate other flow parameters. PIV is also useful because it is a non-intrusive technique.

The PIV system, including the jet mixing tank is shown in Figure 3.28. The driving force for the jet is a 0.3 hp centrifugal pump (McMaster-Carr), which suctions fluid from a holding tank. The jet mixing apparatus included a glass, rectangular tank. The jet nozzles were made from copper tubing (D_{pipe} = 12.7 mm) with solid stream nozzles (D_{nozzle} = 4.32 mm) attached. The jet nozzle clearance was 0.07625 m from the bottom of the tank for all the studies that were run.

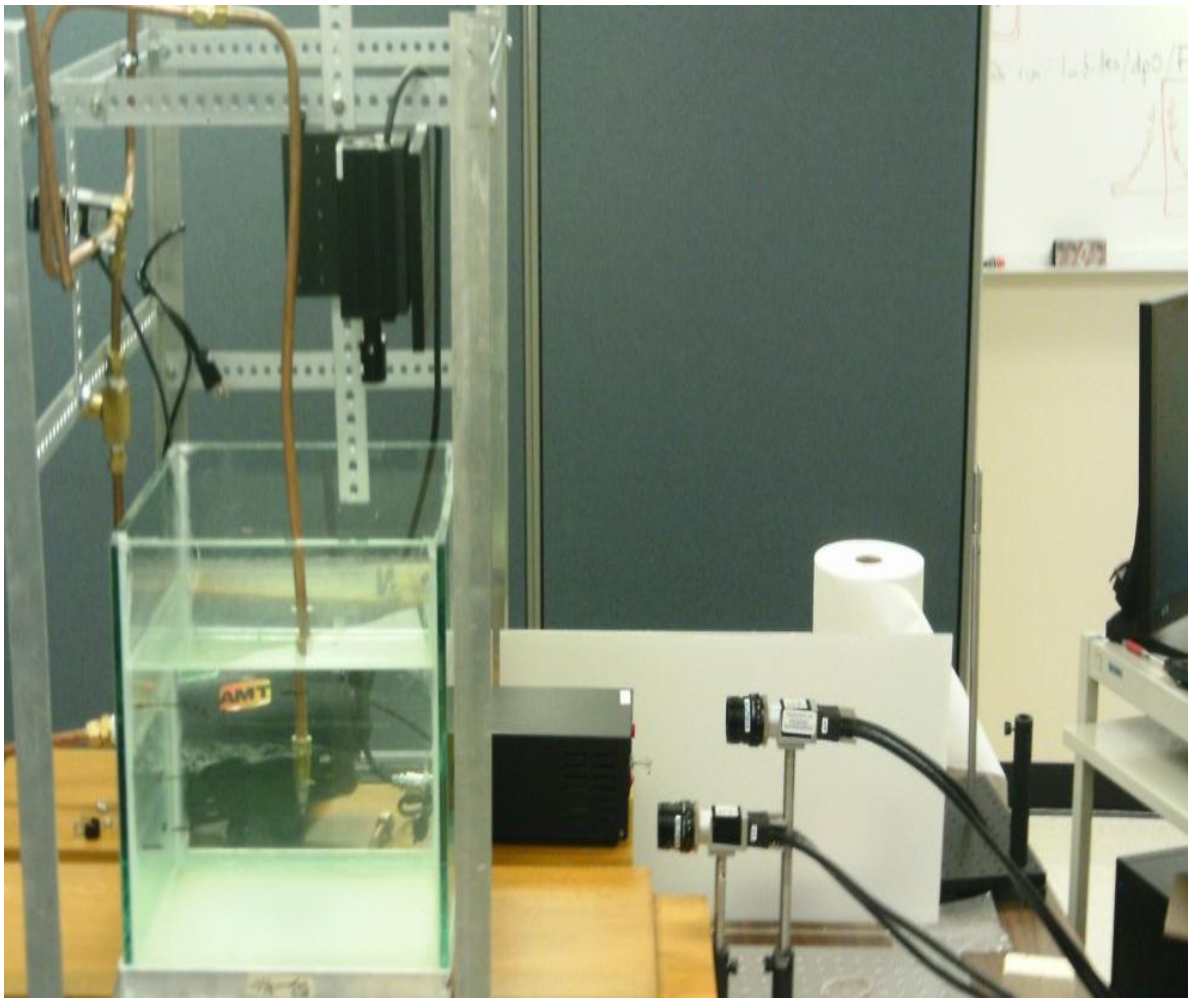

Figure 3.28. PIV setup, including the jet mixing tank.

The mixing tank is filled with tap water and glass particulates are added to the water to seed the flow field. The neutrally buoyant, hollow, glass spheres (Polysciences, Inc.) shown in Figure 3.29 are used as particulates. The particle specific weight is 1.1 g/cm^3 and the average diameter is 8 µm, with a range between 2 and 20 µm. Once the solution is mixed, it is left quiescent for a period of 24 hours to test the usefulness of the particulates. The majority of the particles remained suspended after the 24 hour period. Particle seeding is important for accurate results. About 8 – 10 particles should be present in the interrogation window during image analysis.

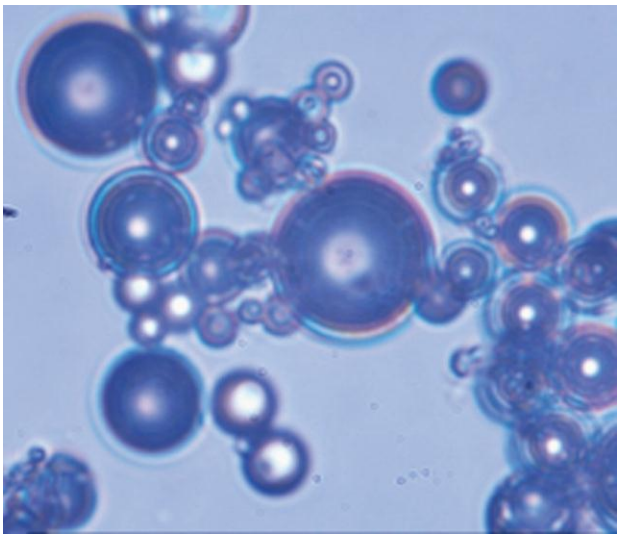

Figure 3.29. Image of hollow glass spheres (2-20 µm) at 100x magnification.

Figure 3.30 shows an actual photograph of the laser and laser power source used during experiments. The flow field is illuminated by creating a laser light sheet using a MGH-H-532, solid-state green laser (Opto Engine) with a power output of 1.4 W. A 60° lens is attached to the laser as a line generator to create the light sheet. The laser operated at a wavelength of 532 nm and it was able to make a light sheet of about 1.5 mm thick.

Figure 3.30. Actual photograph of laser and laser power source used for experiments.

The PIV images are recorded using a Basler acA2040-180 km CMOS camera attached to a PIXC1-E8 frame grabber (Epix, Inc.) housed in a computer. Two cameras were used for experiments to be able to capture a larger field of view in the mixing tank. Figure 3.31 shows an example of the location of the two cameras used during the vertical impinging jet and angled impinging jet location. The location does not contain the wall boundaries due to the erroneous vectors noticed during testing, which will be discussed more later.

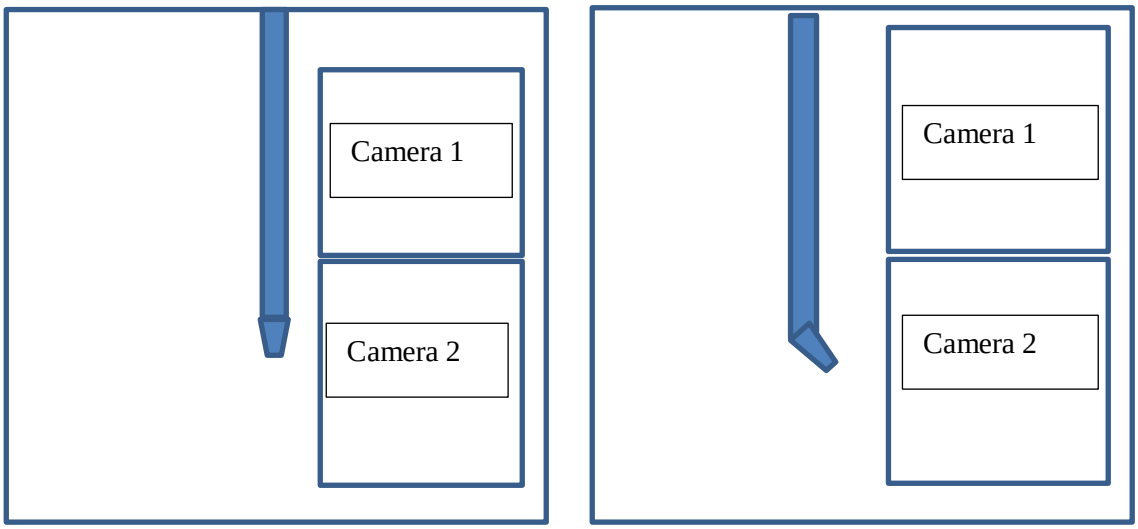

Figure 3.31. Schematic showing the location of the two cameras in reference to the location of the jet for the (a) vertical impinging jet and (b) angled impinging jet.

The specifications of the monochromatic, CMOS camera are organized in Table 3.2. Images are recorded with a resolution of 2048 x 2048 pixels. Navitar NMV-35M1 lenses are used, which have an effective focal length (EFL) of 35 mm. The lenses have a minimum *f*-number of 1.4. The images are taken with an exposure time of about 1 ms. The frame grabber is a Camera Link frame grabber that is able to capture the camera frame rate sequence using 1.4 Gbyte/sec burst transfer. The frame grabber can be housed in a computer with a PCI Express x8

bus slot and 512 MB of memory. The sensor and frame grabber was controlled using XCAP-Std software (Epix, Inc.) which allowed for sequence capture and manipulation of images.

Table 3.2

Specification of the CMOS camera.

Resolution horizontal/vertical	2048 pixels x 2048 pixels
Pixel size horizontal/vertical	5.5 µm x 5.5 µm
Frame Rate	180 fps
Interface	Camera link
Pixel Bit Depth	10 or 12 bits
Sensor type	CMOS
Sensor Size (mm)	11.26 mm x 11.26 mm

The PIV images are evaluated using open-source PIV Matlab code (PIVlab_1.32). The code uses time-resolved PIV to pair images and calculates the velocity distribution. The code is also able to derive, display, and export many other parameters of the flow field (Thielicke, W. and Stamhuis, E., 2010). Images are analyzed using an interrogation area (IA) of 64 x 64 µm with an overlapping IA of 50%. The PIV correlation uses a 2x3 point sub-pixel estimator. Vector validation is completed for all images to remove any erroneous vectors. Validation is done uses a standard deviation filter which removes vectors outside a certain limit of the mean and it also interpolates missing vectors.

One issue that was noticed is erroneous, or spurious, vectors in the flow field, especially near solid boundaries. The erroneous vectors can be partly explained by the construction of the tank, as the outer edges of the tank contain an adhesive material. Erroneous vectors are known

to be a result of particles sticking to surfaces, surface defects, and large velocity gradients in the near-wall region (Doorne, C. and Westerweel, J., 2007). Due mostly to the flaws in the mixing tank, a region of interest was selected for the images which did not include areas very close to the wall.

Initial tests were run to test the "in-house" PIV system. A simple, gravity-driven pipe flow problem was setup to test the system and determine any issues that may arise during future testing. Figure 3.32 shows a schematic of the pipe flow experimental setup. A cylindrical polycarbonate tube was used for testing. The outside diameter was 19.05 cm (3/4") and the length of the pipe was 0.61 m (24"). The tube was constructed so that the fluid was discharged through a circular orifice, 3.57 mm (9/64") in diameter.

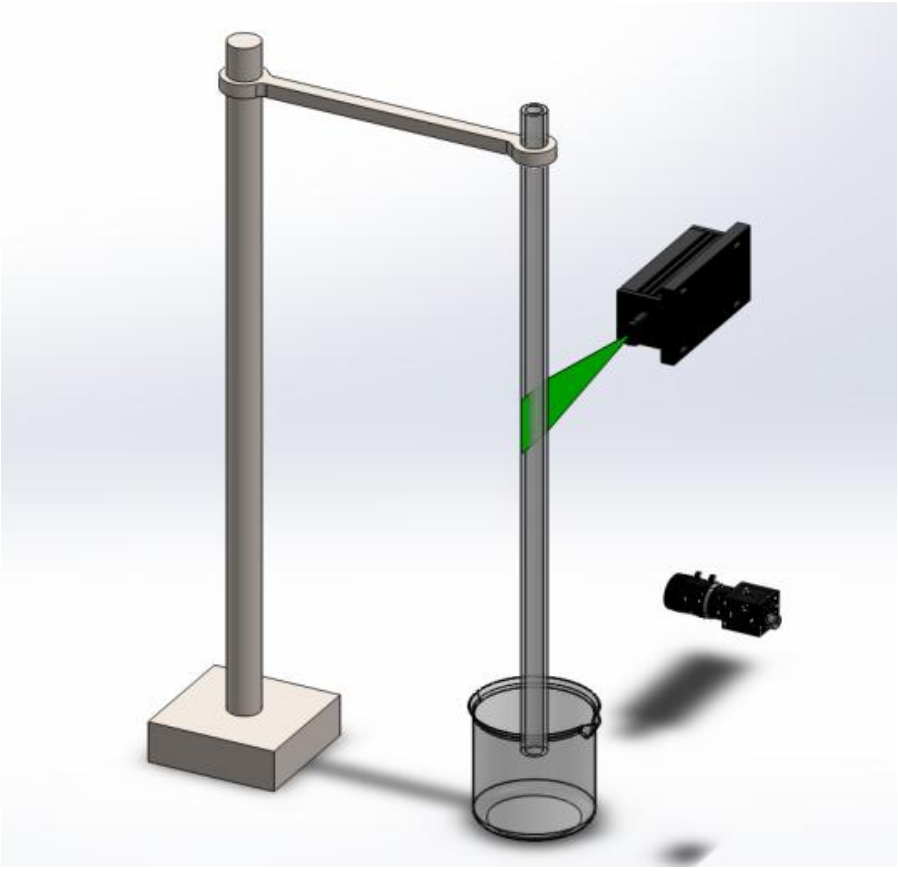

Figure 3.32. Schematic of experimental setup for gravity-driven pipe flow.

An analytical solution was derived for the problem from the Navier-Stokes equation. Assuming one-dimensional (1D) flow, with gravity as the driving force, equation (3.25) was derived.

$$U_z(r) = \frac{1}{4}\frac{\rho g}{\mu}R^2\left(1 - \frac{r^2}{R^2}\right) \tag{3.25}$$

The results of equation (3.25) give a parabolic velocity profile. The volumetric flow rate can be found using

$$\begin{aligned} Q = \int \vec{V} \cdot \overrightarrow{dA} &= \int_0^R U_z(r) \cdot 2\pi r dr \\ &= \frac{\rho g \pi}{8\mu}R^4. \end{aligned} \tag{3.26}$$

The average velocity, V_{avg}, is given by

$$V_{avg} = \frac{Q}{A} = \frac{Q}{\pi R^2} \tag{3.27}$$

The point of maximum velocity is found to be at r = 0, or at the centerline of the pipe. Therefore, the maximum velocity is given by equation (3.28)

$$V_{max} = 2\vec{V} \tag{3.28}$$

The volumetric flow rate in the pipe is equal to the flow rate exiting the orifice due to continuity. So the velocity in the pipe can be ascertained.

Figure 3.33 shows the velocity magnitude of the gravity driven pipe flow. Specifically, Figure 3.33a displays the raw image of the measured velocity, which shows the parabolic nature of the velocity flow field. Figure 3.33b displays the results in a contour. The well-known parabolic shaped profile is observed from the Poiseuille flow problem and is evident in both images. The results show that the velocity is lowest closest to the wall. A maximum velocity

was observed at the centerline. The maximum velocity was found to be 0.12787 m/s on the centerline.

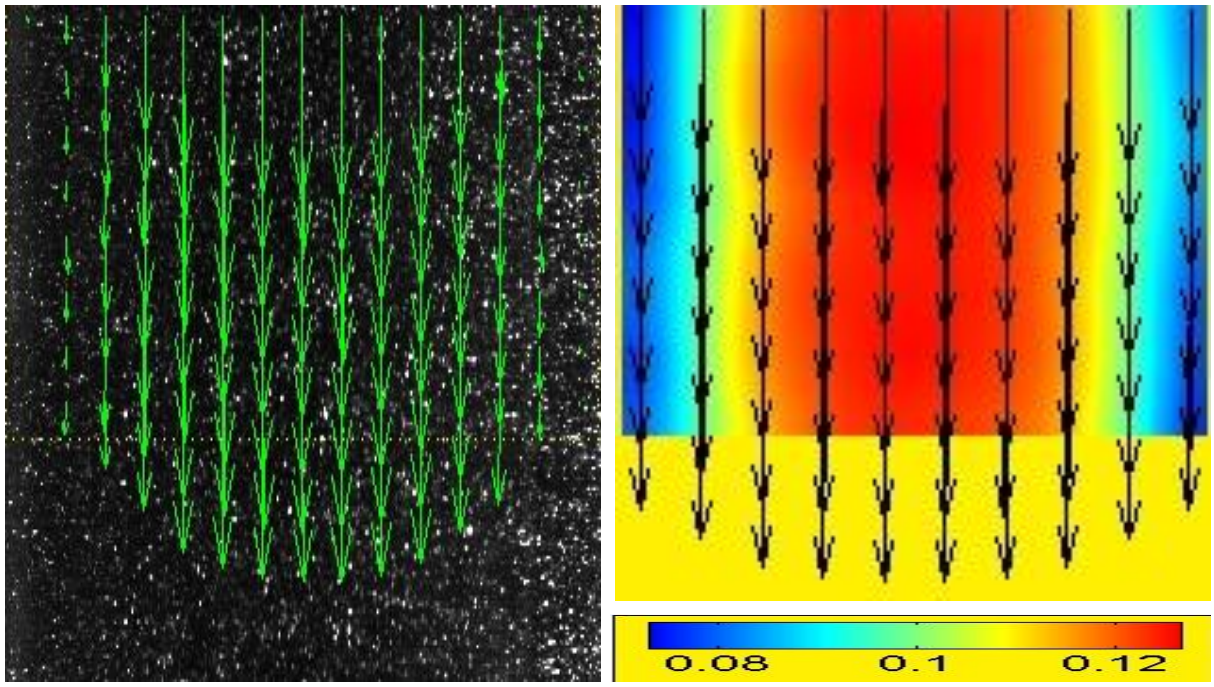

(a) (b)

Figure 3.33. Velocity magnitude (m/s) of gravity-driven pipe flow shown in (a) raw data form and (b) contour form.

Figure 3.34 shows the parabolic flow profile as a function of the horizontal axis of the tube. The results are from a different data set than the results previously shown in Figure 3.33. The plot reinforces the symmetrical nature of the pipe flow problem. The no-slip condition along the tube's boundaries, 0 and 0.019 m, is displayed as the velocity nears zero. The results at the origin actually computed a velocity of 5.76e-05. However, the value is so small that it can be inferred to be zero. The difference between the measured velocity value and zero can be viewed as the experimental uncertainty of the PIV technique. The difference is minimal and provides further confidence in the PIV system.

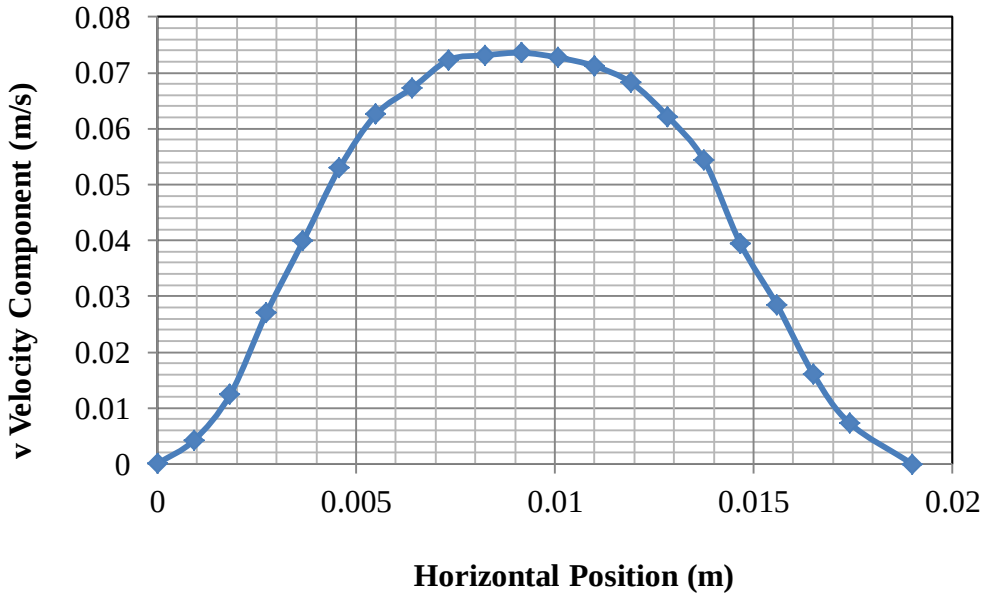

Figure 3.34. Velocity magnitude versus distance, demonstrating the parabolic flow profile.

Comparisons between the theoretical values and the measured values from experiments are compared in Table 3.3. The uncertainty of the measured value from the theoretical value is 3.5%. The small deviation is within the acceptable range of experimental error. Thus, further experiments can be run with confidence that the results are accurate.

Table 3.3

Comparisons of theoretical values and experimental values for gravity flow PIV studies.

	Theoretical	Experimental
Volumetric flow rate (m^3/s)	3.92×10^{-5}	1.903×10^{-5}
Maximum velocity (m/s)	0.1325	0.12787

The jet mixing experiments used the vertical and angled impinging jet mixers as previously displayed in the schematic in Figure 3.31. The aspect ratio in terms of liquid level (AR_L), which is defined as the ratio of liquid level and tank width, was varied from 0.5 to 0.75.

The liquid level aspect ratios were chosen so that the jet remained submerged throughout the studies.

3.5 Computational Methodology

A computational model has been developed in accordance with the first specific objective presented in Chapter 1. The computational model was used to simulate jet mixing performance in liquid blending systems. Well explored computational techniques were used to run initial studies to determine the best configuration to use for jet mixing studies. Computations were run to complete mixing time studies and flow pattern studies, which helped give insight into how the jet mixing system would perform. The commercial CFD package, ANSYS FLUENT, was used for all computational studies. ANSYS FLUENT has the capability to model the flow, heat transfer, turbulence, and chemical reactions found in industrial applications. The software was used in this study to observe the flow field created by the turbulent, unsteady jet and to obtain mixing times under various conditions.

3.5.1 Computational model. The FLUENT software is useful as there are various turbulent models available to choose from. Some of the options include the k-ε realizable with non-equilibrium wall functions, standard k- ε models with standard wall functions, and the Spalart-Allmaras. Other models are also available. Initially the standard k- ε model was used based on its ease of implementation and lack of computational demand as compared to the other turbulent models (Patwardhan, A. W., 2002).

The standard k-ε model is a semi-empirical model based on the transport equations for the turbulence kinetic energy (k) and the dissipation rate (ε). The transport equations for the turbulence kinetic energy and its dissipation rate is expressed as

$$\frac{\partial}{\partial t}(\rho k) + \frac{\partial}{\partial x_i}(\rho k u_i) = \frac{\partial}{\partial x_j}\left[\left(\mu + \frac{\mu_t}{\sigma_k}\right)\frac{\partial k}{\partial x_j}\right] + G_k + G_b - \rho\epsilon - Y_m + S_k \quad (3.29)$$

$$\frac{\partial}{\partial t}(\rho \epsilon) + \frac{\partial}{\partial x_i}(\rho \epsilon u_i) = \frac{\partial}{\partial x_j}\left[\left(\mu + \frac{\mu_t}{\sigma_\epsilon}\right)\frac{\partial \epsilon}{\partial x_j}\right] + C_{1_\epsilon}\frac{\epsilon}{k}\left(G_k + C_{3_\epsilon}G_b\right) - C_{2_\epsilon}\rho\frac{\epsilon^2}{k} + S_\epsilon \quad (3.30)$$

where G_k is the generation of turbulence kinetic energy due to the mean velocity gradients, G_b is the generation of turbulence kinetic energy due to buoyancy, and Y_m is the contribution of the fluctuating dilation in compressible turbulence to the overall dissipation rate. The parameters $C_{1\varepsilon}$, $C_{2\varepsilon}$, $C_{3\varepsilon}$ are constants. The parameters σ_k and σ_ε are the turbulent Prandtl numbers for k and ε. The parameters S_k and S_ε are user defined source terms. The eddy viscosity, μ_t, is calculated as

$$\mu_t = \rho C_\mu \frac{k^2}{\epsilon} \quad (3.31)$$

where C_μ is a constant. The default values for the model constants $C_{1\varepsilon}$, $C_{2\varepsilon}$, C_μ, σ_k, and σ_ε are displayed in equation (3.32).

$$C_{1_\epsilon} = 1.44, C_{2_\epsilon} = 1.92, C_\mu = 0.09, \sigma_k = 1.0, \sigma_\epsilon = 1.3 \quad (3.32)$$

A pressure-based, transient solver was used to model the time-dependent jet flow. The 2nd order Pressure Implicit Splitting of Operators (PISO) algorithm helps maintain stability in the modeling process. The PISO scheme is able to solve the discretized time-dependent Navier-Stokes (N-S) equations in a sequential uncoupled manner and it can be used for incompressible and compressible forms of the N-S equations (Tannehill, J. C. et al., 1997).

3.5.2 Geometry and mesh generation. All geometry development and meshing of the geometry is completed using the CAD software, Gambit. The geometry was created to replicate that of the physical system. Certain minor changes were made in the development of the geometry to ensure a smooth mesh is created and ultimately an accurate solution is calculated.

Models were completed for single, dual, quad, and azimuthal jet mixing configurations, which are shown in three-dimensional views in Figure 3.35. The quad and azimuthal jet mixing systems contained four actual jets. Also, Figure 3.36 shows the top view of the azimuthal jet configuration. When compared to the actual mixing tank used in experiments, the computer geometry is reduced in height to the location of the overflow port.

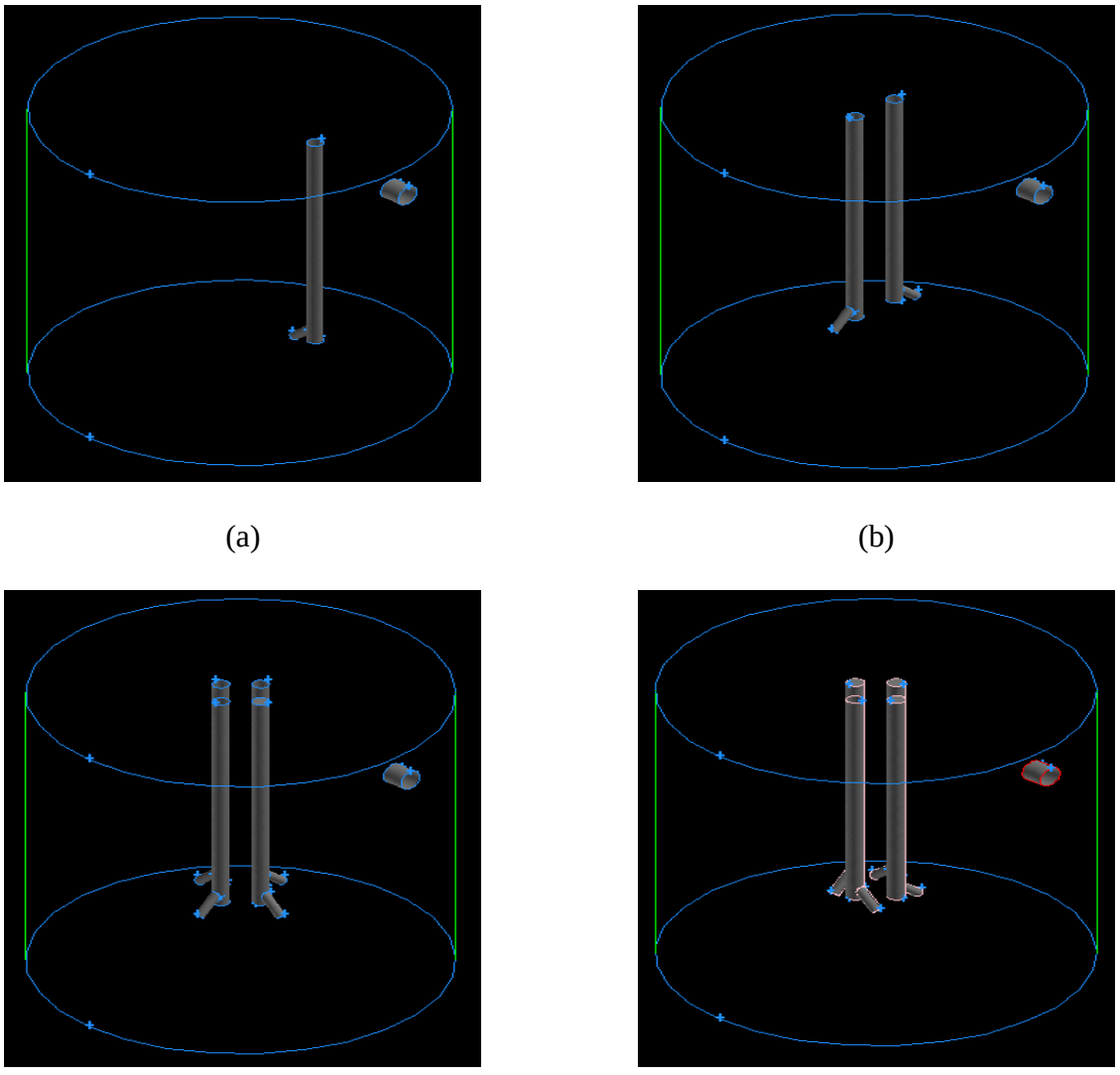

(a) (b)

(c) (d)

Figure 3.35. The different jet mixer arrangements including (a) single jet, (b) dual jet, (c) quad jet, and (d) azimuthal jet systems.

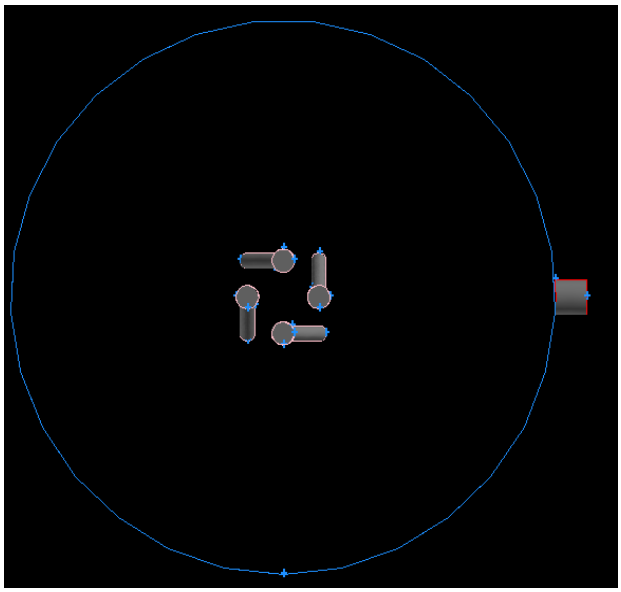

Figure 3.36. Top view of azimuthal oriented jets.

The parameters of the models used in simulations are summarized in Table 3.4. Studies were not only run in which the number of jets were varied, but the jet height from the bottom of the tank was also varied. The other parameters such as jet angle, nozzle diameter, and jet Reynolds number are specified in the table. The fluid used for simulations was water at 20º C.

Table 3.4

Parameters used in computational studies.

No. of jets	1, 2, and 4
Tank diameter	0.305 m (12”)
Tank height	0.305 m (12”)
Liquid height	0.305 m (12”)
Outlet diameter	1.905 cm (3/4”)
Outlet height from bottom	0.29 m

Table 3.4

Cont.

Jet height from bottom	0.025 and 0.07625 m
Nozzle diameter	8 mm
Jet angle	45°
Jet Reynolds number	80,000

A properly meshed geometry is important so that the full nature of the fluid flow is captured. There are various meshing shapes or elements (i.e. quadrilateral, triangular) and scheme types (i.e. pave, map, submap, tri-primitive) that can be applied to the mesh. A triangular, tri-primitive meshing technique was applied for the current study using tetrahedral elements, as can be seen in Figure 3.37. The size of the mesh will be discussed in a later section.

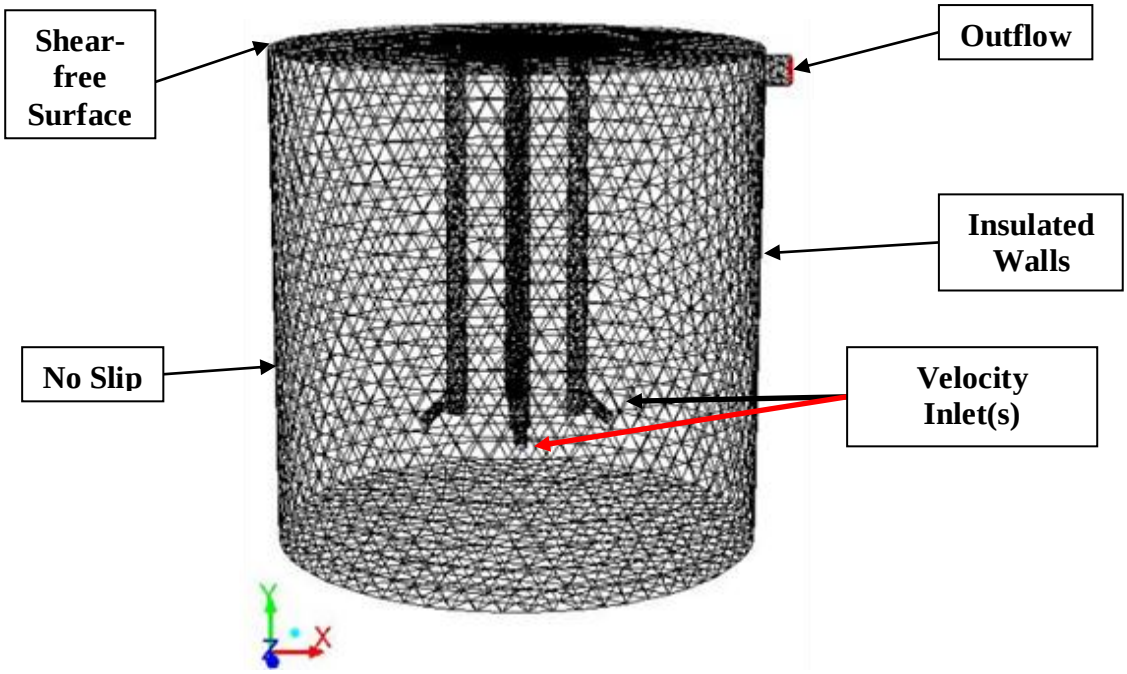

Figure 3.37. Jet mixing tank model, including the mesh and boundary conditions.

3.5.3 Boundary conditions. The locations of the applied boundary conditions are shown in Figure 3.37. The velocity inlet boundary condition was used and set to a constant value for the steady jets. However, for unsteady jets, the velocity of the jet was supplied to the model in such a way to prescribe a jet flow at periodic, square-wave cycles. Figure 3.38 shows an example of the square wave velocity profile used for computations compared to the actual profile from experiments using the solenoid valve. For this, user defined functions (UDF) must be supplied. The UDF is a program which is written in C++ and it has the ability to supply parameters which vary with time.

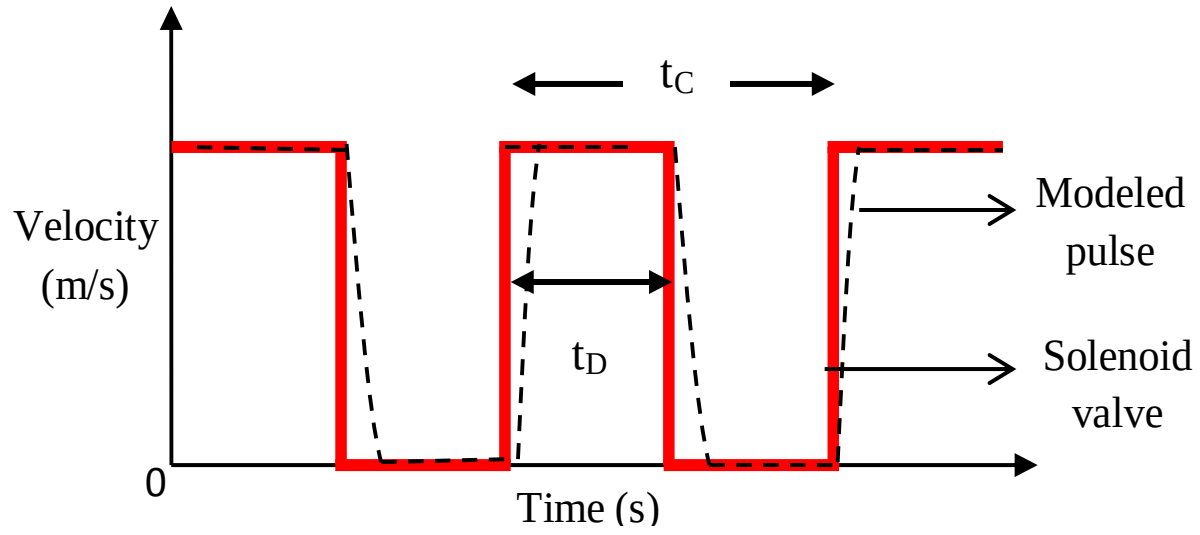

Figure 3.38. Example of pulsing function of jet nozzle used in CFD and by solenoid valve in experimental work.

The walls of the cylindrical was set to be solid walls in which no heat transfer occurs and therefore were assumed insulated. The no-slip condition, in which the velocity of the fluid at the wall is equal to the velocity of the wall, was applied to the solid boundaries. The top boundary of the actual mixing vessel was modeled as a free surface. In the actual vessel which has space at the top of the tank above the liquid level, air occupies the space. Computationally, modeling

the air/liquid interface can be costly to model as an additional phase must be added and therefore it was assumed that the flow rate of air is negligible compared to that of the actual jet (Rosendall, B. et al., 2006). The free surface velocity was assumed to be negligible compared to that of the jet flow. The top surface was modeled as a free shear wall boundary condition.

3.5.4 Grid independence study. Meshing plays a vital role in computing a solution in CFD. A grid independence study is necessary as it determine the extent to which the grid spacing has on the accuracy of the solution. In most studies, a main solution parameter, such as velocity, pressure, shear stress, concentration, etc. is observed during a simulation using a particular mesh size. The mesh is then decreased to smaller intervals and thus more volume elements. The simulation is then repeated and the same solution parameter is observed. The process is repeated until the solution parameter does not vary at all or a very minimal amount. At this point it can be said that the solution is independent of the grid. As the meshing becomes smaller, it consequently demands more computational time. Thus, to save on computational costs, the grid spacing will be used in which it was first noticed that the results did not change. Through this technique, it was determined that 15 mm grid spacing was adequate to provide accurate solutions. The velocity at a specific location on the bottom surface was the monitored parameter for the grid independence studies.

3.5.5 Methodology. The method used to calculate the mixing time for the present system was based on a thermal criterion. The bulk fluid was set to 283° K and the liquid jet entered the tank at a higher temperature, 350° K. A 65% homogeneity criterion was used to find the mixing time for the simulations. The mixing time was calculated as the time between the beginning of the simulation until the time at which the temperature becomes 65% of the equilibrium temperature, or m = 0.35. Equation 1.1 can be rewritten to express this condition as

$$m = \frac{T_{eq} - T}{T_{eq} - T_o} < 0.35 \tag{3.33}$$

where T_{eq} is the equilibrium temperature, T_o is the initial temperature of the bulk fluid in the tank, and T is temperature at any location in the tank at any time. The mixing time criterion was chosen to save on computational time.

Temperature probes were placed in various locations of the mixing tank and the temperature at those locations were recorded as a function of time for the duration of the numerical run. When all locations met the mixing criteria, the tank was considered mixed and the time elapse was reported as the mixing time. A scaling analysis was completed and it was found that the Peclet number, which compares convection time to diffusion time in the flow, was 1.46×10^4. Since the Peclet number was large, the flow was convection dominated and the use of a scalar quantity, like temperature, was deemed to be acceptable.

Initially, the jet mixers were simulated as continuous jets to determine a baseline for comparison throughout the study. The mixing time and the wall shear stress on the bottom surface were calculated and reported. Simulations were then run using pulsing jet mixers.

Table 3.5 shows the four different pulse settings that were used in the present study. One complete pulse system consisted of a discharge time (time on) and an off time for the jet. When the jet was set to on, the inlet velocity was set to 10 m/s and when off, the velocity was fixed at 0 m/s. The settings used in this system are not indicative of all the possible settings that can be used. But the settings used in the study helps give insight into which setting may give the best overall mixing. The pulse settings were used in a manner in which the time off was relatively short when measured in terms of particle settling velocity thus ensuring uniform dispersion of particles.

Table 3.5

Pulse settings used for computational studies.

Pulse Setting Name	Time on (s)	Time off (s)
Pulse 1 (P1)	2.5	0.5
Pulse 2 (P2)	3.5	0.5
Pulse 3 (P3)	5.0	0.5
Pulse 4 (P4)	5.0	0.25

Results from all of the different jet mixing experimental and numerical studies are presented in Chapter 4. Results from the analytical solutions are discussed as well.

CHAPTER 4

Results

All of the data that was collected during experiments are presented in this chapter. Mixing time results are presented from CFD and experimental studies for steady and unsteady jet mixers. Liquid-solid mixing results are presented in terms of cloud height, erosion profiles, and vertical axial concentration profiles. The jet Reynolds number was varied during the solid-liquid experiments.

CFD simulations were used as an additional tool to optimize the jet location and other system parameters and to help get a better understanding of how the parameters affect the performance of the system. The results of the CFD studies were then used to run experimental studies for mixing time, flow studies, and solid suspension studies.

4.1 Mixing Time Studies

Mixing time studies were run using CFD and experiments. The jet Reynolds number was varied throughout the studies. A direct comparison of the quantitative mixing time results cannot be made between the CFD and the experimental results because different criterion was used to determine the mixing time. A homogeneity criterion of 65% was used for the CFD studies and 95% for the experimental studies. A lower criterion was used for the CFD studies due to computational time limitations. The results are presented for both continuous and pulse jet mixers.

4.1.1 CFD mixing time. Some of the results from the computational studies has been published by Muhammad and Kizito (2011). The height of the jet(s) was varied from 0.025 – 0.07625 m from the bottom of the tank. These heights were based on designs by previous researchers and the construction of the current system.

Continuous (steady) jets. Four different pulse setting were used during the CFD studies using a single jet Reynolds number. Figure 4.1 displays the mixing time results for the various types of jet configurations positioned at 0.07625 m from the bottom of the tank. The temperature within the tank was reported in multiple positions at multiple heights to ensure the behavior in critical zones of the tanks was accurately represented. The results showed that to achieve 65% homogeneity at both jet heights, the mixing time decreased as more jets were added.

Figure 4.1 shows that at a jet height of 0.07625 m from the bottom of the tank, the mixing time for the set criteria was decreased about half as the number of jets were doubled. The mixing time increased fairly linear where the slope increased as more jets were added.

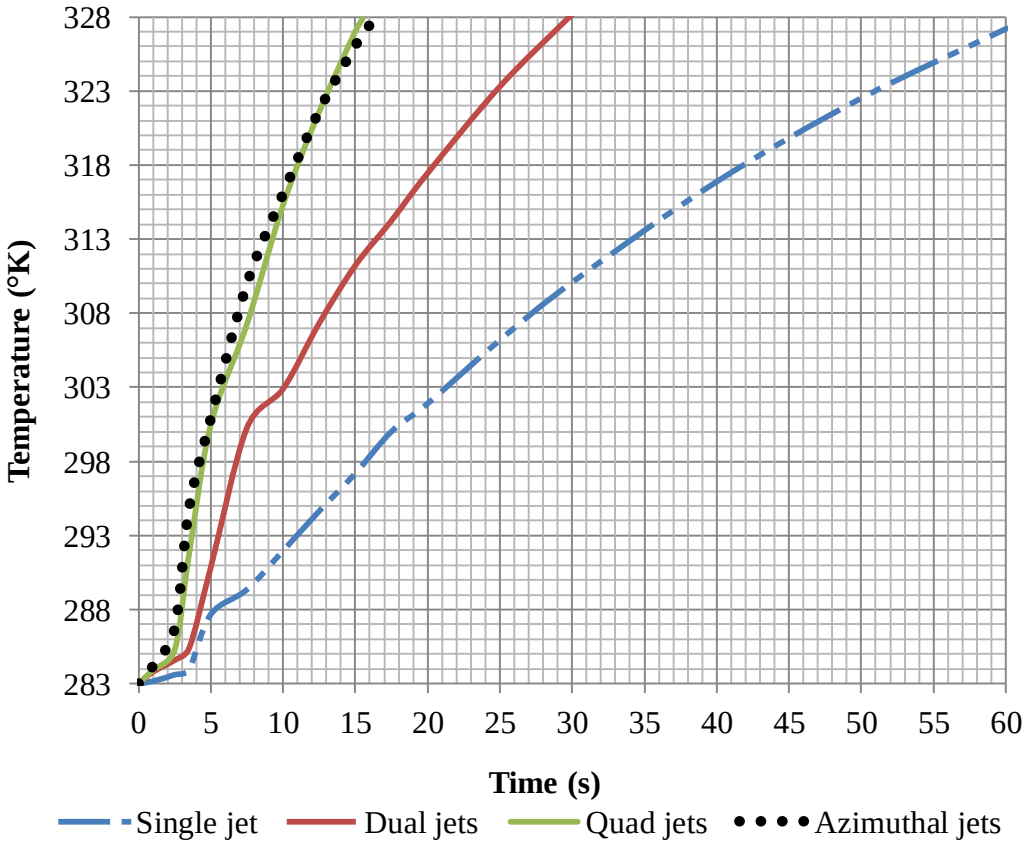

Figure 4.1. Mixing times for continuous jet systems with jets located 0.07625 m from bottom of tank and at a 45° angle.

The best jet arrangements were the quad and azimuthal orientations. The lowest mixing times was expected for the quad and azimuthal jet orientations because the jets introduced more momentum was into the tank from the jets compared to the single and dual configurations. The quad jets arrangement had the overall best mixing time of 15.4 s, though the quad and azimuthal jets had very close mixing times.

Figure 4.2 displays the mixing time results for the different jet configurations at a height of 0.025 m from the bottom of the tank. The same trend occurred at a jet height of 0.025 m as was reported at 0.07625 m. The mixing time decreased as the number of jets increased and the lowest mixing time was found for the jet configurations which used a total of 4 jets.

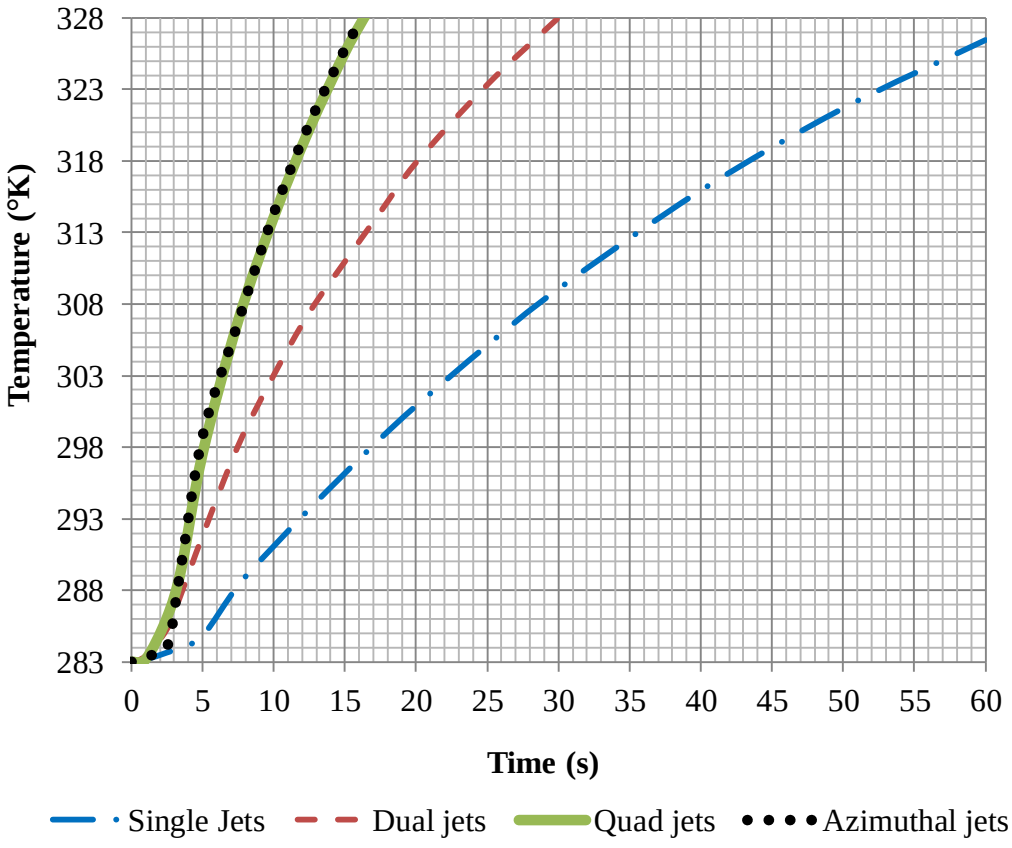

Figure 4.2. Mixing times for continuous jet systems with jets located 0.025 m from bottom of the tank and at a 45° angle.

The azimuthal jets had a mixing time of 15.8 s, which was the lowest at 0.025 m. The result is different than at a height of 0.07625. The discrepancy in results between heights was due to the way the jets were directed and interacted with the walls. The azimuthal jets created jets that travelled along the wall. The strong wall jets, thus, hindered the mixing action in the center of the tank. As the jet nozzles were lowered closer to the bottom of the tank, the jet was not allowed to expand as much before impinging on the bottom surface. Less entrainment of the bulk fluid occurred due to the decrease in jet expansion.

The mixing time results for all of the jet configurations from both heights are summarized in Table 4.1. The table shows that the overall mixing time was lowest with the quad jet configuration. The jet configurations which contained four jets had the best performance and mixing times very close to one another. When a jet height of 0.07625 m was used, the quad jet configuration had a mixing time that was 4.3% less than the azimuthal jet configuration, 47.6% less than the dual jets, and 74.5 % less than the single jet at the same height.

Table 4.1

Mixing time comparisons for continuous jets of different configurations.

Jet Type	H = 0.025 m	H = 0.07625 m
Single	61.6 s	60.5 s
Dual	29.4 s	29.4 s
Quad	16.1 s	15.4 s
Azimuthal	15.8 s	16.1 s

Planar temperature contours were captured for the quad and azimuthal jets since they had the lowest mixing times. Figure 4.3 shows the planar temperature contours for both the quad and

azimuthal jet configurations with the jets positioned 0.07625 m from the bottom of the tank. The planar snapshots were labeled as the xy and yz planes and they intersect at the center of the tank. The snapshots were taken after a time period of 5 seconds. The quad jets, which are shown in Figures 4.3a and 4.3c, created a circulatory pattern in the tank. As the jet impinged on the bottom wall it travelled up the side wall slightly and started to rollover. The rollover effect created the circulatory patterns in the tank, which promotes mixing.

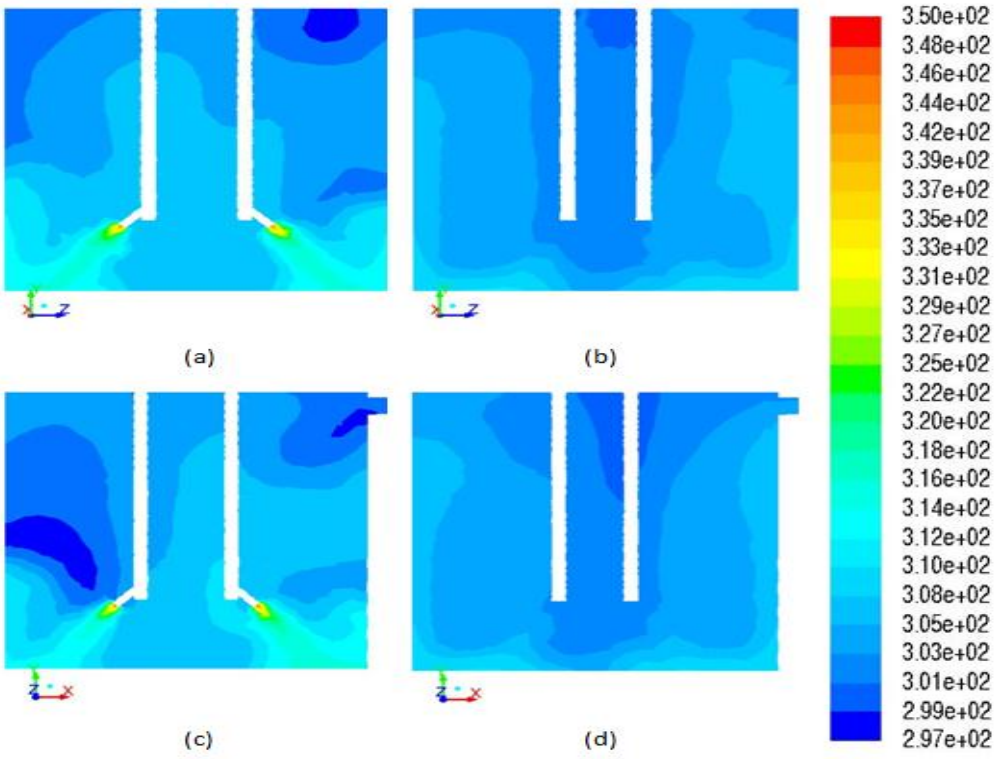

Figure 4.3. Temperature profile in (a) yz- plane of quad jets, (b) yz-plane of azimuthal jets, (c) xy-plane of quad jets, (d) and xy-plane of azimuthal jets at a height of 0.07625 m after 5 seconds flow time.

The azimuthal jets, shown in Figure 4.3b and Figure 4.3d, were directed in such a way that the impinging jets created wall jets that travelled diagonally upwards. The jet discharge is not shown because the jet nozzles were actually directed outside the plane, whereas the plane

split the jet in half for the quad jet configurations. The most prominent mixing action took place at the outer edges of the tank. The least prominent mixing zones are noticeable in the temperature contours, as they are represented by the dark blue regions.

The temperature profiles after 7.5 seconds of flow time for the quad and azimuthal jets in the yz- and xy- planes are shown in Figure 4.4. The minimum temperature in the entire tank has increased from 297º K to 304º K. Comparison of Figures 4.3c and 4.4c, illustrates that the lowest mixing zones after 7.5 seconds are still in the same general location as those after 5 seconds. Figures 4.3a and 4.4a show that the low mixing zone in the yz plane of the quad jet configurations, though still in the upper right hand side, shifts from the top after 5 seconds to the side after 7.5 seconds.

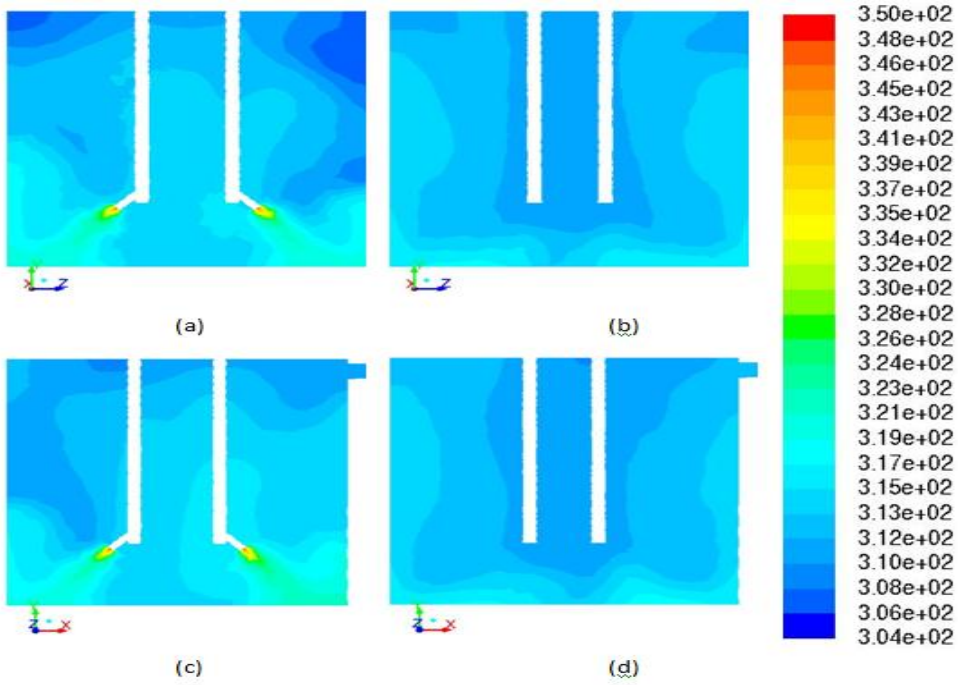

Figure 4.4. Temperature profile in the (a) yz-plane of quad jets, (b) yz-plane of azimuthal jets, (c) xy-plane of quad jet, and (d) xy-plane of azimuthal jets at a height of 0.07625 m after 7.5 seconds flow time.

Comparisons of Figures 4.3b and 4.4b show that the temperature profiles for the azimuthal jets start to create a more uniform flow pattern in the tank. The low mixing areas, however, are still located in the center axis of the tank as expected due to the swirling flow created by the azimuthal jets.

Figure 4.5 shows the planar temperature profiles for the quad and azimuthal jets at a height of 0.0765 m after 10 seconds of flow time. The minimum temperature in the entire tank has now increased to 313 º K. The low mixing zones are still in the general vicinities as observed at previous flow times, but the fluid has been transported through the tank.

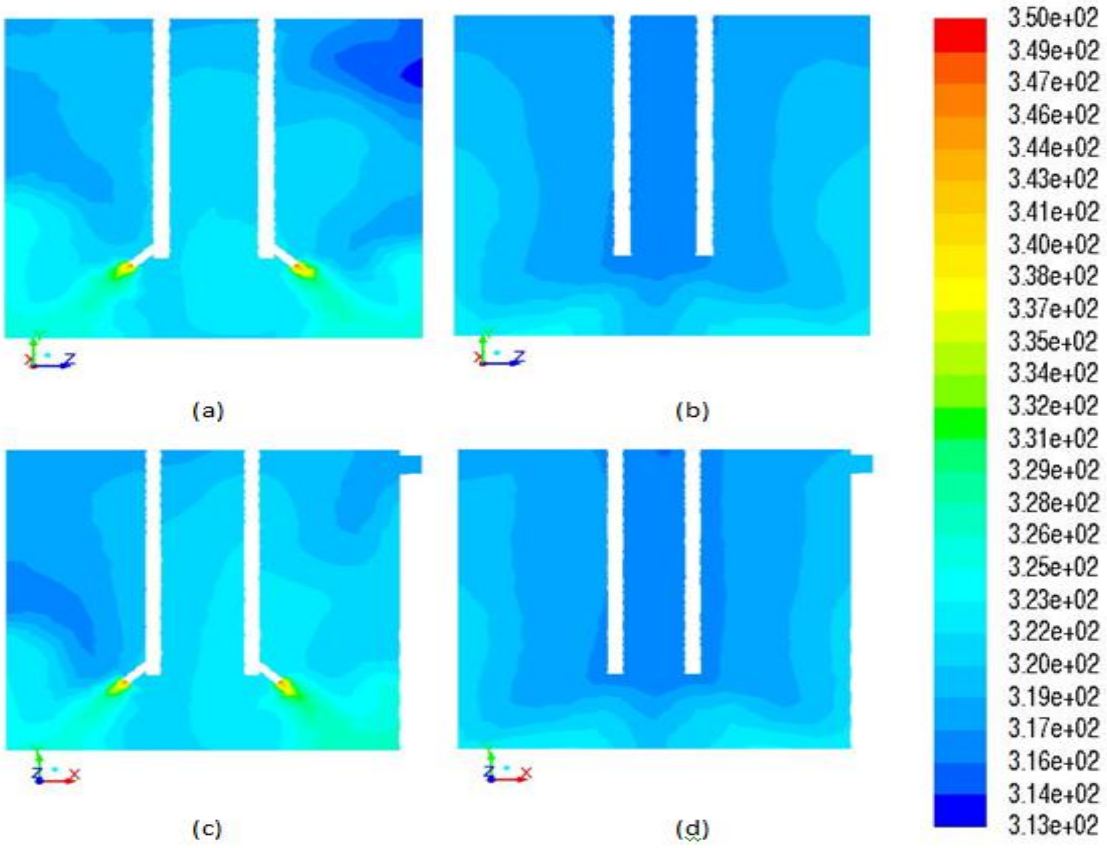

Figure 4.5. Temperature profile in the (a) yz-plane of quad jets, (b) yz-plane of azimuthal jets, (c) xy-plane of quad jet, and (d) xy-plane of azimuthal jets at a height of 0.07625 m after 10 seconds flow time.

Comparison of Figures 4.4c and 4.5c show that the low mixing zones after 10 seconds are very similar to those after 7.5 seconds, but the lowest mixing zones are minimized even further. A comparison of Figures 4.4a and 4.5a show similar observations, as the lowest mixing zones are further minimized. The temperature profiles for the azimuthal jets become very uniform, as noticed from Figure 4.3b, 4.4b, and 4.5b. The temperature contours are able to give insight into how the jets mix the tank over time.

Pulsing jets. The results for the mixing times of the different pulse settings described in Table 3.5 are plotted in Figure 4.6. The different pulse settings were measured using the quad jet system positioned at 0.07625 m from the bottom of the tank since the lowest mixing times were reported for this configuration in earlier studies.

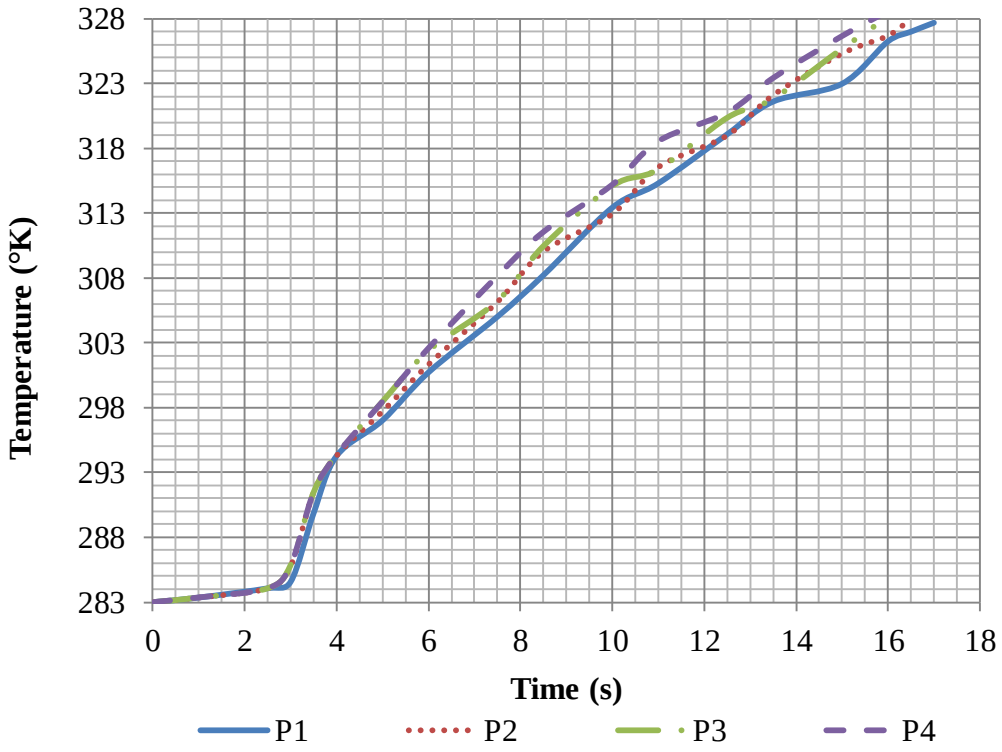

Figure 4.6. Mixing time for different pulse settings in quad jet arrangement with jets 0.07625 m from the bottom of the tank and at an angle of 45°.

The mixing time results are summarized in Table 4.2. The pulse jet mixing time results for each of the settings varied less than 10% from each other. The lowest mixing time was the P4 setting. Table 4.2 shows that as the discharge time was increased and the off time of the jet during the pulses were decreased, then the mixing time was decreased.

Table 4.2

Mixing times for different pulse jet settings.

Pulse Setting	P1	P2	P3	P4
Mixing Time	16.8 s	16.3 s	15.6 s	15.5 s

Figure 4.6 shows that the P4 setting had the lowest mixing time and the P1 setting had the highest mixing time. The mixing time decreased as the period of jet discharge was increased and the off period was decreased. The results in Table 4.2 show that the P4 and P3 settings had mixing times that were very close to that of the continuous jet in the same configuration. The result may be due to there being more local vortices created in the mixing tank compared to the steady jet systems. The vortices are created as the jet is pulsed in a cyclic manner. The mixing time results indicate that it may be possible to increase mixing with some alternate pulsing settings or techniques.

Figure 4.7 shows the temperature profile for the entire first pulse cycle (time on + time off) of the quad jet system using the P1 setting. The P1 setting had a discharge time of 2.5 seconds and an off time of 0.5 seconds. Figures 4.7a and 4.7b show the yz- and xy- planes, respectively, after the initial on period of 2.5 seconds. Figures 4.7c and 4.7d show the yz- and xy- planes, respectively, after the off period of 0.5 seconds. The jet momentum can be seen impinging on the bottom of the tank and spreading up the wall. The results show that the top of

the tank is not well mixed because the total flow time at this snapshot is still short. After the complete first pulse cycle, the flow has been off for 0.5 s, but the convection of the jet continues to spread slowly towards the top of the tank.

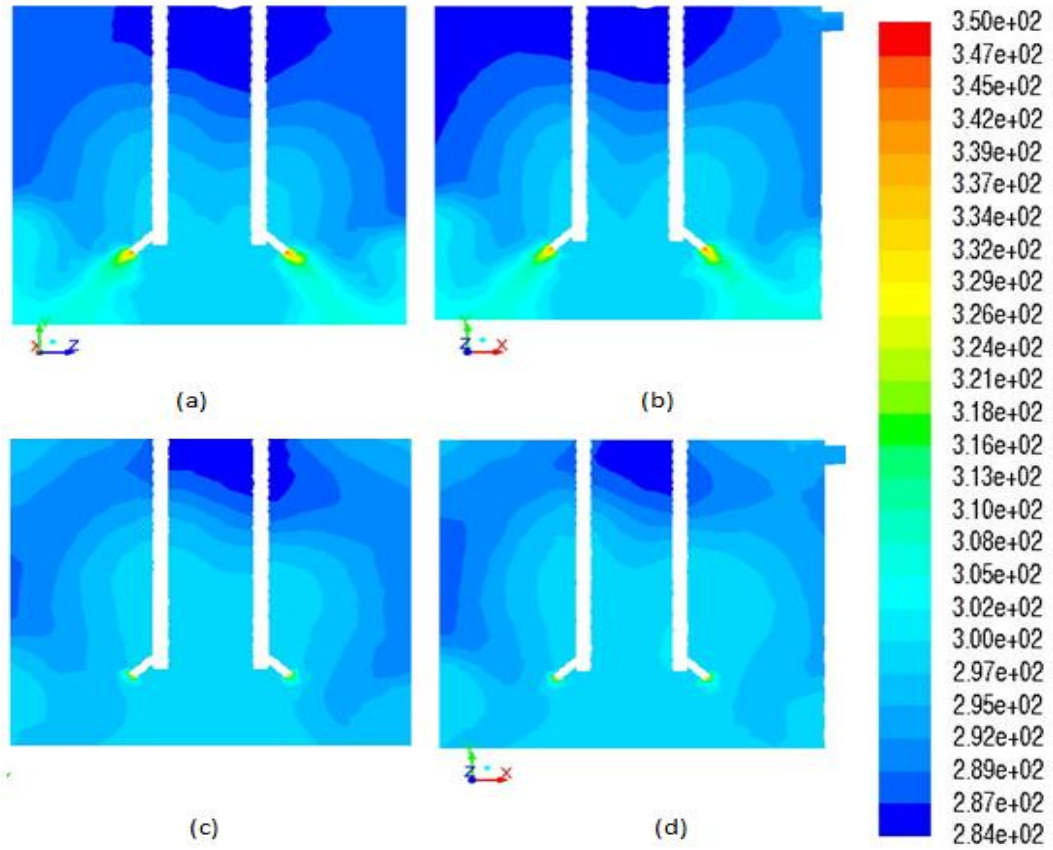

Figure 4.7. Temperature contour of quad jet system of first cycle using P1 setting in the (a) yz-plane after initial on time of 2.5 s, (b) xy-plane after initial on time, (c) yz-plane after initial off time of 0.5 s, and (d) xy-plane after initial off time.

Figure 4.8 shows the temperature profile in the yz and xy plane, respectively, at the end of 3 complete pulse cycles using the P1 pulse cycle. The figures show that though the low mixing zones exist in similar vicinities, the overall profile differs from that of the continuous jets. One of the main mixing locations is near the outlet, as the cooler fluid is forced out of the tank.

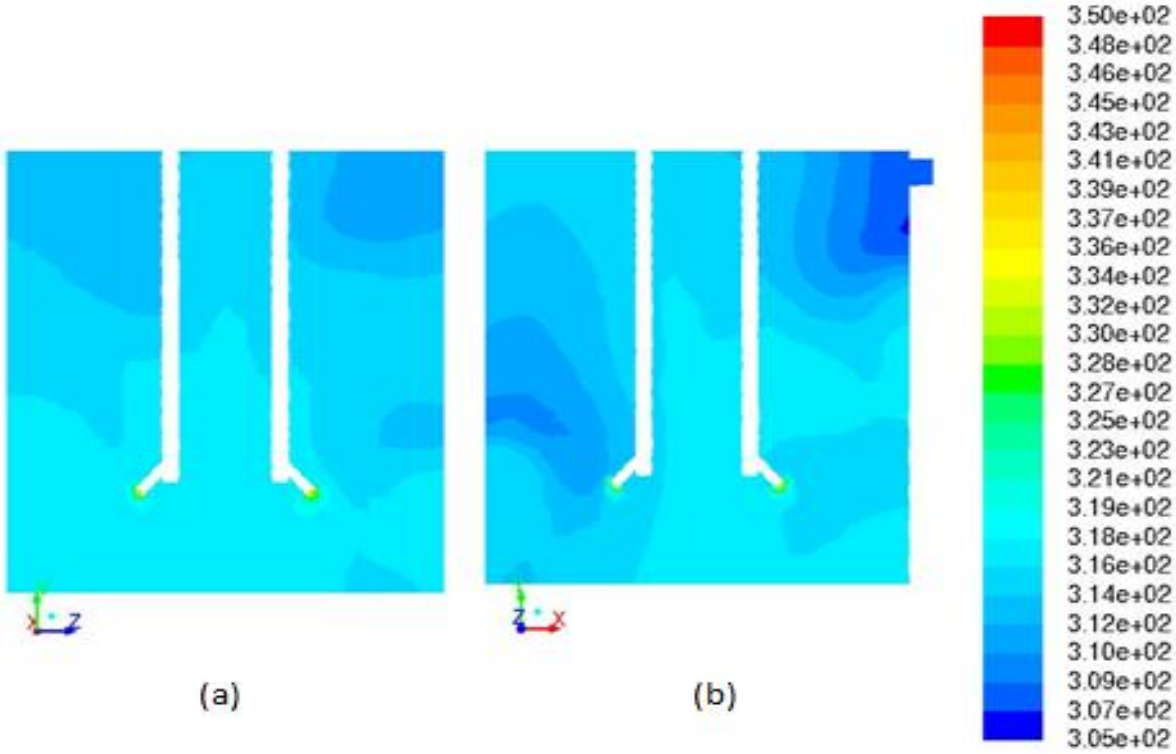

Figure 4.8. Temperature contour of quad jet system after 3 complete pulse cycles using P1 setting in the (a) yz-plane and (b) xy-plane.

Figure 4.9 illustrates the temperature profile of the total first pulse using the P4 setting. The temperature profile after the time on phase for the yz and xy planes, respectively, is shown in Figures 4.9a and 4.9b. The temperature profile after the off phase of the first pulse is shown in Figures 4.9c and 4.9d. The P4 setting had mixing time results just about the same as the continuous jets.

Compared to the P1 setting after a single pulse, more mixing takes place, which is because a single pulse cycle using the P1 setting is a total of 3 seconds while that of the P4 setting is a total of 5.25 second. Comparisons of Figures 4.9a and 4.9c show that during the off period of the pulse cycle, significant mixing still takes place as the low mixing zones are minimized.

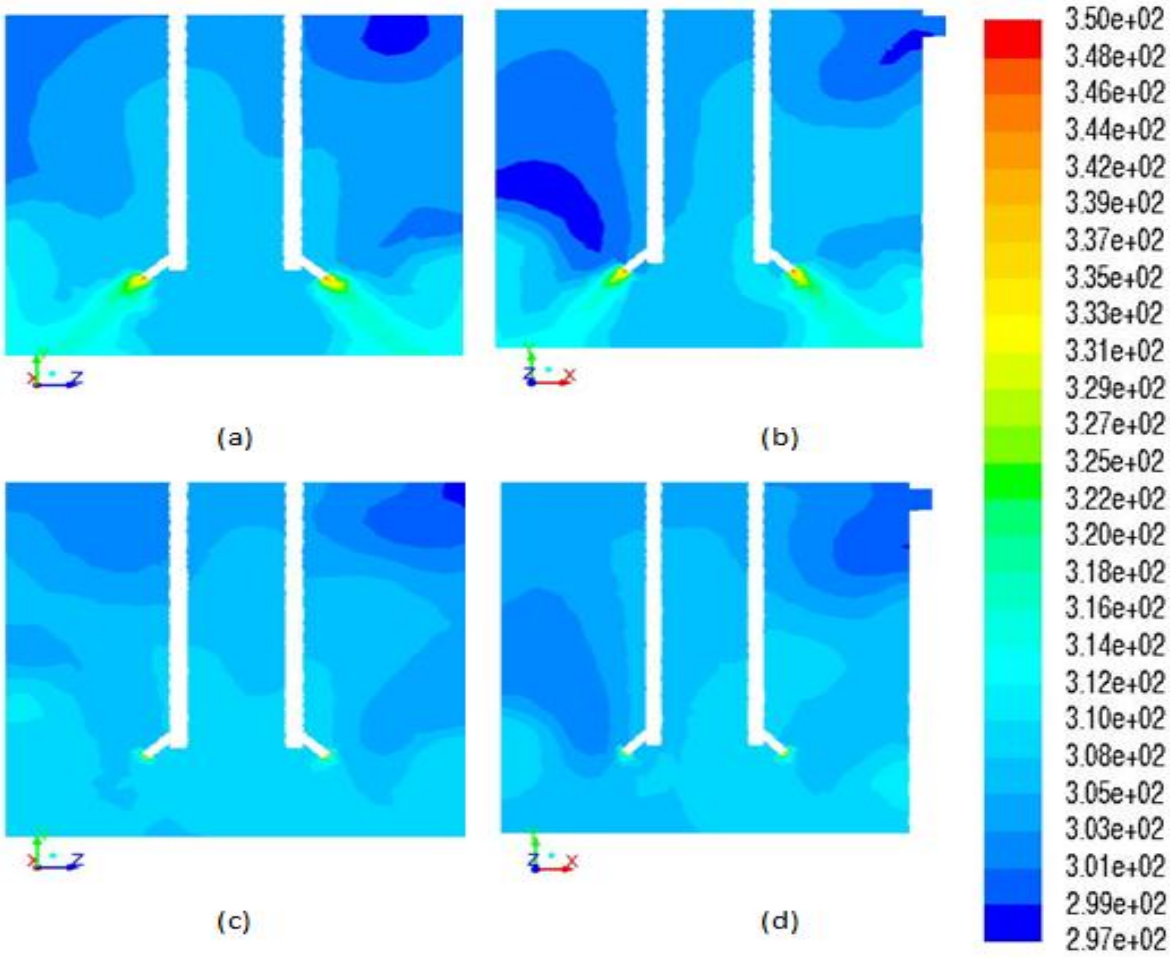

Figure 4.9. Temperature contour of quad jet system of first pulse cycle using P4 setting in the (a) yz-plane after initial on time of 5 s, (b) xy-plane after initial on time, (c) yz- plane after off time of 0.25 s, and (d) xy- plane after off time.

The temperature profile after 3 complete cycles using the P4 setting is shown in Figure 4.10. At this point, the low mixing zones are at a minimum and because the minimum temperature within the tank is about 326, the homogeneity criteria set for the study are almost reached. However, the low mixing zones still appear in the same locations as with the P1 settings and with the continuous jets of this configuration. The low mixing zones did not differ much from case to case, but the temperature profile varied.

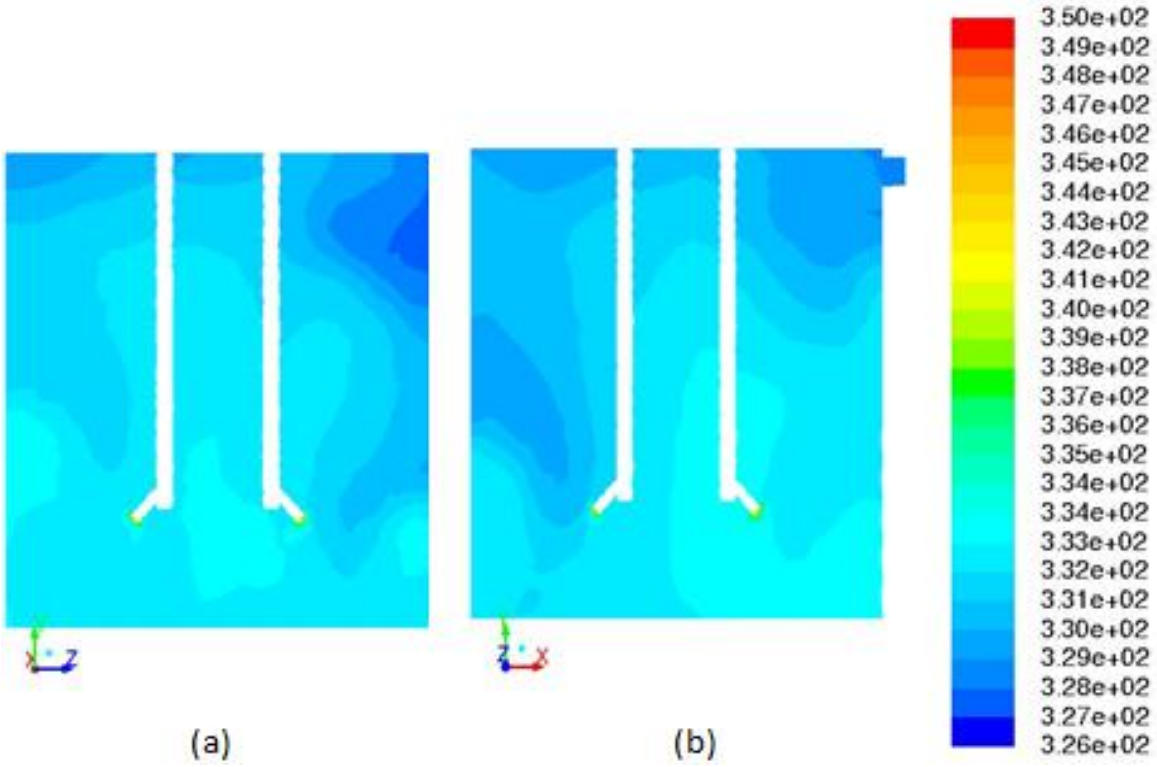

Figure 4.10. Temperature contour of quad jet system after 3 complete pulse cycles using P4 setting in the (a) yz-plane and (b) xy-plane.

The temperature contour profiles in the mixing tank, in some sense, gives an idea of the flow profiles. The temperature contours are able to locate the low mixing zones in the mixing tanks which would become useful when designing jet mixing systems, so that designs can help eliminate them. The temperature contours give great awareness to how long it takes the mixing tanks to reach a certain level of homogeneity.

4.1.2 Experimental mixing time. The mixing time was measured using experimental methods of turbulent, submerged, jet mixer nozzles. Experiments were run for single and dual jet nozzles inclined at 45° from the horizon, directed towards the bottom of the tank. The jet Reynolds numbers (Re_j) ranged from about 6,000 to 22,000. The experimental results are somewhat limited due to the number of sampling locations. Samples of the bulk fluid were taken

at the tank outlet. The sampling location was chosen because the jets were directed towards the bottom of the tank, where the initial and most rapid mixing would occur.

Figure 4.11 displays an example of dimensionless concentration as a function of time for a single jet and dual jet. The mixing time was considered as the time in which the dimensionless concentration deviated less than 5% of the final concentration difference. The peak height represents the distribution of the dye in the tank to the outlet (Patwardhan, A. W. and Gaikwad, S. G., 2003). The dye was dispersed to the outlet for the dual jets more rapidly than in the single jet configuration.

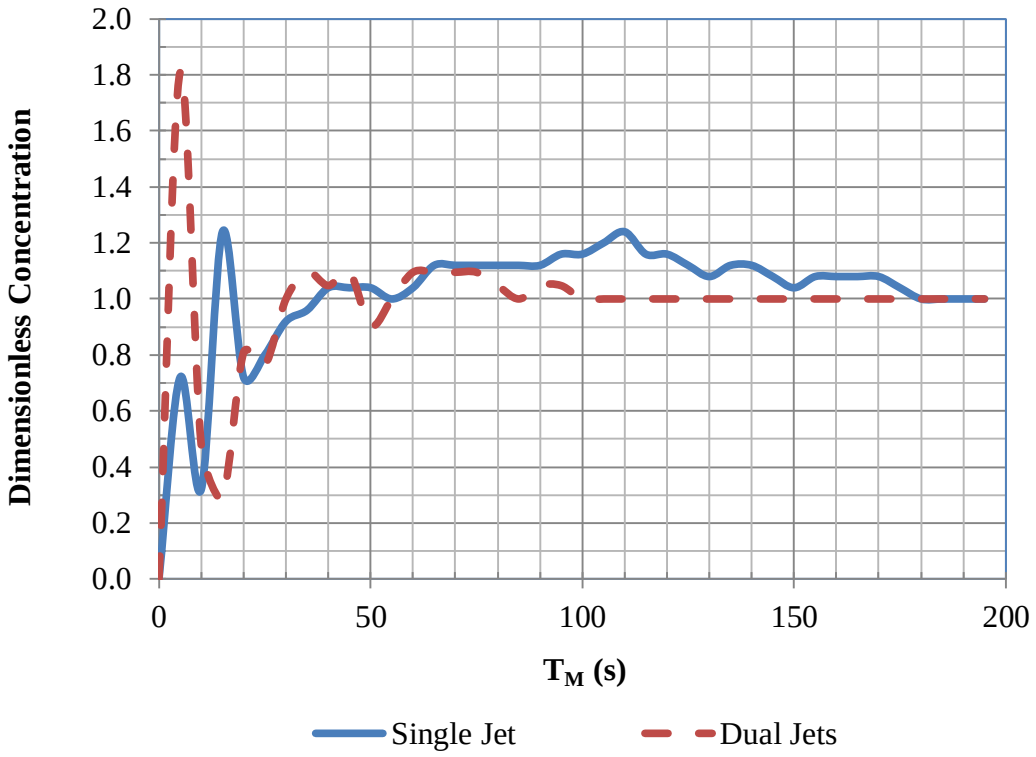

Figure 4.11. Dimensionless concentration as a function of time for single and dual jets.

Figure 4.12 displays mixing time as a function of jet Reynolds number for the steady and pulse single jet. The normal mixing time decreases as Re_j increases. The decrease in mixing

time is expected with increasing Re_j because of an increase of jet momentum force into the mixing time, allowing for quicker circulation of fluid throughout the tank.

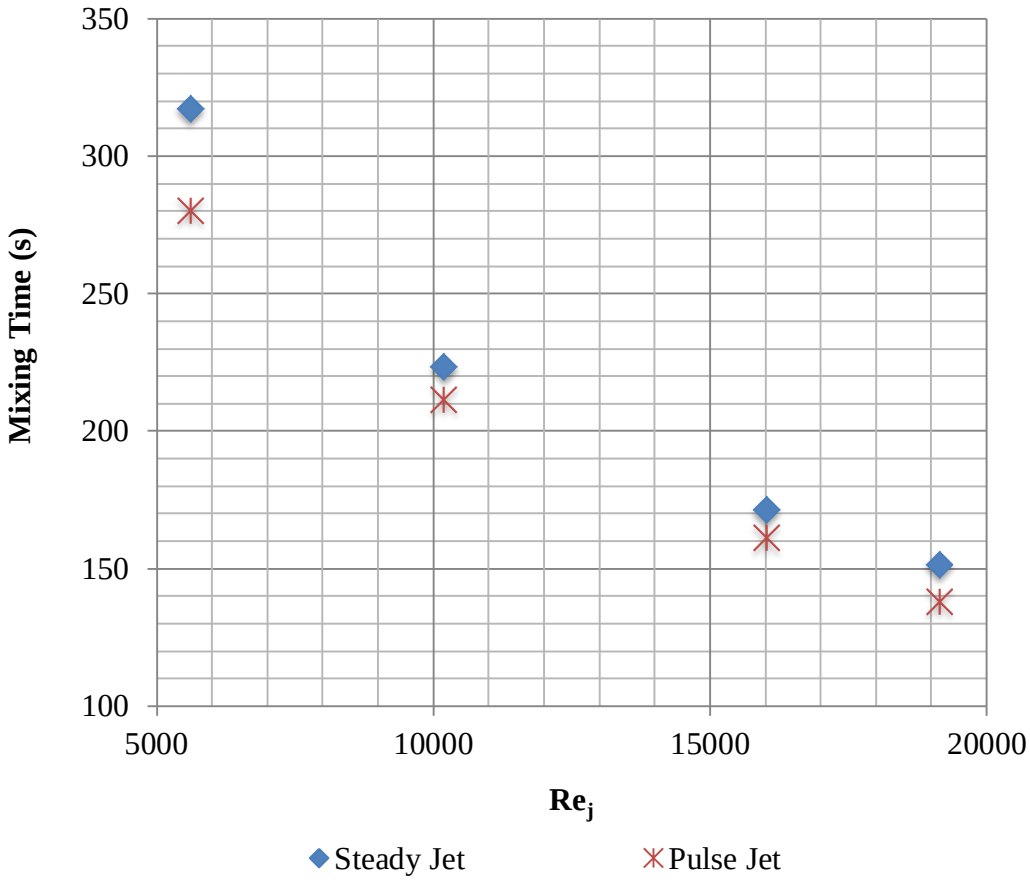

Figure 4.12. Mixing time as a function of jet Reynolds number for a single jet.

The difference between the values of mixing time for the steady jet and the pulse jet is minimal, though the pulse jet mixing time is slightly lower. A Re_j = 19160 resulted in the mixing time of the steady jet being about 9% higher than that of the pulse jet. The mixing time was about 12% higher for the steady jet compared to the pulse jet at Re_j = 5625. The earlier CFD mixing time studies reported that the mixing time was not lower for the pulse jet compared to the steady jet, but a much lower homogeneity criteria was used for mixing time which could account for the for the discrepancy.

Figure 4.13 shows mixing time as a function of jet Reynolds number for steady and pulse dual jets. Similarly to the single jet, the mixing time for the steady and pulse jet does not vary much. When a combined Re_j of about 20000 was used, the mixing time of the steady dual jets was about 9% higher than the pulse jets. When a combined Re_j of about 7000 was used, the steady dual jets had about a 3% higher mixing time than the pulse jet.

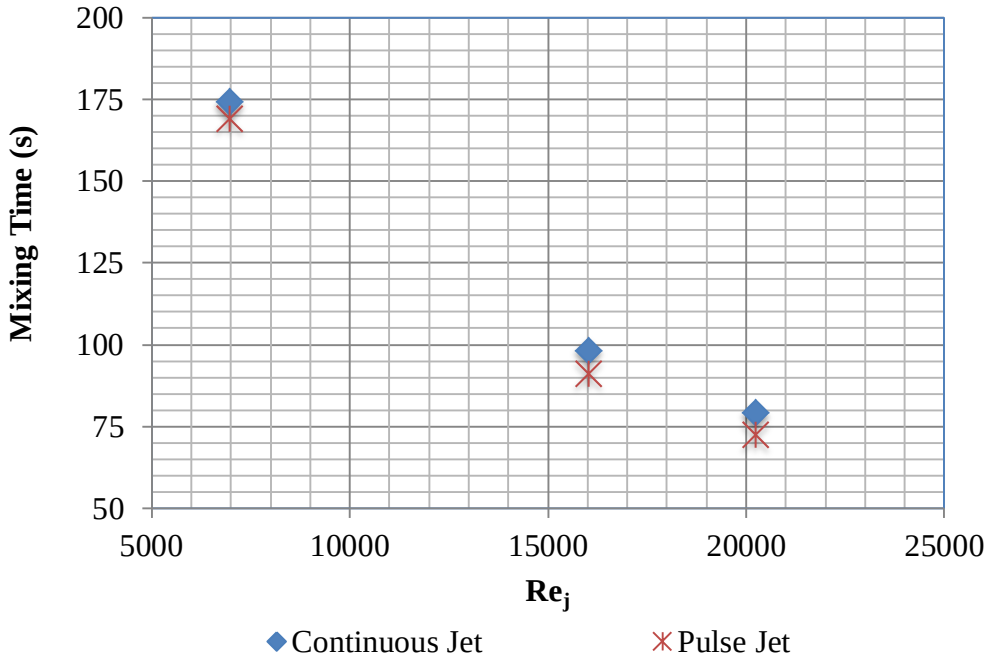

Figure 4.13. Mixing time as a function of jet Reynolds number for dual jet configurations.

Figure 4.14 compares the mixing time for steady single jet and dual jets. The mixing time is significantly reduced with the addition of another jet. The mixing time was reduced by about 47% with the addition of another jet when a Re_j of 16030 was used. The experimental mixing time results coincides with results of the previous CFD studies, as it was found that by doubling the number of jets, the mixing time was decreased by half. The addition of jets not only adds more momentum in the tank and the additional jet helps eliminates the low mixing

zones. Elimination of the low mixing zones is one of the most important factors for enhancing mixing performance in jet mixed tanks.

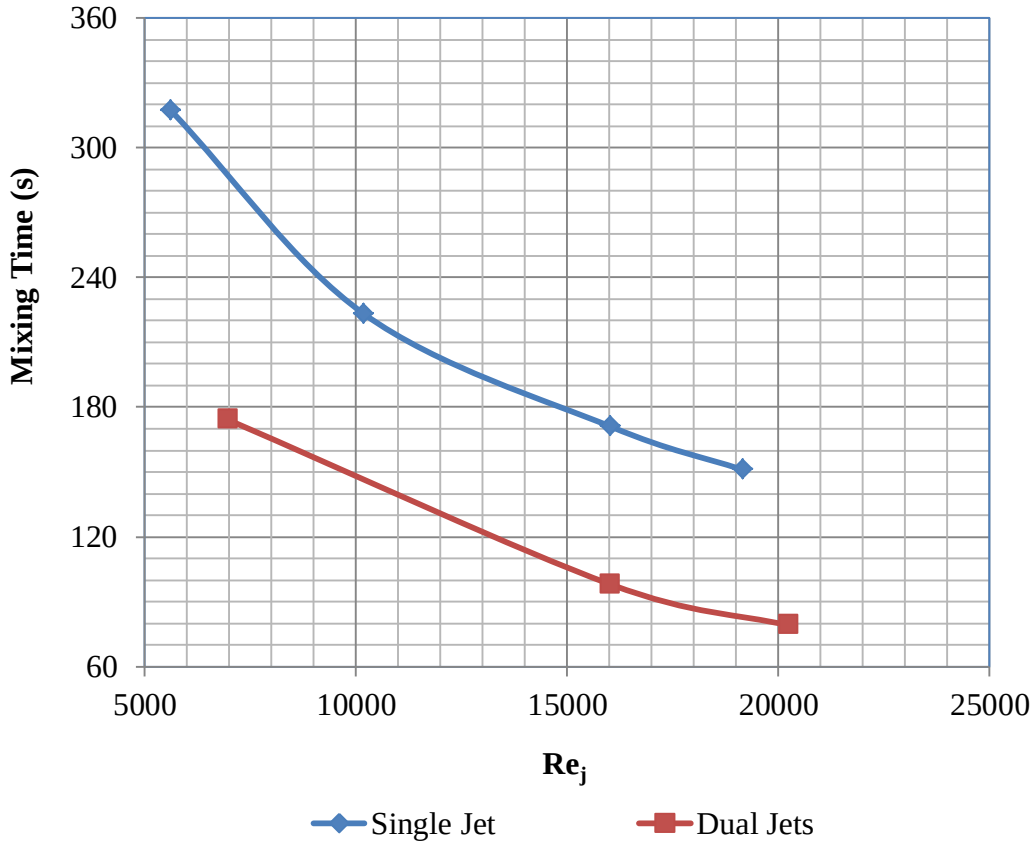

Figure 4.14. Mixing time comparison of single and dual steady jets.

The results from the experimental mixing time studies demonstrated the exponential nature of mixing time. The mixing time decreases exponentially with increased Re_j. The addition of jets increases the momentum introduced into the tank, which lowers the mixing time. The mixing tie can be reduced by almost half by doubling the number of jet mixers.

4.2 Flow pattern studies

4.2.1 Dye mixing studies. The flow patterns created by the jet are pivotal to the mixing performance in the tank. Several parameters affect the flow patterns that are created including the geometry of the tank and the interaction of the jet with boundaries. Flow patterns were found

using experimental dye studies and compared to profiles found from CFD results. Figure 4.15 displays a schematic of the flow patterns created by single and dual jets. The results shown in Figure 4.15 come from qualitative observations from the dye mixing studies. When the jet is discharged, part of it recirculates off the bottom wall and creates a semi-rollover effect. Some of the jet turns into a wall jet and where it travels up the tank to the surface and then a portion of it rolls over and recirculates through the tank. The most prominent low mixing zones are at the top of the tank and the middle of the tank because the jets are directed downwards and most of the energy dissipates before the jet reaches the top of the tank.

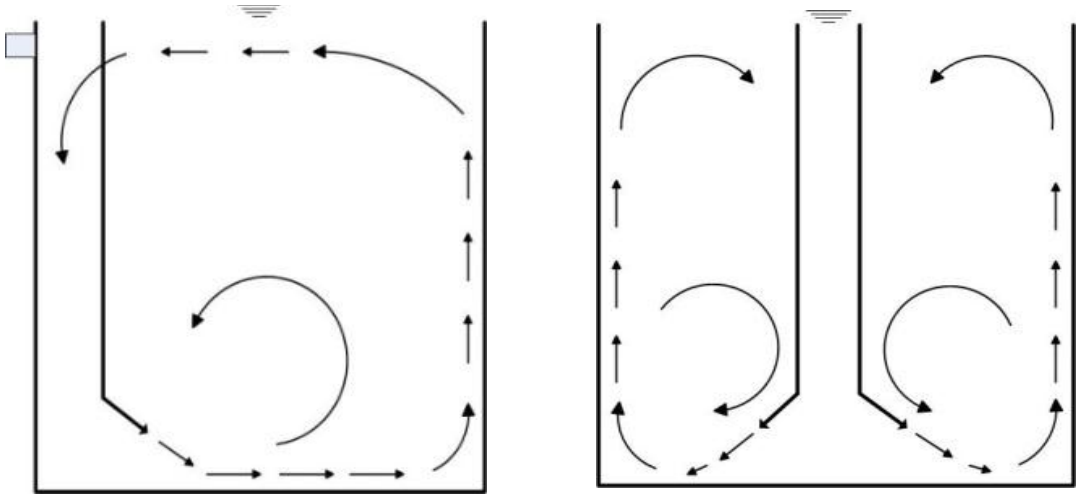

(a) (b)

Figure 4.15. Schematic of flow pattern created by (a) single jet and (b) dual jets.

Figure 4.16 displays the flow patterns of dye at captured by snapshots at different times for a single jet directed away from the tank outlet. The dye was injected slowly, so that the momentum of the dye injection did not greatly affect the results. The most prominent region of low mixing occurs in the area behind the direction of jet discharge. The fluid circulates off the bottom and side walls and travels to the top of the tank and some of the fluid exits through the overflow port, which further inhibits the region behind the jet to become well mixed. Some of

the dye motion is due to diffusion, rather than just convection. The diffusion of the dye is especially noticed as the jet velocity decreases.

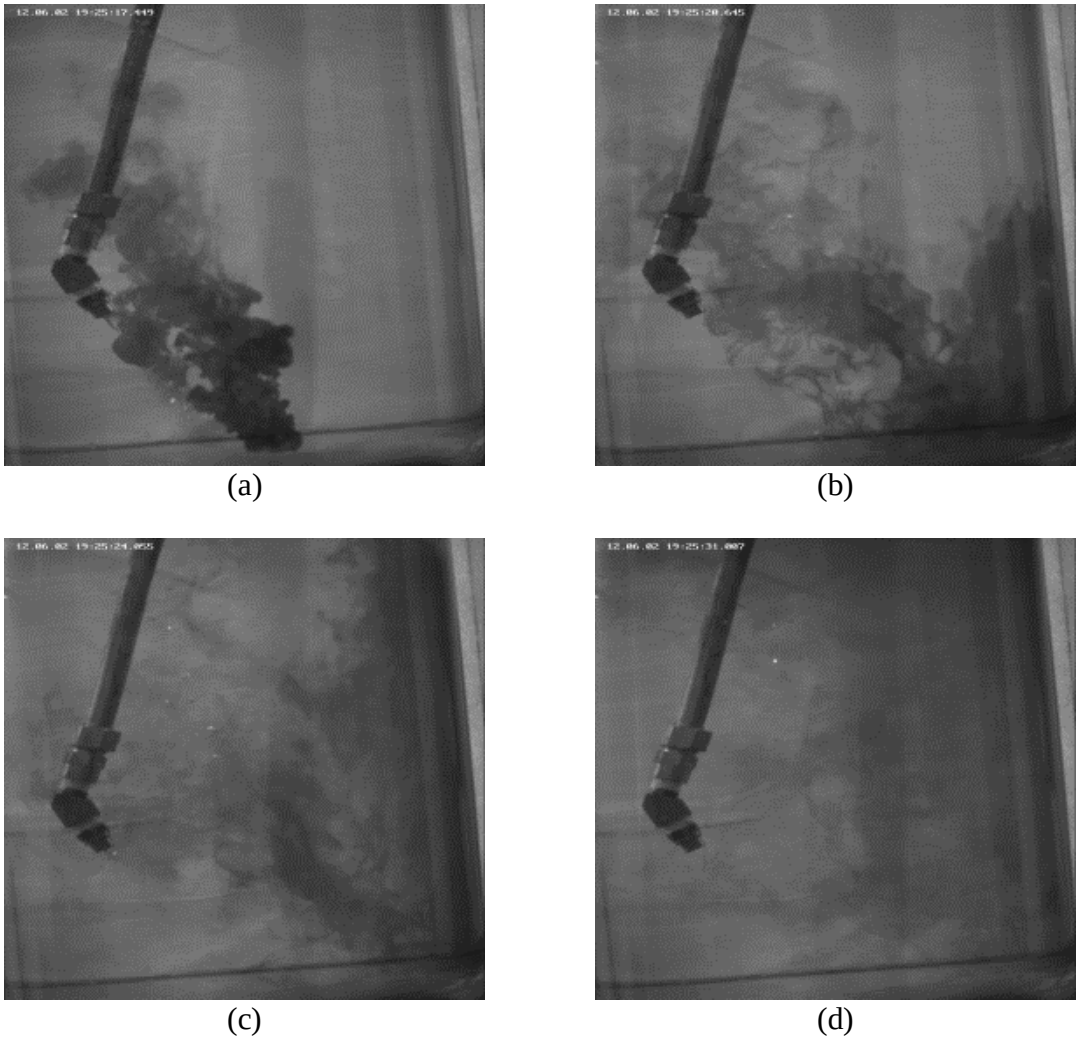

(a) (b)

(c) (d)

Figure 4.16. Snapshots of dye mixing in the jet system at (a) t = 1 s, (b) t = 4 s, (c) 7.5 s, and (d) 14.5 s.

Figure 4.17 shows the pathlines that were found from CFD simulations for a single jet mixer at a height of 0.07625 m from the bottom of the tank. The pathlines were able to give a general idea of what to expect from the dye mixing studies and ultimately the PIV studies over a short period of time.

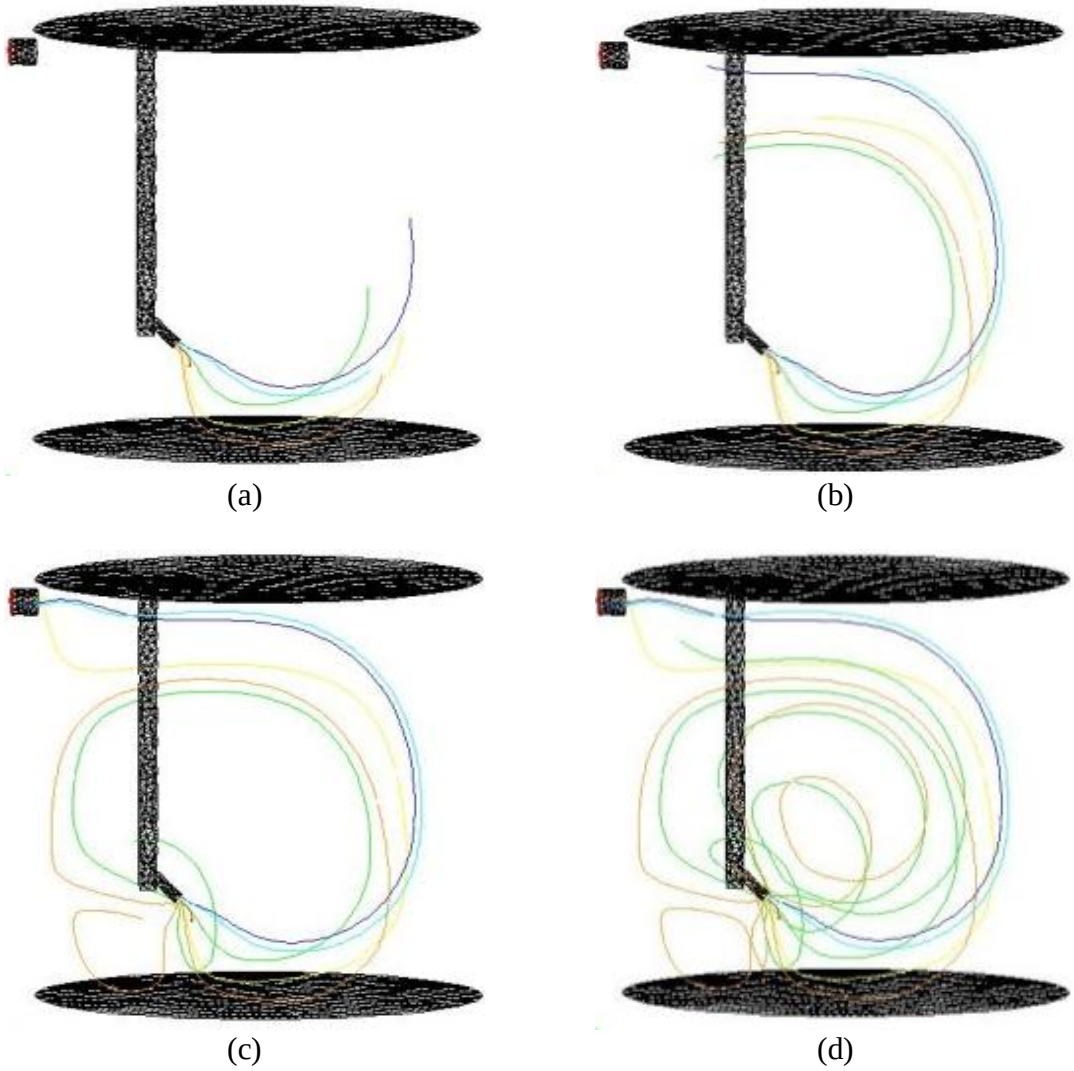

Figure 4.17. Pathlines of single jet mixer at a height of 0.07625 m from the bottom at (a) t = 1 s, (b) t = 4 s, (c) t = 7.5 s, and (d) t = 30 s.

The pathlines in Figure 4.17 shows the jet circulating as it hits the bottom and side walls and then travelling to the outlet. The middle of the tank is not initially well mixed, but after some time, the middle of the tank starts to get mixed more due to the circulatory patterns created in the tank. The mixing in the center of the tank increases as the flow deviates from being uniform to more chaotic. The model however does not do a very good job of capturing the effect of the wall jet. The wall jet effects can most likely be improved by varying the turbulence model

and/or the turbulent parameters used in simulations. The flow pattern results found for the dye mixing studies coincides with that found from the PIV studies.

Figure 4.18 displays the pathlines for the dual jet mixers. As the jet is injected, it hits the bottom wall and travels towards the surface. Most of the flow travels towards the outlet, but some of it recirculates near the middle of the tank. The low mixing zone is located between the two jets at the bottom of the tank. The same low mixing zone was noticed during dye studies as well, though the snapshots are not shown.

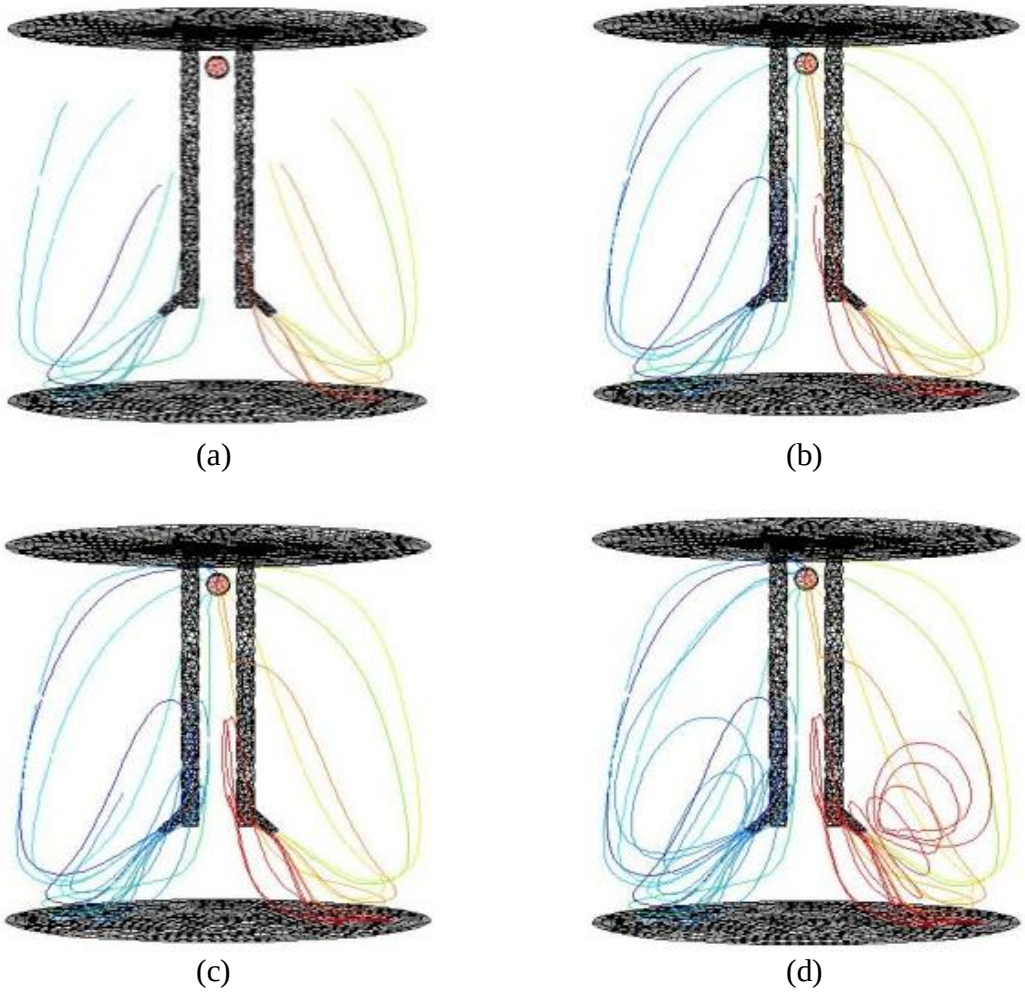

Figure 4.18. Pathlines of dual jet mixers at a height of 0.07625 m from the bottom (a) t = 1 s, (b) t = 4 s, (c) t = 7.5 s, and (d) t = 30 s.

Similar to the single jet, after a period of time, increased mixing occurs in the middle of the tank as the flow becomes more chaotic and the interaction between the circulatory patterns increases. The pathlines results concur with the results of the CFD simulations.

The pathline results for the single and dual jets are very useful for mixing purposes. The pathlines are able to show the effectiveness of mixing. Mixing is more prominent when the pathlines are chaotic. When uniform patterns are created by the pathlines, dead zones in the tank exist. The results show that the dual jets promote mixing more than the single jet as the patterns in the tank are more chaotic in nature.

4.2.2 Particle image velocimetry. Particle image velocimetry is an important tool in measuring fluid velocities in various systems. PIV was used in the current study as an additional tool to monitor the mixing actions in the jet mixing system. The PIV system was used to measure fluid velocities of a vertical impinging jet and an angled impinging jet. The vertical impinging jet was directed at the bottom of the tank at a 0° angle and the angled impinging jet was directed at the bottom of the tank at a 45° from the horizontal.

Vertical impinging jet. Vertical impinging jets can be very useful in mixing applications. Results of the PIV study will lead to a better understanding of mixing processes for not only liquid blending processes, but solid-liquid mixing as well. Results from PIV also give quantitative values for the velocity field, which can be used to calculate other flow parameters such as dynamic pressure and shear stress. The results are actual measured values and can be used to compare with numerical studies as well.

Figure 4.19 show the velocity profile in terms of velocity magnitude for an impinging jet mixer. Although the wall of the mixing tank is not displayed in the images, it can be seen that the highest velocities are found near the wall due to the wall jet that forms after the jet impinges

on the bottom surface. The images also display the circulation zone in the middle of the image. The velocity profile found from the top camera signifies that mixing is greatly diminished. The fluid velocity decreases to almost 0 m/s as distance from the wall increases. The drop in velocity is because of the circulatory pattern that is created in the tank.

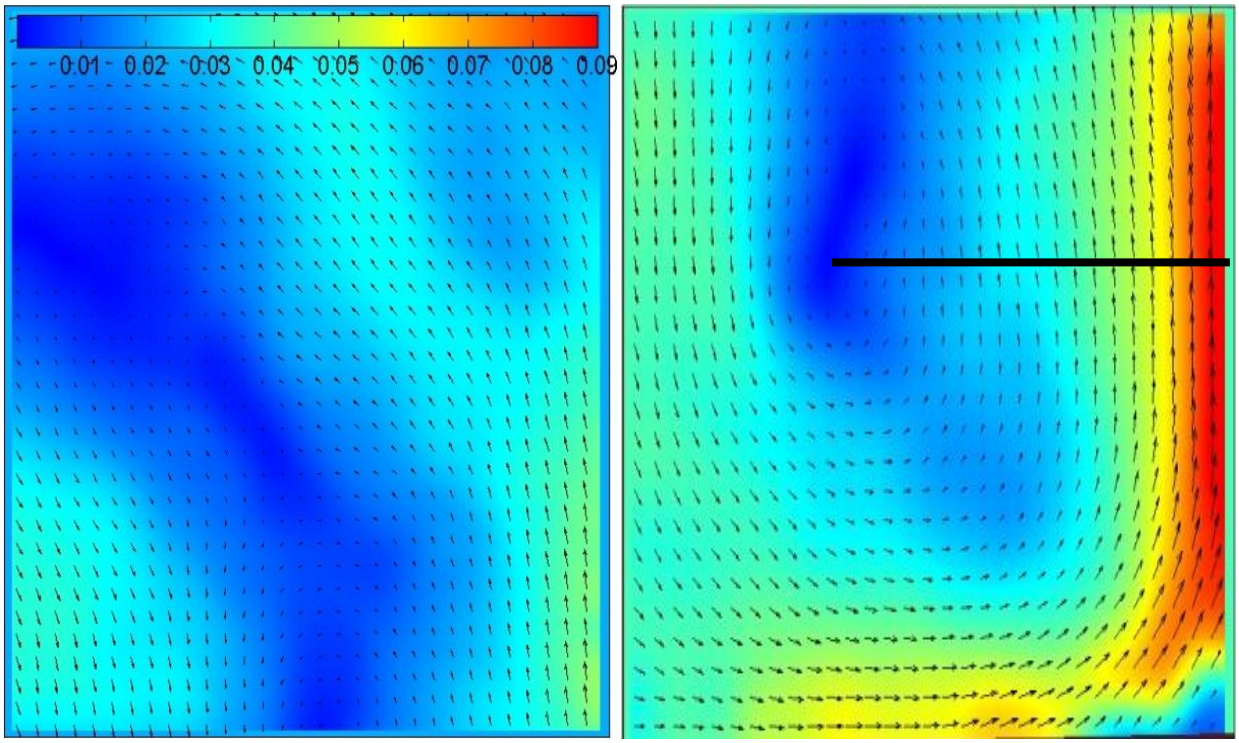

(a) (b)

Figure 4.19. Velocity profile for vertical impinging jet mixer for (a) top camera and (b) bottom camera.

Figure 4.20 exhibits a scatterplot of the velocity magnitude for the bottom camera of the vertical impinging jet. The scatterplot gives some insight into the variation and recurrence of velocity components for the bottom camera. The maximum velocity in the x-direction is about 0.062 m/s. The maximum direction in the y-direction is about 0.09 m/s, which occurs in the negative y-direction.

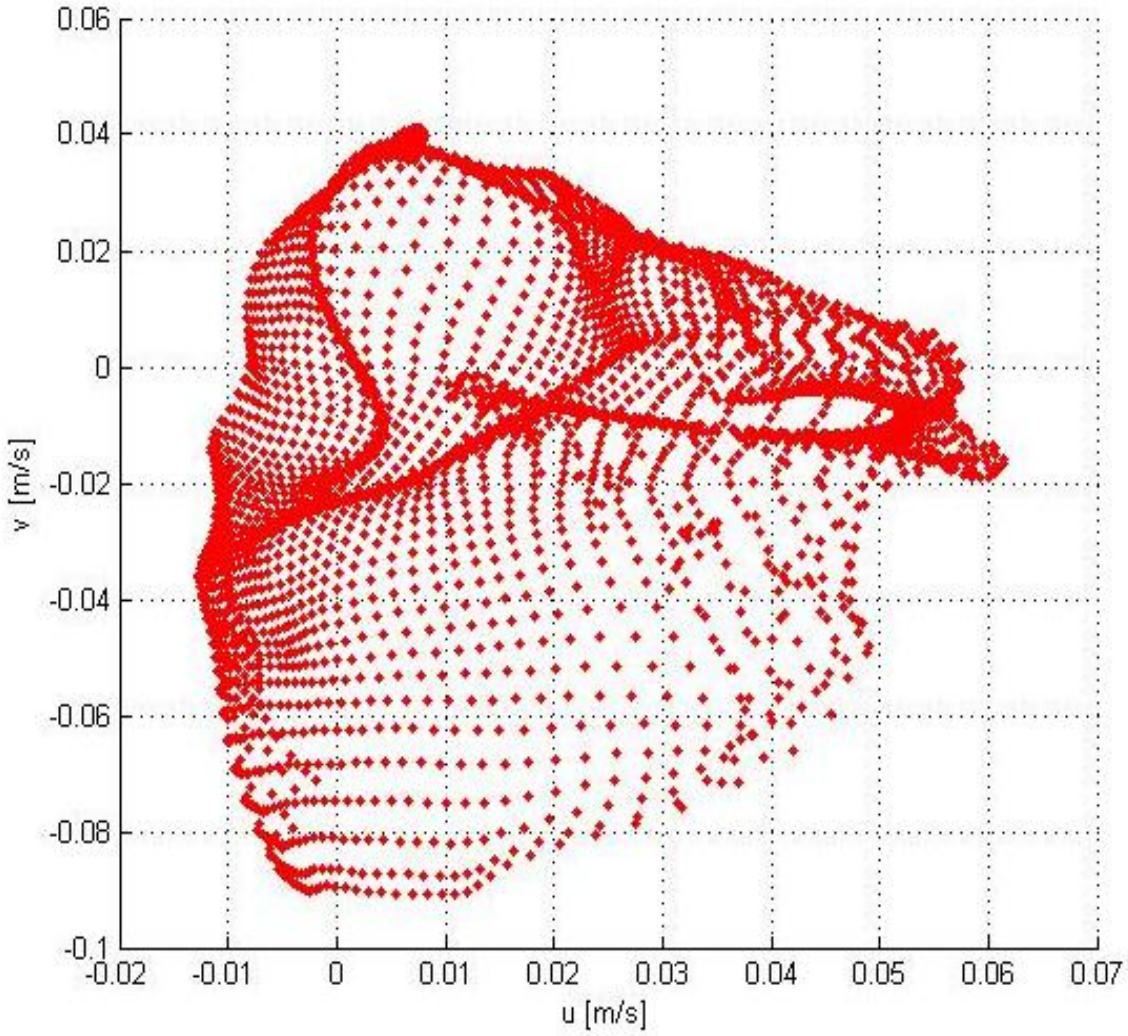

Figure 4.20. Scatterplot of the velocity magnitude for the bottom camera during the impingement of a vertical jet.

Figure 4.21 displays the scatterplot of the velocity magnitude for the top camera of the vertical impinging jet. The profile is much different than that of the bottom camera. The velocities are much lower, which is expected since the jet velocity decays with distance. The scatterplots can provide significant information as they are able to give a range of velocity values to expect in the region of interest.

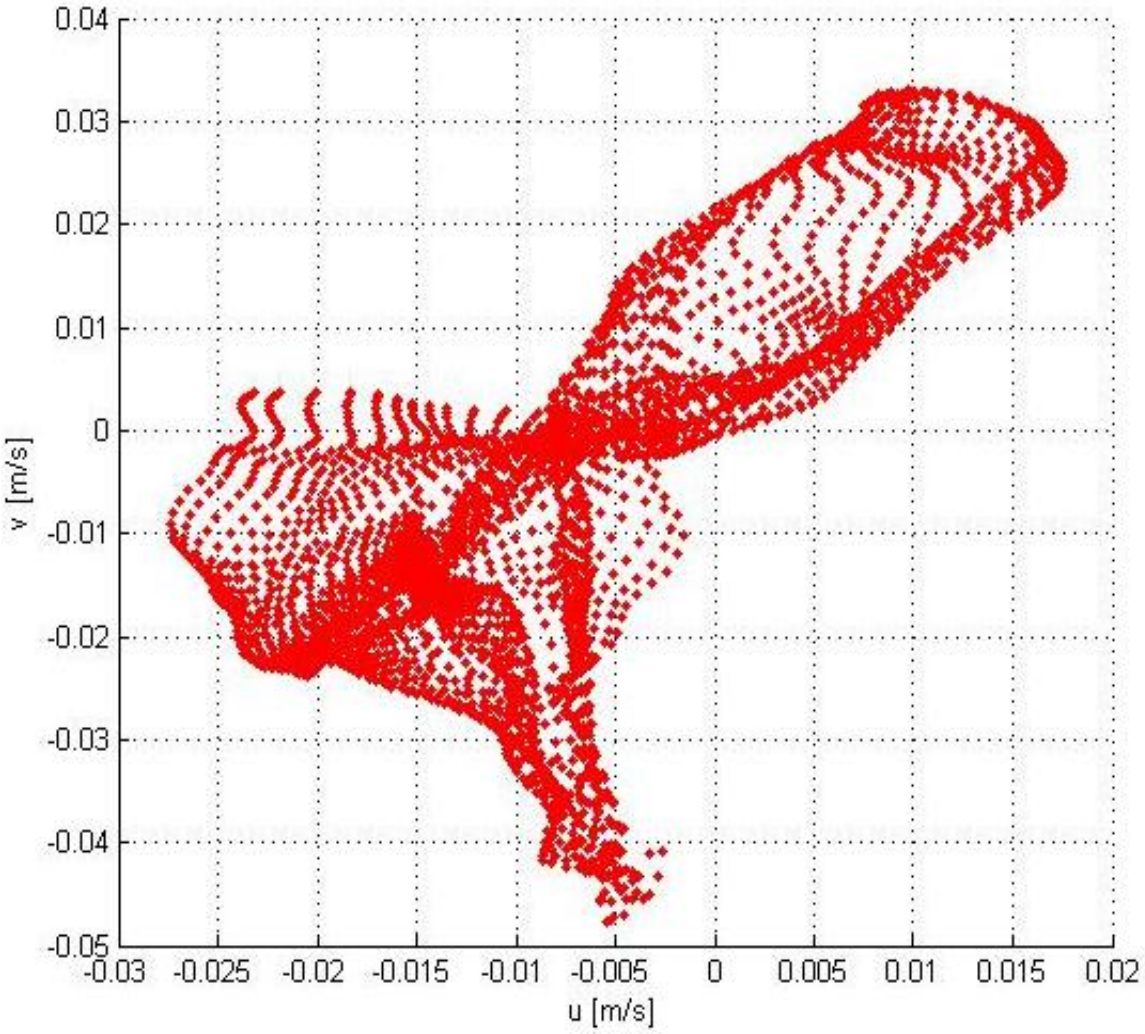

Figure 4.21. Scatterplot of the velocity magnitude for the top camera during the impingement of a vertical jet.

Figure 4.22 shows the velocity magnitude as a function of distance from the wall. The distance corresponds to the solid black line shown in Figure 4.19b. The distance 0.056 m represents the right hand side of the line, closest to the right side wall of the tank, while the distance, 0 m, represents the left end point of the line. The plot shows that the velocity magnitude decreases further away from the wall. At about 5.6 cm from the wall, the velocity is almost 0 m/s, as the point denotes the center of the circulation pattern created in the tank.

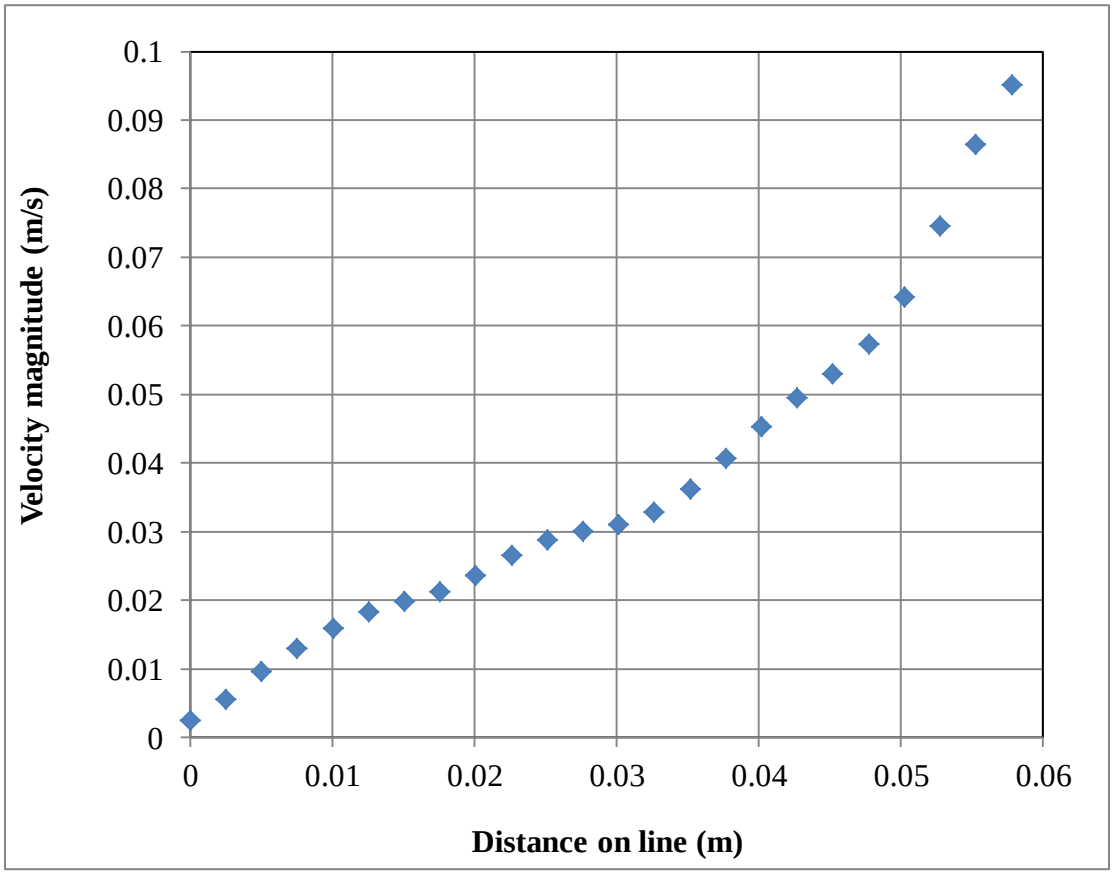

Figure 4.22. Velocity magnitude with distance from the tank's side wall during the impingement of a vertical jet.

Angled impinging jet. PIV studies were run using a 45° angled impinging jet as shown in Figure 3.31. Figure 3.31 also shows the two different cameras that were used to visualize a larger field of view during the PIV studies. Throughout the results will be presented in terms of the top and bottom camera. The liquid level aspect ratio (AR_L) in the system with the impinging jet was varied from 0.50 to 0.75. The heights were chosen so that the jet nozzle remained submerged within the liquid.

Figure 4.23 shows the velocity magnitude for the bottom camera used in the angled impinging jet studies for an AR_L of 0.50. The velocity of the jet was constant; therefore the

results of the bottom jet remained almost exactly the same for each liquid level studied. Thus, the liquid level had minimum effect on the flow profile of the bottom portion of the tank for the heights studied. The blacked-out region represents where the incoming jet traveled. The area was blacked out so that erroneous vectors were not visual. The erroneous vectors were a result of how the PIV experiments were run. The goal of the study was to look at the circulation patterns created by the jet, so the particles were not injected through the jet nozzle during the jet discharge. The bulk fluid was mixed with the particles to create a solution and the incoming jet consisted of just water.

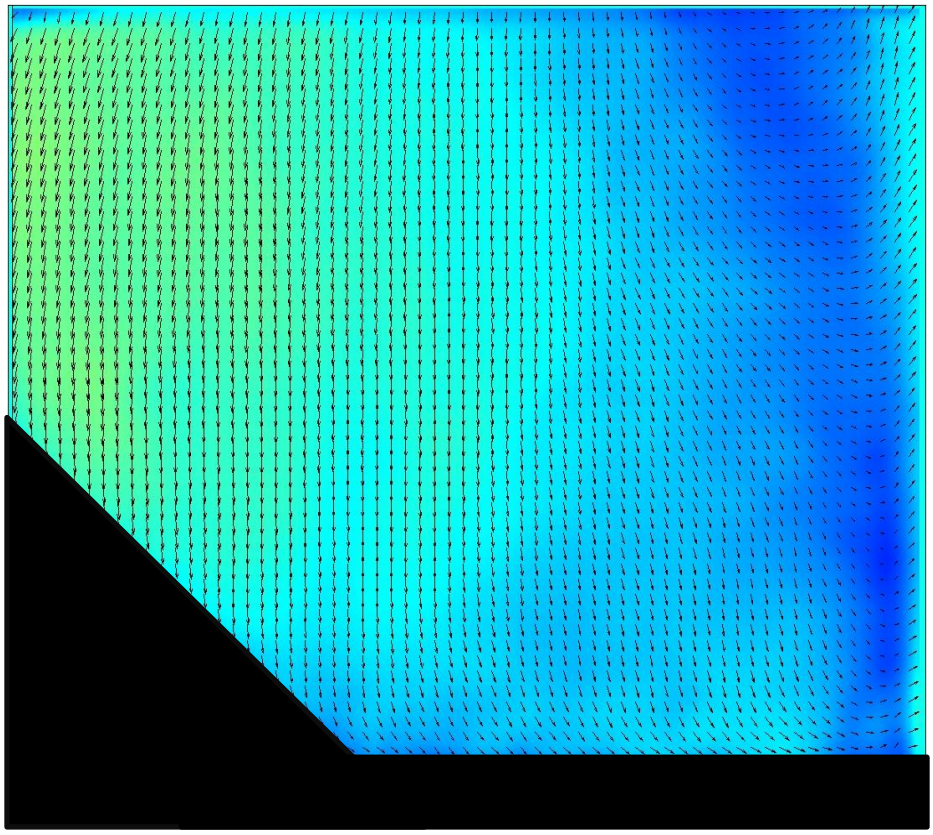

Figure 4.23. Velocity magnitude of bottom camera view using angled impinging jet.

Figure 4.24 displays the scatterplot of the velocity magnitudes that were measured in the bottom portion of the mixing tank during the angled impinging jet experiment. The highest

upward velocity was about 0.04 m/s, which occurred when the horizontal velocity, or the u velocity component, was between -0.01 and 0 m/s.

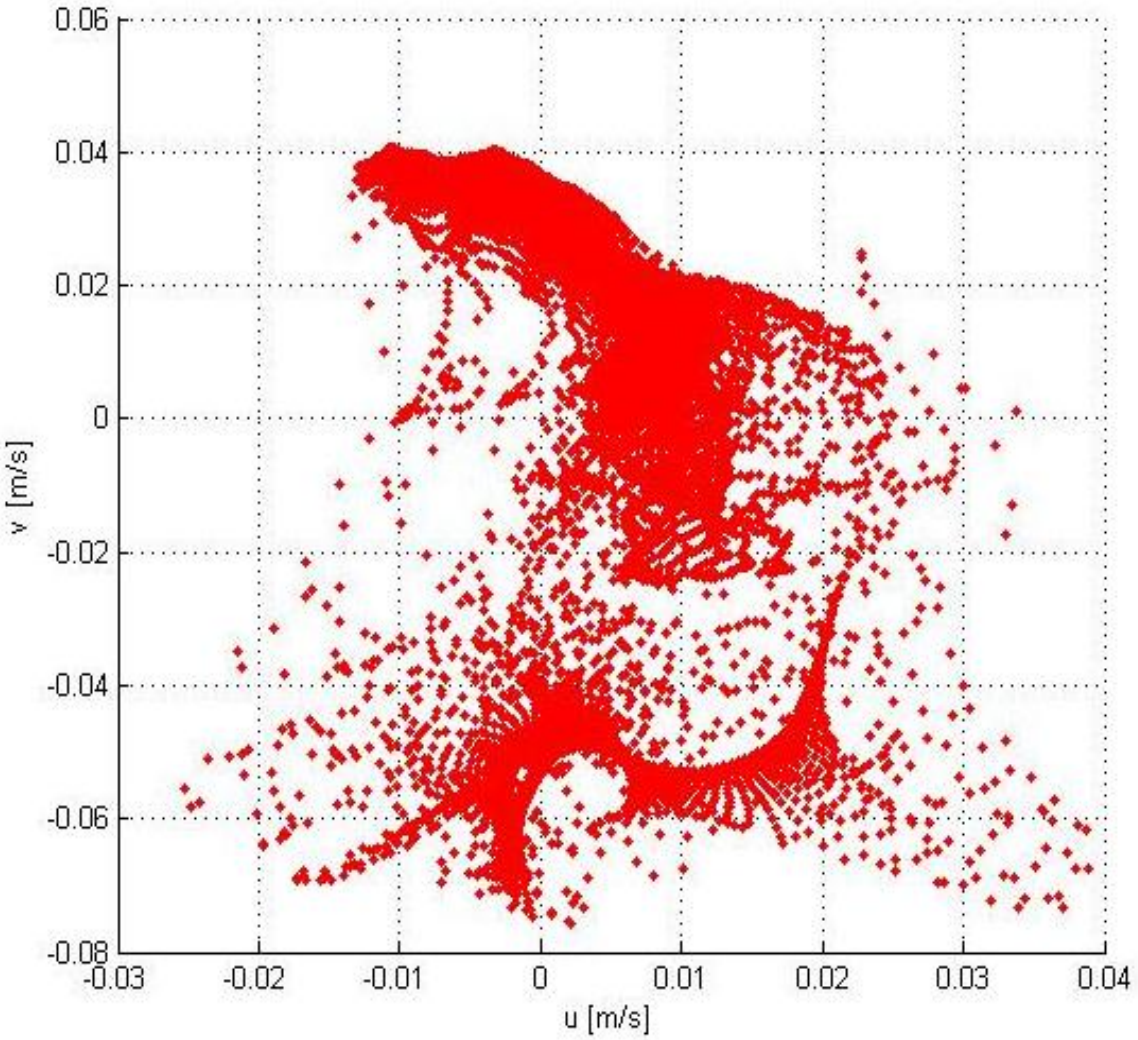

Figure 4.24. Scatterplot of the velocity magnitude for bottom camera during angled impinging jet experiment.

Figure 4.25 shows the velocity profile in terms of velocity magnitude for the top camera with an AR_L of 0.61. The wall jet is created as the angled jet impinges on the bottom surface. The momentum of the jet causes the fluid to travel up the side wall to the top surface. The fluid then starts to rollover off the top surface and travel back down towards the bottom of the tank.

As the jet travels further away from its origin, it decreases in magnitude. As the jet rolls over in the top right hand corner of the image, it decreases in magnitude along the top surface. The low mixing zones are still denoted in the image by the blue shaded areas.

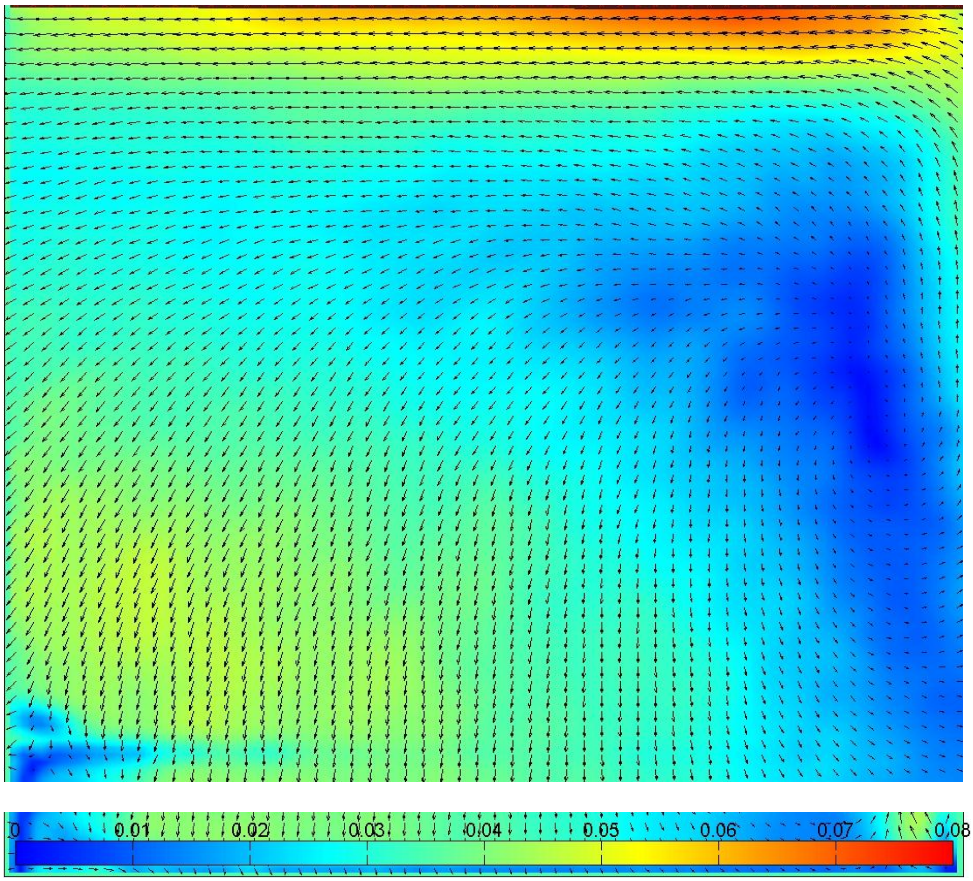

Figure 4.25. Velocity magnitude profile using top camera with an AR_L of 0.61 with an angled impinging jet.

The velocity profiles remained the same at all of the three liquid levels. The only difference was the actual values for the velocity magnitudes. Figure 4.26 shows the velocity magnitudes across the top surface boundary for a distance of 12 cm. The 0 cm point along the horizontal axis represents the top right hand side of the surface closest to the right side wall. The velocity on parallel to the liquid surface decreases, as the liquid level increases. The maximum

velocities using AR_L of 0.50, 0.61, and 0.75 are about 0.095 m/s, 0.084 m/s, and 0.066 m/s, respectively. The velocity increases and then decreases dramatically as the fluid travels further away from the right side wall. The fluid velocity increases to a maximum further away from the wall due to the circulation pattern in the corner of the tank.

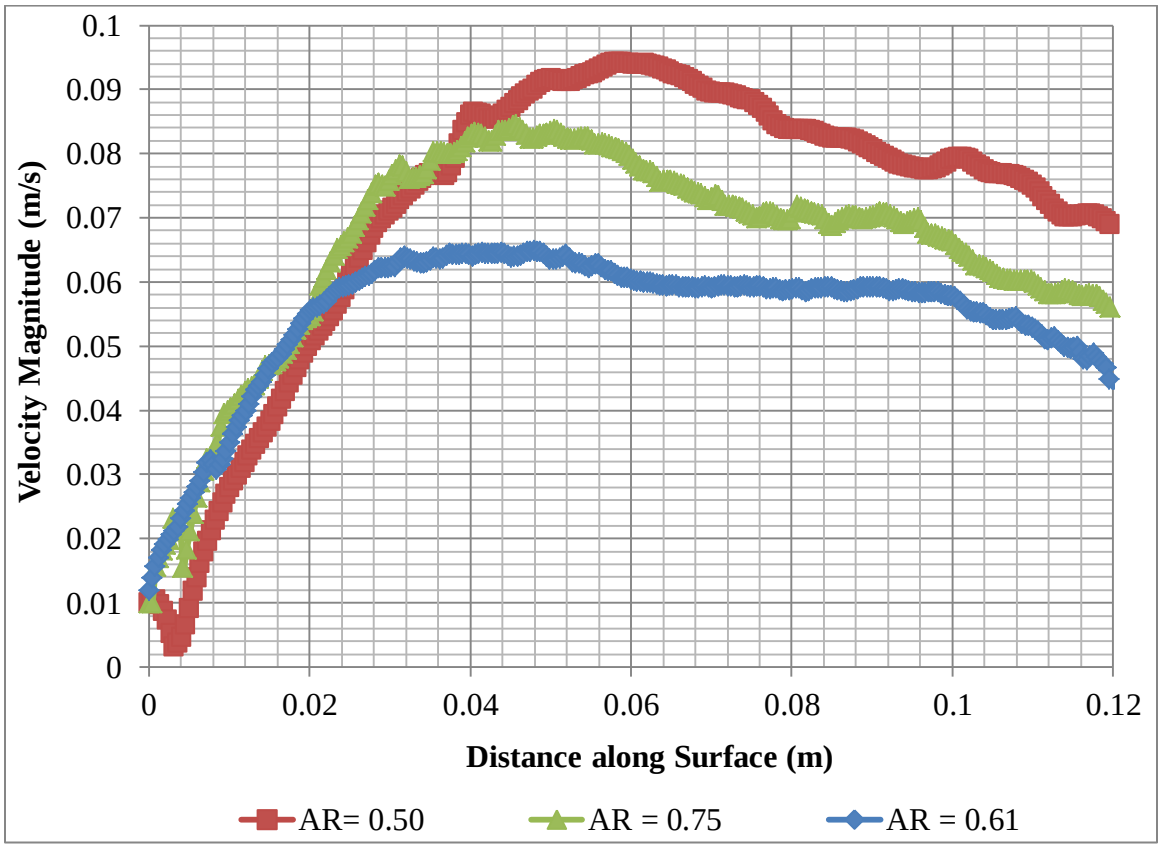

Figure 4.26. Velocity magnitudes as a function of distance along the liquid surface for different liquid levels.

Figure 4.27 displays the scatterplot for the top camera during the angled impinging jet run at an $AR_L = 0.61$. The velocity profiles were the same for the different heights, so the scatterplots for the different liquid levels were the same as well. The velocity profiles at each height were the same; however the only differences were the actual values of the velocity magnitude.

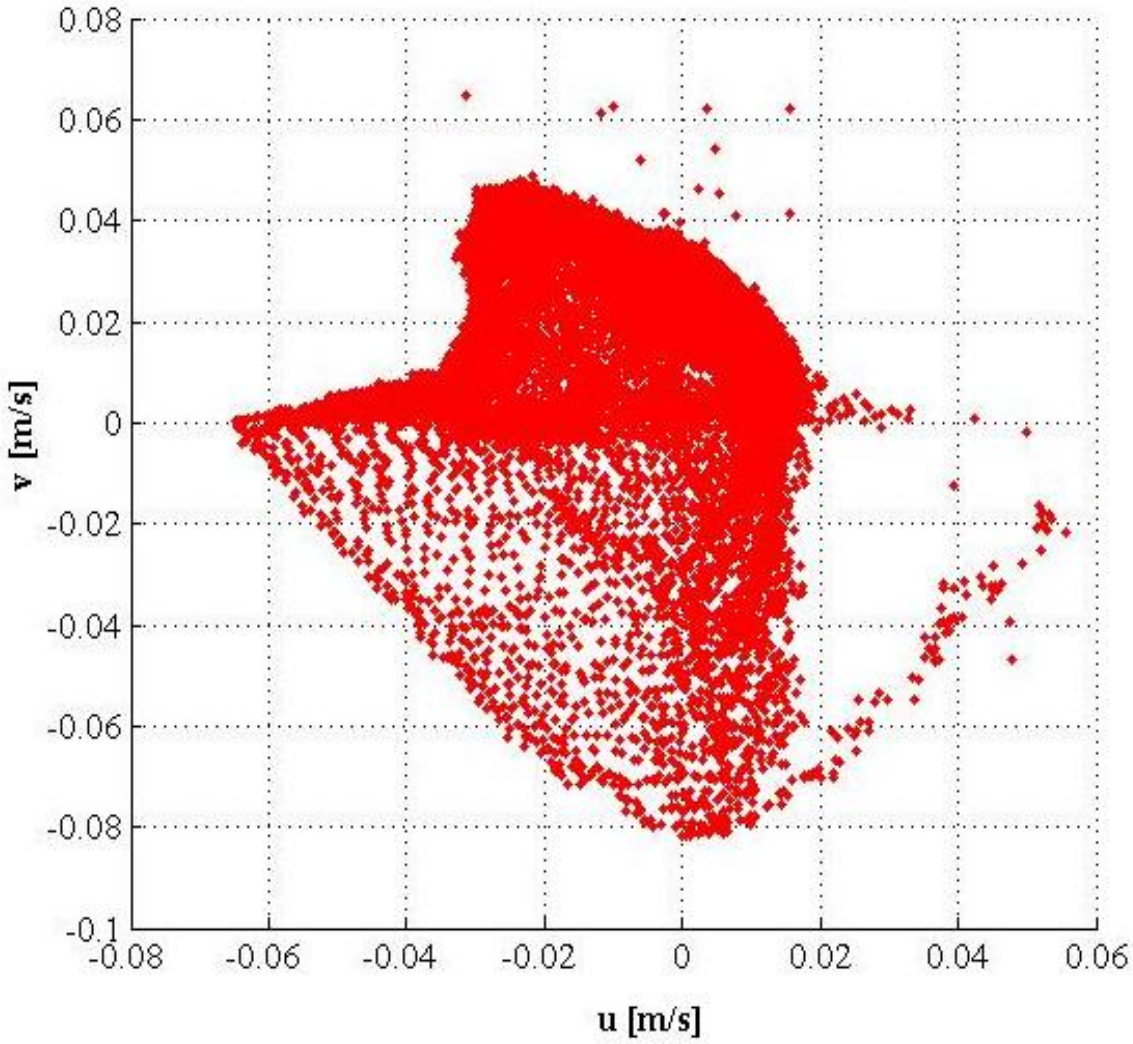

Figure 4.27. Scatterplot for velocity magnitude of the top camera during an angled impinging jet run at an $AR_L = 0.61$.

4.3 Particle Rheology

When dealing with solid mixtures, it is important to characterize its rheological behavior. In some cases, a mixture possesses a critical shear stress that must be overcome before it begins to move as a fluid. The critical shear stress of a substance should be determined especially in mixing applications so that the amount of force needed to completely fluidize the substance can be determined. Mixtures were created in the present study which have a critical yield stress and

can be used as simulants to actual yield stress substances found in industry. Experiments were run to determine the yield stress of kaolin clay/sand mixtures.

4.3.1 Comparisons of tube rheometer and Brookfield viscometer results. An initial test was run testing the shear stress versus shear rate for a mixture of 50 % (wt.) mixture of water and clay. Tests were run using a Brookfield LV Viscometer and the Poiseuille-flow tube rheometer. The results of the Brookfield viscometer are shown in Figure 4.28. The results were modeled using the power law model where the consistency coefficient, K, was found to be 127.95 Pa·s and the power law index, n, was found to be 0.1563. Since n < 1, the model represents a fluid with shear thinning behavior.

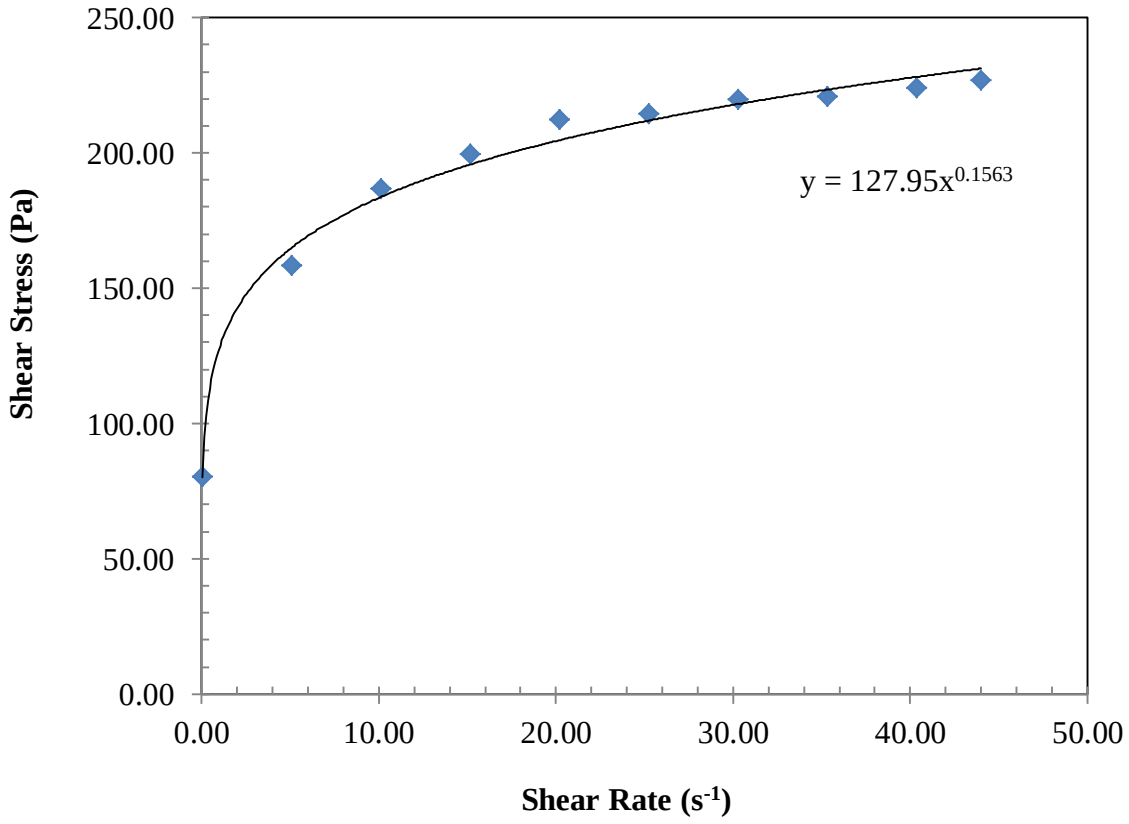

Figure 4.28. Shear stress vs. shear rate for 50/50 mixture of kaolin/water using Brookfield viscometer.

Figure 4.29 combines the results of shear stress versus shear rate for the Brookfield viscometer and the capillary tube rheometer. Figure 4.29 also shows the results for the power law model using parameters found during the Brookfield experiments and the trendline found for the combined results. The Brookfield viscometer is used for low shear rate regions and the capillary tube rheometer is used for high shear rate. The results were modeled using the power law model. The consistency coefficient, K, was found to be 139.8 and the power law index, n, was found to be 0.1028. The calculated parameters differ from the results of the Brookfield viscometer. The results are not expected to be the same since measurements were made using two different instruments.

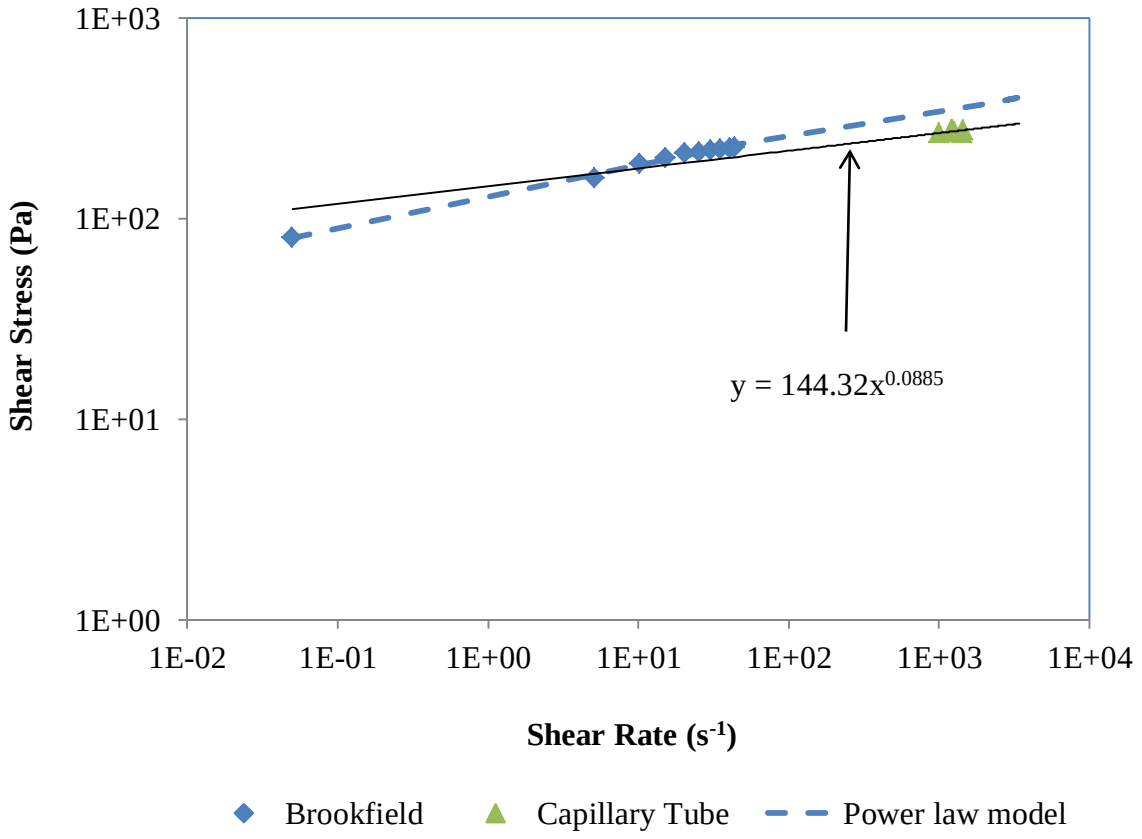

Figure 4.29. Compiled data for shear stress vs. shear rate for 50/50 mixture using Brookfield viscometer and tube rheometer.

The yield stress for the mixture found from the Brookfield viscometer was about 78 Pa. The Brookfield yield stress value is slightly lower than value found for the mixture using the tube rheometer, which was found to be 92.35 Pa. The yield stress for the tube rheometer was 18.4% higher than that found using the Brookfield viscometer. The two values were not expected to be the since the methods were different. The measured values are reasonably close enough to allow for the method of yield stress determination in this study to be used further with some confidence.

Figure 4.30 displays the viscosity as a function of shear rate for the 50/50 mixture of kaolin and water. The viscosity of the mixture decreases as the shear rate increases. The decrease in viscosity with increased shear rate demonstrates the shear thinning behavior of the mixture.

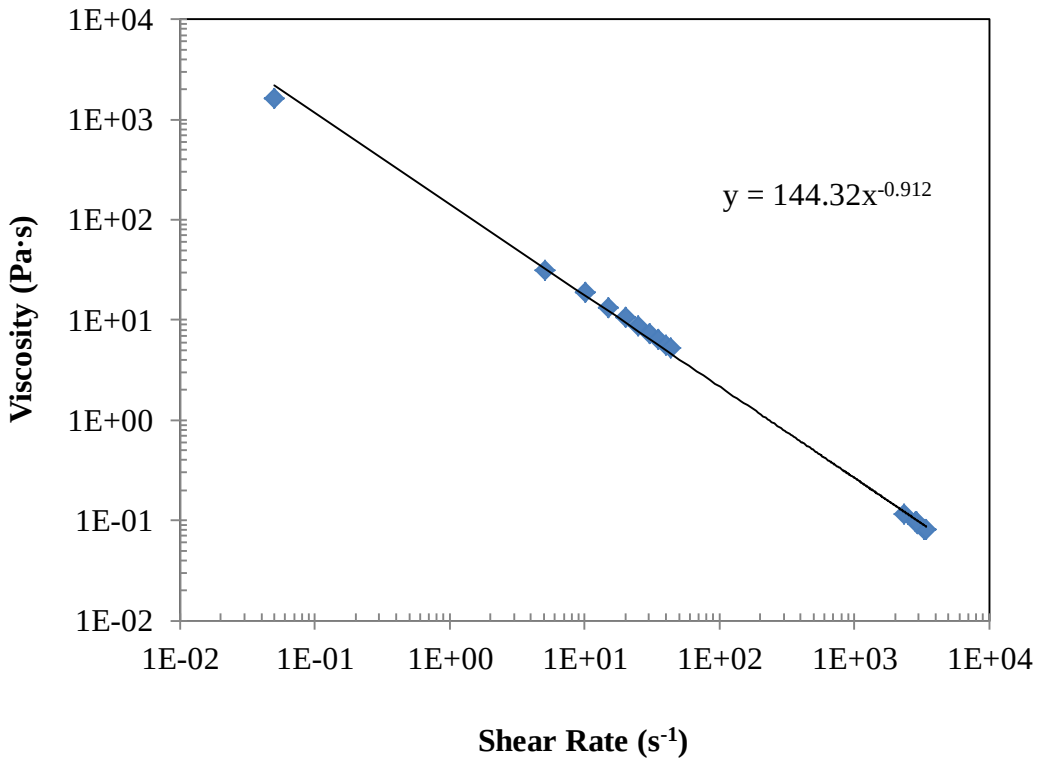

Figure 4.30. Viscosity versus shear rate for 50/50 mixture of kaolin/water.

4.3.2 Kaolin/water mixtures. The same material, preparation procedure, testing procedure and data collection techniques must be consistent for accurate comparisons of the results. Tests were for completed for mixtures containing 50 to 60% total solids by weight of kaolin clay. Figure 4.31 shows the yield stress results as a function of total wt. % when the solid portion of the mixture was comprised completely of the kaolin. There was an increase in yield stress with an increasing amount of solids concentration. The data was fitted with an exponential equation with an R^2 value of 0.9945. The equation is shown in equation (4.1).

$$\tau_y = 9e^{-05}\exp[27.639 \cdot \Phi_k] \quad (4.1)$$

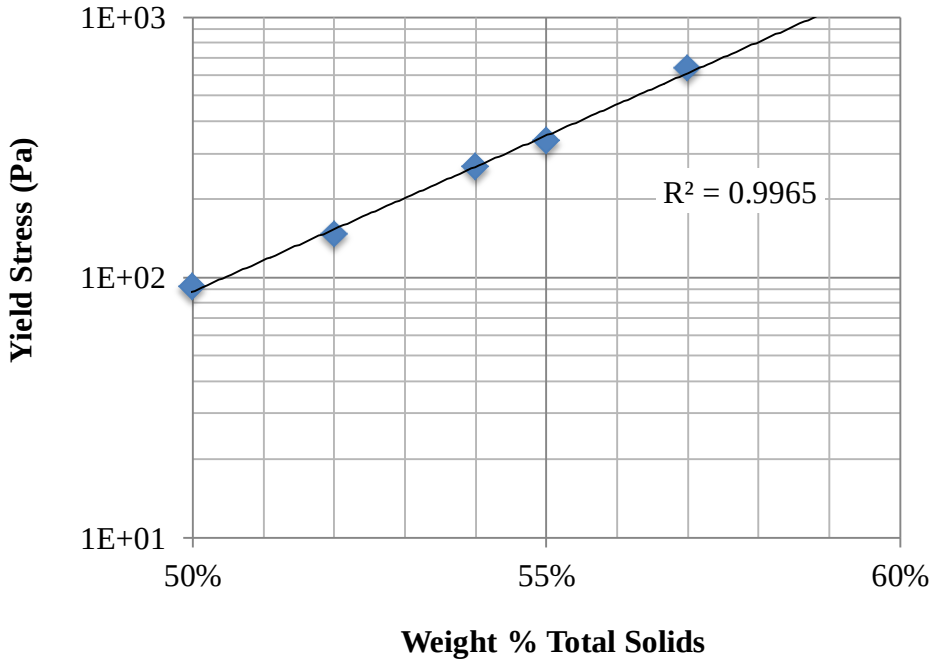

Figure 4.31. Yield stress for different wt. % total solids of kaolin.

The data point for the 60 % solids was not included because of limitations due to the rheometer. The yield stress was higher than the maximum shear that can be measured using the rheometer, 783 Pa. The yield strength of kaolin clay varies depending on the source, so comparisons must be made carefully.

Figure 4.32 compares results from the present study and those of previous authors. Past authors, including Burns et al. (2010), Gauglitz et al. (1999), and Rassat et al. (2003) have studied the shear strength of kaolin/water mixtures for different concentrations of kaolin. The yield stress data and that of the shear strength data from the previous studies can be deemed analogous as they defined the shear strength as the static yield stress (Poloski, A. P. et al., 2004). The static yield stress can be viewed as the property of a material that differentiates it from being a solid and liquid (Xu, N. and O'Hern, C. S., 2006).

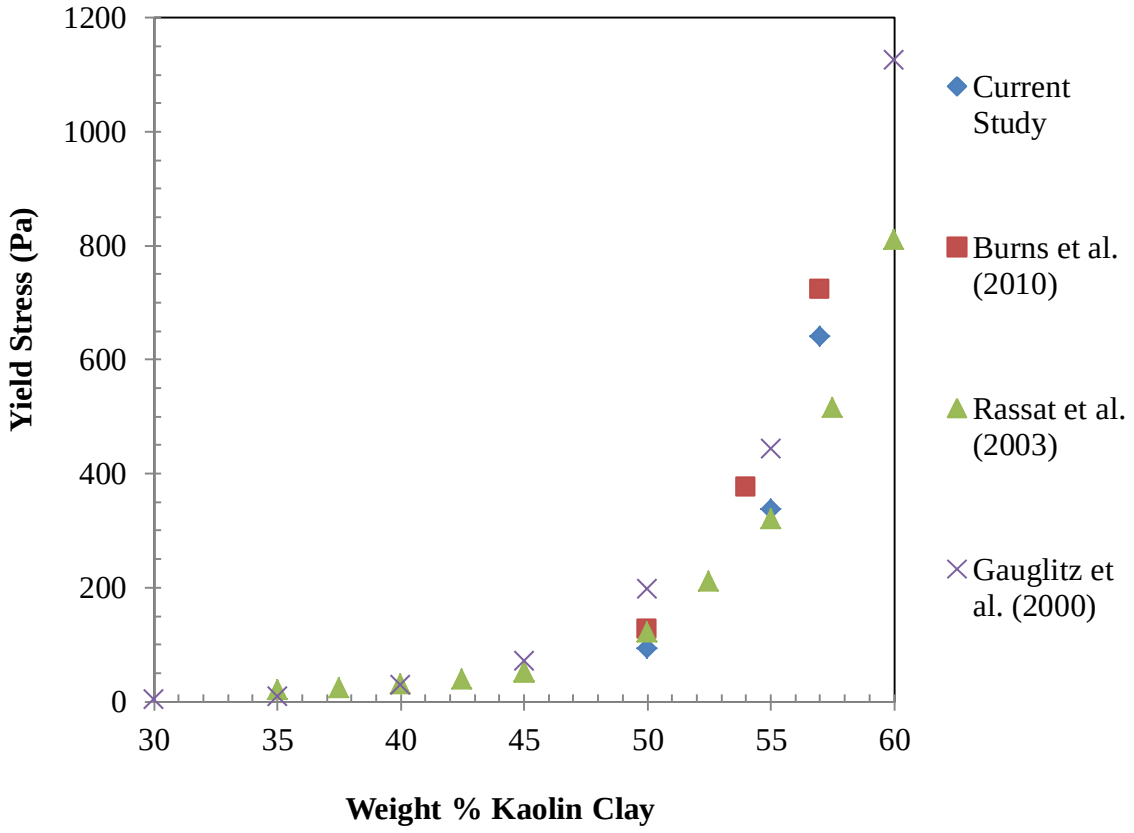

Figure 4.32. Comparison of yield stress results from current study and that of previous studies.

Table 4.3 compares the results of the different studies based on the tests that were run in the current study. All of the studies used EPK kaolin clay. Comparing the sets of data shows that the yield stress results vary greatly. However, results of the current study fall in between

those of previous studies. Variation in results may be due to pre-testing treatment of the samples, such as aging time and how the sample was mixed. The yield stress is affected by pH, which may vary depending on the source of water. The current study tap water was used, but other studies used deionized water.

Table 4.3

Yield stress data for wt. % kaolin used in the current study compared to previous studies at the same wt. %.

	Yield Stress (Pa)			
Wt. % Kaolin	Current Study	Burns et. al. (2010)	Gauglitz et al. (2000)	Rassat et al. (2003)
50	92.35	127	198	122
52	147.10	n/a	n/a	n/a
54	295.83	375	n/a	n/a
55	336.89	n/a	444	321
57	639.88	723	n/a	n/a

4.3.3 Kaolin/sand/water mixtures. Tests were run for different concentrations of total solids, Φ_T. The fraction of kaolin, Φ_K, and fraction of s and, Φ_S, was varied as well. Figure 4.33 shows the yield stress for the kaolin/sand mixtures as a function of varying fractions of kaolin clay. The yield stress is increased as the kaolin concentration is increased, which was expected since kaolin is a cohesive material. When the sand concentration increased, the yield stress decreased. There is a limit of larger particles, or sand, which can be added before the mixture loses its yield strength completely at each concentration of total solids. Such a limit can be

deemed the flowability limit. The yield stress was expected to decrease as larger particles were added to the mixture. The interparticle force decreased as the larger particles were added because the spacing between the particles increased.

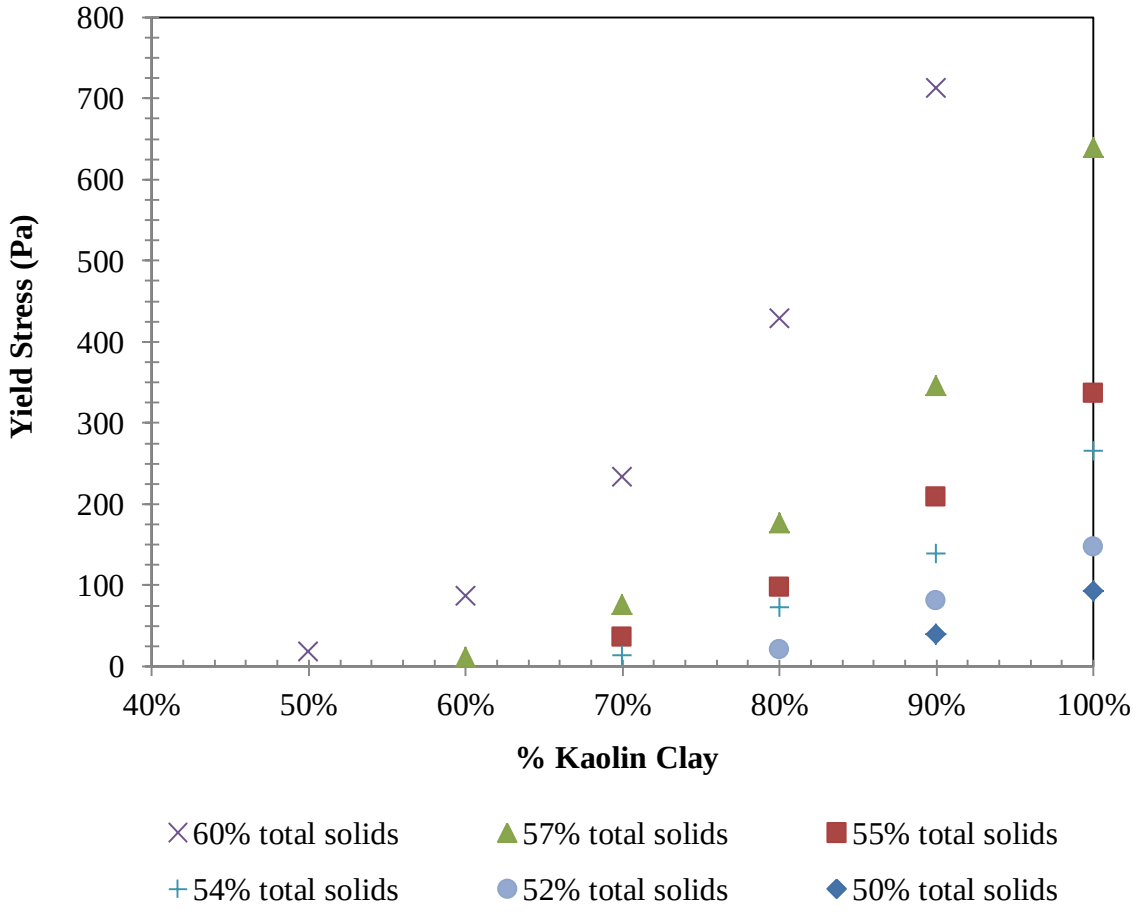

Figure 4.33. Yield stress of mixtures of 50 – 60 wt. % total solids in which the solids were composed of different ratios of kaolin/sand.

Figure 4.34 shows the results for the kaolin/sand mixture of 90/10%. An exponential equation, equation (4.2), was found that fitted the data well as the R^2 value was 0.9928. Equation (4.2) displays the yield stress as a function of Φ_T for a 90/10% mixture of kaolin/sand.

$$\tau_{y,90/10\%} = 2e^{-05}\exp[28.932 \cdot \Phi_T] \quad (4.2)$$

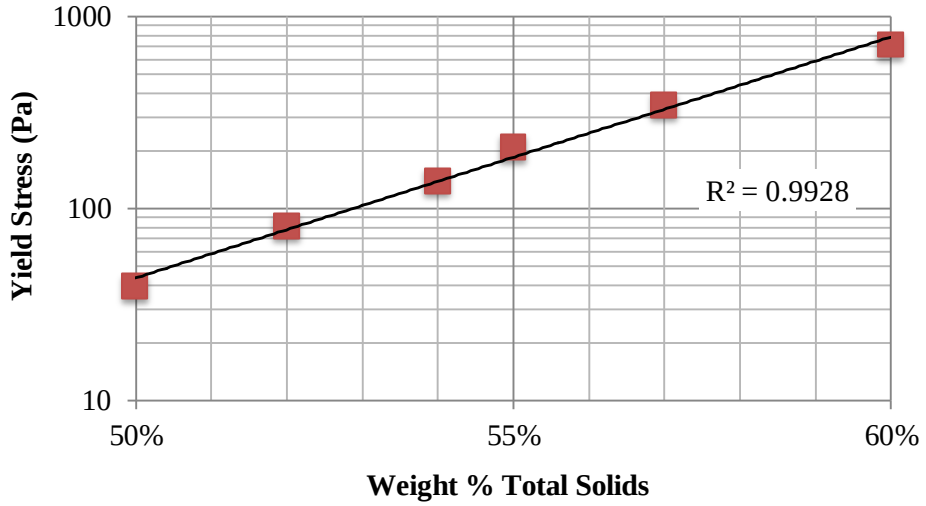

Figure 4.34. Yield stress for 90/10 ratio of kaolin/sand in kaolin/sand/water mixtures.

Figure 4.35 and Figure 4.36 shows the results for kaolin/sand mixtures of 80/20% and 70/30%, respectively. The equations found that fit the data are shown in equations (4.3) and (4.4). As the amount of small particles decreased, the slope of the exponential equation became less steep. The trendline fits the data fairly well.

$$\tau_{y,80/20\%} = 2e^{-07}\exp[37.75 \cdot \Phi_T] \tag{4.3}$$

$$\tau_{y,70/30\%} = 5e^{-10}\exp[44.836 \cdot \Phi_T] \tag{4.4}$$

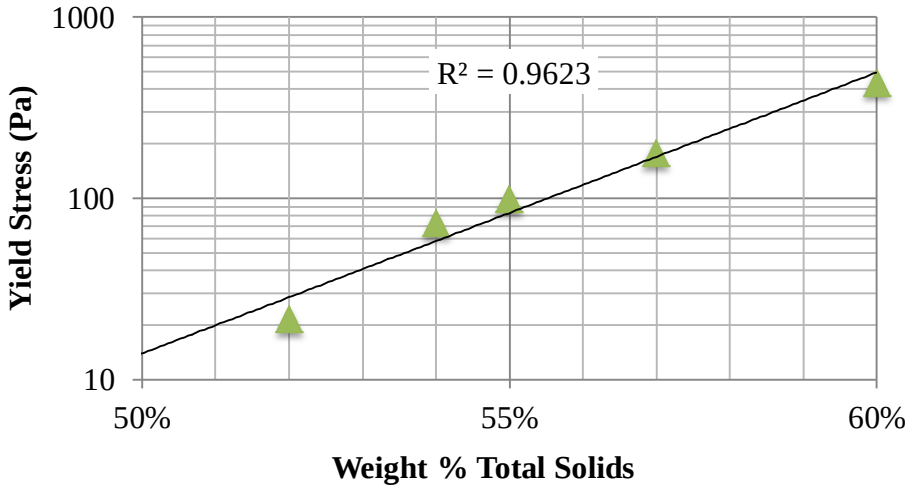

Figure 4.35. Yield stress for 80/20 ratio of kaolin/sand in kaolin/sand/water mixtures.

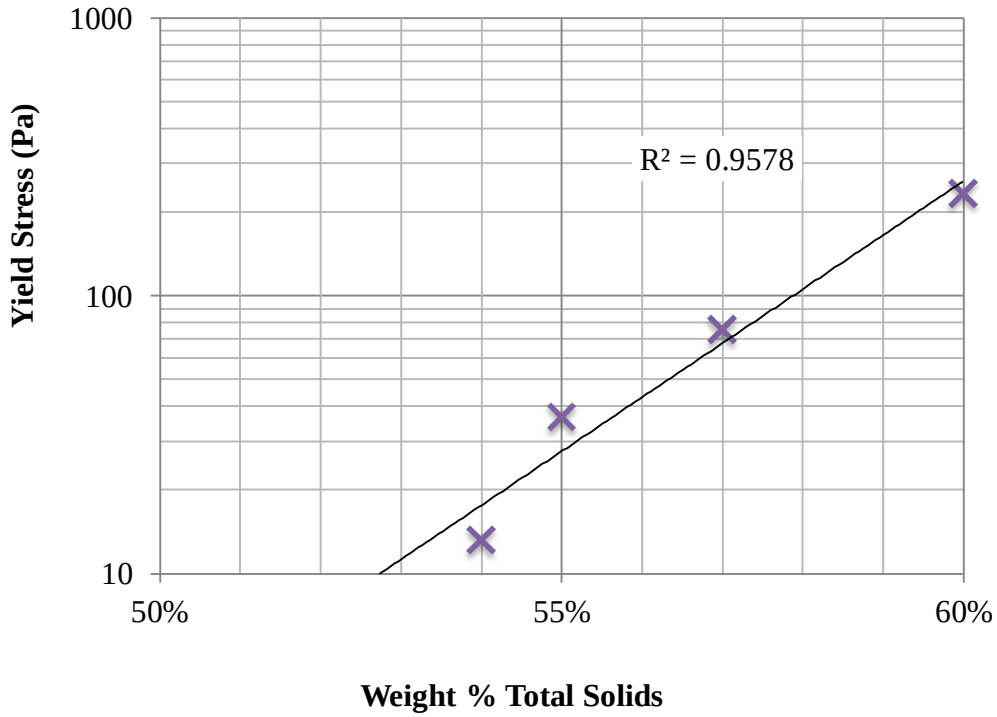

Figure 4.36. Yield stress for 70/30 ratio of kaolin/sand in kaolin/sand/water mixtures.

The yield stress experiments are useful as the results help show the effect that larger particles have on a mixture that exhibits a yield stress due to the cohesive nature of smaller particles. The results showed that an increase in the concentration of larger particles caused the yield stress to decrease. The kaolin/sand mixture was used as a simulant for yield stress substances that can be found in several industries including nuclear waste, biological, and pharmaceutics.

4.4 Experimental Cloud Height

The observed cloud height was measured using non-intrusive optical techniques. Figure 4.37 shows a snapshot of the observed cloud height. The images show the location of the distinct interface and how the high and low cloud height values were calculated. In some of the images, additional particles were noticed above the line, but they were not included in

determining the cloud height. The outlier particles were due to the range of particle sizes in each run. An actual scale was placed in the image to accurately measure the height.

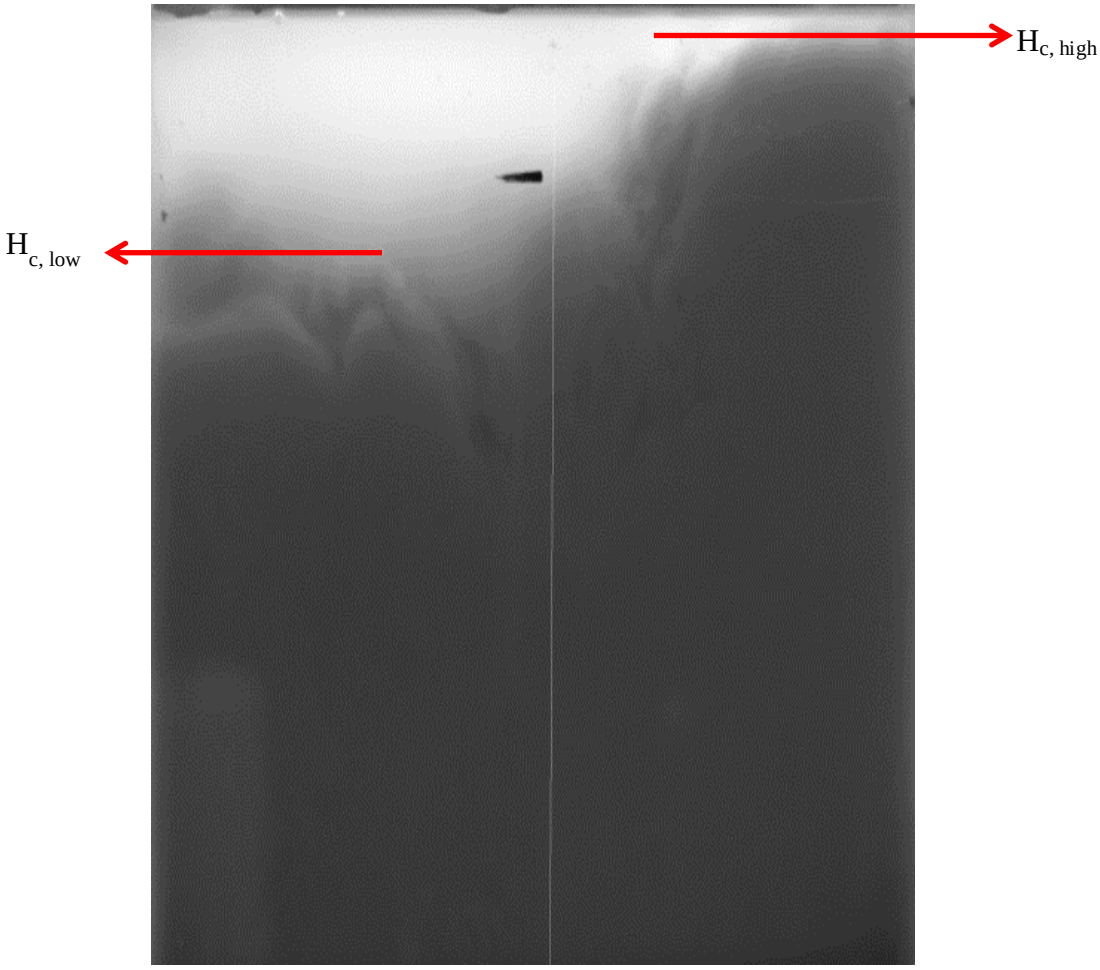

Figure 4.37. Snapshot of particle suspension, showing how the cloud height was measured.

Figure 4.38 displays the maximum cloud height measured for the three different particle samples at a nozzle height of 0.07625 m as a function of Re_j. The maximum cloud height was determined with the jet nozzle positioned at 0.07625 m and 0.038 m from the bottom of the tank. The cloud height was scaled using the liquid fill level height. Overall, there was an increase in cloud height with increase in jet velocity and ultimately Re_j. Once a jet Reynolds number of about 23800 was reached, there was a steeper increase in cloud height.

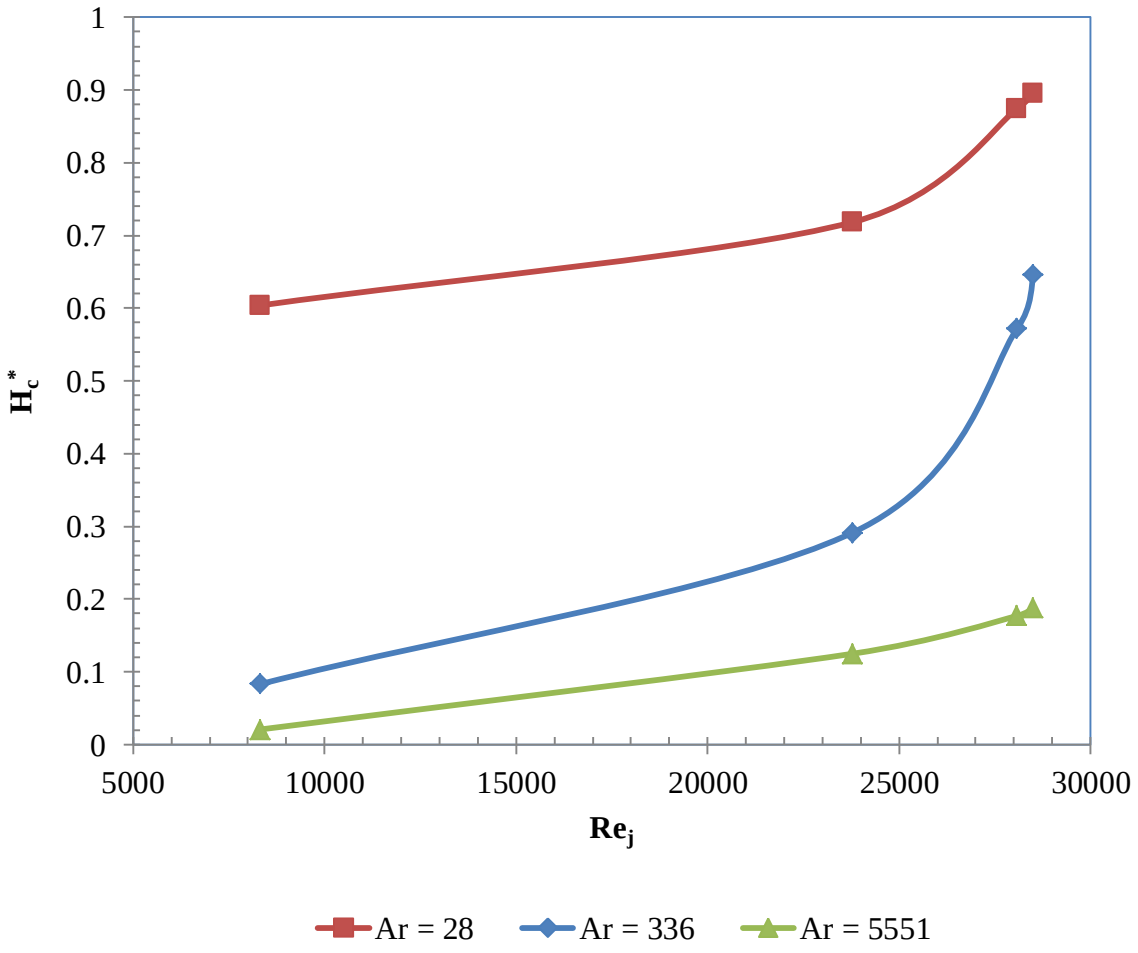

Figure 4.38. Maximum dimensionless cloud height at a nozzle height of 0.07625 m.

Since the particles with Ar = 28 had the smallest diameter and the lowest terminal velocity, they were easily suspended. About 90% homogeneity was achieved using the particles with Ar = 336 at Re_j = 28500. When the same Re_j was used, only 19% homogeneity was achieved using the Ar = 5551 particles. The results were similar to what was found by Ochieng and Lewis (2006) in which the larger particles colliding with one another and decreasing the kinetic energy of the particles. More suspension can be achieved by providing more kinetic energy from the jet. Much suspension was not expected for the large particles as the Archimedes number is so high, meaning the gravity force is more dominate than the drag force.

Figure 4.39 shows the minimum dimensionless cloud height for the three particle sets at a nozzle height of 0.07625 m. The jet force was not sufficient to create a uniform radial cloud height for the Ar = 336 and Ar = 5551 particles at a Re_j of about 8300. The minimum cloud height was negligible when the cloud height did not extend out to the complete diameter of the tank, or when particles near the tank walls were not able to be suspended. Therefore, in Figure 4.39 the particles with an Ar = 5551 were not able to be suspended.

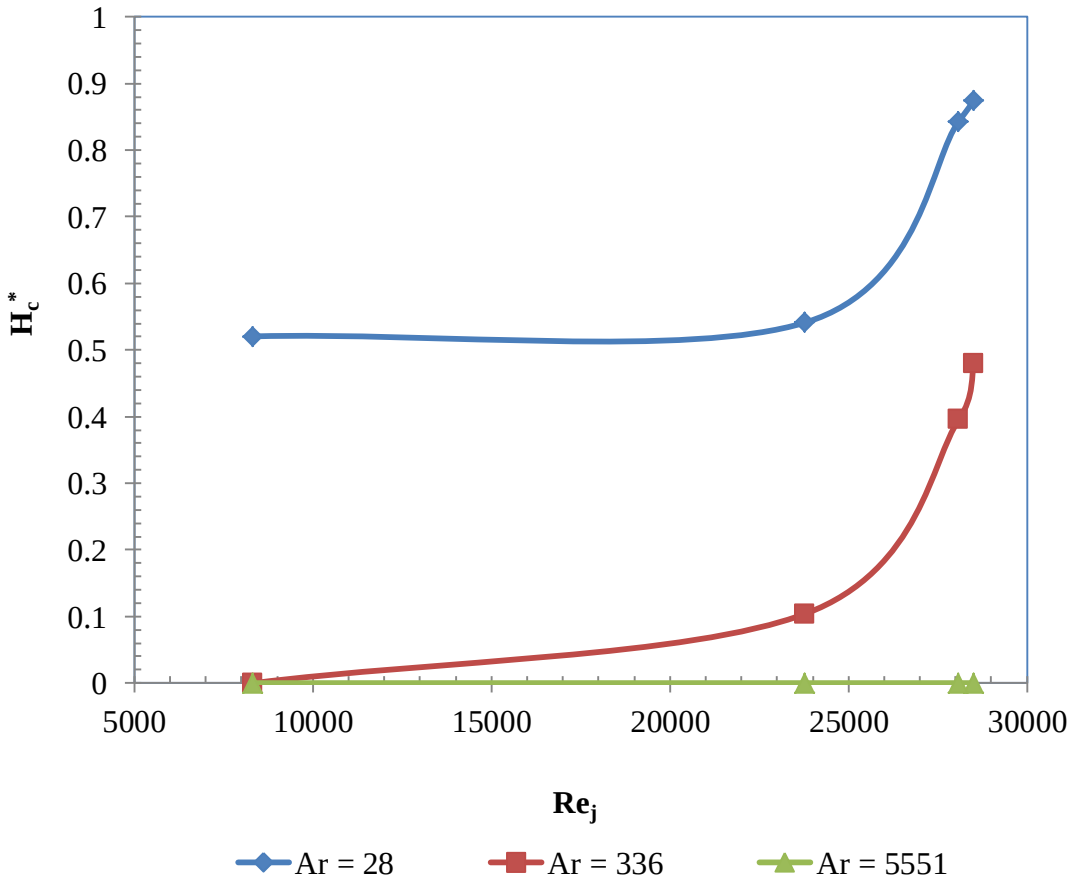

Figure 4.39. Minimum dimensionless cloud height at a jet nozzle height of 0.07625 m.

Figure 4.40 displays the dimensionless cloud height as a function of Re_j for a jet nozzle positioned 0.038 m from the bottom of the tank. The maximum and minimum values of cloud height are displayed. The minimum results for the particles with an Ar = 5551 were all equal to

0, as the cloud did not extend the full diameter of the tank. When the nozzle was closer to the solids bed, the maximum homogeneity did not exceed 25%. For the largest particles, Ar = 5551, a jet Reynolds number of 8300 was not able to suspend the particles.

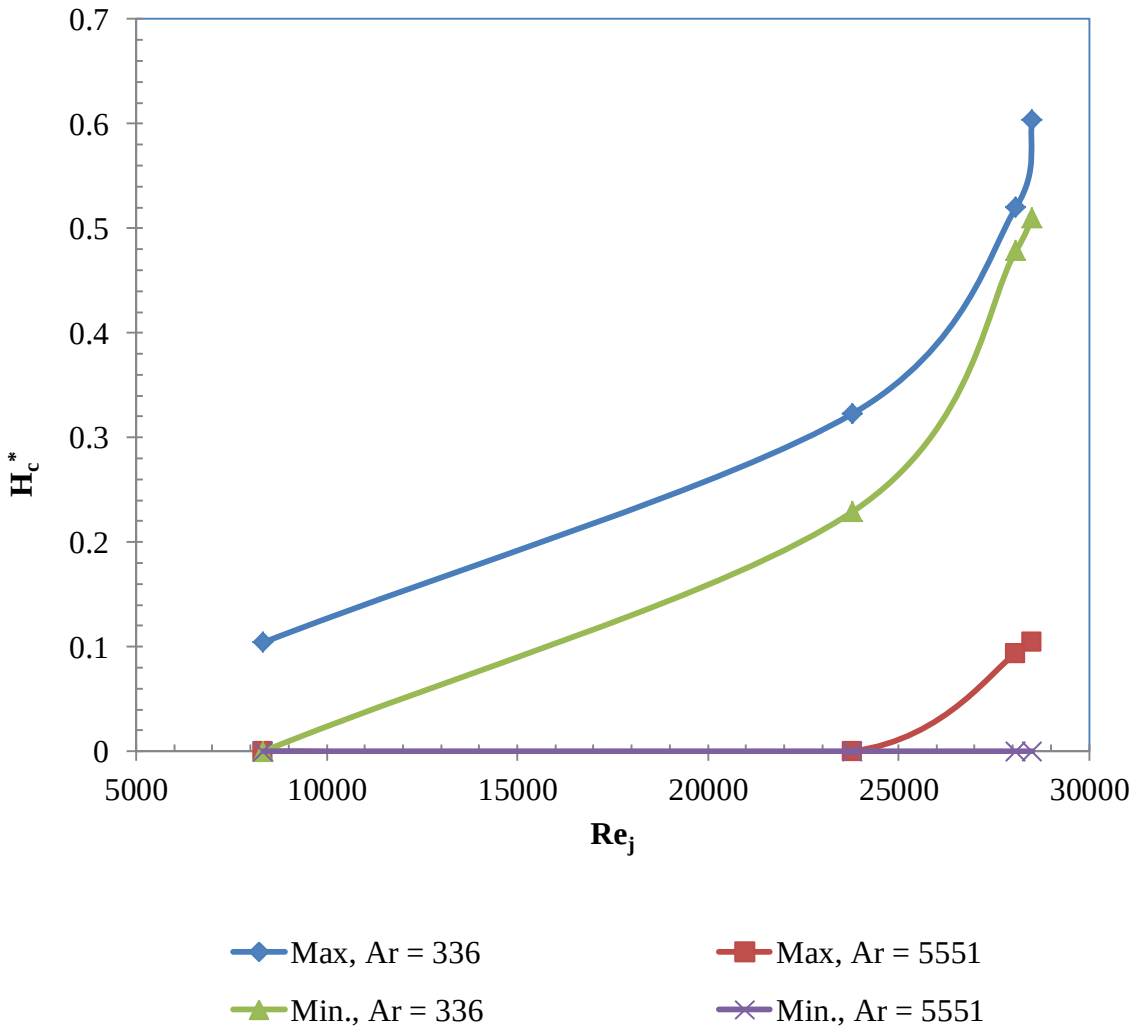

Figure 4.40. Dimensionless cloud height for jet nozzle at a height of 0.038 m.

When the liquid jet is discharged, it expands radially, but when the jet is closer to the bottom of the tank, its expansion is limited. Although a wall jet is created, suspension will not occur if the velocity of the wall jet is not sufficient. The lowered expansion also was a factor in the cloud height not being able to expand the complete diameter of the tank.

Figure 4.41 shows a comparison of the dimensionless cloud height for both jet heights as a function of the Froude number (Fr). More than 60% homogeneity was achieved using Fr = 514 at both heights. The dimensionless cloud height did not exceed 10% of the total liquid height at a Fr = 44. The minimum cloud height value does not vary much at the two different heights. The lower nozzle clearance provided cloud heights greater than that at the higher clearance level at higher Fr.

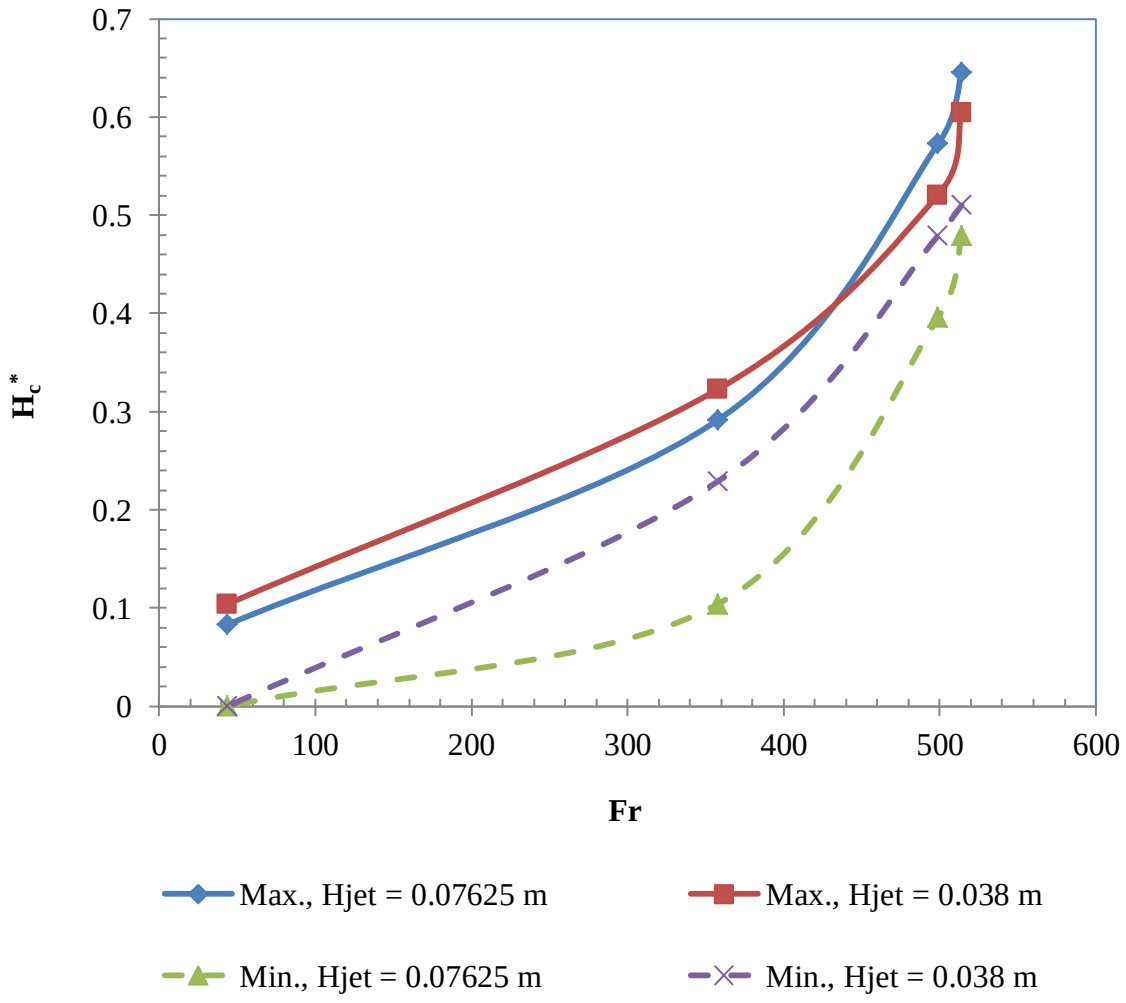

Figure 4.41. Comparison of dimensionless cloud height as a function of Fr for the particles with an Ar = 336.

The results of the physical model and experimental results were compared to determine the validity of the model. Figure 4.42 shows the comparison between the experimental and physical model results for the particles with an Ar = 336. When the Re_j exceeded 25000, the model predicts the cloud height well. The maximum deviation from the experimental values was only 4.6% at the two highest Re_j. However, there is larger uncertainty from the experimental results at a Re_j of 23800 and 8300.

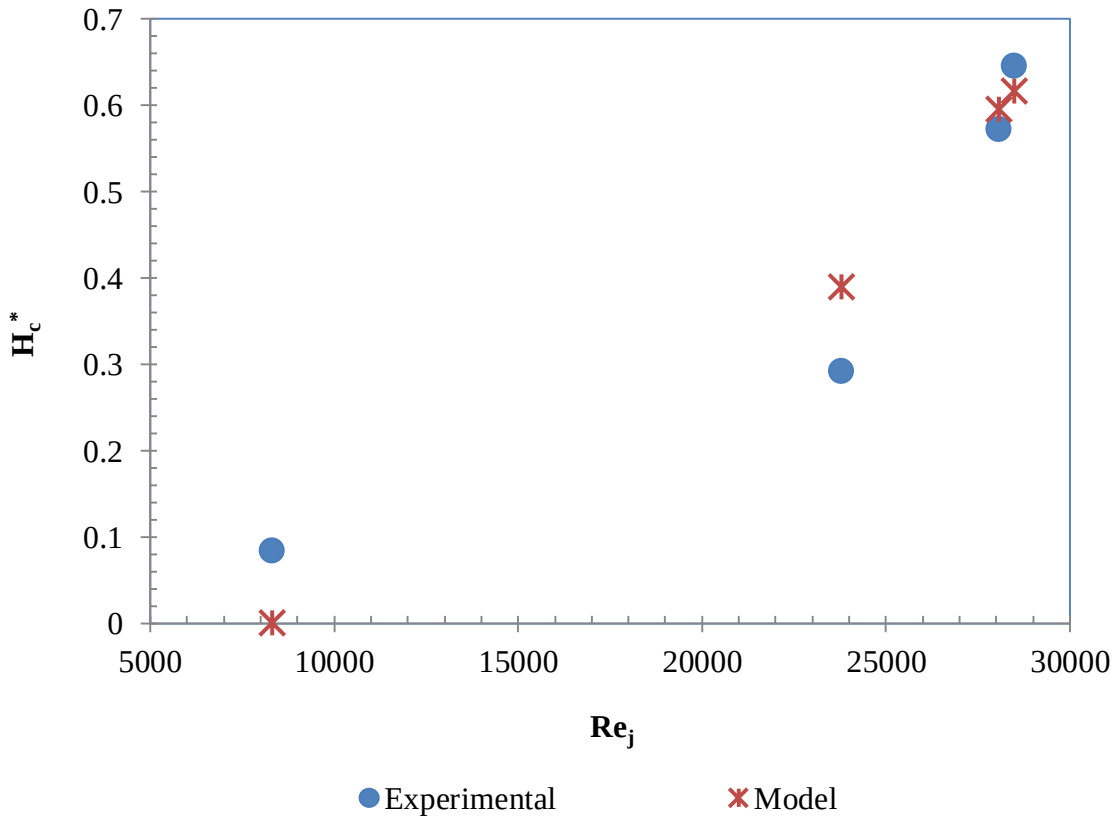

Figure 4.42. Comparison of experimental and physical model results for the Ar = 336 particles.

Figure 4.43 shows a comparison of experimental and model results for the particles with an Ar = 5551. The model predicts the cloud height very accurately at Re_j of 28000 and 28500. The maximum error from the experimental results is only 2%. The error increases as the Re_j decreases. The same results were found for the particles with an Ar = 336.

The discrepancy in the results could be due to the drag model which was used. The model for drag coefficient is a function of Re_p, but it is most accurate at intermediate Re_p values. The model could possibly be improved by incorporating different drag coefficient models for the various Re_p ranges. Uncertainty could also be due to the range of particle sizes in actual experiments, which are not accounted for in the model.

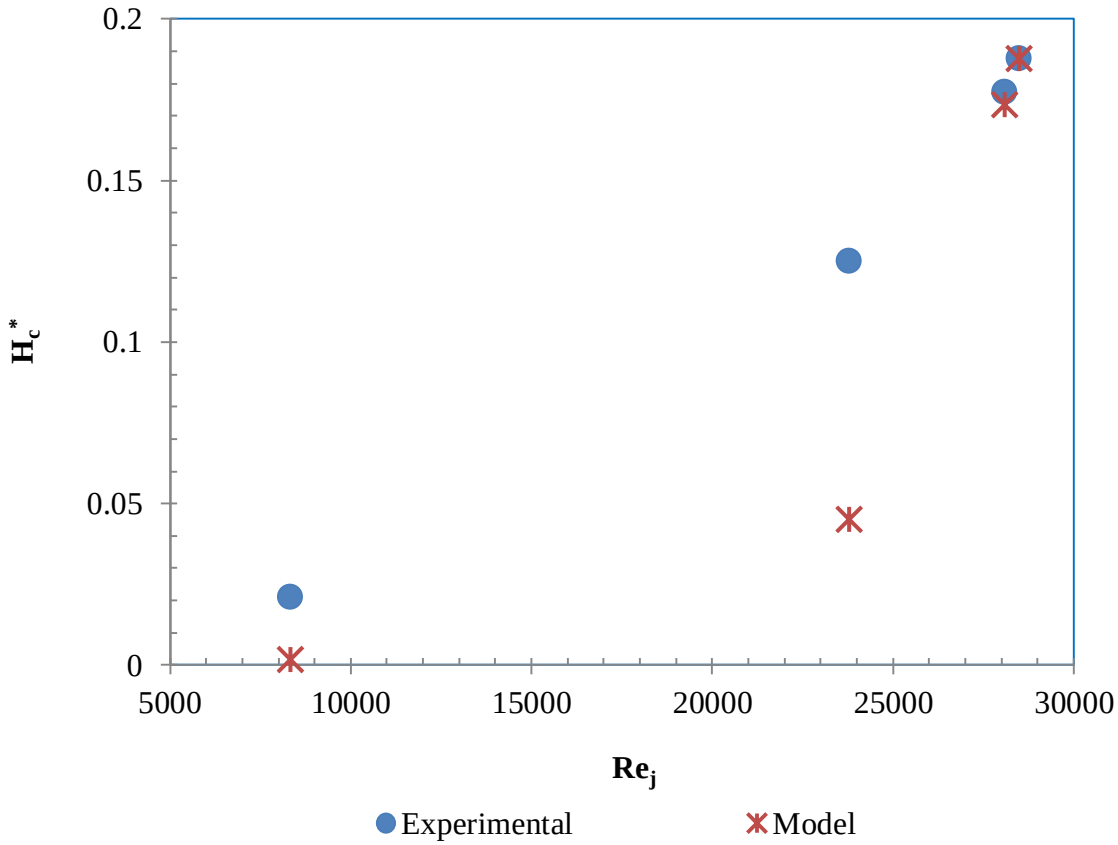

Figure 4.43. Comparison of experimental and physical model results for the Ar = 5551 particles.

The results of the physical model for the particles with an Ar = 28 are shown in Figure 4.44. The model predicts that the tank would be fully mixed at Re_j greater than 23800. Further improvements in the model should be made, but some of the error can be attributed to the drag model used. However, at a Re_j of 8300, the model predicts the non-dimensional cloud height very accurately. There was only 0.2% uncertainty from the experimental results at a Re_j of 8300.

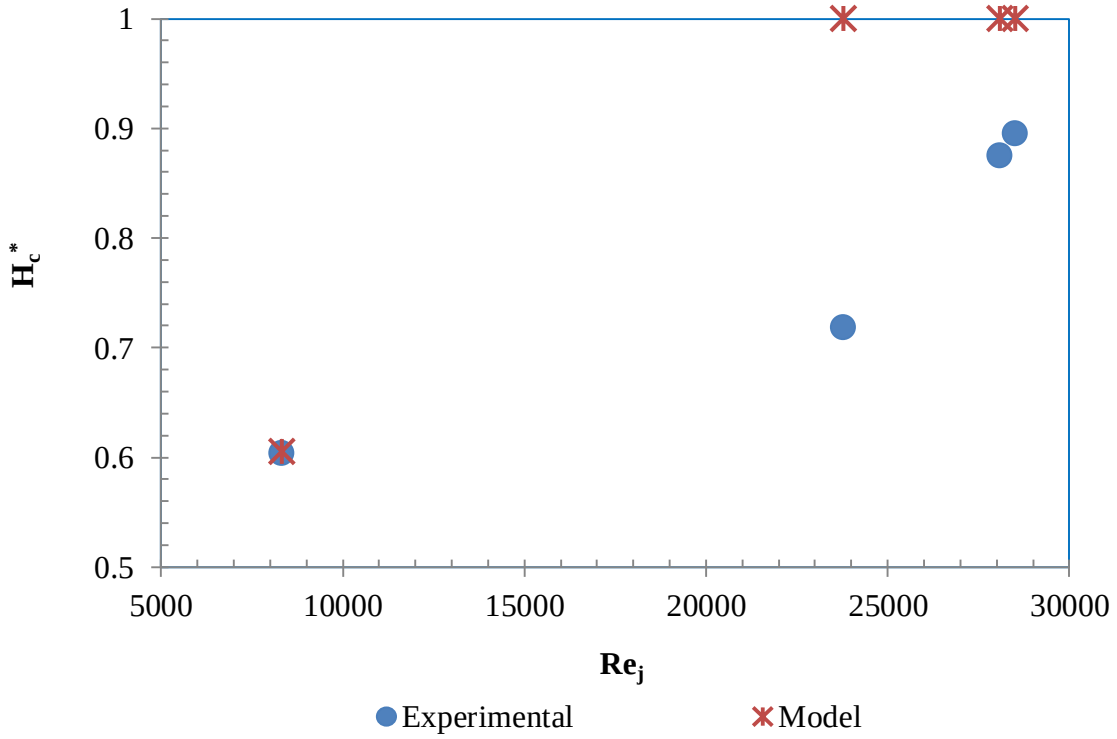

Figure 4.44. Comparison of experimental and physical model results for the Ar = 28 particles.

During experiments at low Re_j (i.e. 8300), the cloud did not extend the full diameter of the tank for the particles. To account for the cloud of particles not extending the full diameter of the tank in the model with an Ar = 336 and 5551, multiple particles should be used. For example, a statistical approach should be used to account for the varying particle size. However, the model does predict the height of a single particle correctly. The model predicted that at a Re_j of 8300, the particle rose very slightly with an Ar = 336 and 5551. Since experiments showed that the cloud height did not extend the full diameter of the tank, the model is actually accurate. For the Ar = 28 particles, the model predicted that the particle forces were not able to equilibrate within the height of the tank and thus it rose to the liquid height of the tank. When measuring the cloud height, there may be outlier particles which extend above the measured cloud height. The model once again was able predict the single particle well.

The model proposed in the present study is just an initial model and further improvements should be made to increase its accuracy in predicting cloud height. For instance, the model is based on a single particle, whereas in the actual experiments, a solids weight percent of 10% was used. Other phenomena like particle-particle interaction should be accounted for when a solids wt. % of at least 10% is used. Another assumption used in the current model was the particles were spherical. The actual particles used in experiments are clearly not spherical as previously shown in Figure 3.15. Different shaped particles behave differently because the geometrical differences affect how the particles are packed and how the particles interact with one another. Further studies should include model parameters to account for geometrical differences in the particles. Also, the model should be tested using solely spherical particles.

Though equation (3.5) given by Rajaratnam has been tested and well documented, a more accurate model for the wall jet created by impinging liquid jets should be used. Another suggestion is to improve the drag function used. Not only should the drag be a function of the different ranges of Re_p, but it should account for the change in drag as an effect of proximity to boundaries and additional particles.

4.5 Solids Bed Erosion Profile

Erosion profiles were determined for two different size particle beds: 265 and 700 μm (Archimedes number, Ar = 336 and 555, respectively). The erosion profile was measured for three different discharge velocities of the impinging jet: 1.39, 3.56, and 4.42 m/s (Re_j = 6000, 15380, 18660, respectively). Erosion profiles are useful as they give insight into how much of a solids bed will be eroded and ultimately suspended using the jet mixers. Shear stress profiles were first obtained from CFD results. The profiles help give insight into the ability of impinging

jet mixers to clear the bottom of the tank of solids and suspend solids. The CFD studies assumed that there were not any solids particles present in the tank.

4.5.1 Shear stress on bottom wall. Table 4.4 summarizes the results for the maximum and the average shear stress on the entire bottom surface for the continuous jets. When the height from the bottom of the tank was decreased, the shear stress on the bottom surface increased. The highest shear stress values were reported for the azimuthal jets at both heights. The azimuthal jets had the highest average shear for the surface at a height of 0.07625 m. The azimuthal jets were able to cover more surface area with higher amounts of shear. Similarly, the quad jets had the highest average shear at the lower height, despite not having the maximum shear stress values.

Table 4.4

Maximum and average shear stress on bottom wall using different continuous jet configurations.

	H = 0.07625 m		H = 0.025 m	
Number of jets	Max Shear	Average Shear on Surface	Max Shear	Average Shear on Surface
Dual Jets	12.36 Pa	2.98 Pa	79.64 Pa	6.79 Pa
Quad Jets	14.19 Pa	4.95 Pa	70.35 Pa	13.39 Pa
Azimuthal Jets	21.81 Pa	6.58 Pa	80.48 Pa	12.92 Pa

Figure 4.45 shows examples of the shear maps on the bottom surface after 10 seconds of flow time at a height of 0.07625 m from the bottom. The shear stress on the bottom wall for the dual, quad, and azimuthal jets are shown in Figure 4.45a, Figure 4.45b, and Figure 4.45c,

respectively. The azimuthal jets had higher shear stress covering the most surface area on the bottom wall, as shown in Figure 4.45c, as previously discussed.

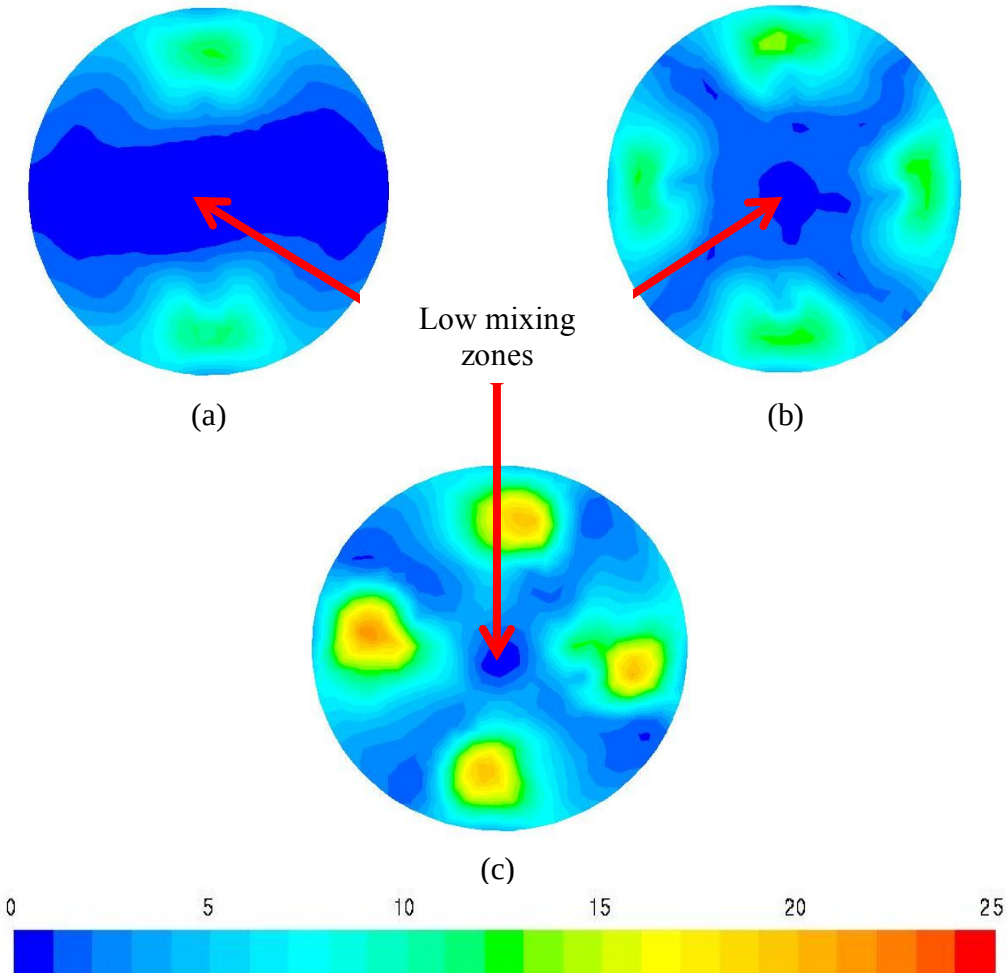

Figure 4.45. Shear stress on bottom surface after 10 seconds of continuous flow time, at a height of 0.07625 m from the bottom, for (a) dual jets, (b) quad jets, (c) and azimuthal jets.

The shear maps can be used to determine the effectiveness of the jets removing the solids off the bottom of the tank and thus creating a suspension. For example, in Figure 4.45a, the dual jets will not be able to suspend a large portion of solids in the middle region of the tank. On the other hand, the quad and azimuthal jets, shown in Figure 4.45b and Figure 4.45c, respectively, have smaller regions where the jets are less effective at the bottom of the tank. The aim was to

minimize the areas in which the jets are least effective relative to the total base of the tank. Through modification of the design or the addition of more jets, the low mixing regions can be further reduced. Figure 4.46 shows the shear stress maps on the bottom surface for one complete pulse using the P4 setting in the quad jet configuration at a jet height of 0.07625 m. The results show that the maximum shear stress found for the P4 pulse settings and the continuous jets were approximately the same. The results were expected because the discharge phase of the jets was long enough that they began to behave like steady jets while on. The only difference was that for the pulsing jets, the shear stress dropped to below 1 Pa during the time off period. The shear stress was not completely reduced to zero because the discharge phase of the pulse provided enough momentum to keep the fluid active during the short off period.

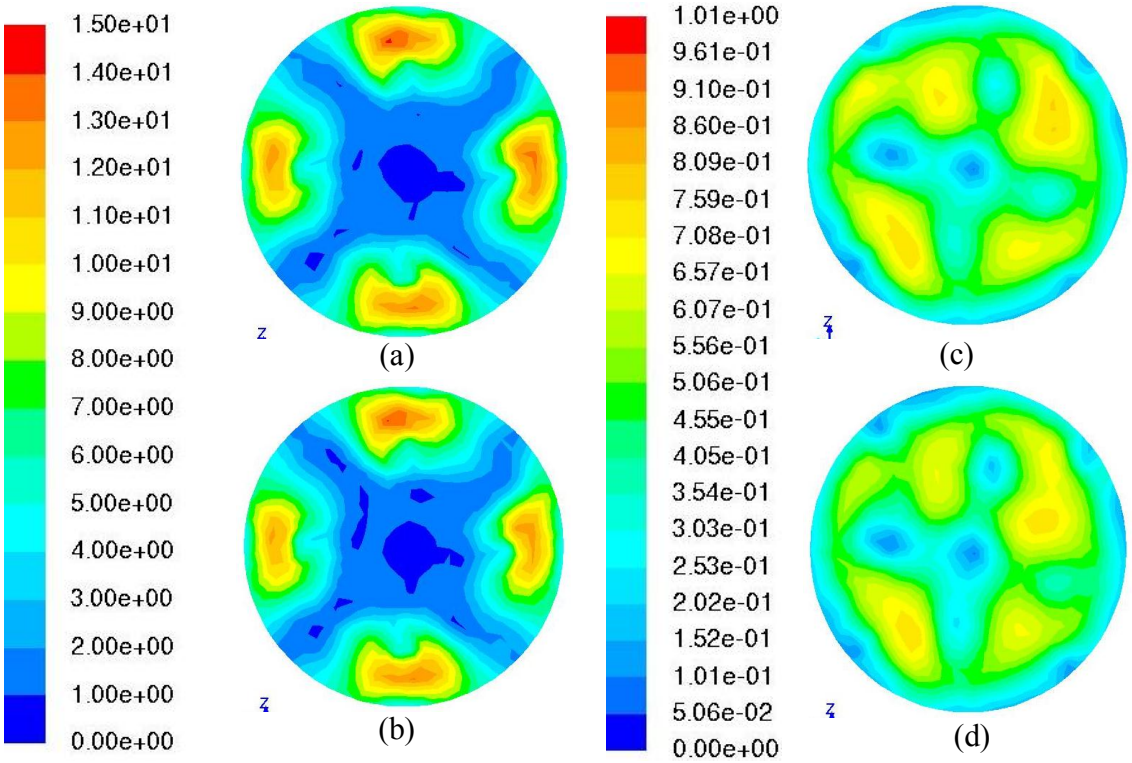

Figure 4.46. The shear stress maps for the P4 settings using the quad jet configurations after (a) 5 s, (b) 10 s, (c) 5.5 s, and (d) 10.5 s.

Figure 4.47 shows the shear stress on the bottom surface after 10 seconds of continuous flow time at a height of 0.025 m from the bottom for the dual, quad, and azimuthal jet configurations. The maximum shear stress on the bottom wall increases at a height of 0.025 m, compared to when the jet was at a height on 0.07625 m from the bottom. The shear stress profiles for the two heights are not the same as the jets impinge different on the bottom surface. Although there are localized higher maximum shear stresses, the overall profile suggests that much of the bottom of the tank remains with very little to no shear created from the jets. The shear map at 0.025 m suggests that the configuration would not be ideal for solid suspension processes.

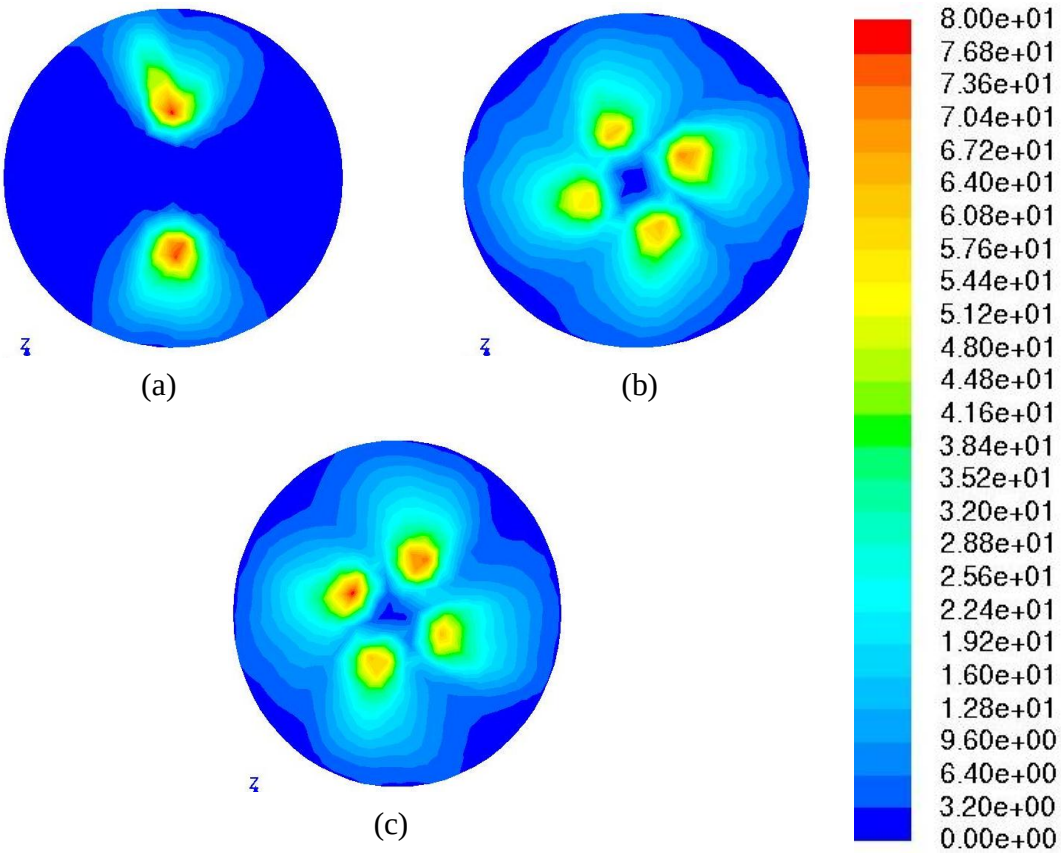

Figure 4.47. Shear stress on bottom surface at a height of 0.025 m from the bottom, for (a) dual jets, (b) quad jets, (c) and azimuthal jets.

4.5.2. Erosion profiles. Erosion depth was measured as a function of time and jet Reynolds number. An example of actual snapshots of the erosion profile found using different impinging jet discharge velocities is shown in Figure 4.48. The snapshots show that as the velocity increases, the profile becomes deeper and wider. The erosion profiles are monitored as a function of time and are summarized in this section.

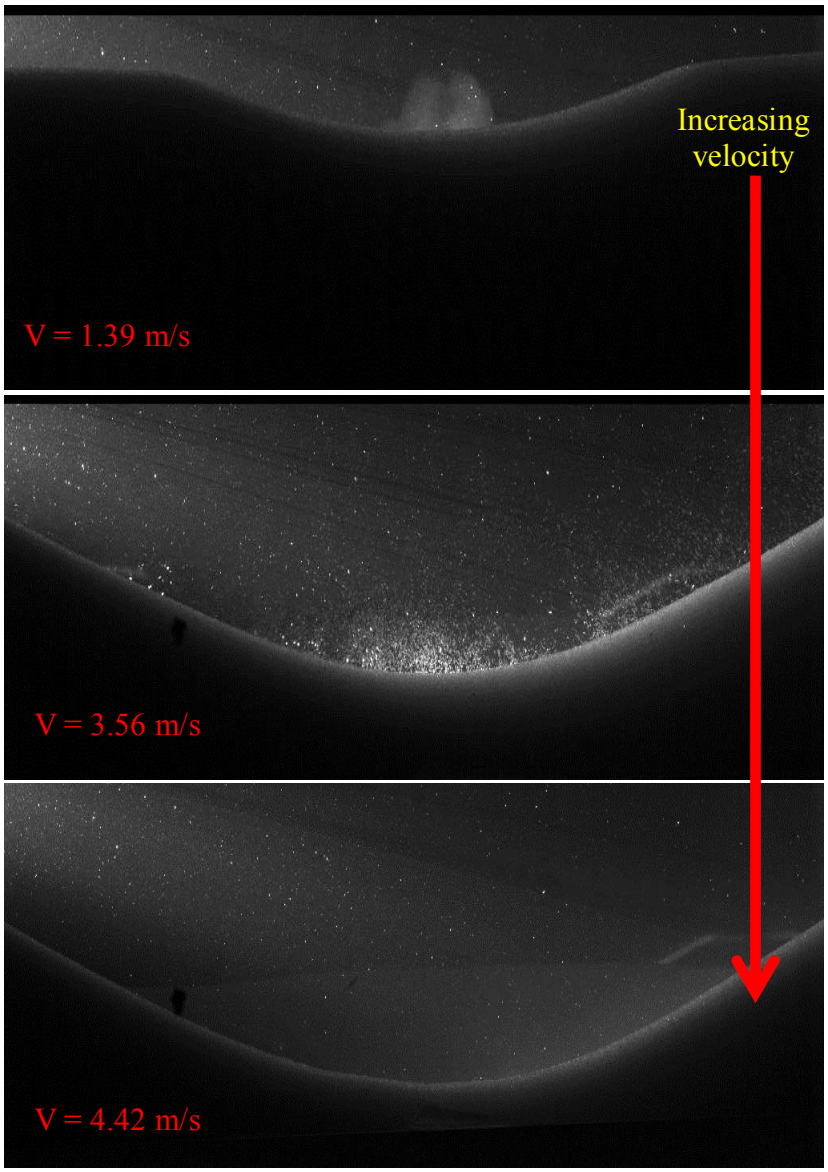

Figure 4.48. Snapshots of erosion profiles using different jet velocities.

The results of the erosion profile are presented in terms of the erosion depth at different horizontal positions for different jet Reynolds numbers. Figure 4.49 displays the erosion profile at different times using a jet Reynolds number of 6000. As time increases, the erosion depth increases. The center of the eroded area increases with time, causing the eroded profile to create steeper angles from the centerline outward.

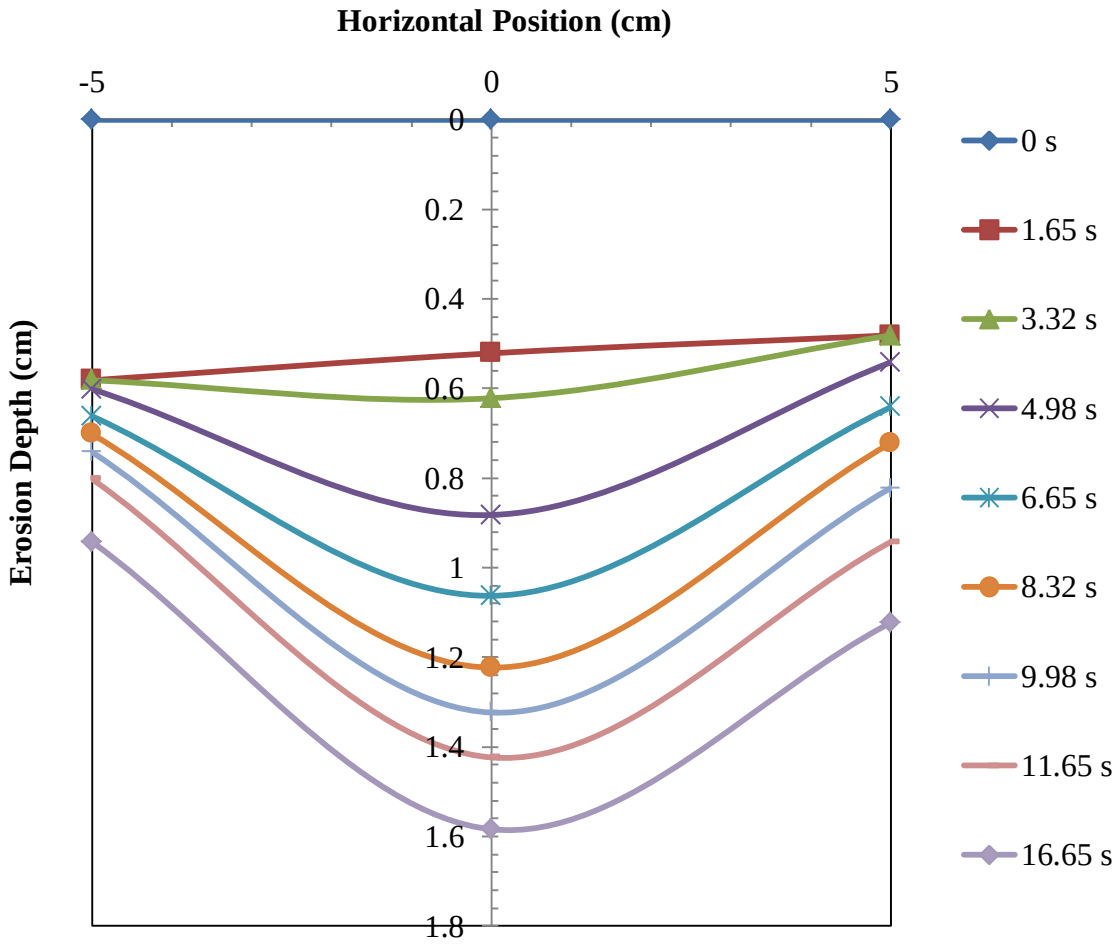

Figure 4.49. Erosion profile of particles with Ar = 5551 at a jet Reynolds number of 6000.

Figure 4.50 shows the erosion profile with increasing time using a jet Reynolds number of 15380. Though the erosion depth increases with time, the angle does not necessarily become steeper. The center of the eroded profile was expected to be the steepest, as the impinging jet

causes the particles to roll radially outward. After a time elapse of about 11.52 seconds, the erosion profile starts to change very little.

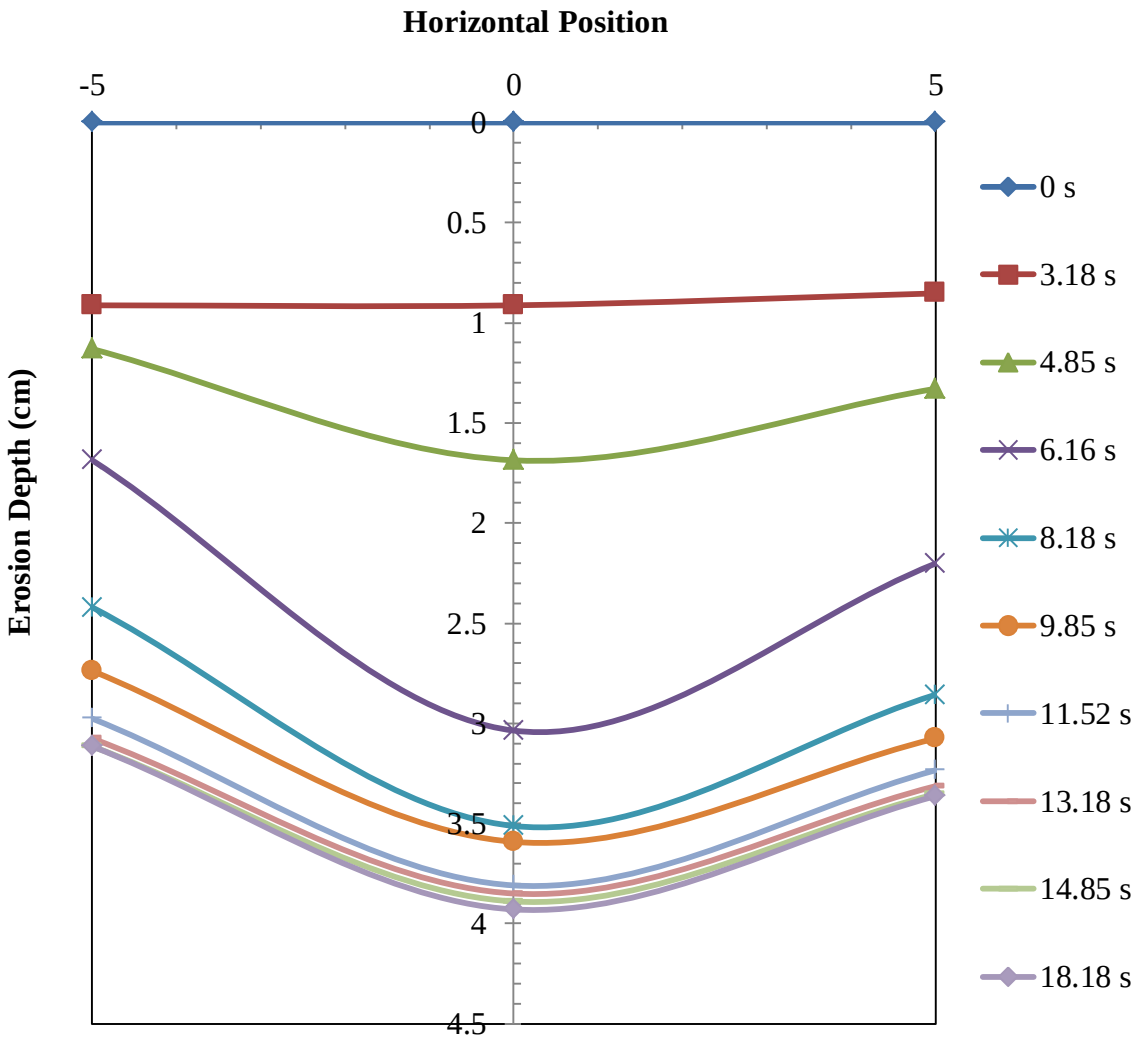

Figure 4.50. Erosion profile of d5 particles with Ar = 55510_700 particles using a jet Reynolds number of 15380.

Figure 4.51 displays the results of the erosion profile for the particles with Ar = 5551 at different times using a jet Reynolds number of 18660. Compared to a jet Reynolds number of 6000 and 15380, the solids bed is eroded to a larger depth. At a jet Reynolds number of 6000, after a time elapse of 16.65 s, the maximum eroded depth is about 1.6 cm. On the other hand, at

a jet Reynolds number of 18660 and a time of 16.65 s, the maximum eroded depth is about 3.9 cm. The increase is about a 143% in erosion depth by using a jet Reynolds number of 18660 rather than 6000.

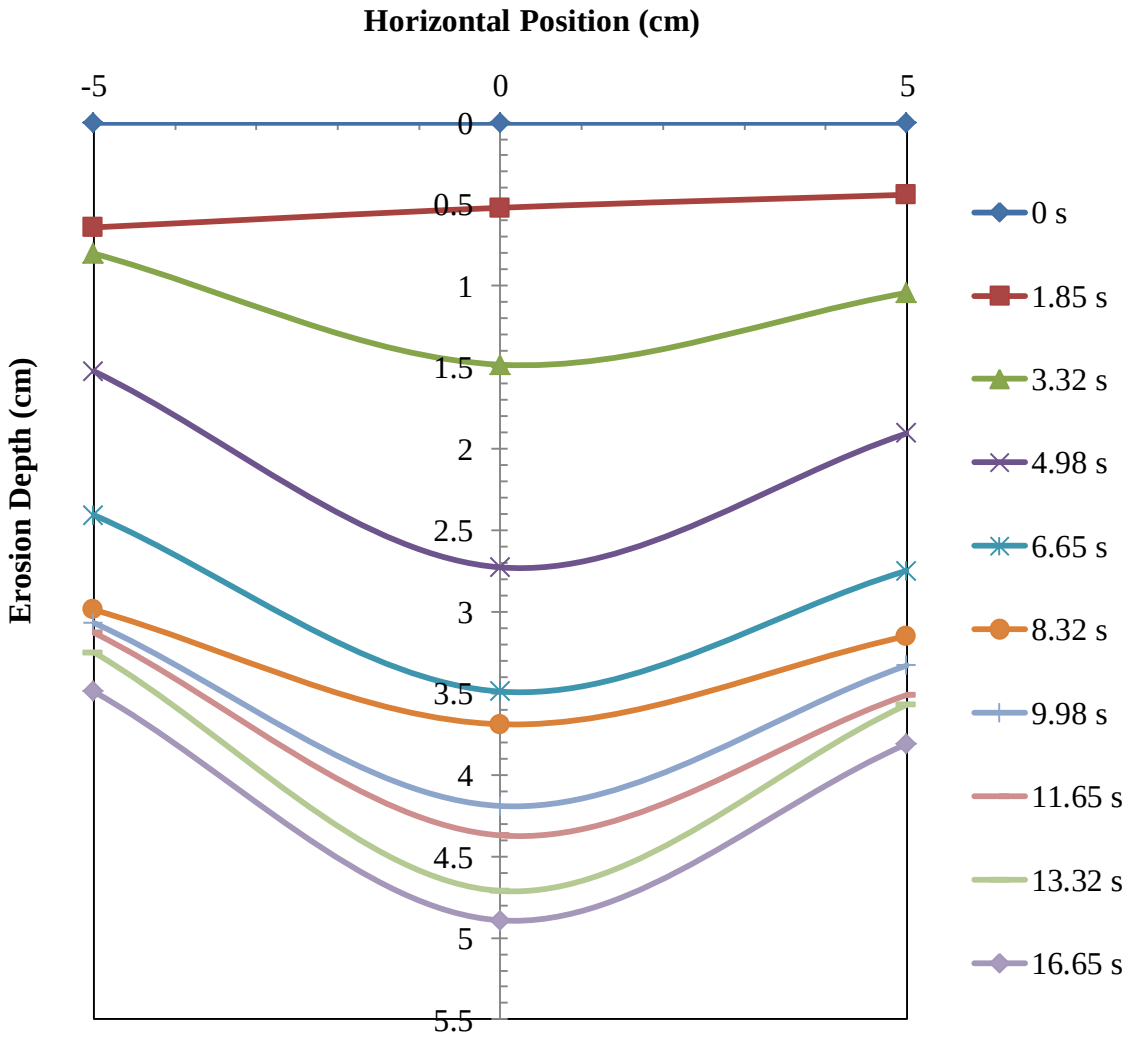

Figure 4.51. Erosion profile of particles with Ar = 5551 using a jet Reynolds number of 18660.

Figure 4.52 shows the erosion depth for the particles with Ar = 5551as a function of time using a jet Reynolds number of 6000. The results show that initially, up to a time of about 1.7 s, the rate of erosion is high. After 1.7 s, the solids bed is eroded at a more constant rate. The

erosion depth at the location of the center axis of the jet is the highest which is expected because the particles roll from the center outwardly.

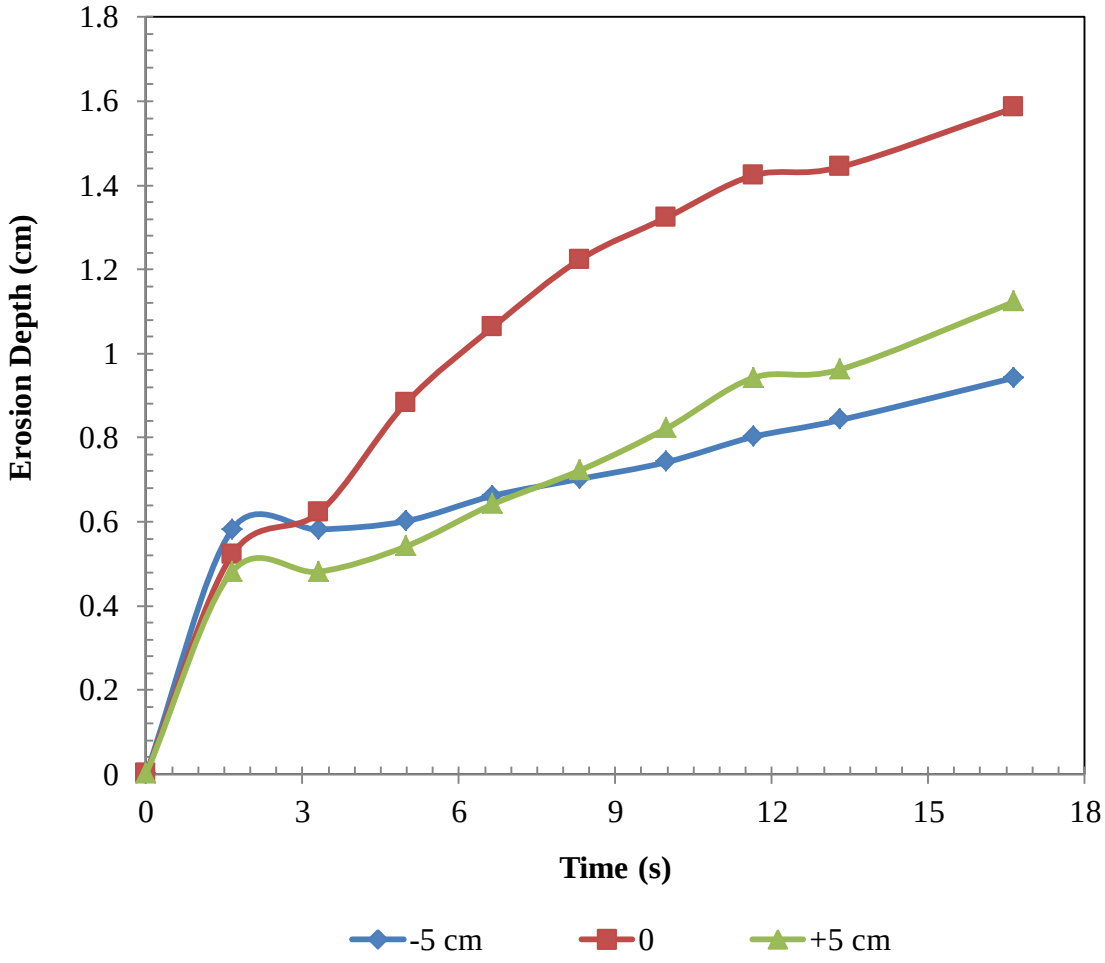

Figure 4.52. Erosion depth versus time for the particles with Ar = 5551 using a jet Reynolds number of 6000.

The erosion depth for the particles with Ar = 5551as a function of time using a jet Reynolds number of 15380 is displayed in Figure 4.53. The initial erosion rate of the solids bed is not as high as at a jet Reynolds number of 6000. There appears to be two different regimes. One regime is spans from the start of the run to about 7 seconds and is labeled, I, in Figure 4.53. The second regime, labeled II, occurs after 7 seconds as the depth starts to level off. The first

regime can be fitted with a 3rd order polynomial curve. Equation (4.5) displays the equation that fits the data for first regime and equation (4.6) is that for the second regime.

$$(erosion\ depth)_I = 0.0252t^3 - 0.1659t^2 + 0.56t \tag{4.5}$$

$$(erosion\ depth)_{II} = -0.000552t^2 + 0.1885t \tag{4.6}$$

The eroded hole that is created is deeper at a jet Reynolds number of 15480 compared to 6000, but it is not necessarily steeper. Meaning, the difference in depth between the center position and the outer positions is not as great with a jet Reynolds number of 15380 compared to 6000.

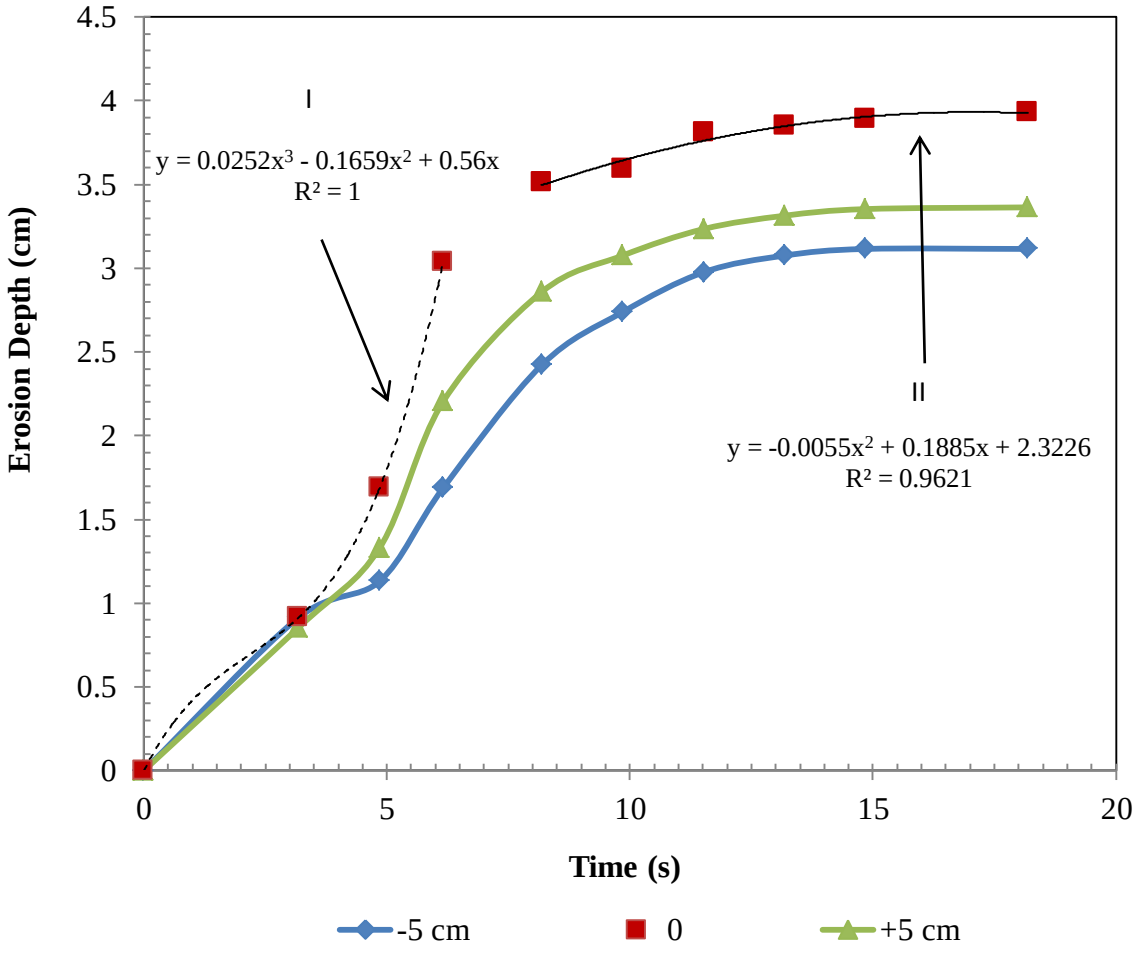

Figure 4.53. Erosion depth versus time for the particles with Ar = 5551 using a jet Reynolds number of 15380.

Figure 4.54 displays the erosion depth as a function of time for the particles with Ar = 5551using a jet Reynolds number of 18660. The depth is the highest in this setting due to it being the highest velocity setting. The maximum erosion depth is at the center position, 0, in which it nears about 5 cm after about 16.7 seconds. Similar to the run using a jet Reynolds number of 15380, there are two different regimes that are present.

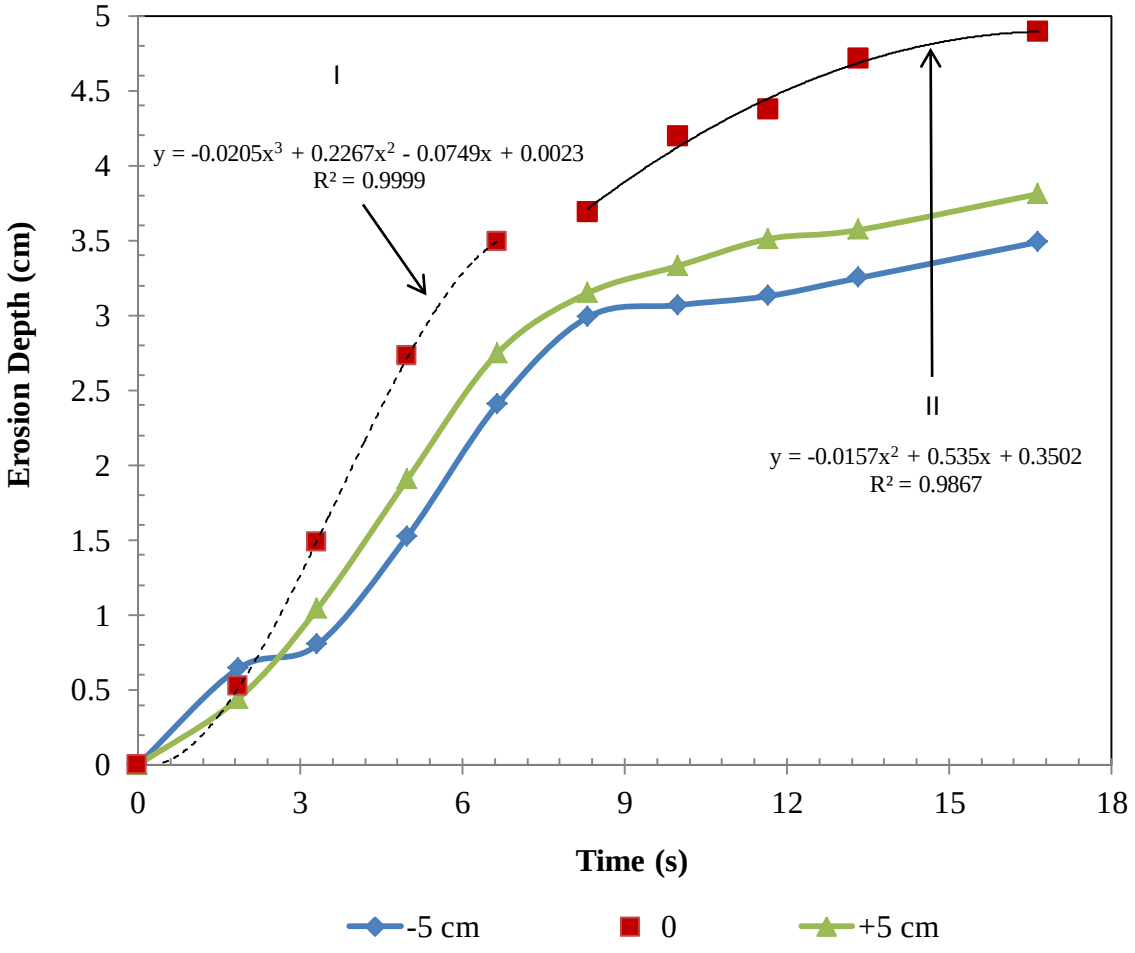

Figure 4.54. Erosion depth versus time for the particles with Ar = 5551 using a jet Reynolds number of 18660.

The first regime, labeled I, has s a steeper erosion rate up until about 7 seconds and then the second regime, II, has a lower erosion rate as the slope the is not as high. Equation (4.7) and

(4.8) represent the curve fit for the data for regimes I and II, respectively. The equation for regime I is fitted with a 3rd order polynomial and the equation for regime II is fitted with a 2nd order polynomial.

$$(erosion\ depth)_I = 0.0205t^3 - 0.2267t^2 + 0.0749t + 0.0023 \quad (4.7)$$

$$(erosion\ depth)_{II} = -0.0157t^2 + 0.535t + 0.3502 \quad (4.8)$$

The two regimes can be explained by the erosion mechanisms previously described in Chapter 2. When the jet is initiated, the nozzle clearance from the top of the solids bed is at a minimum, compared to the entire experimental run. The results suggest that surface erosion and entrainment can be responsible for the initial high erosion rates. The mechanisms occur as the applied stress at the liquid/solid interface is greater than the critical yield stress of the solids bed.

The results also suggest that the decrease in erosion rate during the second regime is most likely due to only one erosion mechanism being present. The particles are more likely to be entrained and transported to the outer edges of the tank or the eroded area as the depth from the jet discharge and the solid/liquid interface increases, creating a mound. Entrainment of the particles still occurs even though the jet discharge and the surface of the solids bed increases over time.

Figure 4.55 shows the eroded area of particles as a function of time for the three different velocities used in the experiments. The eroded area increased with an increase in velocity. When the lowest velocity setting was used, the erosion rate is much lower and more constant than the other two settings. The eroded area increases exponentially and should increase for a much longer time compared to the other settings until it reaches an asymptotic state at the highest velocity setting. Using the jet Reynolds number of 15380, there is a jump in the eroded area between about 6 and 8 seconds.

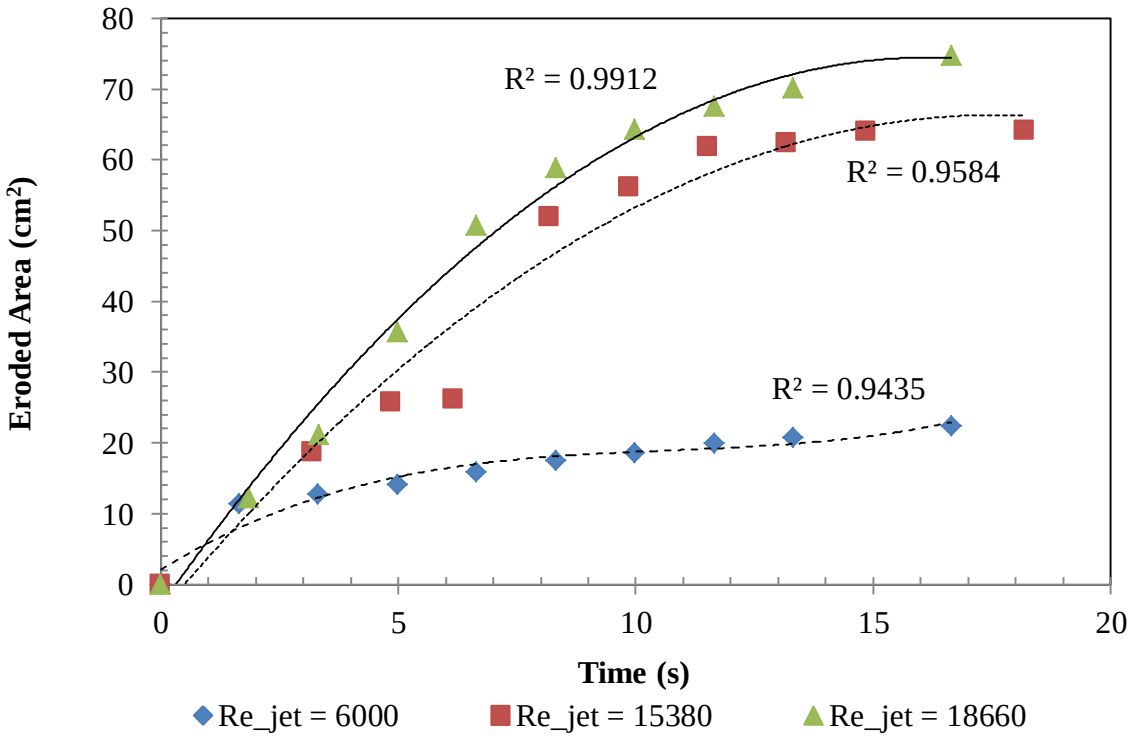

Figure 4.55. Eroded area as a function of time for the three different measured velocities using the Ar = 5551 particles.

The results for the eroded area as a function of time at various Re_j were fitted with polynomial curves. The results are displayed in terms of equations. The 2nd order polynomial fitted equation for the results using a Re_j of 18660 is displayed in equation (4.9). The data was fitted well as the R^2 value was 0.9912.

$$(eroded\ area)_{Re_j=18660} = -0.297t^2 + 9.6023t - 3.0194 \quad (4.9)$$

The 2nd order polynomial equation for the fitted curve for Re_j = 15380 is shown in presented in equation (4.10).

$$(eroded\ area)_{Re_j=15380} = -0.2276t^2 + 7.9981t - 3.9282 \quad (4.10)$$

The results for Re_j = 6000 was fitted using a 3rd order polynomial equation, which is displayed as equation (4.11).

$$(eroded\ area)_{Re_j=6000} = 0.0112t^3 - 0.3595t^2 - 4.1432t + 2.0889 \quad (4.11)$$

The eroded area results for Re_j = 6000 had a different trend then the results at Re_j = 15380 and 18660. The area was eroded in a mostly linear fashion, besides the data point for the origin.

Erosion profiles were found for the particles with Ar = 336 as well. The erosion profile at different times up to about 17 seconds for the Ar = 336 particles, using a jet Reynolds number of 6000 is shown in Figure 4.56. The initial momentum of the jet causes the particles to erode almost consistently across the measured area. The consistent erosion is seen as the profile at 1.65 seconds is almost constant around 1 cm. The trend changes as time goes on though as the depth in the center position, 10 cm, continues to become much greater than the outer positions at the same time.

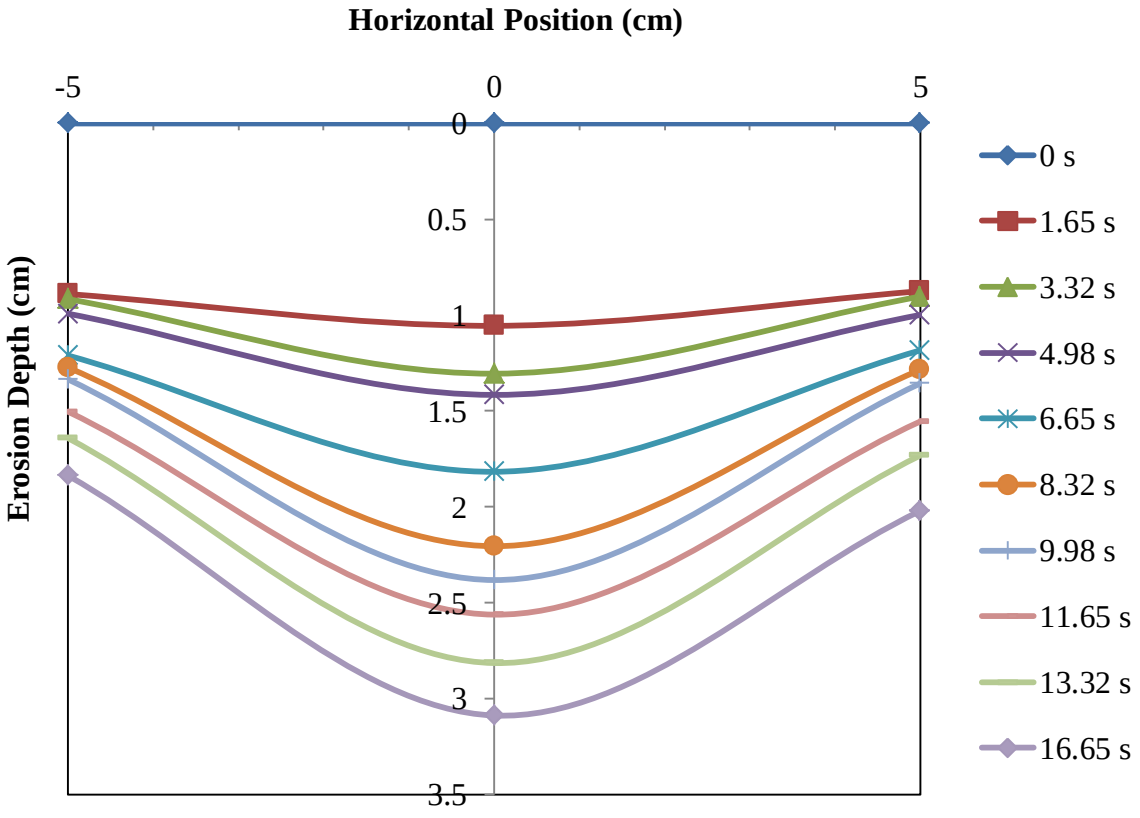

Figure 4.56. Erosion profile of the Ar = 336 particles using a jet Reynolds number of 6000.

Figure 4.57 shows the erosion profile of the Ar = 336 particles at different times using a jet Reynolds number of 15380. The maximum erosion depth is about 8 cm, which occurs after about 18.18 seconds. Compared to the Ar = 5551 particles, the profile is deeper, but not as steep. The deeper profile is because the momentum from discharging jet is sufficient to carry more of the smaller particles out of the impingement zone as compared to the larger particles, whose weight requires more force to be moved.

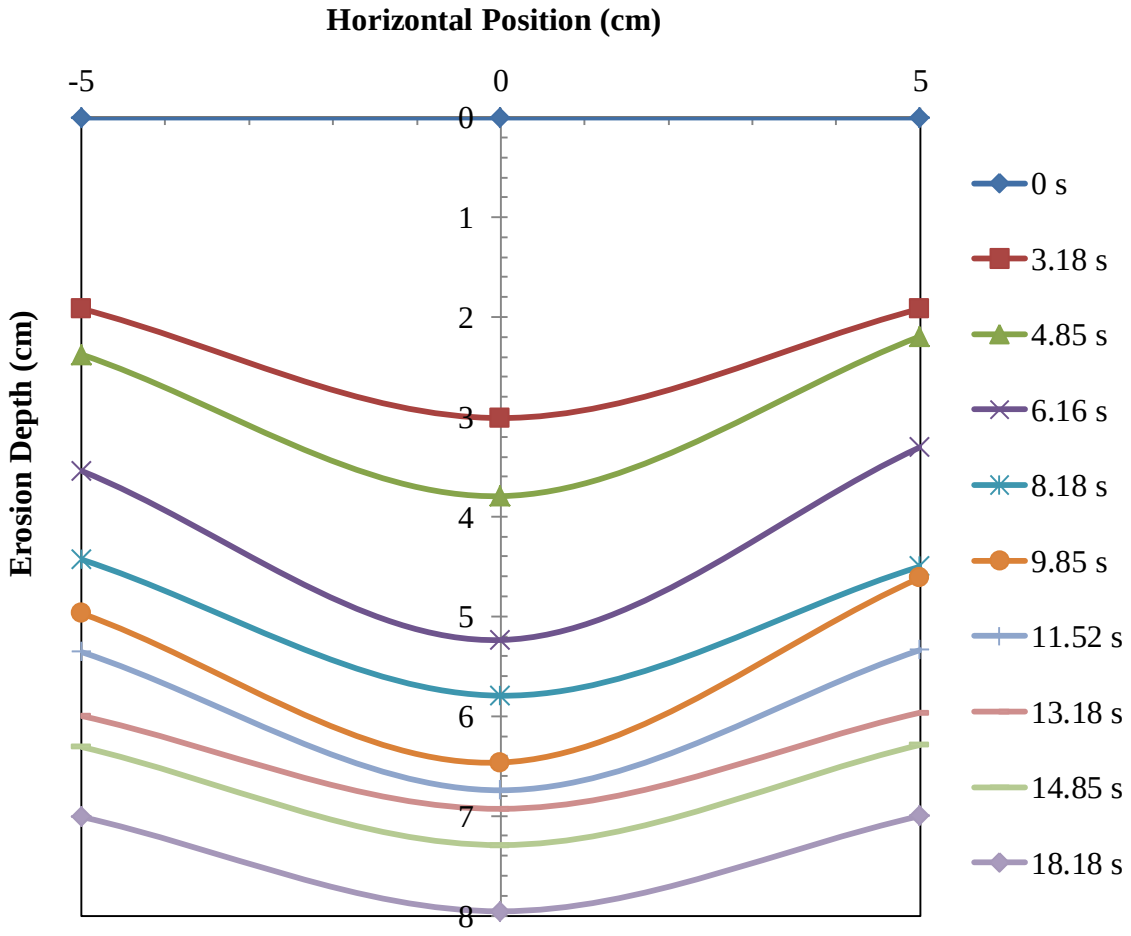

Figure 4.57. Erosion profile of the Ar = 336 particles using a jet Reynolds number of 15380.

Figure 4.58 displays the erosion profile for the particles with Ar = 336 at different times using a jet Reynolds number of 18660. Profiles were only found up to 13.32 seconds because

the initial height of the solids bed was only about 9 cm. However, with a higher solids bed and the current velocity setting, erosion will continue over time. Compared to the run with the jet Reynolds number of 6000, the erosion profile after 1.85 seconds is steeper. The difference is due to the increased velocity.

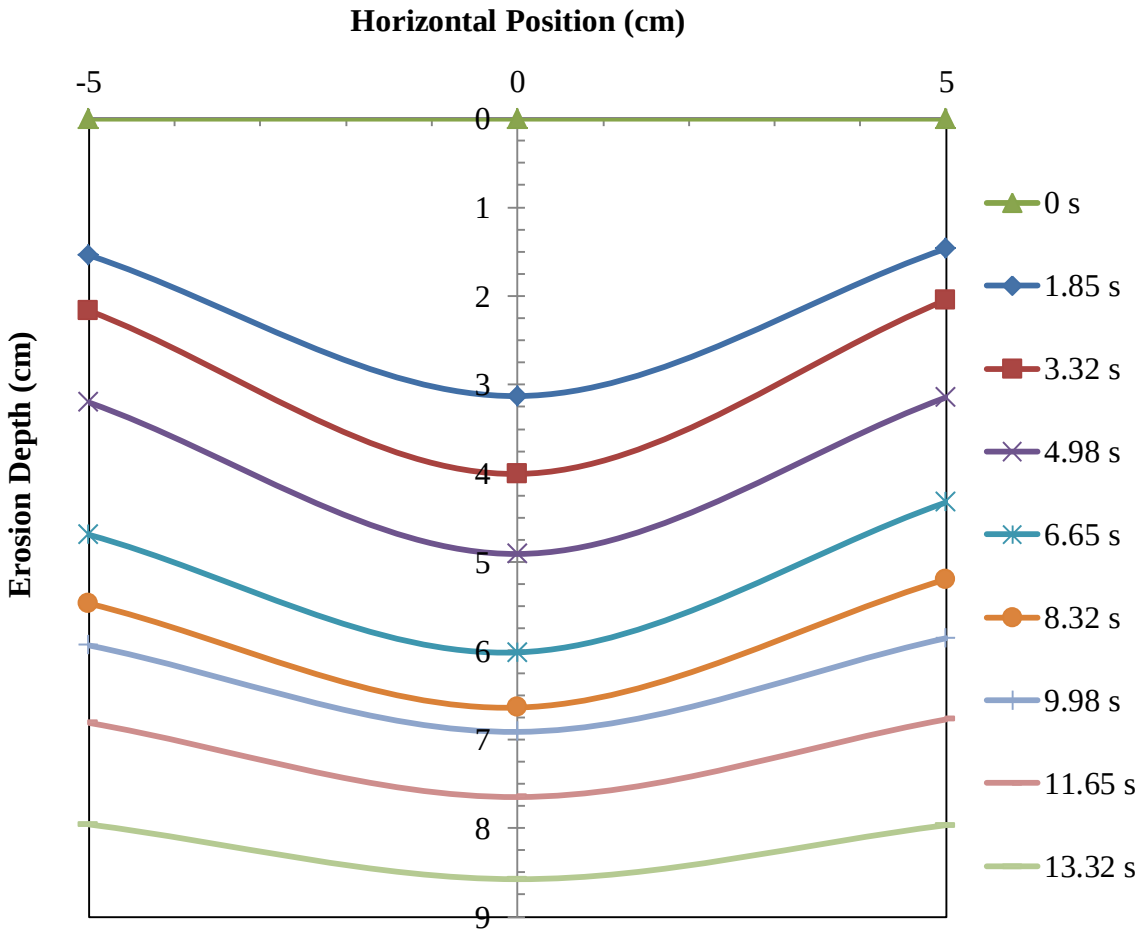

Figure 4.58. Erosion profile of the particles with Ar = 336 using a jet Reynolds number of 18660.

The erosion depth as a function of time for the particles with Ar = 336 using a jet Reynolds number of 6000 can be seen in Figure 4.59. The eroded area is almost completely symmetrical over time as the depths of the outer positions, 5 and 15 cm, are almost identical. All

three of the measured positions show similar trends over time. The erosion depth at the center position for the Ar = 336 particles after 16.65 seconds is a little over 3 cm, compared to the Ar = 5551 particles, where the erosion depth at the same time neared 1.6 cm.

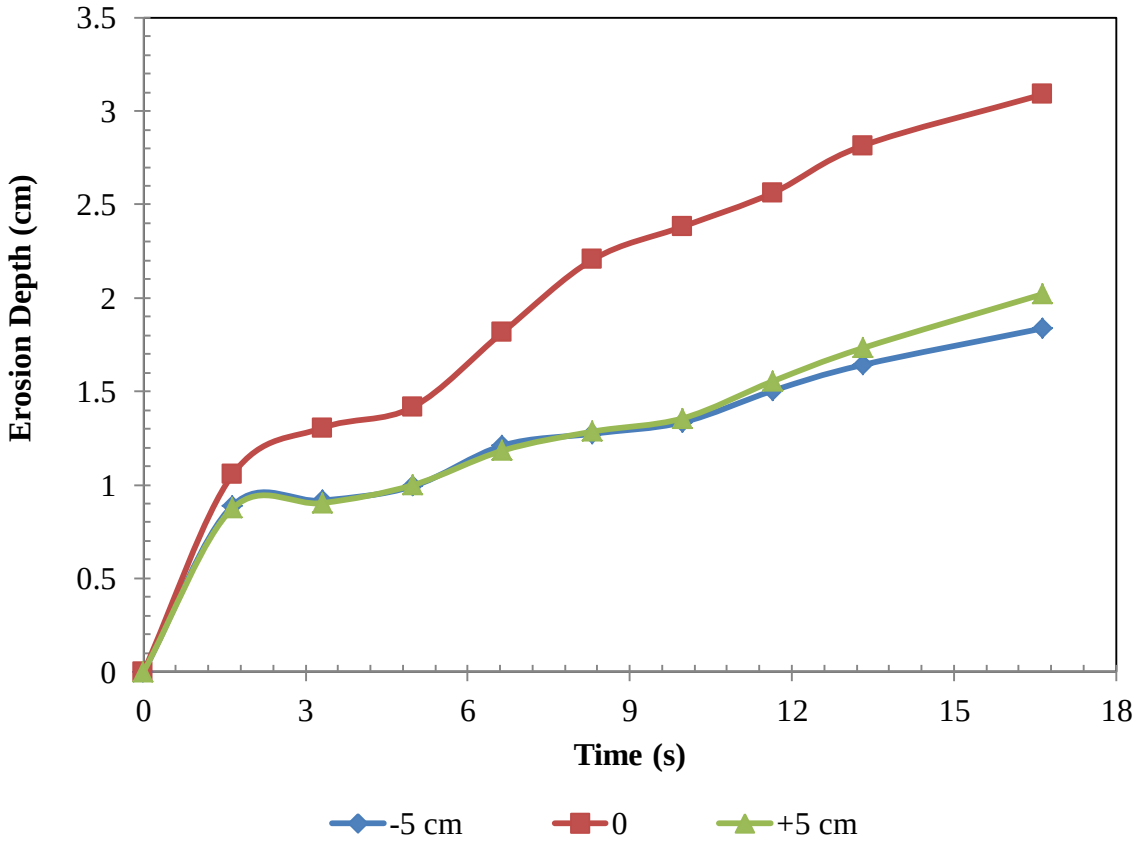

Figure 4.59. Erosion depth versus time for the particles with Ar = 336 using a jet Reynolds number of 6000.

Similarly to the particles with Ar = 5551, the results for the particles with Ar = 336 suggest that two different regimes exist. Regime I cease around 5.2 seconds and then regime II begins. Regimes II for the particles with Ar = 336 has a steeper slope than the same regime for the larger particles. The smaller particles are still easily transported out the zone as the standoff distance between the jet nozzle and the liquid/solid interface increases. The solids bed would need more height for the erosion rate to erosion depth to start leveling off. The results of the

erosion profile for the Ar = 336 particles are much more symmetrical than the results for the Ar = 5551 particles.

The erosion depth as a function of time using a jet Reynolds number of 15380 for the Ar = 336 is shown in Figure 4.60. Once again, the erosion rates measured at the two outer positions are about the same, which shows the expected symmetry. The erosion depth at the center position is around 8 cm and the depth at the outer positions approaches 7 cm. The depth is much greater for the smaller particles, compared to the larger, Ar = 5551, particles. The maximum depth for the larger particles using the same Re_j was almost 4 cm after 18.18 seconds.

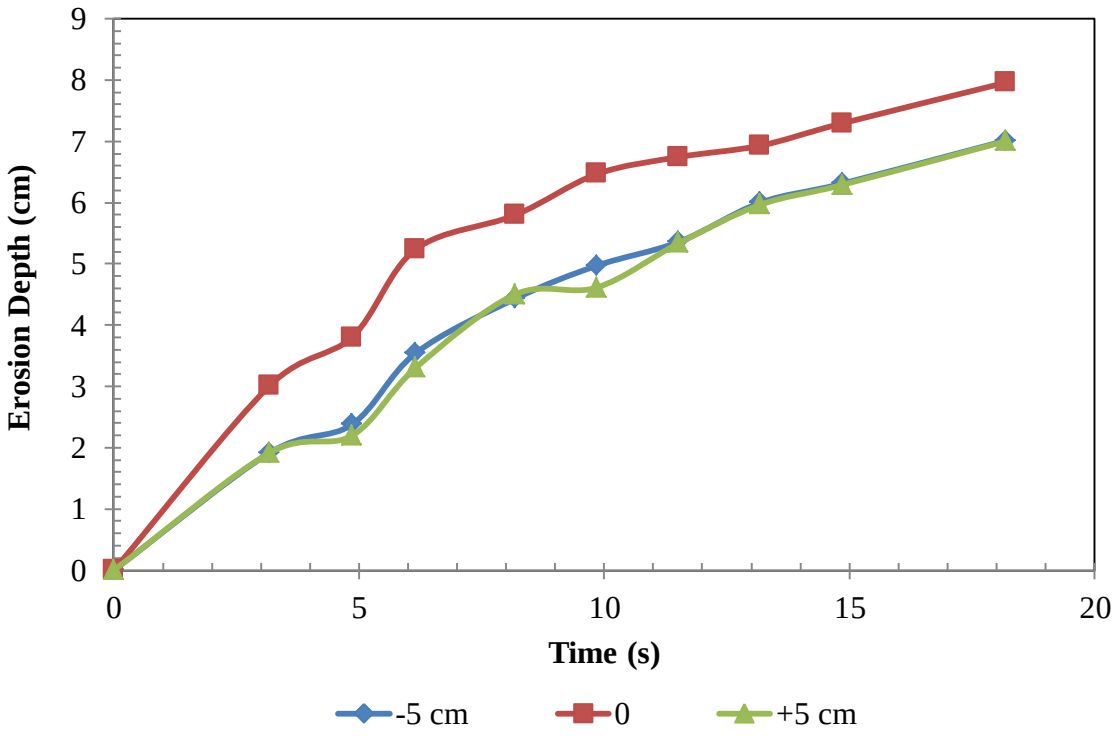

Figure 4.60. Erosion depth versus time for the particles with Ar = 336 using a jet Reynolds number of 15380.

Figure 4.61 shows the erosion depth as a function of time for the Ar = 336 particles using a jet Reynolds number of 18660 The erosion rates at the outer measured positions, 5 and 15 cm,

are very linear. The maximum erosion depth is almost 9 cm at 13.32 seconds. The maximum erosion depth was almost 5 cm, using the particles with Ar = 5551 at the same time.

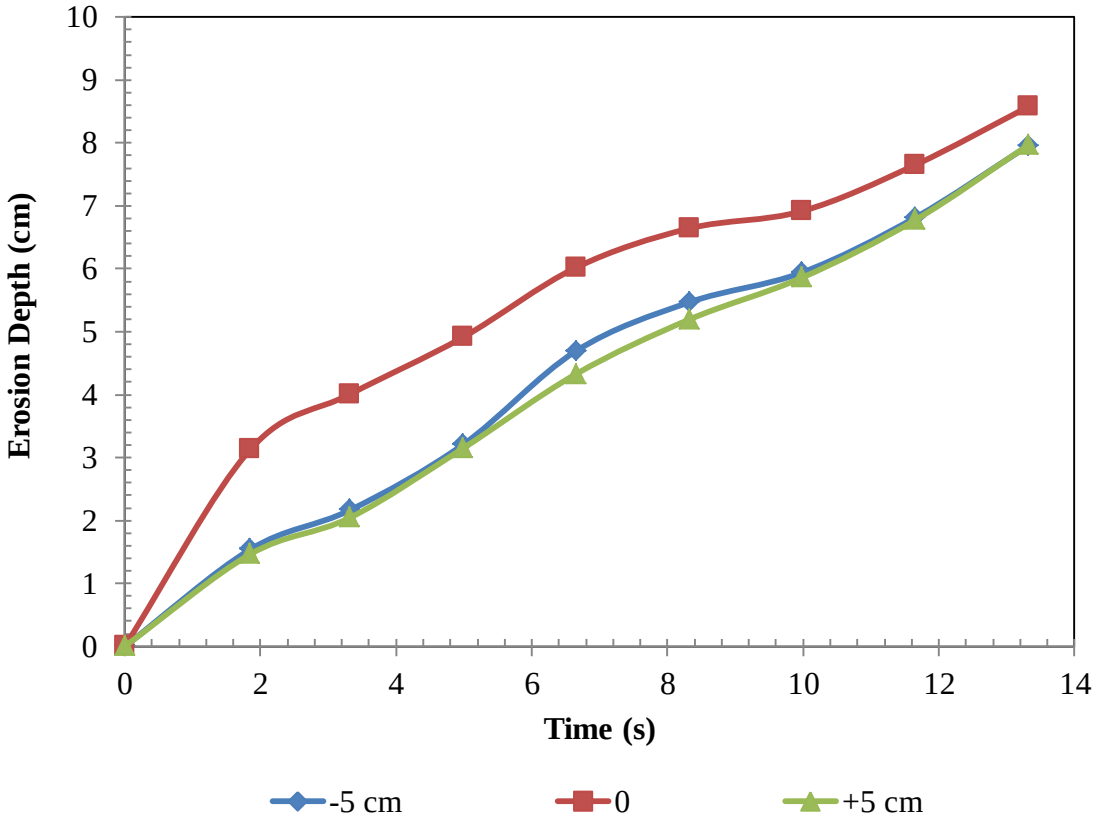

Figure 4.61. Erosion depth versus time for the particles with Ar = 336 using a jet Reynolds number of 18660.

Overall, the erosion of a solids bed increases with increased velocity. Erosion depth is increased, as the particle size is decreased. The point at which erosion of a solids bed stops occurring, or as it reaches an asymptotic state, depends on the bed size, particle size, working jet conditions, and location of the jet in relation to the solids bed. All of the aforementioned factors must be further studied to optimize erosion. Also, particle shape plays a role in how the solids bed is eroded. The shape of the particles was not taken into account in the current study and it should be taken into account in future studies.

Results for erosion depth as a function of time showed that there are two regimes present. The first regime has a higher erosion rate and lasts for a short period of time. The two regimes were described on the basis of the erosion mechanisms described in Chapter 2. Entrainment and surface erosion was proposed to be the cause of the initial high erosion rates found in regime I. Regime II was proposed to be due to entrainment only.

The erosion profiles that were found may be useful for many applications. The determination of erosion profiles may be used for the erosion of sludge material, such as in waste water remediation. The profiles may also be used for geological purposes, such as in the erosion of sand dunes and other particulate structures, if the input velocity can be ascertained. The erosion profiles were fit mostly with polynomial curves and the equations found for the data can be used for future CFD studies. The results will be useful in simulations in which the surface boundary conditions are needed as functions of times.

4.6 Axial Concentration Profiles

The concentration profiles were found for varying concentrations of kaolin clay mixtures following the procedure presented in Chapter 3. The results are presented in terms of non-dimensional parameters. The concentration throughout the tank was scaled with the initial solids concentration and the vertical position was scaled with the liquid level in the tank.

The specific objective of the study was to determine the axial concentration profiles. A test was run to determine if the concentration profiles along the radial axis remains approximately constant once the mixture reaches the liquid height. Figure 4.62 shows the results of the study in which the axial concentration profile was measured at three different points along the radial position. The figure shows that the concentration profiles are almost similar for the

three compared horizontal positions. The results show that the profile varies vertically, but does not vary horizontally.

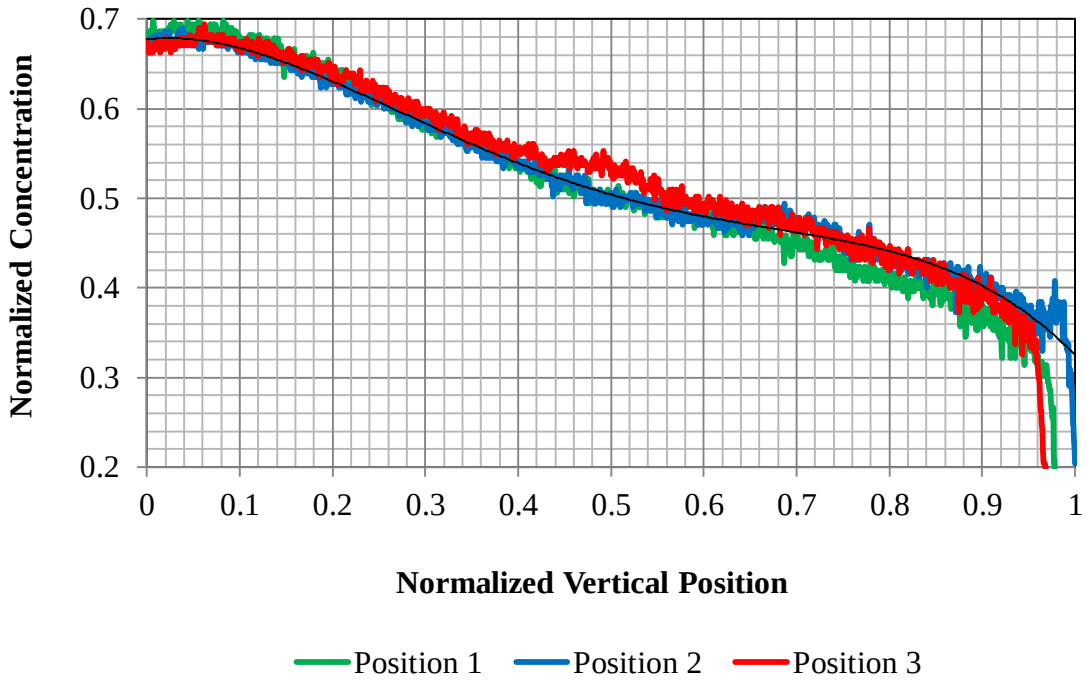

Figure 4.62. Concentration profile at various vertical positions.

Figure 4.63 displays the results for concentration profiles as a function of vertical position for a solids wt. % of 2.2. The results show that at 2.2 wt. %, the concentration profile becomes changes very little after about 16.84 seconds. The data at 34 seconds can be fitted with a third order polynomial law curve with a R^2 value of 0.9885. The equation for the polynomial curve is

$$\frac{C}{Co} = -2.665 \cdot \left(\frac{y}{H}\right)^3 + 2.723 \cdot \left(\frac{y}{H}\right)^2 - 0.90 \cdot \left(\frac{y}{H}\right) + 0.844 \qquad (4.12)$$

where C is the solids concentration at vertical location, y, in the tank, C_o is the initial concentration, and H is the liquid level. The black circle in Figure 4.63 represents spurious data points, which is due to the experimental procedure.

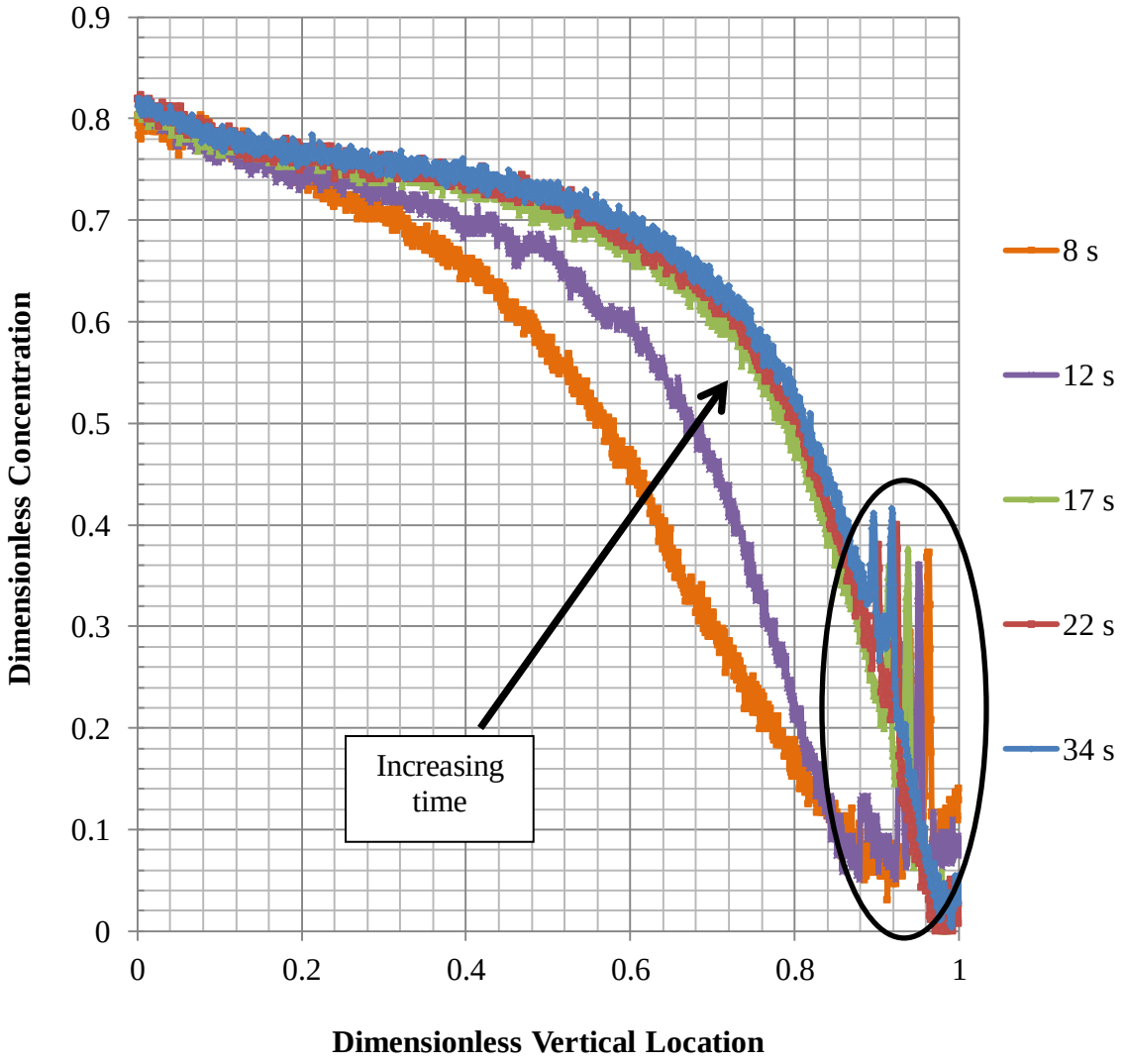

Figure 4.63. Dimensionless concentration as a function of vertical location at different times for a kaolin clay wt. % of 2.22.

Figure 4.64 displays the results of the concentration profile as a function of vertical distance in the mixing tank for a solids wt. % of 4.4. The profile is very similar to that found for the solids wt. % of 2.2 after 16 seconds before about 28 seconds of mixing. However, as time increases, specifically after 35 seconds, the concentration in the tank becomes almost uniform about the center axis of the tank.

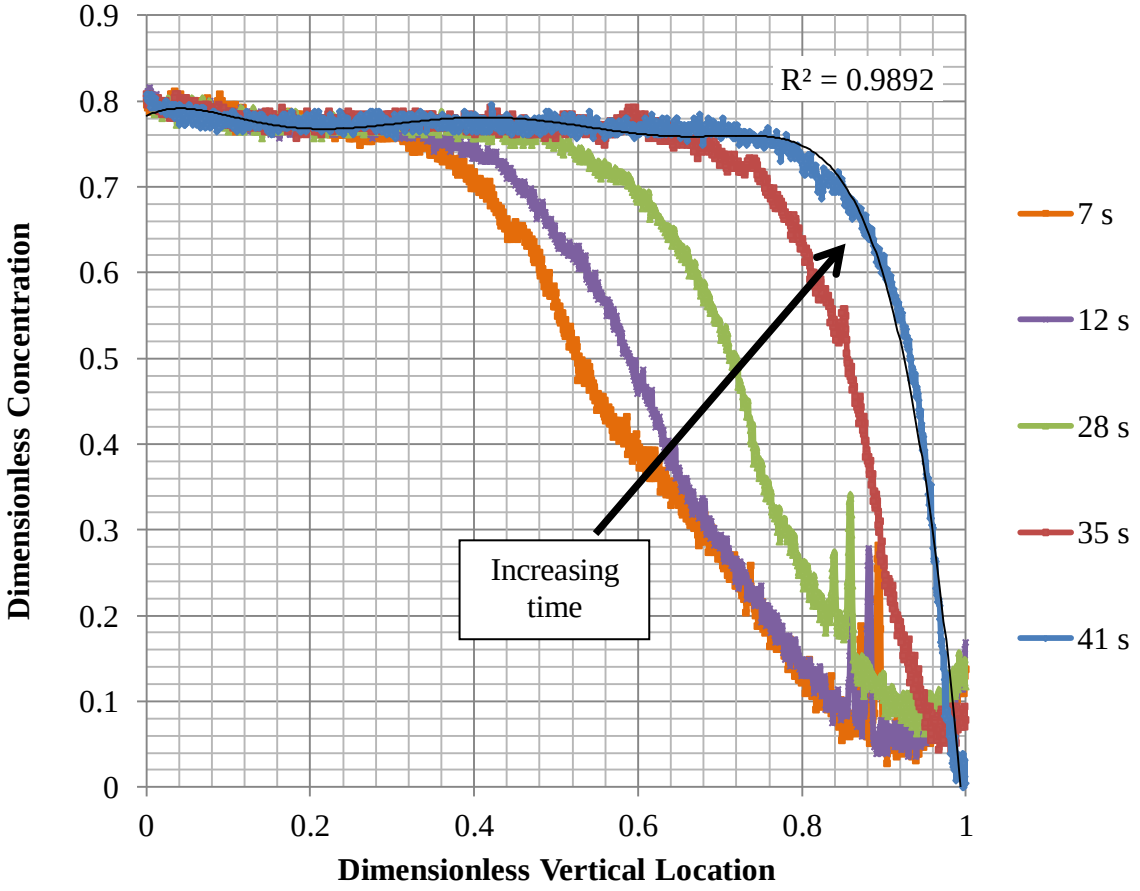

Figure 4.64. Dimensionless concentration as a function of vertical location at different times for a kaolin clay wt. % of 4.4.

The dimensionless concentration levels off at around 0.78 for about 75% of the tank and then the concentration drops off. The data at 41 seconds can be fit with good accuracy (R^2 = 0.9892) with a 6th order polynomial curve. The equation is written as

$$\frac{C}{Co} = -47.18 \cdot \left(\frac{y}{H}\right)^6 + 117 \cdot \left(\frac{y}{H}\right)^5 - 108.79 \cdot \left(\frac{y}{H}\right)^4 + 46.28 \cdot \left(\frac{y}{H}\right)^3 - 8.6609 \cdot \left(\frac{y}{H}\right)^2 + 0.51 \cdot \left(\frac{y}{H}\right) + 0.78 \quad (4.13)$$

The non-dimensional concentration profile as a function of vertical location for a solids wt. % of 7.5% is provided in Figure 4.65. The concentration distribution does not change as a

function of time at around 50 seconds. The concentration remains at about 76% percent of the initial concentration along almost 80% of the center axis of the tank.

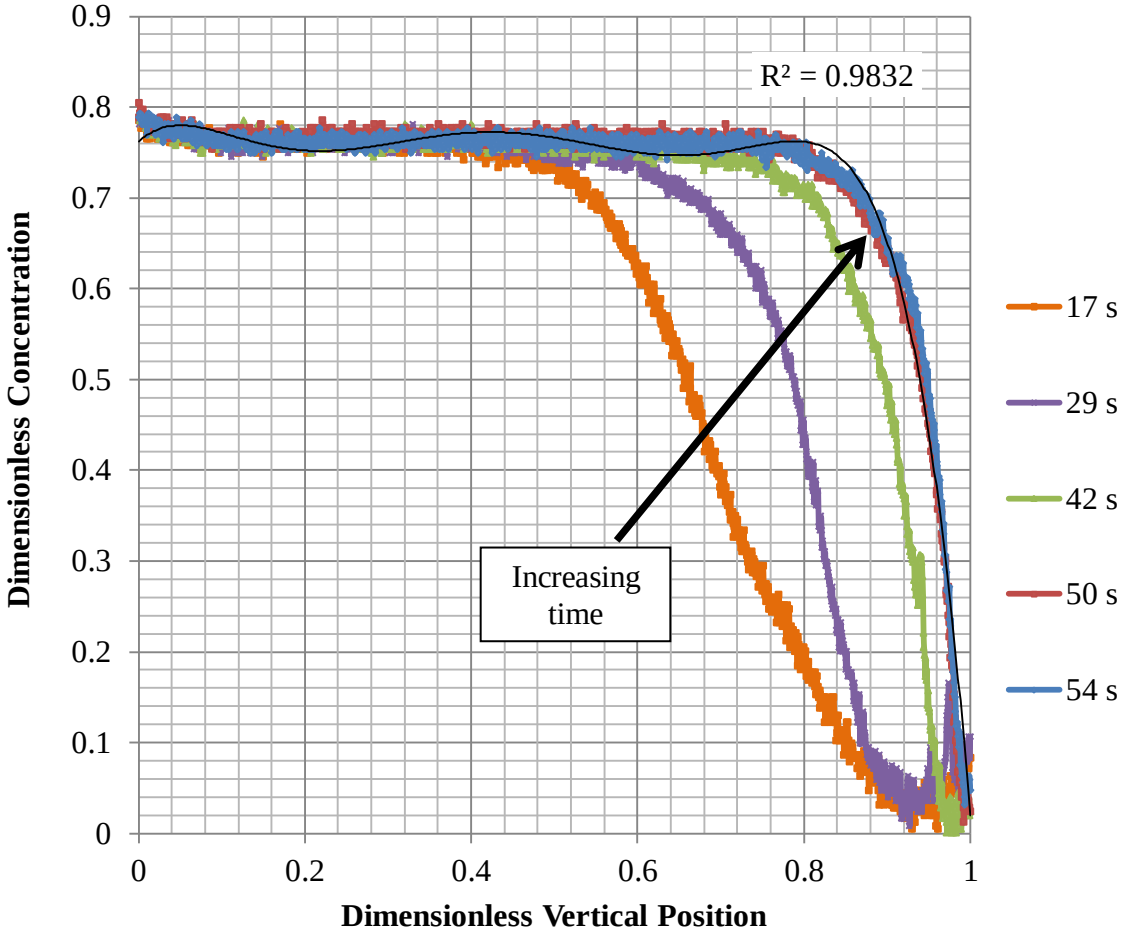

Figure 4.65. Dimensionless concentration as a function of vertical location at different times for a kaolin clay wt. % of 7.5.

Similar to the 4.4 wt. % run, the data can be fit with a 6th order polynomial curve. Equation (4.14) displays the fitted equation.

$$\frac{C}{Co} = -59.11 \cdot \left(\frac{y}{H}\right)^6 + 151.1 \cdot \left(\frac{y}{H}\right)^5 - 144.75 \cdot \left(\frac{y}{H}\right)^4 + 63.69 \cdot \left(\frac{y}{H}\right)^3 - 12.52 \cdot \left(\frac{y}{H}\right)^2 + 0.84 \cdot \left(\frac{y}{H}\right) + 0.76 \quad (4.14)$$

The maximum concentration reaches about 80% of the initial concentration for each of the given wt. % of solids. The maximum concentration occurs at the bottom of the tank and continues to decrease with increased height. The concentration remains position dependent, but after a certain time period is reached, the concentration is no longer time dependent. The concentration remained fairly constant across a larger part of the tank, as the wt. % of the kaolin clay was increased. When a wt. % of 2.2 was used, after about 16.9 s, only about 25% of the tank was at a concentration level of 75% of the initial concentration. On the other hand, at a wt. % of 7.5, after about 16.9 s, more than 50% of the tank was at a concentration level of 75% of the initial concentration.

In solid suspension processes it is important that the mixture is suspended and mixed to the liquid height and information about the concentration profiles can help with various processes such as sampling and additional processing of the mixture. When a mixture has to be pumped out of the tank, information about the concentration at a certain level can be vital to providing the correct pumping conditions.

CHAPTER 5

Conclusion and Suggested Future Work

In the present research work, the hydrodynamics of mixing by a jet mixer was evaluated. Jet mixers were used for liquid blending as well as solid-liquid mixing. Specifically, an experimental and numerical model was developed to simulate the jet mixing operation in both continuous and pulsing mode. The liquid mixing performance was evaluated based on mixing time measurements. Qualitative measurements were of liquid mixing was taken in which the flow patterns created in the mixing tank was observed. Experiments were run to evaluate the flow patterns by dye mixing studies and particle image velocimetry (PIV). The PIV system was constructed and was not only able to provide qualitative results but a direct measurement for the velocity flow field created in the jet mixed tank. Solid suspension studies were run in which the cloud height of different particle sizes were measured. Additional solid-liquid mixing studies were run in which the erosion of a solids bed was measured. Axial concentration profiles were obtained as well to determine the effect of varying amount of cohesive particles on the dispersion of the particulates once suspended.

The results of the CFD studies gave great insight into the jet mixing process. The mixing time decreased exponentially with increasing jet Reynolds number. The mixing time was reduced by half with the addition of a jet. Overall, the quad jet orientation at a height of 0.07625 m had the lowest mixing time of 15.4 s. With the addition of jets, the low mixing zones in the mixing tank is reduced due to increased momentum entering the tank from the discharging jet. When, the jets were pulsed, no enhancement is mixing performance was noticed. However, for the quad jet arrangement, a couple of pulse settings reported mixing times very close to that of the continuous jets. When the jet was pulsed on for 5 seconds and off for 0.5 seconds, the

mixing time was 15.5 s, compared to the continuous jet mixing time in the same configuration, which was 15.4 s. The comparable mixing times can be attributed to local vortices that are created as the jet is first discharged. The local vortices accounts for the time period in which the jet is off and not discharging. One main key in the mixing performance of the jet is the elimination of low mixing zones. As the low mixing zones are decreased, the mixing time decreases.

The mixing time was experimentally measured for single and dual jet mixer configurations. Instead of the 65% homogeneity criteria used for the CFD studies, a 95% homogeneity criterion was used for experiments. Similar to the CFD studies, it was noticed that by adding an extra jet, the mixing time was reduced about half. Also similar to the CFD studies, a pulsing jet did not enhance the mixing performance in the tank. For all the runs, the mixing time of the pulsing jet deviated less than 10% at a maximum from the results of the continuous jets. Though the mixing time is not lowered, one advantage of the pulsing jet is that the operating costs can be lowered because fluid is not continuously being discharged.

Solid suspension studies were run in which the cloud height was measured for different particle sizes for varying jet Reynolds numbers. The cloud height increased for decreasing particle sizes. The cloud height increased, as the jet Reynolds number was increased. When the 120 μm particles were used, the cloud height reached up to 90% of the liquid level. On the other hand, the jets were not able to suspend the 700 μm particles above 20% of the liquid level. The results showed that below a critical value, the cloud height was not very dependent on the jet Reynolds number. Above about 23800, there was a stronger dependence on the jet Reynolds number as there was a steeper increase in cloud height. As the jet nozzle was lowered closer to the bottom of the tank, the homogeneity in the tank was decreased. An analytical model was

developed to compare the results. The model predicted the cloud height fairly well at the highest jet Reynolds numbers studied. At a jet Reynolds number of 28000 – 28500, the maximum error from the experimental results is only 2%. There are however, several improvements that can be made to the model to improve the accuracy.

From the CFD studies, shear stress maps on the bottom surface were also computed. The shear stress maps were able to show the areas on the bottom surface which are least affected by the jet and the shear stress magnitudes. The maximum shear stress and average shear stress on the bottom surface increased as the jet height from the bottom was decreased. On the other hand, as the jet height was decreased, the low mixing zones on the bottom was increased. The shear stress maps provided vital information into the performance of jet mixers in the erosion of solids beds and suspension of solids.

Erosion profiles were measured for different sizes of non-cohesive particles using a non-intrusive technique. Cohesive particles could not be measured in combination with the non-cohesive particles using this technique because the cohesive particles were so small that it tended to cloud the water and make visibility very poor. The erosion depth of a solids bed increased as the jet velocity increased. For example, using particles with an average diameter of 700 μm, the erosion depth increased over the same time period by 143% by increasing the jet Reynolds number to 18660 from 6000. The erosion profiles showed that there tends to be two distinct regimes within the data. One regime occurs initially in which the erosion rate is higher. The two different regimes were attributed to the modes of erosion occurring. The results of the erosion experiments can be used in CFD simulations in which the solid/liquid boundary condition varies with time due to an impinging jet.

Concentration profiles in the center axis of the mixing tank were measured for cohesive particle mixtures. The results showed that the different wt. % of initial kaolin clay material used had very little effect on the overall profile in the tank. The major differences that were found for the runs in which different wt. % of kaolin was used was that for increasing wt. % of kaolin, it took longer under the same conditions to reach the same level of mixing. The less solids particles there were in the tank, the faster they became mixed.

5.1 Future Work

To further increase the knowledge base in the area of jet mixing there are several more studies that can be run and some recommendations to improve some of the existing studies.

1. A much wider range of parametric studies should be run using the pulsing jet mixers. The current study showed that it may be possible to slightly improve the mixing performance in terms of mixing time. Studies should be run with pulses that include varying periods. For example in the current study, experiments were run using a discharge time of 5 seconds and an off period of 0.5 seconds. Future studies can explore using one pulse with a discharge time of 5 seconds and off period of 0.5 seconds, followed by a subsequent pulse which has a different discharge and off time. Also, alternating pulsing jets can possibly be explored where jets are pulsing at different times.
2. Further solid suspension studies should be run to optimize the jet mixer performance. Parametric studies should be run that include a wider range of jet Reynolds numbers, number of jets, different jet angles, and a wider range of solids concentrations.
3. A more in-depth CFD model should be developed that can simulate the erosion of a solids bed. The equations from the fitted curves of the erosion profiles can be used for the solid/liquid boundary condition.

4. The analytical model that was developed to predict the cloud height of suspended particles should be improved. The current model was based on a single particle, so other parameters should be added to the model to include the effects of multiple particles, including particle-particle interactions. The current model used spherical particles as well, so the future model should include term(s) in the model that account for the geometry of the particles. Also, tests should be run with completely spherical models. Though the equation given by Rajaratnam has been widely used in literature, a more accurate model for the wall jet created by an impinging jet can be used. Furthermore, the drag function in the model can be improved by using a model that accounts for the drag when particles are in close proximity to boundaries and additional particles.
5. The effect of cohesion in a solids bed that contains both non-cohesive and cohesive particles should be examined. If possible, the way the solids bed is eroded and the concentration profile that is created due to the mixed particles should be looked at. However, the techniques in the current study will not be applicable. Different equipment, such as one that uses ultrasound technology, will have to be used to perform the study.

References

(June 2009). "Radioactive waste management." Retrieved August, 2010, from http://www.world-nuclear.org/info/inf04.html.

(1999). *AEA fluidic pulse jet mixer. Innovative technology summary report*.

Abramovich, G. N. (1963). *The theory of turbulent jets*. Cambridge, Mass., M.I.T. Press.

Abulnaga, B. E. (2002). *Slurry systems handbook*. New York, NY, McGraw-Hill.

Amiri, T. Y. and J. S. Moghaddas (2010). Experimental study of the mixing time in a jet-mixed gas-liquid system. *Chemical Engineering & Technology*. 33(2), 327-333.

Anders, J., V. Magi and J. Abraham (2008). A computational investigation of the interaction of pulses in two-pulse jets. *Numerical Heat Transfer: Part A -- Applications*. 54(11), 999-1021.

Arm, S. T. (2010). Nuclear energy: A vital component of our energy future. Chemical Engineering Progress. 106: 28-34.

Augeri, M. J., M. Hubbard and J. L. Thomas (2004). Mixing in large scale tanks: Part iv --- cleaning nuclear waste from tanks. *ASME Conference Proceedings*. 2004(46938), 79-87.

Bamberger, J. A., P. A. Meyer and J. R. Bontha (2005). Technical basis for testing scaled pulse jet mixing systems for non-Newtonian slurries. Richland, WA, Battelle - Pacific Northwest Division.

Bathija, P. R. (1982). Jet mixing design and applications. *Chemical Engineering* 89-94.

Bittorf, K. J. and S. M. Kresta (2003). Prediction of cloud height for solid suspensions in stirred tanks. *Chemical Engineering Research and Design*. 81(5), 568-577.

Brooker, L. (1993). Mixing with the jet set. *Chemical engineer* 30(16).

Burns, C. A., P. A. Gauglitz and R. L. Russell (2010). Shear strength correlations for kaolin/water slurries: A comparison of recent measurements with historical data. Richland, WA, Pacific Northwest National Laboratory.

Caldwell, T. and P. Bhatt (2009). Operational challenges in mixing and transfer of high yield stress sludge waste. Aiken, SC, Savannah River Site.

Chang, C. and P. A. Smith (1996). Flow-induced structure in a system of nuclear waste simulant slurries. *Rheologica Acta*. 35(4), 382-389.

Churnetski, B. V. (1982). Prediction of centrifugal pump cleaning ability in waste sludge. *Nuclear and Chemical Waste Management*. 3(4), 199-203.

Coldrey, P. W. (1978). Jet mixing. *Industrial Chemistry Engineering Course*.

Crow, S. C. and F. H. Champagne (1971). Orderly structure in jet turbulence. *Journal of Fluid Mechanics*. 48(03), 547-591.

Donald, M. B. and H. Singer (1959). Entrainment in turbulent fluid jets. *Chemical Engineering Research and Design*. 37a, 246-258.

Doorne, C. and J. Westerweel (2007). Measurement of laminar, transitional and turbulent pipe flow using stereoscopic-piv. *Experiments in Fluids*. 42(2), 259-279.

Fossett, H. (1951). The action of free jets in mixing of fluids. *Transactions of the Institution of Chemical Engineers*.

Fossett, H. and L. E. Prosser (1949). The application of free jets to the mixing of fluids in bulk. *Proceedings of the Institution of Mechanical Engineers*. 160(1), 224-232.

Fox, E. A. and V. E. Gex (1956). Single-phase blending of liquids. *AIChE Journal*. 2(4), 539-544.

Furman, L. and Z. Stegowski (2011). CFD models of jet mixing and their validation by tracer experiments. *Chemical Engineering and Processing: Process Intensification*. 50(3), 300-304.

Gauglitz, P. A., M. M. Denn and W. R. Rossen (1999). Mechanics of bubbles in sludges and slurries. Richland, WA, Pacific Northwest National Laboratory.

Gauglitz, P. A. e. a. (2010). The role of cohesive particle interactions on solids uniformity and mobilization during jet mixing: Testing recommendations. Richland, WA, Pacific Northwest National Laboratory.

Grenville, R. K. and J. N. Tilton (1996). A new theory improves the correlation of blend time data from turbulent jet mixed vessels. *Chemical Engineering Research & Design*. 74(A3), 390-396.

Grenville, R. K. and J. N. Tilton (1997). Turbulent flow or flow as a predictor of blend time in turbulent jet mixed vessels. *Proceedings of 9th European Conference on Mixing*, 67 - 74.

Grenville, R. K. and J. N. Tilton (2011). Jet mixing in tall tanks: Comparison of methods for predicting blend times. *Chemical Engineering Research & Design*. 89(12A), 2501-2506.

Hamm, B. A., W. L. West and G. B. Tatterson (1989). Sludge suspension in waste storage tanks. *AIChE Journal*. 35(8), 1391-1394.

Harnby, N., M. F. Edwards and A. W. Nienow, Eds. (1992). *Mixing in the process industries*, Butterworth-Heinemann.

Hiby, J. W. and M. Modigell (1978). Experiments on jet agitation. 6th CHISA Congress. Prague.

Hoffman, P. D. (1996). Mixing in a large storage tank. *AIChE Symposium Series*. 268(88), 77-82.

Hylton, T. D., R. L. Cummins, E. L. Youngblood and J. J. Perona (1995). Sludge mobilization with submerged nozzles in horizontal cylindrical tanks. Other Information: PBD: Oct 1995: Medium: ED; Size: 101 p.

Jayanti, S. (2001). Hydrodynamics of jet mixing in vessels. *Chemical Engineering Science*. 56(1), 193-210.

Johari, H. and R. Paduano (1997). Dilution and mixing in an unsteady jet. *Experiments in Fluids*. 23, 272-280.

Kalaichelvi, P., Y. Swarnalatha and T. Raja (2007). Mixing time estimation and analysis in a jet mixer. *ARPN Journal of Engineering and Applied Sciences*. 2(5), 35-43.

Kale, R. N. and A. W. Patwardhan (2005). Solid suspension in jet mixers. *The Canadian Journal of Chemical Engineering*. 83(5), 816-828.

Krone, R. B. (1962). Flume studies of the transport of sediment in estuarial shoaling processes. Berkeley, California University Hydraulic Engineering Lab: 110.

Kurath, D. E., P. A. Meyer, C. W. Stewart and S. M. Barnes (2006). Overview of pulse jet mixer/hybrid mixing system development to support the Hanford waste treatment plant. Richland, WA, Pacific Northwest National Laboratory.

Lane, A. G. C. and P. Rice (1982). Comparative assessment of the performance of the three designs for liquid jet mixing. *Industrial & Engineering Chemistry Process Design and Development*. 21(4), 650-653.

Lane, A. G. C. and P. Rice (1982). An investigation of liquid jet mixing employing an inclined side entry jet. *Transactions of the Institution of Chemical Engineers*. 60(3), 171-176.

Lee, S., R. Richard Dimenna and D. David Tamburello (2008). Advanced mixing models. Aiken, SC, Savannah River National Laboratory.

Lee, S. Y., R. A. Dimenna, R. A. Leishear and D. B. Stefanko (2008). Analysis of turbulent mixing jets in a large scale tank. *Journal of Fluids Engineering*. 130(1), 011104-011113.

Lehrer, I. H. (1981). A new model for free turbulent jets of miscible fluids of different density and a jet mixing time criterion. *Transactions of the Institution of Chemical Engineers*. 59(4), 247-252.

Ludwig, W. and J. Dziak (2009). CFD modeling of a jet-pump mixer. Computer aided chemical engineering. J. Jacek and T. Jan, Elsevier. 26: 671-676.

Macosko, C. W. (1994). *Rheology: Principles, measurements, and applications*. New York Wiley-VCH.

Manjula, P., P. Kalaichelvi and K. Dheenathayalan (2010). Development of mixing time correlation for a double jet mixer. *Journal of Chemical Technology & Biotechnology*. 85(1), 115-120.

Manjula, P., P. Kalaichelvi, C. Shanawaskhan and K. Dheenathayalan (2010). Effect of radial angle on mixing time for a double jet mixer. *Asia-Pacific Journal of Chemical Engineering*. 5(3), 544-551.

Maruyama, T., Y. Ban and T. Mizushina (1982). Jet mixing of fluids in tanks. *Journal of Chemical Engineering of Japan*. 15(5), 342-348.

Mehta, A. (1991). Understanding fluid mud in a dynamic environment. *Geo-Marine Letters*. 11(3), 113-118.

Merzkirch, W. (1987). *Flow visualization*. Orlando, FL, Academic Press.

Meyer, P. A., et al. (2009). Pulse jet mixing tests with noncohesive solids. Richland, WA, Pacific Northwest National Laboratory.

Meyer, P. A. and A. W. Etchells (2007). Mixing with intermittent jets with application in handling radioactive waste sludges. *Chemical Engineering Research and Design*. 85(5), 691-696.

Meyer, P. A., D. E. Kurath, J. A. Bamberger, S. M. Barnes and A. W. Etchells (2006). Scaling laws for reduced-scale tests of pulse jet mixing systems in non-Newtonian slurries: Mixing cavern behavior. Richland, WA, Battelle - Pacific Northwest Division.

Meyer, P. A., D. E. Kurath and C. W. Stewart (2005). Overview of the pulse jet mixer non-Newtonian scaled test program. Richland, WA, Battelle - Pacific Northwest Division.

Mordant, N. and J. F. Pinton (2000). Velocity measurement of a settling sphere. *The European Physical Journal B - Condensed Matter and Complex Systems*. 18(2), 343-352.

Muhammad, I. R. and J. P. Kizito (2011). Evaluation of pulse jet mixing using a scalar quantity and shear stress. *2011 ASME Early Career Technical Journal*. 10, 45-51.

Nguyen, Q. D. and D. V. Boger (1992). Measuring the flow properties of yield stress fluids. *Annual Review of Fluid Mechanics*. 24(1), 47-88.

Okita, N. and Y. Oyama (1963). Mixing characteristics in jet mixing. *Jap. Chem. Eng.* 1, 92-101.

Onishi, Y., R. Shekarriz and K. P. Recknagle (1996). Tank SY-102 waste retrieval assessment: Rheological measurements and pump jet mixing simulations. Richland, WA, Pacific Northwest Laboratory.

Orfaniotis, A., C. Fonade, M. Lalane and N. Doubrovine (1996). Experimental study of the fluidic mixing in a cylindrical reactor. *The Canadian Journal of Chemical Engineering*. 74(2), 203-212.

Partheniades, E. (1962). A study of erosion and deposition of cohesive soils in salt water. Berkeley, University of California. Phd

Patwardhan, A. W. (2002). CFD modeling of jet mixed tanks. *Chemical Engineering Science*. 57(8), 1307-1318.

Patwardhan, A. W. and S. G. Gaikwad (2003). Mixing in tanks agitated by jets. *Chemical Engineering Research and Design*. 81(2), 211-220.

Patwardhan, A. W., A. B. Pandit and J. B. Joshi (2003). The role of convection and turbulent dispersion in blending. *Chemical Engineering Science*. 58(13), 2951-2962.

Patwardhan, A. W. and A. R. Thatte (2004). Process design aspects of jet mixers. *The Canadian Journal of Chemical Engineering*. 82(1), 198-205.

Perona, J. J., T. D. Hylton, E. L. Youngblood and R. L. Cummins (1998). Jet mixing of liquids in long horizontal cylindrical tanks. *Industrial & Engineering Chemistry Research*. 37(4), 1478-1482.

Poloski, A. P., et al. (2004). *Non-newtonian slurry simulant development and selection for pulse jet mixer testing*, Battelle Memorial Institute, Pacific Northwest Division.

Powell, M. R., Y. Onishi and R. Shekarriz (1997). Research on jet mixing of settled sludges in nuclear waste tanks at Hanford and other DOE sites: A historical perspective. Richland, Washington, Pacific Northwest Laboratory.

Rácz, I., P. Dees and J. Groot Wassink (1977). Suspendieren von feststoffpartikeln in axialen strahlmischern, VCH.

Rajaratnam, N., Ed. (1976). *Turbulents jets*. Developments in water science. Amsterdam, Elsevier Scientific Publishing Company.

Ranade, V. V. (1996). Towards better mixing protocols by designing spatially periodic flows: The case of a jet mixer. *Chemical Engineering Science*. 51(11), 2637-2642.

Rassat, S. D., et al. (2003). Physical and liquid chemical simulant formulations for transuranic waste in hanford single-shell tanks. Richland, Washington, Pacific Northwest Laboratory.

Reshma, R., Daas, M., Srivastava, R., and Tansel, B. (2007). Resuspension of non-newtonian slurries by submerged jet-nozzles. *Experimental Thermal and Fluid Science*. 31(7), 771-778.

Revill, B. K. (1992). Jet ixing. Mixing in the process industries: 2nd ed. Harnby et al. Oxford, UK, Buttersworth-Heinemann: 159-183.

Rosendall, B., C. Barringer, F. Wen and K. J. Knight (2006). Validating CFD models of multiphase mixing in the waste treatment plant at the hanford site. *ASME Conference Proceedings*. 2006(42452), 393-402.

Rushton, J. H. (1980). The axial velocity of a submerged axially symmetrical fluid jet. *AIChE Journal*. 26(6), 1038-1041.

Saravanan, K., N. Sundaramoorthy, G. Mohankumar and N. Subramanian (2010). Studies on some aspects of jet mixers i: Hydrodynamics. *Modern Applied Science*. 4(3), 51-59.

Schiller, L. and A. Naumann (1933). Uber die grudlegenden berechungen bei der schwerkraftarfbereitung. *Ver. Deut. Ing.* 77, 318.

Schlichting, H. (1979). *Boundary-layer theory*. New York, McGraw-Hill.

Sendilkumar, K., P. Kalaichelvi, M. Perumalsamy, A. Arunagiri and T. Raja (2007). Computational fluid dynamic analysis of mixing characteristics inside a jet mixer for Newtonian and non-Newtonian fluids. *Proceedings of the World Congress on Engineering and Computer Science*. October 24-25, 2007.

Shamlou, A. and A. Zolfagharian, Eds. (1990). *Suspension of solids in liquid jet stirred vessels*. Fluid mixing 4. New York, NY, Instn. Chem. Eng. Symp. Series.

Simon, M. and C. Fonade (1993). Experimental study of mixing performances using steady and unsteady jets. *The Canadian Journal of Chemical Engineering*. 71(4), 507-513.

Sovacool, B. K. and A. D'Agostino (2010). Nuclear renaissance: A flawed proposition. Chemical Engineering Progress. 106: 29-35.

Tannehill, J. C., D. A. Anderson and R. H. Pletcher (1997). *Computational fluid mechanics and heat transfer* Philadelphia, PA, Taylor & Francis.

Tatterson, G. B. (1991). *Fluid mixing and gas dispersion in agitated tanks*. New York, NY, McGraw-Hill.

Tennekes, H. and J. L. Lumley (1972). *A first course in turbulence*. Cambridge, Massachusetts, The MIT Press.

Thielicke, W. and E. Stamhuis (2010). PIVlab–time-resolved digital particle image velocimetry tool for matlab.

Thien, M. G., B. E. Wells and D. J. Adamson (2010). High-level waste feed certification in hanford double-shell tanks. Richland, WA, Pacific Northwest National Laboratory.

van de Vusse, J. G. (1959). Vergleichende ruhrversuche zum mischen loslicher lussigkeiten 12000 m^3 behalter. *Chem. Ing. Tech.* 31, 583-587.

Wasewar, K. L. (2006). A design of jet mixed tank. *Chemical and Biochemical Engineering Quarterly*. 20(1), 31-46.

Wells, B. E., C. W. Enderlin, P. A. Gauglitz and R. A. Peterson (2009). Assessment of jet erosion for potential post-retrieval k-basin settled sludge. Richland, WA, Pacific Northwest National Laboratory.

White, F. M. (1991). *Viscous fluid flow* Boston, MA, McGraw Hill.

Xu, N. and C. S. O'Hern (2006). Measurements of the yield stress in frictionless granular systems. *Physical Review E*. 73(6), 061303.

Yan-Fang, Y. (2011). Numerical study of the turbulent characteristic in a novel circulating jet mixer.

Yan-fang, Y., M. Hui-bo and W. Jian-hua (2010). A numerical study of the effect of geometrical factors on jet mixing. *2010 2nd International Conference on Computer Engineering and Technology*. 5, 116-120.

Zhang, Q. and H. Johari (1996). Effects of acceleration on turbulent jets. *Physics of Fluids*. 8(8), 2185-2195.

Zughbi, H. D. (2006). Numerical simulation of mixing in a jet agitated horizontal cylindrical tank. *International Journal of Computational Fluid Dynamics*. 20(2), 127 - 136.

Zughbi, H. D. and I. Ahmad (2005). Mixing in liquid-jet-agitated tanks: Effects of jet asymmetry. *Industrial & Engineering Chemistry Research*. 44(4), 1052-1066.

Zughbi, H. D. and M. A. Rakib (2002). Investigations of mixing in a fluid jet agitated tank. *Chemical Engineering Communications*. 189(8), 1038-1056.

Zughbi, H. D. and M. A. Rakib (2004). Mixing in a fluid jet agitated tank: Effects of jet angle and elevation and number of jets. *Chemical Engineering Science*. 59(4), 829-842.